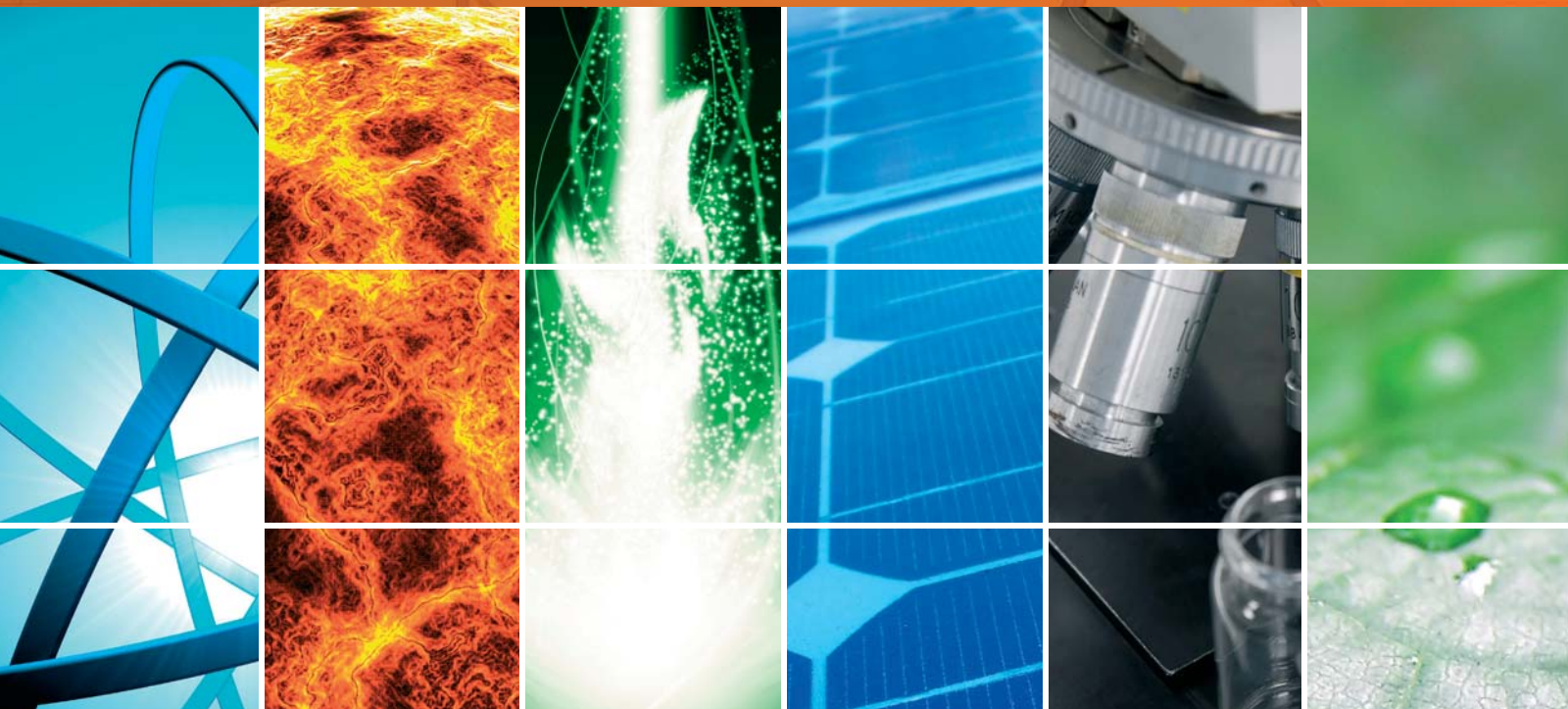


Nanotechnology and Solar Energy

Guest Editors: M. S. A. Abdel-Mottaleb, J. A. Byrne,
and D. Chakarov





Nanotechnology and Solar Energy

International Journal of Photoenergy

Nanotechnology and Solar Energy

Guest Editors: M. S. A. Abdel-Mottaleb, J. A. Byrne,
and D. Chakarov



Copyright © 2011 Hindawi Publishing Corporation. All rights reserved.

This is a special issue published in volume 2011 of “International Journal of Photoenergy.” All articles are open access articles distributed under the Creative Commons Attribution License, which permits unrestricted use, distribution, and reproduction in any medium, provided the original work is properly cited.

Editorial Board

M. Sabry Abdel-Mottaleb, Egypt
Muhammad Abdul Rauf, UAE
Nihal Ahmad, USA
Nicolas Alonso-Vante, France
Wayne A. Anderson, USA
Vincenzo Augugliaro, Italy
Detlef W. Bahnemann, Germany
Ignazio Renato Bellobono, Italy
Raghu N. Bhattacharya, USA
Gion Calzaferri, Switzerland
Vikram L. Dalal, USA
D. Demetriou Dionysiou, USA
Abderrazek Douhal, Spain
Samy El-Shall, USA
Beverley Glass, Australia
Shahed Khan, USA

Cooper H. Langford, Canada
Yuexiang Li, China
Gianluca Li Puma, UK
Panagiotis Lianos, Greece
Stefan Lis, Poland
Gilles Mailhot, France
Ugo Mazzucato, Italy
Jacek Miller, Poland
Franca Morazzoni, Italy
Leonardo Palmisano, Italy
David Lee Phillips, Hong Kong
Xie Quan, China
Tijana Rajh, USA
Saffa Riffat, UK
Peter Robertson, UK
Jean-Louis Scartezzini, Switzerland

P. Joseph Sebastian, Mexico
Panagiotis Smirniotis, USA
Sam-Shajing Sun, USA
Masanori Tachiya, Japan
Gopal N. Tiwari, India
Veronica Vaida, USA
Roel van De Krol, The Netherlands
Mark van Der Auweraer, Belgium
Johannes Vos, Ireland
David Worrall, UK
F. Yakuphanoglu, Turkey
Jimmy C. Yu, Hong Kong
Klaas Zachariasse, Germany
Jincai Zhao, China

Contents

Nanotechnology and Solar Energy, M. S. A. Abdel-Mottaleb, J. A. Byrne, and D. Chakarov
Volume 2011, Article ID 194146, 2 pages

Nanostructures for Enhanced Light Absorption in Solar Energy Devices, Gustav Edman Jonsson, Hans Fredriksson, Raja Sellappan, and Dinko Chakarov
Volume 2011, Article ID 939807, 11 pages

Photocatalytic Enhancement for Solar Disinfection of Water: A Review, J. Anthony Byrne, Pilar A. Fernandez-Ibañez, Patrick S. M. Dunlop, Dheaya M. A. Alrousan, and Jeremy W. J. Hamilton
Volume 2011, Article ID 798051, 12 pages

Studying the Properties of RF-Sputtered Nanocrystalline Tin-Doped Indium Oxide, Abd El-Hady B. Kashyout, Marwa Fathy, and Moataz B. Soliman
Volume 2011, Article ID 139374, 6 pages

Characterization of the Pore Filling of Solid State Dye Sensitized Solar Cells with Photoinduced Absorption Spectroscopy, Carol Olson, Dirk Veldman, Klaas Bakker, and Frank Lenzmann
Volume 2011, Article ID 513089, 11 pages

Synthesis and Application of New Ruthenium Complexes Containing β -Diketonato Ligands as Sensitizers for Nanocrystalline TiO_2 Solar Cells, Ashraful Islam, Surya Prakash Singh, and Liyuan Han
Volume 2011, Article ID 204639, 8 pages

Development of a New Class of Thiocyanate-Free Cyclometalated Ruthenium(II) Complex for Sensitizing Nanocrystalline TiO_2 Solar Cells, Surya Prakash Singh, Ashraful Islam, Masatoshi Yanagida, and Liyuan Han
Volume 2011, Article ID 520848, 5 pages

Nanostructured Mesoporous Titanium Dioxide Thin Film Prepared by Sol-Gel Method for Dye-Sensitized Solar Cell, Yu-Chang Liu, Yun-Fang Lu, Yz-Zhen Zeng, Chi-Hung Liao, Jen-Chieh Chung, and Tsong-Yang Wei
Volume 2011, Article ID 619069, 9 pages

TiO_2 -Based Organic Hybrid Solar Cells with Mn^{+2} Doping, Zühal Alparslan, Arif Kösemen, Osman Örneç, Yusuf Yerli, and S. Eren San
Volume 2011, Article ID 734618, 8 pages

Amphiphilic Ruthenium(II) Terpyridine Sensitizers with Long Alkyl Chain Substituted β -Diketonato Ligands: An Efficient Coadsorbent-Free Dye-Sensitized Solar Cells, Ashraful Islam, Surya Prakash Singh, Masatoshi Yanagida, Mohammad Rezaul Karim, and Liyuan Han
Volume 2011, Article ID 757421, 7 pages

Metal-Free Counter Electrode for Efficient Dye-Sensitized Solar Cells through High Surface Area and Large Porous Carbon, Pavuluri Srinivasu, Surya Prakash Singh, Ashraful Islam, and Liyuan Han
Volume 2011, Article ID 617439, 4 pages

Conversion of Dagang Vacuum Residue into Oxygen-Containing Organic Compounds by Photo-Oxidation with H₂O₂ over TiO₂, Heng-Shen Xie, Zhi-Min Zong, Qing Wei, Tong Liu, Jian-Jun Zhao, Pei-Zhi Zhao, Shi-Hua Zhang, and Xian-Yong Wei
Volume 2011, Article ID 869589, 9 pages

Photocatalytic Activity of Nanosized Cadmium Sulfides Synthesized by Complex Compound Thermolysis, Yingchun Yu, Youxian Ding, Shengli Zuo, and Jianjun Liu
Volume 2011, Article ID 762929, 5 pages

Structure and Physical Properties of Polymer Composite Films Doped with Fullerene Nanoparticles, R. M. Ahmed and S. M. El-Bashir
Volume 2011, Article ID 801409, 6 pages

Structure-Dependent 4-Tert-Butyl Pyridine-Induced Band Bending at TiO₂ Surfaces, Mats Göthelid, Shun Yu, Sareh Ahmadi, Chenghua Sun, and Marcelo Zuleta
Volume 2011, Article ID 401356, 6 pages

Nanocomposite Hole-Extraction Layers for Organic Solar Cells, Jiao Li, Juncheng Liu, Congjie Gao, and Guohua Chen
Volume 2011, Article ID 392832, 5 pages

Nanostructural Materials for Energy Storage Systems, Bronislaw Buczek
Volume 2011, Article ID 340540, 4 pages

Editorial

Nanotechnology and Solar Energy

M. S. A. Abdel-Mottaleb,¹ J. A. Byrne,² and D. Chakarov³

¹ NanoPhotochemistry and Solar Chemistry Lab, Department of Chemistry, Faculty of Science, Ain Shams University, Cairo 11566, Egypt

² Nanotechnology and Integrated BioEngineering Centre, School of Engineering, Faculty of Computing and Engineering, University of Ulster, Newtownabbey BT37 0QB, UK

³ Department of Applied Physics, Chalmers University of Technology, 41296 Gothenburg, Sweden

Correspondence should be addressed to M. S. A. Abdel-Mottaleb, phochem08@photoenergy.org

Received 24 July 2011; Accepted 24 July 2011

Copyright © 2011 M. S. A. Abdel-Mottaleb et al. This is an open access article distributed under the Creative Commons Attribution License, which permits unrestricted use, distribution, and reproduction in any medium, provided the original work is properly cited.

Interest in solar energy conversion and the associated materials research and development has been inspired due to concerns regarding carbon dioxide emissions, job creation, and market instabilities due to the geopolitics and widespread consumption of fossil fuels. The wide introduction of solar powered devices made from nanomaterials has the potential to revolutionize global economic development. Increasing the efficiency and decreasing the costs of solar power are two key areas where nanoscience and nanotechnology can contribute most.

Nanotechnology has assumed a special status in semiconductor materials and catalysts. These two classes of materials could be considered as the key for solar energy conversion. Nanomaterials applied in solar energy conversion may be classified depending on their proposed application. Photocatalysts are a big family of nanomaterials (semiconductors or transition metal oxides) mostly applied in water treatment and solar water splitting for hydrogen production, among other useful applications.

Nanomaterials possess certain desirable properties like high catalytic activity, better stability in aqueous media, comparatively easier preparation techniques, and material economy. Still, nanomaterials suffer from certain drawbacks when they are used in photocatalytic and photoelectrochemical devices.

The fascinating optical properties of nanostructured materials find important applications in a number of solar energy utilization schemes and devices. Nanotechnology provides methods for fabrication and use of structures and systems with size corresponding to the wavelength of visible light. This opens a wealth of possibilities to explore the new,

often of resonance character, phenomena observed when the object size and the electromagnetic field periodicity (light wavelength λ) match.

Titanium dioxide (TiO_2) is an n-type semiconductor that has attracted tremendous attention from researchers worldwide due to its potential applications in environmental protection and energy generation. It has demonstrated unique properties such as high adsorption ability and good photocatalytic activity. Dye-sensitized solar cells (DSSCs) are molecular system that consists of TiO_2 , an anchored molecular photosensitizer, a redox electrolyte, and a platinumized photocathode. The sensitizers play a vital role in DSSCs, and a large number of Ru-complex sensitizers and organic sensitizers have been developed and tested. So far, sensitizers such as black dye, N719, and N3 are known as best sensitizers in DSSC. Black dye-sensitized nanocrystalline TiO_2 solar cells have been reported to yield a solar to electric power conversion efficiency of over 11% under standard AM 1.5 conditions. Much effort has been made to increase photovoltaic performance (stability) of the DSSCs with the development of new sensitizers, electrodes, and nanostructured photoanode materials.

This special issue shows the current trends of research in this branch by presenting two reviews and 14 research articles covering several important areas, ranging from fundamental to applied topics.

Acknowledgments

The present issue would not be possible without the contribution of many persons. We would like to thank

International Journal of Photoenergy and the staff, who have contributed to achieve the best possible quality for this publication. All authors of this issue, and many others, have enthusiastically responded to our call for papers and offered their best scientific knowledge. Around seventy top scientists and engineers in the field have been involved in the peer review of the papers. We wish to thank everyone for his or her contributions, which have made this special issue possible.

M. S. A. Abdel-Mottaleb

J. A. Byrne

D. Chakarov

Review Article

Nanostructures for Enhanced Light Absorption in Solar Energy Devices

Gustav Edman Jonsson, Hans Fredriksson, Raja Sellappan, and Dinko Chakarov

Department of Applied Physics, Chalmers University of Technology, 412 96 Gothenburg, Sweden

Correspondence should be addressed to Gustav Edman Jonsson, gustav.jonsson@chalmers.se

Received 1 November 2010; Accepted 23 March 2011

Academic Editor: Mohamed Sabry Abdel-Mottaleb

Copyright © 2011 Gustav Edman Jonsson et al. This is an open access article distributed under the Creative Commons Attribution License, which permits unrestricted use, distribution, and reproduction in any medium, provided the original work is properly cited.

The fascinating optical properties of nanostructured materials find important applications in a number of solar energy utilization schemes and devices. Nanotechnology provides methods for fabrication and use of structures and systems with size corresponding to the wavelength of visible light. This opens a wealth of possibilities to explore the new, often of resonance character, phenomena observed when the object size and the electromagnetic field periodicity (light wavelength λ) match. Here we briefly review the effects and concepts of enhanced light absorption in nanostructures and illustrate them with specific examples from recent literature and from our studies. These include enhanced optical absorption of composite photocatalytically active TiO_2 /graphitic carbon films, systems with enhanced surface plasmon resonance, field-enhanced absorption in nanofabricated carbon structures with geometrical optical resonances and excitation of waveguiding modes in supported nanoparticle assemblies. The case of Ag particles plasmon-mediated chemistry of NO on graphite surface is highlighted to illustrate the principle of plasmon-electron coupling in adsorbate systems.

1. Motivation

Solar radiation is the main long-term source of energy on earth. All other known energy sources are depletable (fossil), restricted (geothermal and gravitational), or currently not socially adequate (e.g., nuclear, because of the risks of proliferation). Though important, the density of solar power impinging on earth is a mere 1.4 kW/m^2 [1], consequently making efficient energy conversion ever so important in light harvesting devices.

Practiced solar light harvesting schemes can be divided into two basic concepts: solar thermal and solar quantum. The former transforms solar radiation to heat, the latter into electricity or chemical fuels.

Typical devices exemplifying these concepts are the solar heat collectors and photovoltaic systems extracting solar energy in the form of electricity or by inducing a chemical reaction, for instance to produce a chemical fuel such as hydrogen. The difference in the approaches and demands on the light absorber might be understood in comparison with the natural analogues of these alternatives: in the first

case, these are the atmospheric and ocean processes driven by solar radiation (wind, rain, streams, etc.) and in the second the natural photosynthesis and photolytic processes [2] of converting light energy to chemical energy and storing it in the bonds of sugar in plants, algae, and bacteria.

When solar energy is purposefully converted to heat, the aim is simply to absorb as much as possible of all available radiation. In the case of quantum transformation of the photon energy, attention must be paid to the different steps in the transforming process. Therefore, the processes of initial photon absorption, generation of charge carries, their transport, separation, and attachment should be designed in a fashion to achieve a good match between the spectral distribution of the incoming light, absorption properties of the system, and the energy levels of the transition and final states.

Transition energy levels are known to vary with the size and geometry of the active structure [3], and precise structural manipulation has become possible in the wake of nanotechnology and nanoscience hereby allowing fine tuning of transition energy levels. With this stance, all

new construction concepts may be employed to quantum transforming devices.

In this paper, we briefly review some of the novel concepts for photon capture based on the achievements of nanoscience and nanotechnology and illustrate them with specific examples from our studies.

2. Background

The interaction of electromagnetic radiation with matter is classically described by the Maxwell equations in combination with the wavelength-dependent complex dielectric function

$$\hat{\epsilon}(\omega) = \epsilon_1(\omega) + i\epsilon_2(\omega) \quad (1)$$

and the complex refractive index,

$$\hat{n}(\omega) = n(\omega)(1 + i\kappa(\omega)) \equiv \sqrt{\epsilon_1(\omega) + i\epsilon_2(\omega)}. \quad (2)$$

Being a consequence of these fundamental properties, Beer's law explicitly expresses the light field intensity at a given point, along its propagation line in some medium, according to the formula:

$$I_2 = I_1 \exp\left(-\int_{P_1}^{P_2} \alpha(\bar{r}) dl\right), \quad (3)$$

where I_1 and I_2 denote the intensities at the points P_1 and P_2 , respectively, and $\alpha(\bar{r}) = (4\pi/\lambda_0)n\kappa$ where λ_0 denotes the wavelength in vacuum and $n\kappa$ is the purely imaginary part of the refractive index at point \bar{r} [4]. A variant of Beer's law is the Lambert-Beer law which may be formulated as

$$\Delta I_{\text{ext}} = I_0 \left(1 - e^{-\#(\sigma_{\text{abs}} + \sigma_{\text{sca}})z}\right). \quad (4)$$

Here ΔI_{ext} denotes the intensity loss at a point z due to extinction, σ_{abs} and σ_{sca} are the absorption and scattering cross sections, respectively, and $\#$ is the number density of such sites [5]. The term cross section should in this case strictly be interpreted as a measure of probability for a scattering or an absorption event to occur albeit it has area dimensionality. A "cross section" may be attributed to atoms, molecules, or even larger particles, making the Lambert-Beer law generally applicable.

The extinction depth, sometimes referred to as penetration depth, is a quantity defined as the physical distance into a material at which the field intensity has dropped to $1/e$ (barely 37%) relative to the initial intensity [4]. In this case, the Lambert-Beer law states that $-\gamma_e z_{\text{e.d.}} = -1 \Leftrightarrow z_{\text{e.d.}} = 1/\gamma_e$, where $z_{\text{e.d.}}$ is the extinction depth. Using terms of refractive index, we instead obtain $z_{\text{e.d.}} = \lambda_0/4\pi n\kappa$. Structures showing strong optical attenuation are often denoted as optically thick. That is when the physical thickness exceeds $z_{\text{e.d.}}$.

While the behavior of the electromagnetic field, inside a medium, is adequately described as above, the affiliating excitation processes within this medium are also essential to perceive: absorption of photons occurs when the photon energy, $h\nu$, and momentum match those required for an

energy state transition within the absorbing material. A transition strived for in solar quantum transforming devices is the electron-hole pair generation with energy sufficient to drive the envisaged process.

When devising photon capturing structures, for electron-hole pair generation, a conflict arises between the profound properties of light mentioned above and the minority carrier diffusion lengths. On one hand, designing thin solar devices is a virtue, both as smaller dimensions minimize material costs and weight but also as it minimizes the probability for unwanted intrinsic electron-hole pair recombination. Electronic diffusion length is typically $40 \mu\text{m}$ for Si [6], and to minimize bulk recombination processes the cell thickness must not exceed this diffusion length of minority carriers [7]. On the other hand, the Lambert-Beer law states the minimum thickness to obtain reasonable light absorption for a given material system: the typical semiconductor materials have extinction depths on the μm scale, exceeding $100 \mu\text{m}$ for Si in the red end of the solar spectrum. The physical constraints imposed by the mismatch between the optical and electronic length scales constitute a serious challenge for the construction of effective solar devices.

The path to circumvent this dilemma is to find innovative ways of increasing the optical thickness through manipulation of the optical density and/or the optical path length while maintaining smaller physical dimensions. Several prospects of this kind are presented in the following sections.

3. State of the Art

It has long been recognized that the light absorption in Si solar cells can be enhanced by the use of well-designed optical structures. Historically, one of the first approaches to trap light inside an absorbing structure is to use wavelength-scale textured substrates [9]. These include antireflection coatings to minimize the reflection losses at the front surface as well as structures designed to help trap the light within the cell. A frequently used structure consists of pyramids or inverted pyramids anisotropically etched into the top and also often into the rear cell surface [9, 10].

Diffractive optical structures [11], which allow increment of the optically effective cell thickness by a factor of 4-5, are more generally applicable both as the absorbing layers can be thinner and also not necessarily single crystalline in opposition to the method described above.

In the case of dye-sensitized solar cells, light trapping has been achieved by light scattering layers of polycrystalline anatase. These layers have proved to increase the photon to electricity conversion factor by 10%. In addition, the layers have shown to be active in charge carrier generation themselves [12].

Also, photonic crystals, mimicking the electronic band structures in periodic crystals by inclusion of periodic arrays of different refractive index media into an absorbing structure have been investigated as a mean to extending the optical thickness [13–15]. In a longer perspective, more exotic so-called metamaterials [16, 17] with optical properties not

achievable by naturally occurring materials might contribute to this development.

In contrast to the massive, nanostructured semiconductor materials feature stronger light absorption similarly to the metallic systems. On the other hand, semiconductor quantum dots (QDs) are of particular interest for application in solar devices for a different reason. Due to momentum delocalization and relaxation of selection, rules cross sections are enhanced compared to the bulk counterpart [18]. On the basis of impact ionization, single photon generation of multiple excitons has been demonstrated in PbSe, CdSe, and PbS QDs, which raises the theoretical efficiency limit of the solar cells impressively [19–21]. It is noteworthy that carrier multiplication may potentially be achieved with this approach [22].

Concentration and guiding of light on the nanometer scale can be engineered with the help of surface and particle polaritons. Plasmonic structures exhibit large extinction cross sections and present a promising way of increasing the optical thickness of solar energy devices while maintaining a physically thin structure. Plasmons are electromagnetic modes formed by light-matter coupling in the respective material and geometry. This coupling requires materials (medium) with appropriate (sometimes negative) dielectric function and particle dimensions, or surface features, smaller than the wavelength of light. The collective oscillation of conduction electrons (plasmon-polariton) or lattice vibrations in polar crystals (phonon-polariton) provide the necessary conditions [4]. Other aspect of the emerging area of plasmonics is to develop devices that will replace some electric currents with plasmon waves, because plasmons can theoretically carry huge amounts of information squeezed into the nanometer-sized wires. The practical application of plasmonics concepts suffers, however, from the fact that plasmons “live” for only 10 to 100 femtoseconds (see Figure 2) before they decay radiatively into normal light waves or transform to electron-hole pairs and eventually to vibrations (heat). The big challenge is to overcome these losses in order to put the captured light energy in work or to transfer information.

Below we present several approaches, which summarize the different principles of light utilization in nanostructures (see also Figure 1). More could be found in a recent review by Atwater and Polman [23].

Nanoparticles on a thin film of a high refractive index semiconductor may couple impinging light into wave-guided modes propagating in the film. In this way, the lateral extension of the semiconductor defines its optical thickness while the vertical extension defines its physical. Hence the correlation between the two interfering quantities is abolished. This process has been demonstrated to be surprisingly efficient for waveguides with thicknesses on the nanometer scale [24–26].

Whispering gallery modes, WGM, as so-called after the acoustic phenomenon at St. Paul’s Cathedral in London, occur at particular resonant wavelengths of light for a given cavity size and shape. Here the light undergoes total internal reflection at the inner surface of a cavity and becomes trapped within the void (or guide) for timescales of the

order of nanoseconds [27]. Due to ellipsoidal reflection even lateral extension may be miniaturized. Obviously, the increased photon path length increases the total absorption. An illustrative example of this enhanced absorption is the observation of photolysis of water-soluble components inside cloud droplets by ultraviolet/visible radiation [28].

A similar concept for achievement of light guiding is realized by placing a plasmonic metal structure on the backside of a thin semiconductor film. The structure may couple light into surface plasmon polaritons, SPPs, propagating along the metal semiconductor interface and eventually coupling with an e-h pair excitation in the semiconductor as have been shown [29, 30]. The principle of using perpendicular directions for absorption and diffusion is the same as above.

Nanostructures may furthermore be designed to manage the electromagnetic near field; the field energy can be spatially confined to a photoactive region in a way sometimes inspired by the natural photosynthetic antenna system. Optical nanoantennae are small plasmonic particles that resonate at visible and near-IR frequencies. In a semiconductor proximity, the antenna acts as the photon absorber while the energy is coupled to e-h pair excitations within the semiconductor via the enhanced near field [31].

Approaches to realize such structures involve, for instance, carbon nanotubes [32, 33], zeolites [34], and metallic nanoparticles [35–37]. In this context, one may also mention optical rectennas, with the aim to miniaturize the successful radio wave counterpart and directly convert light into a dc current by means of a combined antenna and rectifier structure [18, 38].

Our final example is the utilization of the plasmonic excitations in solar devices by tuning the decay to e-h pairs (Landau damping) [37]. In such systems, the semiconductor is redundant as a generator of charge carriers; both light absorption and charge carrier generation are facilitated in the plasmonic particle. More on plasmonic decay specificity on the nanoparticle material is presented in a paper by Langhammer et al. [39].

4. Illustrative Examples

Our primary interest lies in the enhanced light harvesting in photovoltaic and photocatalytic devices in which the solar light is quantum converted in photochemical or photoelectric processes by the absorbing system. The conversion of solar energy into electricity usually occurs either directly or through thermal conversion. However, it is worth noting that a new mechanism, photon-enhanced thermionic emission, which combines electric as well as thermal conversion mechanisms, is now shown to lead to enhanced conversion efficiencies that potentially could even exceed the theoretical limits of conventional photovoltaic cells [40].

4.1. Optically Active Metal (Plasmonic) Nanoparticles. As articulated above, localized surface plasmon resonances (LSPRs) are collective oscillations of the conduction electrons, which may result in optical absorption cross sections that exceed the geometric cross section by several orders of

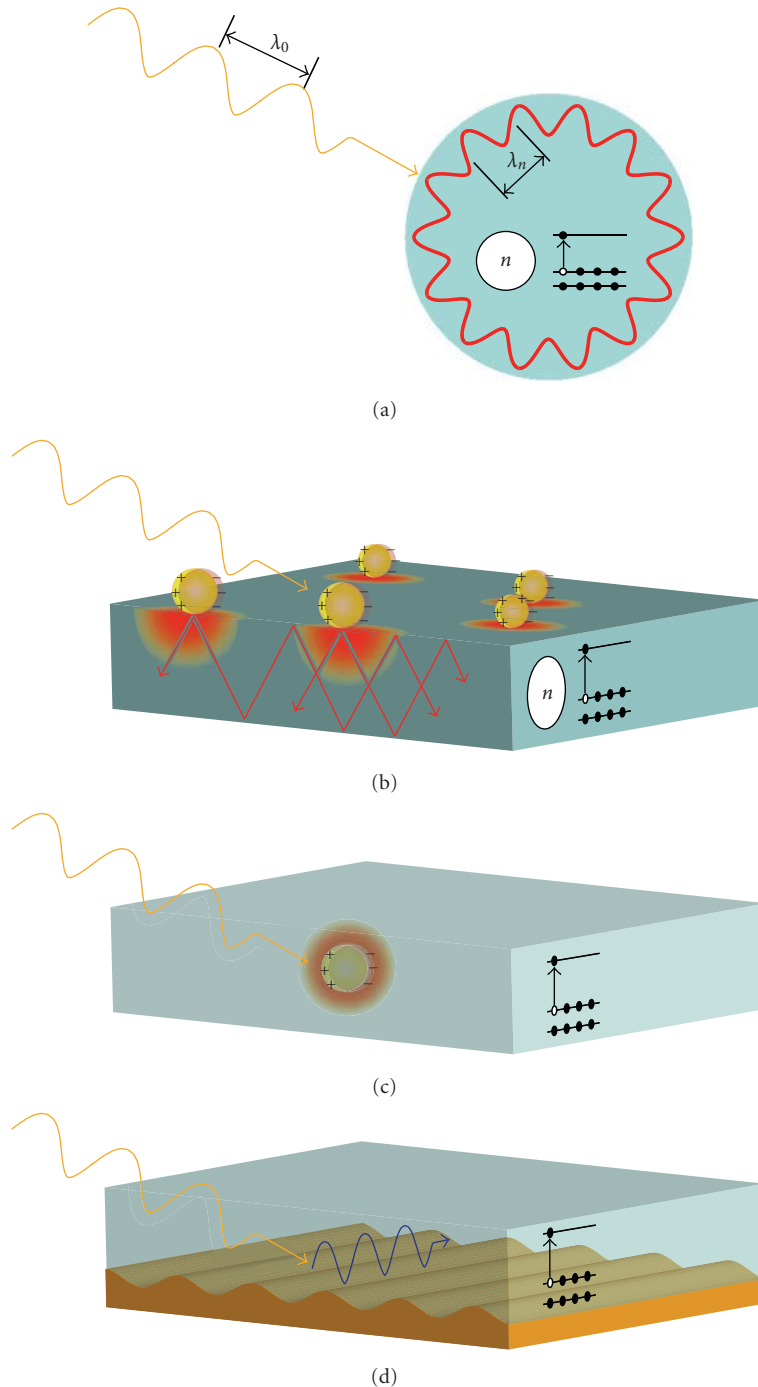


FIGURE 1: Different coupling modes of light in nanostructures and main mechanisms for charge carrier generation following the particle generation. (a) The principle of geometrical optical resonances (WGM) (note the high diffractive index). (b) Plasmon nanoparticles scatter and efficiently couple light into waveguided modes. The prolonged optical paths in (a, b) lead to enhanced total absorption and enhanced e-h-pair generation. (c) The near field intensity and gradients lead to locally increased e-h generation rates. (d) A plasmonic grating at the backside of a semiconductor couples light into SPPs that excite e-h pairs in the semiconductor with direct injection of the carriers to the empty electron bands.

magnitude. The plasmons decay either radiatively (giving rise to dramatic electromagnetic field enhancements, as used for instance, in surface-enhanced Raman spectroscopy) or into (quasi) particles such as electron-hole (e-h) pairs. See Figure 2. For many metals, the resonance wavelength

falls into the near ultraviolet, visible and near infrared regime for nanostructure sizes covering the range of 20–200 nm. What is typical for the mentioned spectral range is that it covers (most of) the energetics of important chemical transformations, for example, bond breaking and

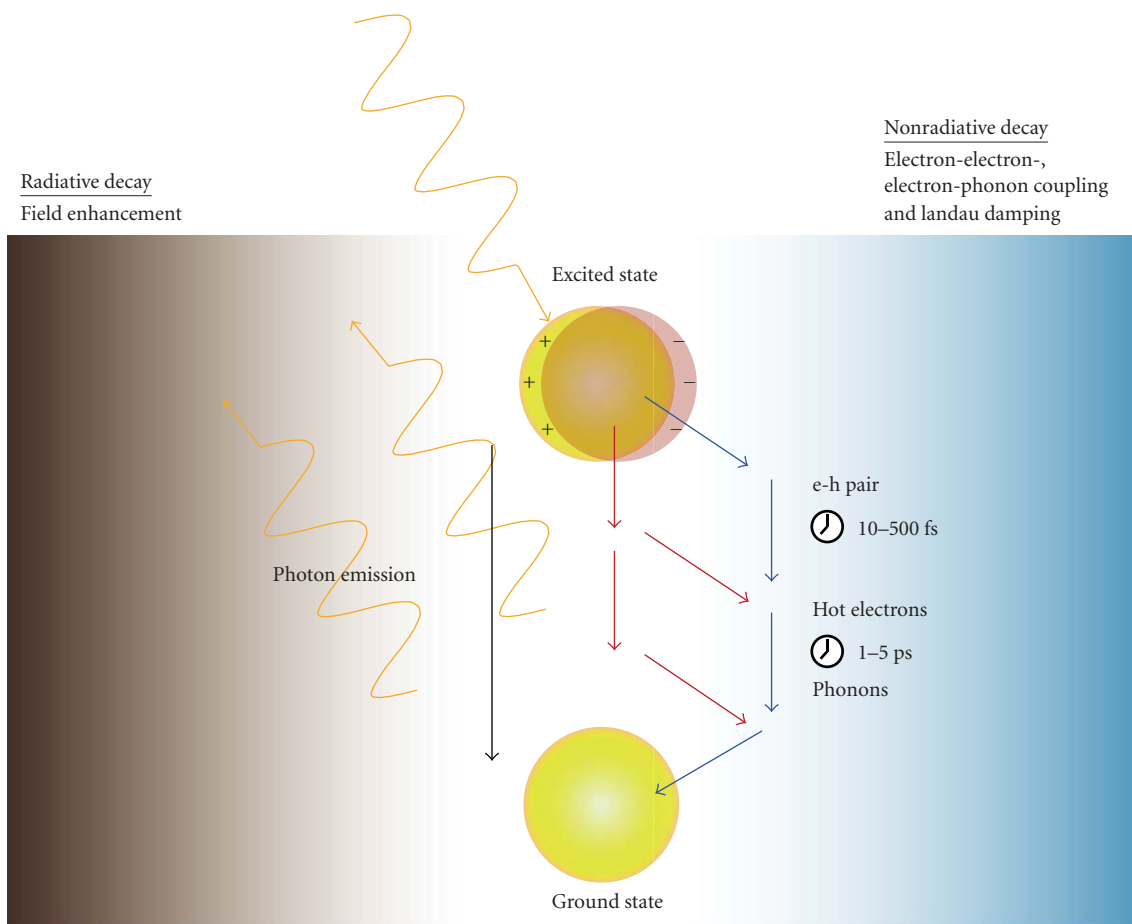


FIGURE 2: The principal decay paths for a localized (particle) plasmon excitation. On the left hand side, the radiative damping by photon emission and accompanying interferential effects. On the right hand side, the nonradiative damping by charge carrier- and direct heat generation. For details see [5].

bond formation (0.5–6.5 eV). This should allow one to create conditions and propose schemes for enhanced (solar) light absorption in nanostructured materials and utilize the deposited energy to run chemical transformations such as water splitting. Figure 4, presenting previously unpublished results, shows that the extinction spectra of these structures are readily tuned via the metal particles' size.

In the case of plasmon-enhanced photochemistry, an area pioneered by Brus in the early eighties [41], both radiative and nonradiative enhancement pathways have been pursued, as illustrated in an extensive review article by Watanabe et al. [42]. To give two representative examples, the photocatalytic degradation of methylene blue was found to be significantly increased on nanocomposite photocatalysts consisting of silver nanoparticles embedded in titania. Radiative energy transfer from the Ag nanoparticles to the semiconductor was claimed to be the origin of increased efficiency [43, 44]. Tian and Tatsuma, on the other hand, reported that ethanol and methanol can be photocatalytically oxidized by gold nanoparticle—nanoporous TiO₂ composites (at the expense of oxygen reduction) under visible light illumination [45]. In this case, photoexcitation of the gold nanoparticles was followed by simultaneous charge transfer

of electrons from the gold to the TiO₂ conduction band and from a donor in solution to the gold nanoparticle.

The main idea behind our photodesorption study [8] was to investigate how the shape and size of silver clusters on a graphite surface will influence the interaction of light with adsorbate covered surface. Since the optical properties of the clusters are dominated by plasmon excitations, the photoinduced transformations will be indicative for their decay mechanisms. This was done by monitoring the changes in cross section for photodesorption of NO. NO was chosen as the probe molecule since its photoactivity on silver is well known. The photodesorption of NO from a silver substrate occurs via hot-electron scattering at the $2\pi^*$ resonance of adsorbed NO with the hot carriers created in the substrate upon photon absorption (substrate-mediated hot electron driven process) [46, 47]. Therefore, an experiment allowing comparison between the desorption cross sections in the cases of resonantly and nonresonantly excited nanoparticles will be indicative for the role of the plasmon particles and their energy dissipation.

The composition of the experimental model system was based on the following reasons. Silver clusters are known for their strong plasmonic response in the blue and near UV

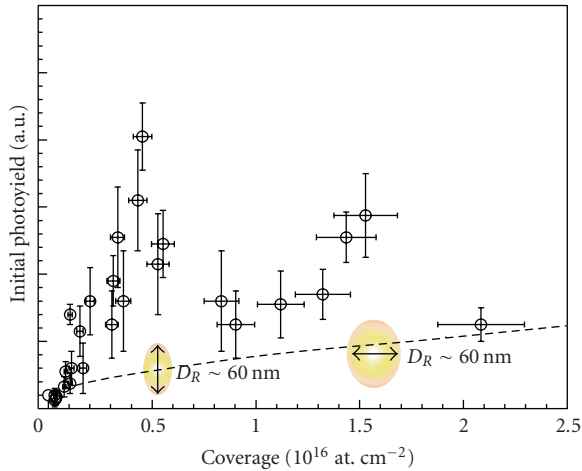


FIGURE 3: Elliptically-shaped silver nanoparticles show two separate plasmon resonance frequencies for light polarized parallel to the short and long axes, respectively. The graph demonstrates the effect of plasmon-mediated photodesorption of NO from Graphite surface (from [8]). The strong size dependent variation of the photoyield is in contrast with the smooth increase of the total Ag coverage (see dashed line).

part of the spectrum [5]. The plasmon resonance energy, when transferred to e-h pairs, will be sufficient to drive the bondbreaking of NO from the surface. From an experimental point of view, it is relatively simple to prepare silver clusters on graphite. Ag clusters on graphite grow in the Volmer-Weber mode, resulting in well-defined individual particles with ellipsoidal shape [48].

The similar work functions of silver and graphite (4.5–4.8 eV) are also beneficial for our study since any changes in photodesorption cross sections will not be related to changes of work-function with increasing silver coverage.

Under pulsed irradiation with 355 nm photons, we observed a clear dependence of the initial photoyield on the average cluster size with a maximum yield at a silver coverage of $4.5 \cdot 10^{15}$ and $1.4 \cdot 10^{16}$ at./cm² (Figure 3). Cluster size is dependent on surface coverage, and these amounts correspond to elliptical clusters with long, respectively short axis of ca. 60 nm. The dashed line in Figure 3 shows that the expected signal increase as due to the larger surface area of the clusters. Obviously, the observations cannot be explained only by the higher cross-section ($\sim \times 6$) from silver surface. We speculate that the enhancement of the total cross-section for NO photodesorption results from the enhanced optical absorption leading to increased hot charge carrier generation in graphite and the hot charge carrier generation in clusters.

4.2. Resonance Cavities and Waveguiding. Previously we have described how plasmonic particles may couple light into thin film waveguides. Here [49] we demonstrate how such coupling may be utilized to self-assemble periodic structures of the light scattering particles.

The experiments were done using suspended $100 \times 100 \mu\text{m}^2$ wide and 40 nm thick membranes of Si₃N₄, supported on the edges by bulk Si [50]. Upon the membranes,

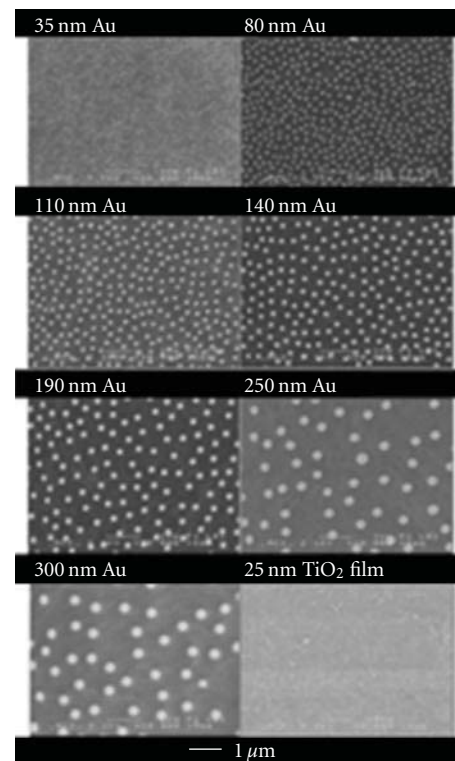
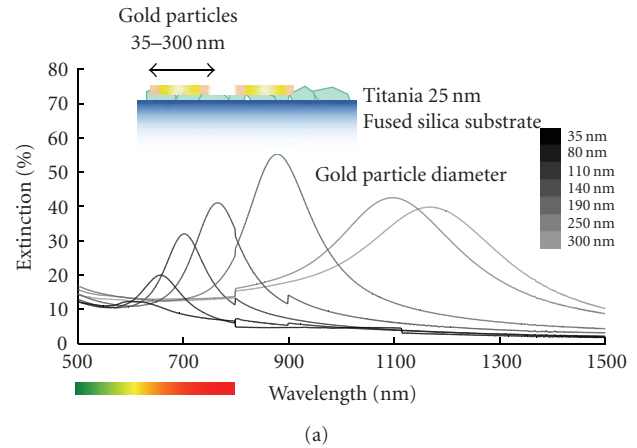


FIGURE 4: (a) Optical extinction spectra for gold nanoparticles with different diameters on a titania thin film. Inset is a schematic of the prepared nanoparticle photocatalysts. (b) SEM image of prepared films and their schematic composition.

a layer of gold, with thickness equivalent of 3 nm, was thermally evaporated. Since gold, in this case, grows in the Volmer-Weber mode; the layer consisted of 15 ± 12 nm sized islands.

When these structure were irradiated with single 5 ns laser pulses in the wavelength range of 532 to 640 nm, gratings formed on the edge of the laser spot and on the edge of the Si₃N₄ membrane. The latter grating formation occurred when the membrane edge and the laser spot coincided. A schematic picture of the grating formation

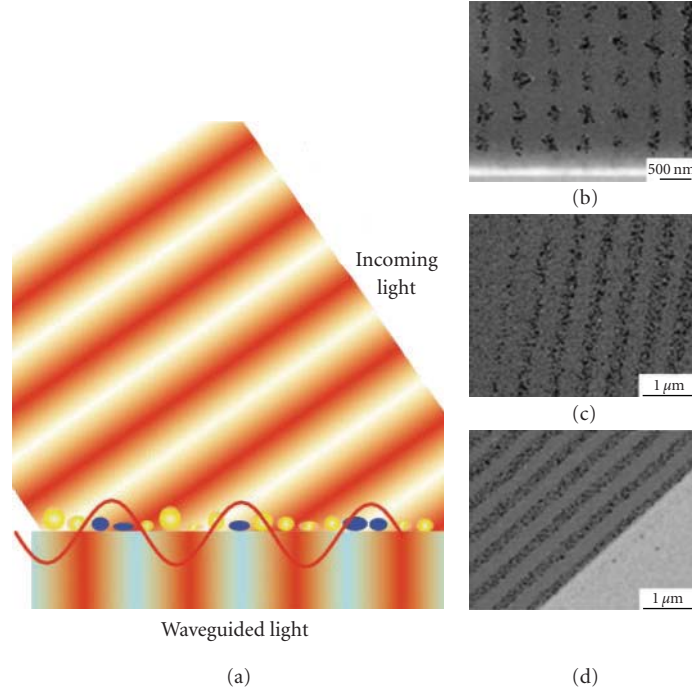


FIGURE 5: (a) Plasmonic particles scatter incoming coherent light into the underlying waveguide analogously with Figure 1(b). Due to stimulated emission of radiation from the particles into the waveguide, the guided light is coherent. Superposition of the incident light and the waveguided results in an amplitude modulated standing wave. Its time averaged intensity is here depicted as a sine curve. The plasmonic particles anneal (coalesce) at the time averaged intensity maxima of this modulated wave (blue particles) hereby forming the gratings. (b) Fringes formed at the intersection of the laser spot edge and the membrane edge. (c) Fringes formed on the laser spot edge. (d) Fringes formed on the membrane edge.

mechanism is presented in Figure 5(a) together with SEM micrographs of resulting gratings, from Figures 5(b) to 5(d).

The key mechanism behind the grating formation is the amplitude modulation of the field intensity on the metal surface arising when the waveguided field and the incident field superimpose. The time averaged energy density may be expressed according to

$$\frac{E_0^2 + E_{wg}^2}{2} + E_0 E_{wg} \cos[(k_{0x} - k_{wg})x + \varphi_0 - \varphi_{wg}]. \quad (5)$$

Here E_0 and E_{wg} denote the amplitudes of the incident and waveguided electric fields, respectively, k_{0x} and k_{wg} denote their wavevectors projected on the propagation direction of the guided wave, and finally, φ_0 and φ_{wg} their phases. The periodicity of the fringes is hereby given by

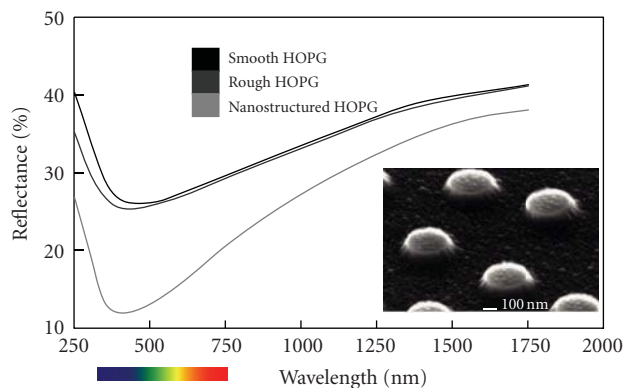
$$\frac{2\pi}{|k_{0x} - k_{wg}|}. \quad (6)$$

This self-assembly of periodic gratings on a waveguide might become a useful tool in the fabrication of plasmonic light trapping devices in combination with particle shape control methods [51].

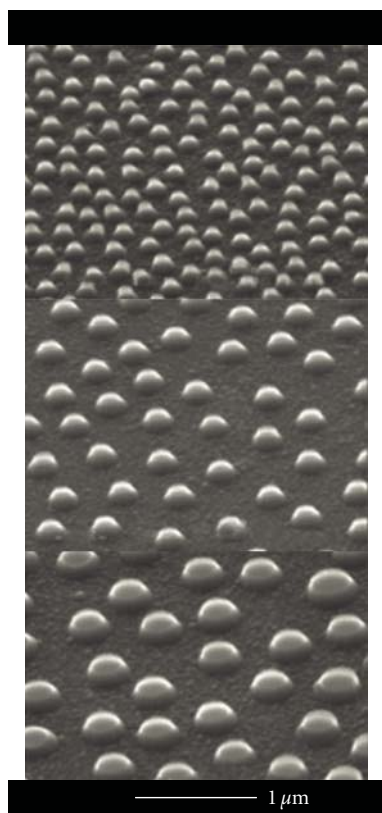
4.3. Geometrical Optical Resonance. Carbon materials are known for their very specific optical properties. For example, the relative high refractive index and moderate dispersion

explain the brilliance of diamonds; the electron structure of amorphous carbon and graphite explains their strong absorption in the visible range [52]. The discovery of new carbon allotropes, the fullerenes, carbon nanotubes, and more recently graphene (single layers of graphite) [53–55] was noticed by directing most of the optical studies of nanosize carbon structures toward them. However, fabrication and exploration of the properties of nanostructures of the conventional carbon materials, glassy carbon (GC), and highly oriented pyrolytic graphite (HOPG) is of great interest per se and for comparison. Recently, we performed a systematic investigation of the correlation between optical absorption and the size of graphite nanostructures [56]. Samples with structure diameters ranging from 160 to 330 nm and heights from 60 to 190 nm were prepared.

In order to better understand the role and properties of carbon (graphite) substrate, we developed a process for fabrication of carbon nanostructures on the surfaces of highly oriented pyrolytic graphite (HOPG) and glassy carbon (GC) samples, using hole-mask colloidal lithography and oxygen reactive ion etching (RIE). Identical preparation schemes applied to the two materials yield structures with remarkably different shape and sizes. For example, 361 nm high and 37 nm diameter structures on glassy carbon compared to 120 nm high and 119 nm diameter structures on HOPG, see Figure 6(b). An important property of these structures, in the context of photo catalytic applications, is their strong optical absorption in the visible range.



(a)



(b)

FIGURE 6: (a) Absorbance spectra recorded for different carbon structures. Nanostructured HOPG corresponds to inset micrograph. Rough HOPG corresponds to a surface like the one observed between the nanoparticles in the inset. (b) Graphite nanostructures fabricated on HOPG with HCL and reactive O-plasma etching.

The disk-like nanostructures were etched out of the basal plane surface of highly oriented pyrolytic graphite, using hole-mask colloidal lithography and oxygen reactive ion etching. Optical absorption spectra for wavelengths between 200 and 2500 nm were measured. Furthermore, electrostatics calculations were conducted to model the optical properties of graphite nanostructures of similar sizes. Both the experimental and the theoretical work revealed

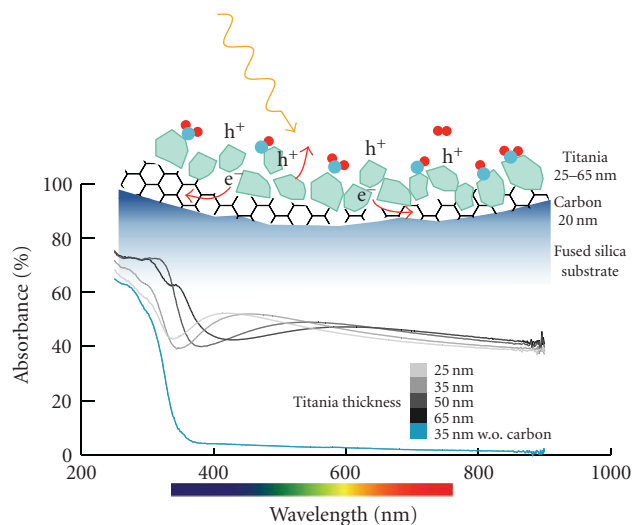


FIGURE 7: Optical absorption of TiO_2/C composite films of different thicknesses compared to 35 nm thick pure titania film. All films are deposited on fused silica substrate.

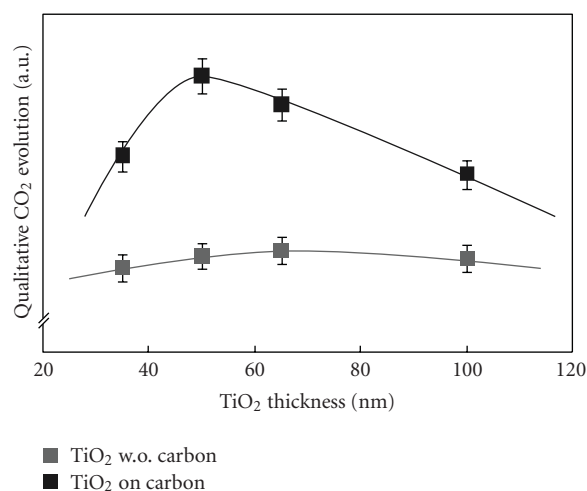


FIGURE 8: CO_2 formation as result of photocatalytic oxidation of methanol under UV illumination. The results for composite films (dark data points) are compared with these for pure titania films (light data points) at several thickness. The solid lines are guides for the eye.

that resonant absorption correlated to the nanostructure diameters and heights. These absorption peaks are red-shifted, from the visible for the smallest structures to near infrared for the largest. Simultaneously, the intensity of the absorption peaks increases for increasing structure heights, while increasing diameters results in decreased absorption.

4.4. Scattering Structures. Nanocrystalline TiO_2 is widely used as photocatalyst due to its exceptional physiochemical properties. However, its wide bandgap (~ 3.2 eV) is the main restriction for it to be used for practical applications in solar energy conversion schemes. Similarly to many other studies [57], our aim is to improve the overall efficiency by enhanced

solar light absorption in the visible regime. We work with TiO₂ deposited on graphitic-like carbon film [58] as shown in Figure 7. Additionally to the enhanced absorption in the visible, the carbon film is expected to promote efficient separation of photogenerated charge carriers because of its anisotropic conductivity for electrons and holes [59, 60]. As the photoreaction occurs on the surface of the TiO₂ catalyst, it is of great interest to investigate thickness dependence of charge transport in the titania films and how the presence of carbon film affects the size of crystallites.

Both carbon and titania films were prepared by e-beam evaporation and DC reactive magnetron sputtering, respectively, at room temperature on a fused silica substrate. Postdeposition annealing was carried out to reduce internal stresses and improve crystallinity in the film at 800°C and 500°C for carbon and TiO₂, respectively. Optical measurements of the composite films with different thicknesses are illustrated in Figure 7. The general observation is that composite films absorb more in the visible than pure titania films. Most importantly, the absorption threshold of TiO₂ has red shifted for composite films.

The catalytic activity of the films was tested in the reaction of photo-oxidation of methanol to CO₂ and water. The measurements were made in a, for this purpose constructed, mini-reactor (~880 μL volume) in batch mode under UV light illumination of 120 mW/cm². The products were monitored in situ by a mass spectrometer coupled to the reactor via a capillary. The rates of CO₂ formation as a function of photocatalysts composition were obtained by monitoring $m/z = 44$ mass spectrometer signal and are summarized in Figure 8. According to Figure 8, composite films clearly have enhanced photoactivity compared to pure titania films. The observed enhancement of photocatalytic activity is assigned to synergy effects at the carbon/TiO₂ interface, resulting in smaller titania crystallites and anisotropic charge carrier transport, which in turn reduces their recombination probability.

Variation in photoactivity with the thickness of the titania layer, both for pure and composite films, can be seen from the figure. The activity gradually increases up to certain thickness after which it starts to decrease. Once the film thickness reaches optimum value (~mean free path distance), it encounters more scattering on its way to the surface. As a consequence, the photoactivity decreases at thicknesses beyond the optimum due to enhanced trapping of charge carriers although the optical absorption volume of the films increases. Overall, this measurement clearly discriminates the effect of thickness on charge transport and photoactivity as discussed above.

5. Conclusions

With this paper, we have brushed the surface of what is possible to achieve in light harvesting with the aid of nanoscience and nanotechnology. Owing to miniaturized light trapping structures and enhanced absorption cross sections, solar devices may be designed with thicknesses well below the charge carrier diffusion lengths with maintained, or even altered, light harvesting efficiency.

Acknowledgments

Support by Swedish Foundation for Strategic Research (SSE, RAM08-0109) and Northern European Innovative Energy Research Programme (N-INNER, project #30938-Solar Hydrogen) is gratefully acknowledged.

References

- [1] R. C. Willson and A. V. Mordvinov, "Secular total solar irradiance trend during solar cycles 21-23," *Geophysical Research Letters*, vol. 30, no. 5, 2003.
- [2] M. B. McElroy, *The Atmospheric Environment : Effects of Human Activity*, Princeton University Press, Princeton, NJ, USA, 2002.
- [3] J. T. Yates Jr., "Photochemistry on TiO₂: mechanisms behind the surface chemistry," *Surface Science*, vol. 603, no. 10-12, pp. 1605-1612, 2009.
- [4] M. Born and E. Wolf, *Principles of Optics : Electromagnetic Theory of Propagation, Interference and Diffraction of Light*, Cambridge University Press, New York, NY, USA, 7th edition, 1999.
- [5] U. Kreibig and M. Vollmer, *Optical Properties of Metal Clusters*, Springer Series in Materials Science, Springer, New York, NY, USA, 1995.
- [6] C. J. Wu and D. B. Wittry, "Investigation of minority-carrier diffusion lengths by electron bombardment of Schottky barriers," *Journal of Applied Physics*, vol. 49, no. 5, pp. 2827-2836, 1978.
- [7] H. J. Hovel, *Solar Cells. Semiconductors and Semimetals*, Academic Press, New York, NY, USA, 1975.
- [8] K. Wettergren, B. Kasemo, and D. Chakarov, "Photodesorption of NO from graphite(0 0 1) surface mediated by silver clusters," *Surface Science*, vol. 593, no. 1-3, pp. 235-241, 2005.
- [9] P. Campbell and M. A. Green, "Light trapping properties of pyramidally textured surfaces," *Journal of Applied Physics*, vol. 62, no. 1, pp. 243-249, 1987.
- [10] P. Campbell and M. A. Green, "High performance light trapping textures for monocrystalline silicon solar cells," *Solar Energy Materials and Solar Cells*, vol. 65, no. 1-4, pp. 369-375, 2001.
- [11] C. Heine and R. H. Morf, "Submicrometer gratings for solar-energy applications," *Applied Optics*, vol. 34, no. 14, pp. 2476-2482, 1995.
- [12] S. Ito, T. N. Murakami, P. Comte et al., "Fabrication of thin film dye sensitized solar cells with solar to electric power conversion efficiency over 10%," *Thin Solid Films*, vol. 516, no. 14, pp. 4613-4619, 2008.
- [13] L. I. Halaoui, N. M. Abrams, and T. E. Mallouk, "Increasing the conversion efficiency of dye-sensitized TiO photocatalytic cells by coupling to photonic crystals," *The Journal of Physical Chemistry B*, vol. 109, no. 13, pp. 6334-6342, 2005.
- [14] P. Bermel, C. Luo, L. Zeng, L. C. Kimerling, and J. D. Joannopoulos, "Improving thin-film crystalline silicon solar cell efficiencies with photonic crystals," *Optics Express*, vol. 15, no. 25, pp. 16986-17000, 2007.
- [15] K. J. Vahala, "Optical microcavities," *Nature*, vol. 424, no. 6950, pp. 839-846, 2003.
- [16] J. B. Pendry, "Negative refraction makes a perfect lens," *Physical Review Letters*, vol. 85, no. 18, pp. 3966-3969, 2000.
- [17] C. M. Soukoulis, M. Kafesaki, and E. N. Economou, "Negative-index materials: new frontiers in optics," *Advanced Materials*, vol. 18, no. 15, pp. 1941-1952, 2006.

- [18] A. P. Alivisatos, "Semiconductor clusters, nanocrystals, and quantum dots," *Science*, vol. 271, no. 5251, pp. 933–937, 1996.
- [19] R. D. Schaller and V. I. Klimov, "High efficiency carrier multiplication in PbSe nanocrystals: implications for solar energy conversion," *Physical Review Letters*, vol. 92, no. 18, Article ID 186601, 4 pages, 2004.
- [20] R. D. Schaller, M. Sykora, J. M. Pietryga, and V. I. Klimov, "Seven excitons at a cost of one: redefining the limits for conversion efficiency of photons into charge carriers," *Nano Letters*, vol. 6, no. 3, pp. 424–429, 2006.
- [21] A. Shabaev, A. L. Efros, and A. J. Nozik, "Multiexciton generation by a single photon in nanocrystals," *Nano Letters*, vol. 6, no. 12, pp. 2856–2863, 2006.
- [22] I. Paci, J. C. Johnson, X. Chen et al., "Singlet fission for dye-sensitized solar cells: can a suitable sensitizer be found?" *Journal of the American Chemical Society*, vol. 128, no. 51, pp. 16546–16553, 2006.
- [23] H. A. Atwater and A. Polman, "Plasmonics for improved photovoltaic devices," *Nature Materials*, vol. 9, no. 3, pp. 205–213, 2010.
- [24] H. R. Stuart and D. G. Hall, "Enhanced dipole-dipole interaction between elementary radiators near a surface," *Physical Review Letters*, vol. 80, no. 25, pp. 5663–5666, 1998.
- [25] H. R. Stuart and D. G. Hall, "Island size effects in nanoparticle-enhanced photodetectors," *Applied Physics Letters*, vol. 73, no. 26, pp. 3815–3817, 1998.
- [26] F. U. J. Tsai, J. Y. Wang, J. J. Huang, Y. W. Kiang, and C. C. Yang, "Absorption enhancement of an amorphous Si solar cell through surface plasmon-induced scattering with metal nanoparticles," *Optics Express*, vol. 18, no. 13, pp. A207–A220, 2010.
- [27] D. S. Wiersma, R. Sapienza, S. Mujumdar, M. Colocci, M. Ghulinyan, and D. L. Pavesi, "Optics of nanostructured dielectrics," *Journal of Optics A: Pure and Applied Optics*, vol. 7, no. 2, pp. S190–S197, 2005.
- [28] B. Mayer and S. Madronich, "Actinic flux and photolysis in water droplets: mie calculations and geometrical optics limit," *Atmospheric Chemistry and Physics*, vol. 4, no. 8, pp. 2241–2250, 2004.
- [29] V. E. Ferry, L. A. Sweatlock, D. Pacifici, and H. A. Atwater, "Plasmonic nanostructure design for efficient light coupling into solar cells," *Nano Letters*, vol. 8, no. 12, pp. 4391–4397, 2008.
- [30] W. Bai, Q. Gan, F. Bartoli et al., "Design of plasmonic back structures for efficiency enhancement of thin-film amorphous Si solar cells," *Optics Letters*, vol. 34, no. 23, pp. 3725–3727, 2009.
- [31] M. Kirkengen, J. Bergli, and Y. M. Galperin, "Direct generation of charge carriers in c-Si solar cells due to embedded nanoparticles," *Journal of Applied Physics*, vol. 102, no. 9, Article ID 093713, 2007.
- [32] K. Kempa, J. Rybczynski, Z. Huang et al., "Carbon nanotubes as optical antennae," *Advanced Materials*, vol. 19, no. 3, pp. 421–426, 2007.
- [33] P. V. Kamat, "Harvesting photons with carbon nanotubes," *Nano Today*, vol. 1, no. 4, pp. 20–27, 2006.
- [34] G. Calzaferri, M. Pauchard, H. Maas, S. Huber, A. Khatyr, and T. Schaafsma, "Photonic antenna system for light harvesting, transport and trapping," *Journal of Materials Chemistry*, vol. 12, no. 1, pp. 1–13, 2002.
- [35] V. P. Zhdanov and B. Kasemo, "Nanometer-sized antenna for enhancement of absorption of light by dye molecules," *Applied Physics Letters*, vol. 84, no. 10, pp. 1748–1749, 2004.
- [36] D. M. Schaadt, B. Feng, and E. T. Yu, "Enhanced semiconductor optical absorption via surface plasmon excitation in metal nanoparticles," *Applied Physics Letters*, vol. 86, no. 6, Article ID 063106, pp. 1–3, 2005.
- [37] M. Westphalen, U. Kreibitz, J. Rostalski, H. Lüth, and D. Meissner, "Metal cluster enhanced organic solar cells," *Solar Energy Materials and Solar Cells*, vol. 61, no. 1, pp. 97–105, 2000.
- [38] R. Corkish, M. A. Green, and T. Puzzer, "Solar energy collection by antennas," *Solar Energy*, vol. 73, no. 6, pp. 395–401, 2002.
- [39] C. Langhammer, B. Kasemo, and I. Zorić, "Absorption and scattering of light by Pt, Pd, Ag, and Au nanodisks: absolute cross sections and branching ratios," *The Journal of Chemical Physics*, vol. 126, no. 19, Article ID 194702, 11 pages, 2007.
- [40] J. W. Schwede, I. Bargatin, D. C. Riley et al., "Photon-enhanced thermionic emission for solar concentrator systems," *Nature Materials*, vol. 9, no. 9, pp. 762–767, 2010.
- [41] L. Brus, "Noble metal nanocrystals: plasmon electron transfer photochemistry and single-molecule raman spectroscopy," *Accounts of Chemical Research*, vol. 41, no. 12, pp. 1742–1749, 2008.
- [42] K. Watanabe, D. Menzel, N. Nilius, and H. J. Freund, "Photochemistry on metal nanoparticles," *Chemical Reviews*, vol. 106, no. 10, pp. 4301–4320, 2006.
- [43] K. Awazu, M. Fujimaki, C. Rockstuhl et al., "A plasmonic photocatalyst consisting of silver nanoparticles embedded in titanium dioxide," *Journal of the American Chemical Society*, vol. 130, no. 5, pp. 1676–1680, 2008.
- [44] P. Christopher, D. B. Ingram, and S. Linic, "Enhancing photochemical activity of semiconductor nanoparticles with optically active Ag nanostructures: photochemistry mediated by Ag surface plasmons," *The Journal of Physical Chemistry C*, vol. 114, no. 19, pp. 9173–9177, 2010.
- [45] Y. Tian and T. Tatsuma, "Mechanisms and applications of plasmon-induced charge separation at TiO₂ films loaded with gold nanoparticles," *Journal of the American Chemical Society*, vol. 127, no. 20, pp. 7632–7637, 2005.
- [46] S. K. So, R. Franchy, and W. Ho, "Photodesorption of NO from Ag(111) and Cu(111)," *The Journal of Chemical Physics*, vol. 95, no. 2, pp. 1385–1399, 1991.
- [47] R. T. Kidd, D. Lennon, and S. R. Meech, "Comparative study of the primary photochemical mechanisms of nitric oxide and carbonyl sulfide on Ag(111)," *The Journal of Physical Chemistry B*, vol. 103, no. 35, pp. 7480–7488, 1999.
- [48] H. Hövel, B. Grimm, M. Pollmann, and B. Reihl, "Cluster-substrate interaction on a femtosecond time scale revealed by a high-resolution photoemission study of the fermi-level onset," *Physical Review Letters*, vol. 81, no. 21, pp. 4608–4611, 1998.
- [49] L. Eurenium, C. Häglund, E. Olsson, B. Kasemo, and D. Chakarov, "Grating formation by metal-nanoparticle-mediated coupling of light into waveguided modes," *Nature Photonics*, vol. 2, no. 6, pp. 360–364, 2008.
- [50] A. W. Grant, Q. H. Hu, and B. Kasemo, "Transmission electron microscopy 'windows' for nanofabricated structures," *Nanotechnology*, vol. 15, no. 9, pp. 1175–1181, 2004.
- [51] R. Jin, Y. C. Cao, E. Hao, G. S. Métraux, G. C. Schatz, and C. A. Mirkin, "Controlling anisotropic nanoparticle growth through plasmon excitation," *Nature*, vol. 425, no. 6957, pp. 487–490, 2003.
- [52] N. Laidani, R. Bartali, G. Gottardi, M. Anderle, and P. Cheyssac, "Optical absorption parameters of amorphous carbon films from Forouhi-Bloomer and Tauc-Lorentz models: a

- comparative study," *Journal of Physics Condensed Matter*, vol. 20, no. 1, Article ID 015216, 2008.
- [53] A. K. Geim and K. S. Novoselov, "The rise of graphene," *Nature Materials*, vol. 6, no. 3, pp. 183–191, 2007.
- [54] S. Iijima, "Helical microtubules of graphitic carbon," *Nature*, vol. 354, no. 6348, pp. 56–58, 1991.
- [55] H. W. Kroto, J. R. Heath, S. C. O'Brien, R. F. Curl, and R. E. Smalley, "C60: buckminsterfullerene," *Nature*, vol. 318, no. 6042, pp. 162–163, 1985.
- [56] H. Fredriksson, T. Pakizeh, M. Käll, B. Kasemo, and D. Chakarov, "Resonant optical absorption in graphite nanostructures," *Journal of Optics A: Pure and Applied Optics*, vol. 11, no. 11, Article ID 114022, 2009.
- [57] A. L. Linsebigler, G. Lu, and J. T. Yates, "Photocatalysis on TiO₂ surfaces: principles, mechanisms, and selected results," *Chemical Reviews*, vol. 95, no. 3, pp. 735–758, 1995.
- [58] R. Sellappan and D. Chakarov, "Nanostructured TiO₂/Carbon films with enhanced photocatalytic activity for water dissociation," *Journal of Molecular Catalysis A*, vol. 335, no. 1-2, pp. 136–144, 2011.
- [59] P. R. Wallace, "The band theory of graphite," *Physical Review*, vol. 71, no. 9, pp. 622–634, 1947.
- [60] Y. Yao, G. Li, S. Ciston, R. M. Lueptow, and K. A. Gray, "Photoreactive TiO₂/carbon nanotube composites: synthesis and reactivity," *Environmental Science and Technology*, vol. 42, no. 13, pp. 4952–4957, 2008.

Review Article

Photocatalytic Enhancement for Solar Disinfection of Water: A Review

**J. Anthony Byrne,¹ Pilar A. Fernandez-Ibañez,² Patrick S. M. Dunlop,¹
Dheaya M. A. Alrouسان,¹ and Jeremy W. J. Hamilton¹**

¹*Nanotechnology and Integrated BioEngineering Centre, University of Ulster, Newtownabbey BT37 0QB, Northern Ireland, UK*

²*Plataforma Solar de Almería (CIEMAT), Crta Senés km 4, 04200 Tabernas, Spain*

Correspondence should be addressed to J. Anthony Byrne, j.byrne@ulster.ac.uk

Received 31 August 2010; Accepted 24 December 2010

Academic Editor: Mohamed Sabry Abdel-Mottaleb

Copyright © 2011 J. Anthony Byrne et al. This is an open access article distributed under the Creative Commons Attribution License, which permits unrestricted use, distribution, and reproduction in any medium, provided the original work is properly cited.

It is estimated that 884 million people lack access to improved water supplies. Many more are forced to rely on supplies that are microbiologically unsafe, resulting in a higher risk of waterborne diseases, including typhoid, hepatitis, polio, and cholera. Due to poor sanitation and lack of clean drinking water, there are around 4 billion cases of diarrhea each year resulting in 2.2 million deaths, most of these are children under five. While conventional interventions to improve water supplies are effective, there is increasing interest in household-based interventions to produce safe drinking water at an affordable cost for developing regions. Solar disinfection (SODIS) is a simple and low cost technique used to disinfect drinking water, where water is placed in transparent containers and exposed to sunlight for 6 hours. There are a number of parameters which affect the efficacy of SODIS, including the solar irradiance, the quality of the water, and the nature of the contamination. One approach to SODIS enhancement is the use of semiconductor photocatalysis to produce highly reactive species that can destroy organic pollutants and inactivate water pathogens. This paper presents a critical review concerning semiconductor photocatalysis as a potential enhancement technology for solar disinfection of water.

1. Introduction

Water is the most important natural resource in the world and availability of safe drinking water is a high priority issue for human existence and quality of life. Unfortunately, water resources are coming under increasing pressure due to population growth, over-use and wastage. The World Health Organization (WHO) estimates that 884 million people lack access to improved water supplies. Many more are forced to rely on sources that are microbiologically unsafe, resulting in a higher risk of waterborne disease transmission, including typhoid, hepatitis and cholera [1–3].

As ever, the poor are the worst affected and, in developing countries, 50% of the population are exposed to polluted water sources which, along with inadequate supplies of water for personal hygiene and poor sanitation, are the main

contributors to an estimated 4 billion cases of diarrhea each year. These factors result in an estimated 2.2 million deaths each year, the majority of which are children under the age of five [1].

The provision of piped-in water supplies is an important long-term goal; however, the WHO and the United Nations Children's Fund (UNICEF) acknowledge that we are unlikely to meet the Millennium Development Goal (MDG) target of halving the proportion of the people without sustainable access to safe drinking water and basic sanitation by 2015. While conventional interventions to improve water supplies at source (point of distribution) have long been recognized as effective in preventing diarrhoea, more recent reviews have shown household-based (point-of-use) interventions to be significantly more effective than those at the source. As a result, there is increasing interest in such household-based

interventions that deliver the health benefits associated with consumption of safe drinking water via low cost technologies [4].

In 2008, Clasen and Haller reported on the cost and cost effectiveness of house-hold based interventions to prevent diarrhoea [4]. They compared the following: chlorination using sodium hypochlorite following the “Safe Water System” (SWS) developed and promoted by the US Centers for Disease Control and Prevention (CDC), gravity filtration using either commercial “candle” style gravity filters or locally fabricated pot-style filters developed by Potters for Peace, solar disinfection following the “SODIS” method in which clear 2 L PET bottles are filled with raw water and then exposed to the sun for 6–48 h, and flocculation disinfection using Procter & Gambles PUR sachets, which combine an iron-based flocculant with a chlorine-based disinfectant and treat water in 10 L batches. They concluded that household-based chlorination was the most cost-effective. Solar disinfection (SODIS) was only slightly less cost-effective, owing to its almost identical cost but marginally lower overall effectiveness. Given that household-based chlorination requires the distribution of sodium hypochlorite, solar disinfection has a major advantage in terms of nonreliance on chemical distribution. Sunlight is widely and freely available on Earth and the combined effects of IR, visible and UV energy from the sun can inactivate pathogenic organisms present in water. There are a number of parameters which affect the efficacy of the SODIS process, including the solar irradiance, the quality of the water to be treated, and the nature of the contamination—as some pathogens are more resistant to SODIS than others. Furthermore, SODIS enhancement technologies may improve the process effectiveness without substantially increasing the cost. One such approach is the use of semiconductor photocatalysis.

Semiconductor photocatalysis uses light along with a semiconductor material to produce highly oxidative species that destroy organic pollutants in water and inactivate pathogenic microorganisms [5–10]. The process occurs at atmospheric pressure and ambient temperature, without the requirement for consumable chemicals (except for oxygen from the air). Photocatalysis may be able to provide a low cost and simple solution to the purification of water in developing regions where solar irradiation can be employed.

This paper presents a critical review concerning semiconductor photocatalysis as a potential enhancement technology for the solar disinfection of water. The purpose of this review is to inform the nonexpert with respect to solar disinfection, and photocatalytic disinfection. For more detailed information the reader is referred to the scientific papers cited.

2. Solar Disinfection of Water (SODIS)

SODIS is a simple and low cost technique used to disinfect contaminated drinking water. Transparent bottles (preferably PET) are filled with contaminated water and placed in direct sunlight for a minimum of 6 hours. Following exposure, the water is safe to drink as the viable pathogen load can be significantly decreased. Simple guidance for the use of SODIS is given in Figure 1. SODIS is used by an estimated

4.5 million regular users worldwide, predominately in Africa, Latin America, and Asia, and is recognised and promoted by the WHO [11, 12].

SODIS harnesses light and thermal energy to inactivate pathogens via a synergistic mechanism [13]. Around 4–6% of the solar spectrum reaching the surface of the Earth is in the UV domain, with maximum reported value of around 50 W/m^2 [14]. UV radiation (200–400 nm) can be classified as UVA (320–400 nm), UVB (280–320 nm), and UVC (200–280 nm). UVC is absorbed by the ozone layer along with a proportion of the UVB; therefore UVA represents the main fragment of solar ultraviolet radiation reaching the earth's surface.

Disinfection of water using solar energy has been carried out since Egyptian times. The process was first studied and reported in scientific literature by London-based scientists Downes and Blunt in the late 1870s [15] and was effectively rediscovered as a low-cost water disinfection method by Acra et al. in the late 1970s [16, 17]. The main findings of this work were that *Escherichia coli* was more resistant to SODIS than other organisms tested, and as such *E. coli* should be used as an indicator organism for SODIS efficiency, akin to the presence of viable faecal coliforms as an indicator of efficacy for conventional disinfection processes. Furthermore, it is the UV component of sunlight, and to a lesser extent the blue end of the visible spectrum, that is mainly responsible for the biocidal action observed during SODIS. Wegelin et al. from the Swiss Federal Institute of Aquatic Science and Technology (Eawag) reported on SODIS in terms of the scope of the process and the dose of radiation required [18]. They concurred with the conclusions of Acra et al. and reported that to obtain a 3-log reduction in the viable numbers of *E. coli* a cumulative exposure dose of 2000 kJ/m^2 (350–450 nm) was required. The same dose was found to inactivate bacteriophage $\phi 2$ whereas picornavirus required twice this dose. Water temperatures above 50°C significantly increased the rate of bacterial inactivation. The research team at Eawag have significantly contributed to the scientific development, standardisation, and promotion of the SODIS process through the development of the online information network and the publication and distribution of the SODIS Manual and associated education resources [12].

Laboratory studies have demonstrated the effects of key operational parameters such as light intensity and wavelength, solar exposure time, availability of oxygen, turbidity, and temperature [19, 20]. The SODIS mechanism is understood to involve a number of biocidal pathways based upon absorption of UVA radiation and thermal inactivation. Direct UVA exposure can induce cellular membrane damage and delay microbial growth [21]. The biocidal action of UVA has also been attributed to the production of reactive oxygen species (ROS) which are generated from dissolved oxygen in water [22] and the photosensitisation of molecules in the cell, and/or any naturally occurring dissolved organic matter that can absorb photons of wavelengths between 320–400 nm, to induce photochemical reactions [23]. The thermal effect has been attributed to the high absorption of red and infrared photons by water. At temperatures below 40°C , the thermal effect is negligible with UVA inactivation

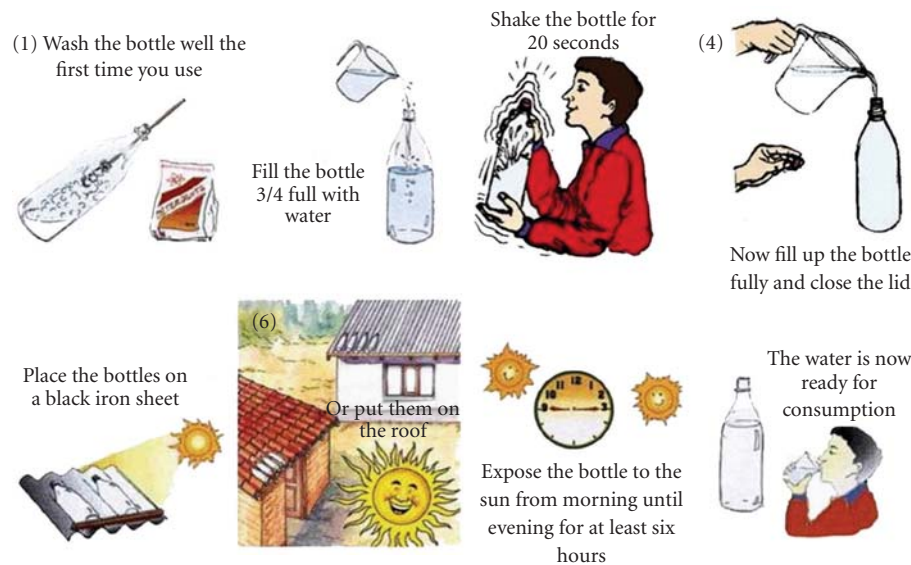


FIGURE 1: SODIS process—www.sodis.ch.

mechanisms dominating the inactivation process. Significant bactericidal action is evident at temperatures above 40–45°C with a synergistic SODIS process observed at temperatures above 45°C [13, 19, 23–25]. Detailed genetic assessment has also been used to probe the biocidal mechanism of SODIS [26, 27].

Researchers have shown SODIS to be effective against a wide range of microorganisms responsible for diarrheal illness [28–30]. The inactivation of resistant protozoa has also been reported [31–33]. Field trials have demonstrated a significant health benefits from consumption of SODIS treated water [34, 35]. The effectiveness of SODIS against cholera was also demonstrated in a Kenyan health impact assessment, where an 86% reduction cholera cases was observed in households regularly using SODIS [36].

Studies to improve the efficiency of the SODIS process using low-cost, commonly available materials have been conducted [37–40]; however, the simple approach of exposing a 2 L PET bottle to full sun for a minimum of 6 hours is the most commonly promoted and practiced method.

3. Enhancement Technologies for SODIS

There are several drawbacks of “conventional” SODIS technology. The use of PET bottles allows for only small volumes to be treated (2–3 L), and the process efficiency is dependent on a range of environmental parameters including the solar irradiance (which depends on the latitude, time of day, and atmospheric conditions), the initial water quality for example organic loading, turbidity, level, and nature of the bacterial contamination. The resistance that microorganisms display to solar disinfection leads to variation in treatment times. Malato et al. reviewed the reported inactivation time required for a range of microorganisms using SODIS under ca. 1 kW/m² global irradiance [10]. These vary enormously from 20 min for *Campylobacter jejuni* to 8 h for *Cryptosporidium parvum* oocysts. For *Bacillus subtilis* endospores,

no inactivation was observed after 8 hours of SODIS treatment. SODIS is user dependent in that it requires the user to ‘time’ the exposure and as such there is no quality assurance in the process and as such, lack of compliance with the recommended protocol is a major issue.

There are a number of ways to improve or enhance the conventional SODIS process, including the design of SODIS bags where the solar dose per volume is increased, the use of UVA dosimetric sensors which indicate to the user when the desired dose has been received by the water, the design of customised SODIS treatment systems which maximise the solar dose using compound parabolic collectors (CPC) and may include UVA feedback sensors for automated control, and the use of semiconductor photocatalysis to enhance the treatment efficacy.

3.1. SODIS Bags. The SODIS method can be enhanced by use of a personal SODIS-reactor which would maximise the area for photon collection and minimise the path length for light penetration through the water to be treated. Furthermore, these SODIS bags could be deployed in emergency situations where access to drinking water is an immediate issue for example flooding or earthquake. The latter application can be limited due to the lack of PET bottles in disaster areas whereas bags have the advantage that they can easily be transported and stored in large quantities. Eawag has launched a project to develop specific SODIS bags, and several bag models are being developed in collaboration with partners from the private sector. A prototype is currently being field tested together with local organisations in Bolivia, DR Congo, Kenya, Nepal, and Nicaragua [41].

3.2. UV Dosimetric Indicators. Professor Mills’ group at the University of Strathclyde has been investigating the use of photocatalytic systems as intelligent inks [42, 43]. As titanium dioxide (TiO₂) is excited by UVA light, these

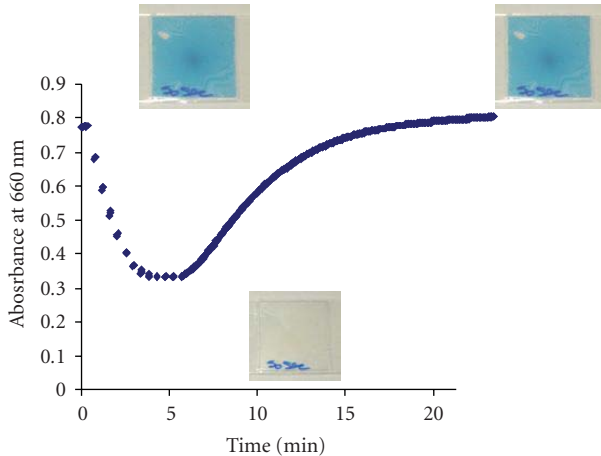


FIGURE 2: Colourimetric UVA dosimetric indicators—UVA exposure photo-reduced MB (blue) the LMB (white) (UVA dose = 9.0 kJ/m^2), MB subsequently reformed via oxidation in the dark.

systems may be used as UVA dosimetric indicators. At the University of Ulster, we have tested a simple prototype system to measure UVA dose utilising the photocatalytic reduction of methylene blue (MB) to leuco-Methylene Blue (LMB) (method adopted from Mills, Lee, and Sheridan [43]).

In the presence of the hole scavenger (glycerol), methylene blue is photocatalytically reduced to colorless leuco-methylene blue, and the rate of decolouration is dependent on the UVA intensity (Figure 2). In the dark and in the presence of oxygen, the reduced form is reoxidised back to methylene blue. This results in a simple reversible UVA dosimetric indicator which could be utilised to provide some quality assurance for the SODIS user. There are a wide range of dyes or inks that could be utilised in these systems to provide simple dosimetric indicators for corresponding to UVA doses required for SODIS.

3.3. Compound Parabolic Collectors. Fernandez-Ibanez and Malato at the Plataforma Solar de Almeria (PSA) in Spain have focused on the use of nonconcentrating solar collectors for the enhancement of solar disinfection. Compound Parabolic Collectors (CPC's) are nonimaging systems which collect diffuse radiation. The collected energy is homogeneously distributed across the absorber surface. CPCs do not rely solely on direct solar radiation and are therefore effective even on cloudy days. In addition, they collect radiation independently of the direction of sunlight and do not require sun tracking.

The SODIS process relies heavily on the solar UVA which, as received at sea level, is composed of roughly similar portions of both direct and diffuse electromagnetic radiation. Given the diffuse nature of the UVA and the cylindrical shape of SODIS bottles, the use of sunlight collecting systems based on nonimaging optics has obvious potential. Navntoft et al. demonstrated the use of CPC technology to enhance the efficacy of SODIS on sunny and cloudy days [25]. The major advantage of CPC technology is that the concentration factor remains constant for all

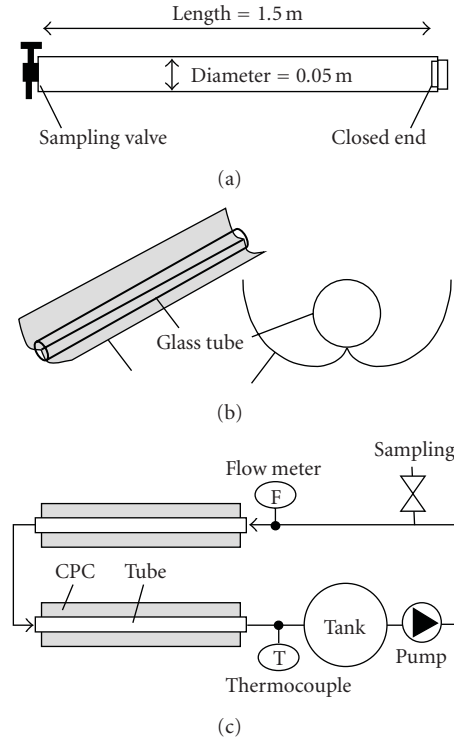


FIGURE 3: (a) Glass tube configuration. (b) Tube with CPC collector configuration. (c) Flow diagram of the solar CPC reactor (with permission from [48]).

values of sun zenith angle within the acceptance angle limit; therefore, it is theoretically possible to design larger volume SODIS systems. For example, recent work showed the effective inactivation of *E. coli* K12 in well water using a 25 L SODIS reactor with CPC [44]. Studies using CPC solar reactors including titanium dioxide as a photocatalyst have shown increased disinfection in comparison to SODIS alone [45–47].

Ubomba-Jaswa et al. investigated the effect of UVA dose on the inactivation efficiency of 3 types of SODIS reactors: borosilicate glass tubes (static batch), borosilicate glass tubes with compound parabolic collector (recirculating batch), and borosilicate glass tubes with CPC (recirculating batch) (Figures 3 and 4) [48]. They used *E. coli* K12 as the model microorganism suspended in natural well water and demonstrated inactivation of approximately 6-log colony forming units (CFU) mL^{-1} following receipt of a total uninterrupted minimum dose of $>108 \text{ kJ/m}^2$ (295–385 nm).

4. Semiconductor Photocatalysis

4.1. Mechanism of Photocatalysis. When a semiconductor is irradiated with light of wavelength equal or greater than its band gap, energy is absorbed resulting in the promotion of electrons from the valence band to the conduction band, and the formation of electron-hole pairs (e^- and h^+) [5]. These charge carriers can recombine, with the energy being reemitted as light or heat, or they may migrate to the catalyst surface where they can participate in redox reactions at the



FIGURE 4: Borosilicate glass tubes with CPC.

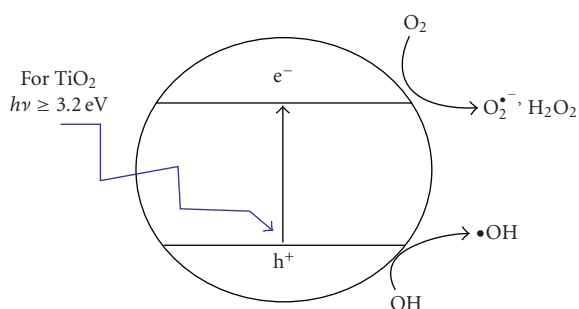


FIGURE 5: Schematic representation of the mechanism of photocatalysis on titanium dioxide particles.

particle-solution interface [8] (Figure 5). The reactive oxygen species (ROS) produced, including the hydroxyl radical, are very active, indiscriminate oxidants [49] destroying a large variety of chemical contaminants in water and also causing fatal damage to microorganisms [50]. The final products of the photocatalytic degradation of pollutants (given long enough treatment time) are CO_2 , H_2O , and respective inorganic acids or salts.

For more detailed information on the mechanisms of semiconductor photocatalysis, the reader is referred to one of the many excellent reviews [5–10].

4.2. Photocatalytic Materials. Several compounds have been investigated as potential semiconductor photocatalysts, including metal oxides (TiO_2 , ZnO , ZrO_2 , V_2O_5 , Fe_2O_3 , SnO_2) and metal sulphides (CdS , ZnS) [51, 52]. Amongst these, the most popular photocatalyst for use in water treatment applications is titanium dioxide. TiO_2 is a wide band semiconductor (band gap = 3.2 eV for anatase); therefore, it requires UV excitation. To improve efficiency in solar applications, visible light active materials are desirable. However, while absorbing a greater number of solar photons, the smaller band gap gives a narrower voltage window to drive the redox reactions at the particle-solution interface. Metal sulphide semiconductors, which absorb in the visible region of the spectrum, tend to undergo photo-anodic corrosion [53]. Considering cost, chemical and photochemical stability,

availability, and lack of toxicity, the most suitable catalyst reported to date for the treatment of water is TiO_2 [54].

4.3. Immobilised versus Suspended Photocatalyst. The photocatalyst can be utilised in aqueous suspension or it may be immobilised on a supporting solid substrate. Most studies have reported that suspension reactors are more efficient due to large surface area available for redox reactions [55], however; the main drawback of using nano or micro-particles in suspension is the requirement for posttreatment separation and recycling of the catalyst, potentially making the treatment more complex and expensive. Therefore, treatment reactors utilising immobilised TiO_2 have gained attention. There are a wide range of methodologies available for the preparation of immobilised photocatalyst films on a range of supporting substrates, and a careful reactor design is required to prevent efficiency loss due to a reduction in catalyst surface area and poor mass transfer of reactants to the photocatalyst surface [56].

4.4. Photocatalytic Disinfection of Water. Matsunaga et al. reported the first application of TiO_2 photocatalysis for the inactivation of bacteria in 1985 [57]. Since then, there have been a large number of research publications dealing with the inactivation of microorganisms including bacteria, viruses, protozoa, fungi, and algae. Blake et al. carried out an extensive review of the microorganisms reported to be inactivated by photocatalysis [51]. In 2007, McCullagh et al. reviewed the application of photocatalysis for the disinfection of water contaminated with pathogenic microorganisms [58]. In 2009, Malato et al. published an extensive review on the decontamination and disinfection of water by solar photocatalysis [10] and, in 2010, Dalrymple et al. reviewed the proposed mechanisms and kinetic models widely used in photocatalytic disinfection studies [59].

In most photocatalytic disinfection studies, the hydroxyl radical is suggested to be the primary species responsible for microorganism inactivation; however, some papers do report involvement of other ROS, such as H_2O_2 , $\text{O}_2^{\bullet-}$ [60–63]. These reactive species can cause fatal damage to microorganisms by disruption of the cell membrane or by attacking DNA and RNA [51]. Other modes of action TiO_2 photocatalysis have been proposed, including damage to the respiratory system within the cells [64] and loss of fluidity and increased ion permeability in the cell membrane [62]. Detailed spectroscopy-based studies attributed cell death to lipid peroxidation of bacterial cell membrane [61–63]. The peroxidation of the unsaturated phospholipids contained in the bacterial cell membrane results in loss of respiratory activity [65] and/or leads to a loss of fluidity and increased ion permeability [62]. It has also been suggested that cell membrane damage can open the way for further oxidative attack of internal cellular components, ultimately resulting in cell death [65].

Research at the University of Ulster has been mainly concerned with the use of immobilised TiO_2 films prepared by the deposition of Evnoik (Degussa) P25 onto a range of supporting substrates, including borosilicate glass, ITO glass, and titanium metal. For example, Alrousan et al.

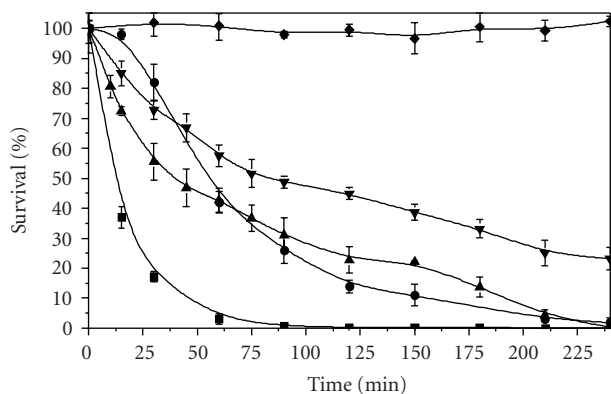


FIGURE 6: Comparison between photocatalytic and photolytic inactivation of *E. coli* in surface and distilled water (TiO_2 , UV, Distilled water) ■, (TiO_2 , UV, Surface water) ●, (UV, Distilled water) ▲, (UV, Surface water) ▼, Dark control ◆ (with permission, from [66]).

reported on the photocatalytic inactivation of *E. coli* in surface water using immobilised nanoparticle TiO_2 films [66]. In this work, P25 was immobilized onto borosilicate glass using a dip coating method. The photoreactor was a custom-built stirred tank reactor which had excellent mixing and good mass transfer properties. The catalyst was irradiated in a back-face configuration that is, the light passed through the glass to excite the photocatalyst on the surface. It was found that the rate of photocatalytic inactivation of *E. coli* was more efficient with UVA- TiO_2 than direct photolytic inactivation with UVA alone, for *E. coli* suspended in both distilled water and surface water (Figure 6). The optimum catalyst loading for the inactivation was determined to be 0.5 mg/cm^2 , approximately half that reported for photocatalytic degradation of formic acid and atrazine in the same reactor, under the same incident light intensity.

The organic and inorganic content of the surface water led to a reduction in the rate of photocatalytic disinfection in comparison to that observed in distilled water. The effect of selected individual constituents present in the surface water was examined to identify the main constituent responsible for the reduction in the rate of photocatalytic disinfection. The presence of inorganic ions, that is, sulphate and nitrate reduced the rate of photocatalytic inactivation, with sulphate having a more pronounced effect than nitrate. The presence of organic matter was found to be the dominating parameter responsible for the decrease in the rate of photocatalytic disinfection. The presence of inorganic ions will lead to a reduction in efficiency either by absorption of light, competing for ROS, or by adsorption to the catalyst surface. Organic matter will compete for ROS and may compete for photon absorption. The efficacy of photocatalytic disinfection will therefore be strongly dependent on the initial water quality. Where the water to be treated is of poor quality, a pre-treatment stage, for example, simple filtration or settling, may be desirable prior to photocatalytic treatment.

Bacterial cells have been described as a rather easy target for disinfectants, with bacterial spores and protozoa

suggested as more robust target organisms. *Clostridium perfringens* spores have been reported to be chlorine resistant at levels used in potable water supplies. Dunlop et al. reported on the photocatalytic inactivation of *Clostridium perfringens* spores on TiO_2 electrodes [67]. The TiO_2 electrodes were made using electrophoretic immobilisation of commercially available TiO_2 powders onto conducting supports, that is, indium-doped tin oxide-coated glass, titanium metal, and titanium alloy. The photocatalytic inactivation of *E. coli* and *C. perfringens* spores in water was observed on all immobilised TiO_2 films under UVA irradiation. The rate of photocatalytic inactivation of *E. coli* was found to be one order of magnitude greater than that of *C. perfringens* spores, demonstrating the greater resistance of the spores to environmental stress. In this work, it was shown that the application of an external electrical bias (electrochemically assisted photocatalysis) significantly increased the rate of photocatalytic disinfection of *C. perfringens* spores. The effect of incident light intensity and initial spore loading were investigated, and disinfection kinetics were determined to be pseudo-first order. This work demonstrated that UVA photocatalysis is effective against bacterial spores which are more resistant to environmental stress, including UVA irradiation, than bacterial cells.

Cryptosporidium species are waterborne, protozoan parasites that infect a wide range of vertebrates. The life cycle involves the production of an encysted stage (oocyst) which is discharged in the faeces of their host. The disease, Cryptosporidiosis, in humans usually results in self-limited watery diarrhoea but has far more devastating effects on immunocompromised patients (e.g., AIDS patients) and can be life-threatening as a result of dehydration caused by chronic diarrhoea. Owing to their tough outer walls, the oocysts are highly resistant to disinfection and can survive for several months in standing water. Cryptosporidium oocysts therefore present as an excellent challenge for disinfection technologies. Sunnotel et al. reported on the photocatalytic inactivation of *Cryptosporidium parvum* oocysts on nanostructured titanium dioxide films (Figure 7) [68].

The photocatalytic inactivation of the oocysts was shown to occur in Ringer's buffer solution (78.4% after 180 min) and surface water (73.7% after 180 min). Scanning electron microscopy (SEM) confirmed cleavage at the suture line of oocyst cell walls, revealing large numbers of empty (ghost) cells after exposure to photocatalytic treatment. No significant inactivation was observed in the oocysts exposed to UVA radiation alone demonstrating the substantial benefit in the addition of TiO_2 as a photocatalyst.

It is clear from the literature, that in lab scale reactors, photocatalysis under UVA irradiation is more efficient than UVA irradiation alone for the disinfection of water contaminated with pathogenic microorganisms. Therefore, it is essential that photocatalytic reactors are tested for disinfection under real sun conditions either on small scale batch (personal use) or at pilot scale (aimed at household or small community use), and using real water sources.

Gelover et al. studied small-scale batch disinfection in plastic bottles containing spring water naturally polluted with coliform bacteria, with and without the addition of

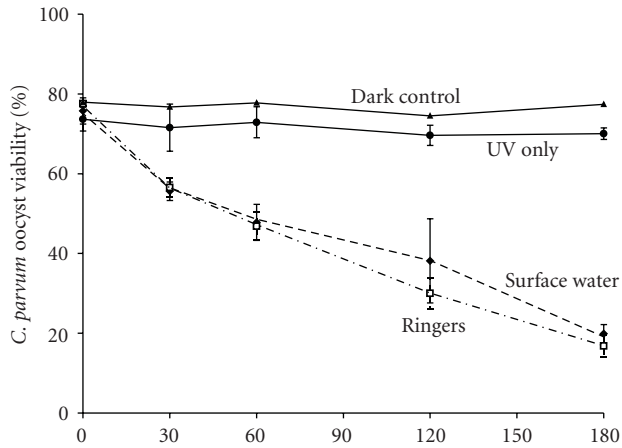


FIGURE 7: Photocatalytic inactivation of *C. parvum* oocysts suspended in Ringer's solution and surface water (with permission from [68]).

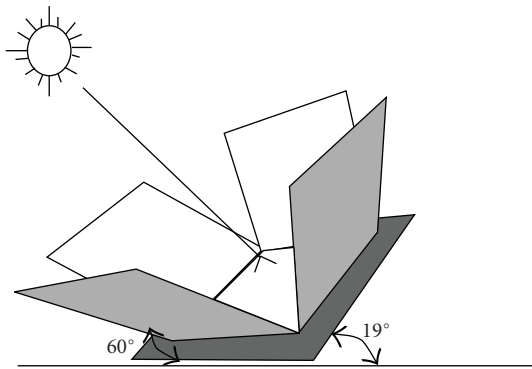


FIGURE 8: Simple solar collector made from 5 wooden sheets covered with aluminium foil (with permission from [69]).

TiO₂ [69]. The bottles were mounted in simple homemade solar collectors (Figure 8). Two litre PET bottles were filled with spring water and exposed to direct sunlight. The microbial loading was typically 2.5×10^3 MPN/100 mL (most probable number) of total coliforms and 9.0×10^2 MPN/100 mL of faecal coliforms.

TiO₂ was coated onto small Pyrex-glass cylinders, using a sol-gel method, and these were placed inside each bottle. It was found that photocatalytically enhanced SODIS was by far more effective than SODIS alone for the inactivation of both the total coliforms and the faecal coliforms (Figure 9). They measured bacterial regrowth following treatment and found that regrowth was observed with SODIS alone, but not with photocatalytically enhanced SODIS. This is an important finding, as bacteria have repair mechanisms which allow recovery following stress/injury and demonstrates the differences in the kill mechanisms involved in SODIS and photocatalytic disinfection.

With respect to larger-scale systems, Fernandez-Ibanez et al. reported on the pilot-scale photocatalytic disinfection of water under real sun conditions using a photoreactor with CPC [70]. The experiments were carried out under

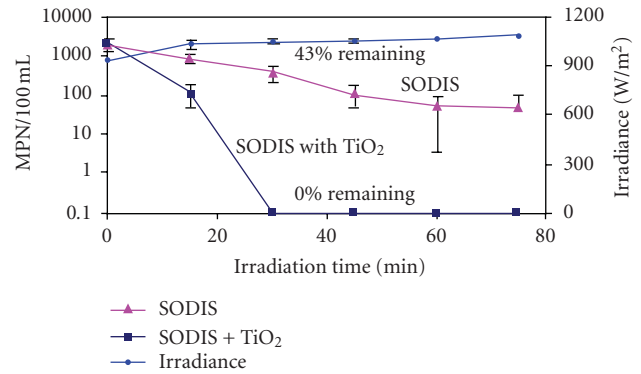


FIGURE 9: Decrease in faecal coliforms in natural spring water exposed to direct sunlight, comparing SODIS to TiO₂-enhanced SODIS (with permission from [69]).

sunlight at the Plataforma Solar de Almeria in southern Spain using compound parabolic collectors. The pilot plant consisted of three CPC collectors, each containing two Pyrex tubes (50 mm inner diameter, 1.5 m long), with a collector surface area of 0.25 m² and a total reactor volume treated of 11 L. Experiments were performed with suspended TiO₂ and, following modification to the reactor, with supported/immobilised TiO₂. In both cases, Degussa, P25 was employed as the photocatalyst. In the immobilised study, the catalyst was fixed onto glass fibre using SiO₂ as an inorganic binder. *E. coli* was used as the model microorganism suspended in distilled water. The photocatalytic suspension reactor was the most efficient, followed by the immobilised photocatalytic reactor, with SODIS being the least efficient treatment (Figure 10).

Further work undertaken by the group at Plataforma Solar de Almeria investigated the effect of UV intensity and dose on SODIS and photocatalytically enhanced SODIS [71]. The aim of the work was to study the dependence on solar irradiation conditions under natural sunlight using three microorganisms, *E. coli* K-12 culture and two wild strains *Fusarium solani* and *Fusarium anthophilum*. Photocatalytic disinfection experiments were carried out with TiO₂ supported on a paper matrix held concentrically within the CPC glass tube reactors described above, and with TiO₂ in the form of a slurry in Pyrex glass bottle reactors. The experiments were performed with different illuminated reactor surfaces, in different seasons of the year, and under changing weather conditions (i.e., cloudy and sunny days). Photocatalysis did not increase the rate of disinfection following receipt of the minimum solar dose; however, the solar-only disinfection was more susceptible to changes in solar irradiation than photocatalytic disinfection, that is, where light intensities were generally low or there was greater availability of diffuse UVA, the inclusion of the photocatalyst provided a significant benefit.

5. Issues to Be Addressed

5.1. *Photoreactor Design.* The SODIS process depends mainly on the UVA wavelengths present in sunlight. Solar

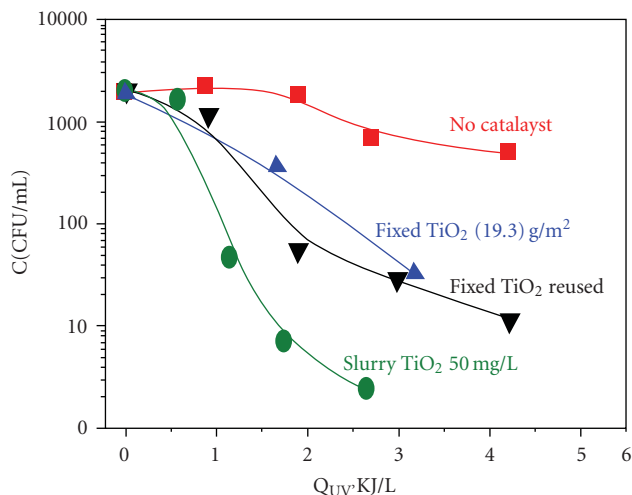


FIGURE 10: *E. coli* inactivation ($C_0 = 1 \times 10^4$ CFU/mL) versus Q_{UV} (energy per unit of volume, kJ/L) in the CPC solar photoreactor. Comparison of TiO_2 slurry (50 mg/L), with supported photocatalyst KN47 ($19.3 \text{ g } TiO_2 \cdot m^{-2}$) and SODIS. With permission from [70].

UV at sea level is composed of roughly similar portions of both direct and diffuse electromagnetic radiation. Without cloud cover, the solar UVA spectrum is ca. 60% direct and ca. 40% diffuse. Therefore, the use of collecting systems based on nonimaging optics has a clear potential, compared to expensive imaging/concentrating optic-based systems. The major advantage with compound parabolic collectors is that collection factor remains constant for all values of sun zenith angle within the acceptance angle limit. Therefore, CPC enhancement can be utilised in the design of larger-scale solar disinfection systems which can be used for household or small community use. A photoreactor for use in developing countries should have the following attributes; high illuminated volume to total volume ratio; ability to operate under a low flow rate when utilising immobilised photocatalyst to maximise the residence time in flow systems; UVA dosimetric indicator (as both SODIS and photocatalytic disinfection are dose dependant); CPC of good quality that is, high UVA reflectivity (for aluminium this is typically 87–90%); reaction vessel with high (90%) UVA transmission (e.g., borosilicate glass); robust under potentially harsh environmental conditions; minimal life-cycle cost; low environmental impact; low maintenance requirements and ease of access to replacement parts; and minimal external power requirement.

If the system is to include a photocatalyst, the reactor design must also ensure the sufficient supply of an electron acceptor, typically dissolved oxygen from the air. In static batch systems, the concentration of dissolved oxygen will be rapidly consumed in the initial stages of the reaction and as water temperature increases the solubility of oxygen in water will be further reduced. For applications in developing countries, this is of paramount importance as the temperature within SODIS reactors can reach 55°C . An alternative may be to introduce other oxidants for example, H_2O_2 ; however, this

would give rise to a dependence on consumable chemicals which is undesirable.

5.2. Photocatalyst Longevity. For application in remote locations and developing regions, the treatment system must be robust, noncomplex, and require only low-level maintenance. Therefore, photocatalyst regeneration is undesirable and more research is required to understand and predict photocatalyst longevity under typical working conditions. To reduce the complexity of the treatment system, immobilised photocatalyst systems are preferred; however, catalyst stripping may be a problem if the immobilisation protocol does not produce a robust hard wearing coating. Also, catalyst fouling by inorganic species present in the water can lead to a reduction in the photocatalytic efficiency over time. Miranda-García et al. investigated the degradation of 15 emerging contaminants (ECs) in a photocatalytic pilot plant utilising TiO_2 immobilised onto glass beads [72]. The CPC plant consisted of two modules of 12 Pyrex glass tubes mounted on a fixed platform tilted 37° (local latitude). Two of the glass tubes were packed with TiO_2 -coated glass spheres (coated with a titania sol-gel). The total illuminated area was 0.30 m^2 and total volume was 10 L, of which 0.96 L was constantly irradiated. The system operated in recirculating batch mode with a flow rate of 3.65 Lmin^{-1} . They found that the degradation of the organic pollutants in distilled water was achieved under solar irradiation, and importantly, after 5 cycles of photocatalysis, the photocatalyst activity was not decreased significantly. Experiments using real water may present catalyst fouling problems.

5.3. Visible Light Active Photocatalyst Materials. The overall efficiency of TiO_2 under natural sunlight is limited to the UV-driven activity (for anatase $\lambda \leq 400 \text{ nm}$), accounting only to ca. 4% of the incoming solar energy on the Earth's surface. Therefore, there has been substantial research effort towards shifting the absorption spectrum of TiO_2 towards the visible region of the electromagnetic spectrum. Different approaches have been attempted including doping the TiO_2 with metal ions [73]. According to the literature, one of the more promising approaches to achieve visible light activity is doping with nonmetal elements including N and S. Since Asahi et al. [74] reported the visible-light photo-activity of TiO_2 with nitrogen doping, many groups have demonstrated that anion doping of TiO_2 extends the optical absorbance of TiO_2 into the visible-light region. However, the number of publications concerning the photocatalytic activity of these materials for the inactivation of microorganisms is limited. Li et al. reported the inactivation of MS2 phage under visible light irradiation using a palladium-modified nitrogen-doped titanium oxide ($TiON/PdO$) photocatalytic fiber, synthesized on a mesoporous-activated carbon fiber template by a sol-gel process [75]. Dark adsorption led to virus removal, and subsequent visible light illumination (wavelengths greater than 400 nm and average intensity of 40 mW/cm^2) resulted in additional virus removal of 94.5–98.2% within 1 h of additional contact time. By combining adsorption and visible-light photocatalysis, $TiON/PdO$ fibers reached final virus removal rates of 99.75–99.94%. EPR

measurements confirmed the production of $\bullet\text{OH}$ radicals by TiON/PdO under visible light illumination. Wu et al. also reported visible-light-induced photocatalytic inactivation of bacteria by composite photocatalysts of palladium oxide and nitrogen-doped TiO₂ [76]. The PdO/TiON catalysts were tested for visible-light-activated photocatalysis using gram-negative organisms that is, *E. coli* and *Pseudomonas aeruginosa* and the gram-positive organism *Staphylococcus aureus*. Their disinfection data showed that the PdO/TiON photocatalysts had a much better visible photocatalytic activity than either palladium-doped (PdO/TiO₂) or nitrogen-doped titanium oxide (TiON). The light source used in this work was a metal halogen desk lamp with a low UV output ($<0.01 \text{ mW/cm}^2$ for $\lambda \leq 400 \text{ nm}$). While these photocatalysts show promise, there was no comparison with undoped TiO₂ and solar-simulated light (which has around 5% UV) was not used.

In many cases, the UV activity of undoped TiO₂ is much greater than the visible light activity of the doped material. Therefore, for solar applications, the photocatalysts should be tested under simulated solar irradiation or under real sun conditions. Indeed, Rengifo-Herrera and Pulgarin recently reported on the photocatalytic activity of N, S codoped and N-doped commercial anatase (Tayca TKP 102) TiO₂ powders towards phenol oxidation and *E. coli* inactivation under simulated solar light irradiation [77]. However, these novel materials did not present an enhancement for the photocatalytic degradation of phenol or the photocatalytic inactivation of *E. coli* under simulated solar light, as compared to Degussa P25. They suggest that while the N, or N-S co-doped TiO₂, may show a visible light response, the localized states responsible for the visible light absorption do not play an important role in the photocatalytic activity.

More research is required to determine if visible light active materials can deliver an increase in the efficiency of photocatalysis under solar irradiation.

6. Conclusions

SODIS is a simple and low cost technique used to disinfect contaminated drinking water. Transparent bottles (preferably PET) are filled with contaminated water and placed in direct sunlight for a minimum of 6 hours. Following exposure, the water is safe to drink as the viable pathogen load can be significantly decreased. The process has approximately 4.5 million regular users, predominately in Africa, Latin America, and Asia and is recognised and promoted by the WHO. However, there are several drawbacks with "conventional" SODIS technology. The use of PET bottles allows for only small volumes to be treated (2-3 L) and the process efficiency is dependent on a range of environmental parameters including the solar irradiance (which depends on the latitude, time of day, and atmospheric conditions), the initial water quality for example, organic loading, turbidity, and level and nature of the bacterial contamination. There are a number of ways to improve or enhance the conventional SODIS process and these include the design of SODIS bags where the solar dose per volume is increased, the use of UV dosimetric indicators which measure the UV

dose and indicate to the user when the desired dose has been received by the water, design of customised SODIS treatment systems which maximise the solar dose and the inclusion of UV feedback sensors for automated control, and the use of semiconductor photocatalysis to enhance the treatment efficacy. Semiconductor photocatalysis has been shown to be effective for the inactivation of a wide range of microorganisms at lab scale and under real sun conditions for both small-scale and large-scale applications. The use of CPC reactors enhances the efficiency of solar disinfection and photocatalytically enhanced solar disinfection. Nevertheless, there are a number of issues to be addressed before photocatalytically enhanced solar disinfection can be effectively deployed in developing regions. These include improvements in photoreactor design and the assessment of photocatalyst longevity under real operating conditions. Future developments in relation to visible light active photocatalytic materials may lead to more efficient solar photocatalysis for the disinfection of water.

Acknowledgments

The authors wish to thank the European Commission for financial support in relation to the SODISWATER project (INCO-CT-2006-031650), the Spanish Ministry of Science and Innovation under the Consolider-Ingenio 2010 programme (Project CSD2006-00044 TRAGUA), and the Department of Employment and Learning (Northern Ireland) for funding DMA Alrousan, and the Department of Employment and Learning (Northern Ireland) for funding DMA Alrousan, and DEL and Invest Northern Ireland for funding under the US-Ireland Initiative for "Degradation Mechanism of Cyanotoxins Using Novel Visible Light-Activated Titania (TiO₂) Photocatalysts".

References

- [1] T. Clasen and P. Edmondson, "Sodium dichloroisocyanurate (NaDCC) tablets as an alternative to sodium hypochlorite for the routine treatment of drinking water at the household level," *International Journal of Hygiene and Environmental Health*, vol. 209, no. 2, pp. 173–181, 2006.
- [2] WHO, "Economic and health effects of increasing coverage of low cost household drinking-water supply and sanitation interventions to countries off-track to meet MDG target 10," 2007.
- [3] J. D. Burch and K. E. Thomas, "Water disinfection for developing countries and potential for solar thermal pasteurization," *Solar Energy*, vol. 64, no. 1–3, pp. 87–97, 1998.
- [4] T. F. Clasen and L. Haller, *Water Quality Interventions to Prevent Diarrhoea: Cost and Cost-Effectiveness*, WHO, 2008.
- [5] A. Mills and S. Le Hunte, "An overview of semiconductor photocatalysis," *Journal of Photochemistry and Photobiology A*, vol. 108, no. 1, pp. 1–35, 1997.
- [6] D. A. Tryk, A. Fujishima, and K. Honda, "Recent topics in photoelectrochemistry: achievements and future prospects," *Electrochimica Acta*, vol. 45, no. 15–16, pp. 2363–2376, 2000.
- [7] D. Bahnemann, "Photocatalytic water treatment: solar energy applications," *Solar Energy*, vol. 77, no. 5, pp. 445–459, 2004.
- [8] V. Augugliaro, M. Litter, L. Palmisano, and J. Soria, "The combination of heterogeneous photocatalysis with chemical

- and physical operations: a tool for improving the photoprocess performance," *Journal of Photochemistry and Photobiology C*, vol. 7, no. 4, pp. 127–144, 2006.
- [9] A. Fujishima, X. Zhang, and D. A. Tryk, "TiO₂ photocatalysis and related surface phenomena," *Surface Science Reports*, vol. 63, no. 12, pp. 515–582, 2008.
- [10] S. Malato, P. Fernández-Ibáñez, M. I. Maldonado, J. Blanco, and W. Gernjak, "Decontamination and disinfection of water by solar photocatalysis: recent overview and trends," *Catalysis Today*, vol. 147, no. 1, pp. 1–59, 2009.
- [11] "SODIS Newsletter 2010 No. 1," Swiss Federal Institute of Aquatic Science and Technology, 2010.
- [12] SODIS, August 2010, <http://www.sodis.ch/index>.
- [13] K. G. McGuigan, T. M. Joyce, R. M. Conroy, J. B. Gillespie, and M. Elmore-Meegan, "Solar disinfection of drinking water contained in transparent plastic bottles: characterizing the bacterial inactivation process," *Journal of Applied Microbiology*, vol. 84, no. 6, pp. 1138–1148, 1998.
- [14] Y. D. Goswami, F. Kreith, and J. F. Kreider, *Principles of Solar Engineering*, Taylor and Francis, Philadelphia, Pa, USA, 2nd edition, 2000.
- [15] A. Downes and T. P. Blunt, "The influence of light upon the development of bacteria," *Nature*, vol. 16, pp. 402–218, 1877.
- [16] A. Acra, Y. Karahagopian, Z. Raffoul, and R. Dajani, "Disinfection of oral rehydration solutions by sunlight," *The Lancet*, vol. 2, no. 8206, pp. 1257–1258, 1980.
- [17] A. Acra, Z. Raffoul, and Y. Karahagopian, *Solar Disinfection of Drinking Water and Oral Rehydration Solutions*, UNICEF, Paris, France, 1984.
- [18] M. Wegelin, S. Canonica, K. Mechsner, T. Fleischmann, F. Pesaro, and A. Metzler, "Solar water disinfection: scope of the process and analysis of radiation experiments," *Journal of Water Supply Research and Technology—Aqua*, vol. 43, no. 4, pp. 154–169, 1994.
- [19] M. Berney, H. U. Weilenmann, A. Simonetti, and T. Egli, "Efficacy of solar disinfection of *Escherichia coli*, *Shigella flexneri*, *Salmonella Typhimurium* and *Vibrio cholerae*," *Journal of Applied Microbiology*, vol. 101, no. 4, pp. 828–836, 2006.
- [20] R. H. Reed, "The inactivation of microbes by sunlight: solar disinfection as a water treatment process," *Advances in Applied Microbiology*, vol. 54, pp. 333–365, 2004.
- [21] A. Hamamoto, M. Mori, A. Takahashi et al., "New water disinfection system using UVA light-emitting diodes," *Journal of Applied Microbiology*, vol. 103, no. 6, pp. 2291–2298, 2007.
- [22] R. Khaengraeng and R. H. Reed, "Oxygen and photoinactivation of *Escherichia coli* in UVA and sunlight," *Journal of Applied Microbiology*, vol. 99, no. 1, pp. 39–50, 2005.
- [23] P. M. Oates, P. Shanahan, and M. F. Polz, "Solar disinfection (SODIS): simulation of solar radiation for global assessment and application for point-of-use water treatment in Haiti," *Water Research*, vol. 37, no. 1, pp. 47–54, 2003.
- [24] J. Blanco, S. Malato, P. Fernández-Ibáñez, D. Alarcón, W. Gernjak, and M. I. Maldonado, "Review of feasible solar energy applications to water processes," *Renewable and Sustainable Energy Reviews*, vol. 13, no. 6-7, pp. 1437–1445, 2009.
- [25] C. Navntoft, E. Ubomba-Jaswa, K. G. McGuigan, and P. Fernández-Ibáñez, "Effectiveness of solar disinfection using batch reactors with non-imaging aluminium reflectors under real conditions: natural well-water and solar light," *Journal of Photochemistry and Photobiology B*, vol. 93, no. 3, pp. 155–161, 2008.
- [26] M. Berney, H. U. Weilenmann, and T. Egli, "Flow-cytometric study of vital cellular functions in *Escherichia coli* during solar disinfection (SODIS)," *Microbiology*, vol. 152, no. 6, pp. 1719–1729, 2006.
- [27] M. Berney, H. U. Weilenmann, and T. Egli, "Gene expression of *Escherichia coli* in continuous culture during adaptation to artificial sunlight," *Environmental Microbiology*, vol. 8, no. 9, pp. 1635–1647, 2006.
- [28] S. C. Kehoe, M. R. Barer, L. O. Devlin, and K. G. McGuigan, "Batch process solar disinfection is an efficient means of disinfecting drinking water contaminated with *Shigella dysenteriae* type I," *Letters in Applied Microbiology*, vol. 38, no. 5, pp. 410–414, 2004.
- [29] J. Lonnen, S. Kilvington, S. C. Kehoe, F. Al-Touati, and K. G. McGuigan, "Solar and photocatalytic disinfection of protozoan, fungal and bacterial microbes in drinking water," *Water Research*, vol. 39, no. 5, pp. 877–883, 2005.
- [30] M. Boyle, C. Sichel, P. Fernández-Ibáñez et al., "Bactericidal effect of solar water disinfection under real sunlight conditions," *Applied and Environmental Microbiology*, vol. 74, no. 10, pp. 2997–3001, 2008.
- [31] K. G. McGuigan, F. Méndez-Hermida, J. A. Castro-Hermida et al., "Batch solar disinfection inactivates oocysts of *Cryptosporidium parvum* and cysts of *Giardia muris* in drinking water," *Journal of Applied Microbiology*, vol. 101, no. 2, pp. 453–463, 2006.
- [32] W. Heaselgrave, N. Patel, S. Kilvington, S. C. Kehoe, and K. G. McGuigan, "Solar disinfection of poliovirus and *Acanthamoeba polyphaga* cysts in water—a laboratory study using simulated sunlight," *Letters in Applied Microbiology*, vol. 43, no. 2, pp. 125–130, 2006.
- [33] S. Mtapuri-Zinyowera, N. Midzi, C. E. Muchaneta-Kubara, T. Simbini, and T. Mduluzi, "Impact of solar radiation in disinfecting drinking water contaminated with *Giardia duodenalis* and *Entamoeba histolytica/dispar* at a point-of-use water treatment," *Journal of Applied Microbiology*, vol. 106, no. 3, pp. 847–852, 2009.
- [34] R. M. Conroy, M. Elmore-Meegan, T. Joyce, K. G. McGuigan, and J. Barnes, "Solar disinfection of drinking water and diarrhoea in Maasai children: a controlled field trial," *The Lancet*, vol. 348, no. 9043, pp. 1695–1697, 1996.
- [35] R. M. Conroy, M. Elmore Meegan, T. Joyce, K. McGuigan, and J. Barnes, "Solar disinfection of water reduces diarrhoeal disease: an update," *Archives of Disease in Childhood*, vol. 81, no. 4, pp. 337–338, 1999.
- [36] R. M. Conroy, M. E. Meegan, T. Joyce, K. McGuigan, and J. Barnes, "Solar disinfection of drinking water protects against cholera in children under 6 years of age," *Archives of Disease in Childhood*, vol. 85, no. 4, pp. 293–295, 2001.
- [37] B. Sommer, A. Mariño, Y. Solarte et al., "SODIS—an emerging water treatment process," *Journal of Water Supply Research and Technology—Aqua*, vol. 46, no. 3, pp. 127–137, 1997.
- [38] S. C. Kehoe, T. M. Joyce, P. Ibrahim, J. B. Gillespie, R. A. Shahar, and K. G. McGuigan, "Effect of agitation, turbidity, aluminium foil reflectors and container volume on the inactivation efficiency of batch-process solar disinfectors," *Water Research*, vol. 35, no. 4, pp. 1061–1065, 2001.
- [39] M. B. Fisher, C. R. Keenan, K. L. Nelson, and B. M. Voelker, "Speeding up solar disinfection (SODIS): effects of hydrogen peroxide, temperature, pH, and copper plus ascorbate on the photoinactivation of *E. coli*," *Journal of Water and Health*, vol. 6, no. 1, pp. 35–51, 2008.
- [40] S. K. Mani, R. Kanjur, I. S. B. Singh, and R. H. Reed, "Comparative effectiveness of solar disinfection using small-scale batch reactors with reflective, absorptive and transmissive rear surfaces," *Water Research*, vol. 40, no. 4, pp. 721–727, 2006.

- [41] M. Saladin, "SODIS bags for humanitarian aid," March 2010, <http://www.sodis.ch/index>.
- [42] S. K. Lee, M. Sheridan, and A. Mills, "Novel UV-activated colorimetric oxygen indicator," *Chemistry of Materials*, vol. 17, no. 10, pp. 2744–2751, 2005.
- [43] A. Mills, S. K. Lee, and M. Sheridan, "Development of a novel UV indicator and dosimeter film," *Analyst*, vol. 130, no. 7, pp. 1046–1051, 2005.
- [44] E. Ubomba-Jaswa, P. Fernández-Ibáñez, C. Navntoft, M. Inmaculada Polo-López, and K. G. McGuigana, "Investigating the microbial inactivation efficiency of a 25 L batch solar disinfection (SODIS) reactor enhanced with a compound parabolic collector (CPC) for household use," *Journal of Chemical Technology and Biotechnology*, vol. 85, no. 8, pp. 1028–1037, 2010.
- [45] A. Vidal, A. I. Díaz, A. El Hraiki et al., "Solar photocatalysis for detoxification and disinfection of contaminated water: pilot plant studies," *Catalysis Today*, vol. 54, no. 2-3, pp. 283–290, 1999.
- [46] O. A. McLoughlin, P. Fernández-Ibáñez, W. Gernjak, S. Malato Rodriguez, and L. W. Gill, "Photocatalytic disinfection of water using low cost compound parabolic collectors," *Solar Energy*, vol. 77, no. 5, pp. 625–633, 2004.
- [47] C. Navntoft, P. Araujo, M. I. Litter et al., "Field tests of the solar water detoxification SOLWATER reactor in Los Pereyra, Tucumán, Argentina," *Journal of Solar Energy Engineering*, vol. 129, no. 1, pp. 127–134, 2007.
- [48] E. Ubomba-Jaswa, C. Navntoft, M. I. Polo-López, P. Fernandez-Ibáñez, and K. G. McGuigan, "Solar disinfection of drinking water (SODIS): an investigation of the effect of UV-A dose on inactivation efficiency," *Photochemical and Photobiological Sciences*, vol. 8, no. 5, pp. 587–595, 2009.
- [49] C. Lee, Y. Lee, and J. Yoon, "Oxidative degradation of dimethylsulfoxide by locally concentrated hydroxyl radicals in streamer corona discharge process," *Chemosphere*, vol. 65, no. 7, pp. 1163–1170, 2006.
- [50] D. M. Blake, P. C. Maness, Z. Huang, E. J. Wolfrum, J. Huang, and W. A. Jacoby, "Application of the photocatalytic chemistry of titanium dioxide to disinfection and the killing of cancer cells," *Separation and Purification Methods*, vol. 28, no. 1, pp. 1–50, 1999.
- [51] J.-M. Herrmann, "Heterogeneous photocatalysis: fundamentals and applications to the removal of various types of aqueous pollutants," *Catalysis Today*, vol. 53, no. 1, pp. 115–129, 1999.
- [52] C. Karunakaran, S. Senthilvelan, S. Karuthapandian, and K. Balaraman, "Photooxidation of iodide ion on some semiconductor and non-semiconductor surfaces," *Catalysis Communications*, vol. 5, no. 6, pp. 283–290, 2004.
- [53] K. G. Kanade, J. O. Baeg, U. P. Mulik, D. P. Amalnerkar, and B. B. Kale, "Nano-CdS by polymer-inorganic solid-state reaction: visible light pristine photocatalyst for hydrogen generation," *Materials Research Bulletin*, vol. 41, no. 12, pp. 2219–2225, 2006.
- [54] M. I. Litter, "Heterogeneous photocatalysis: transition metal ions in photocatalytic systems," *Applied Catalysis B*, vol. 23, no. 2-3, pp. 89–114, 1999.
- [55] J. A. Byrne, B. R. Eggins, N. M. D. Brown, B. McKinney, and M. Rouse, "Immobilisation of TiO₂ powder for the treatment of polluted water," *Applied Catalysis B*, vol. 17, no. 1-2, pp. 25–36, 1998.
- [56] T. A. McMurray, J. A. Byrne, P. S. M. Dunlop, J. G. M. Winkelman, B. R. Eggins, and E. T. McAdams, "Intrinsic kinetics of photocatalytic oxidation of formic and oxalic acid on immobilised TiO₂ films," *Applied Catalysis A*, vol. 262, no. 1, pp. 105–110, 2004.
- [57] T. Matsunaga, R. Tomoda, T. Nakajima, and H. Wake, "Photoelectrochemical sterilization of microbial cells by semiconductor powders," *FEMS Microbiology Letters*, vol. 29, no. 1-2, pp. 211–214, 1985.
- [58] C. McCullagh, J. M. C. Robertson, D. W. Bahnemann, and P. K. J. Robertson, "The application of TiO₂ photocatalysis for disinfection of water contaminated with pathogenic microorganisms: a review," *Research on Chemical Intermediates*, vol. 33, no. 3-5, pp. 359–375, 2007.
- [59] O. K. Dalrymple, E. Stefanakos, M. A. Trotz, and D. Y. Goswami, "A review of the mechanisms and modeling of photocatalytic disinfection," *Applied Catalysis B*, vol. 98, no. 1-2, pp. 27–38, 2010.
- [60] Z. Huang, P. C. Maness, D. M. Blake, E. J. Wolfrum, S. L. Smolinski, and W. A. Jacoby, "Bactericidal mode of titanium dioxide photocatalysis," *Journal of Photochemistry and Photobiology A*, vol. 130, no. 2-3, pp. 163–170, 2000.
- [61] M. Wainwright, "Methylene blue derivatives—suitable photoantimicrobials for blood product disinfection?" *International Journal of Antimicrobial Agents*, vol. 16, no. 4, pp. 381–394, 2000.
- [62] K. Sunada, T. Watanabe, and K. Hashimoto, "Studies on photokilling of bacteria on TiO₂ thin film," *Journal of Photochemistry and Photobiology A*, vol. 156, no. 1–3, pp. 227–233, 2003.
- [63] M. Cho, H. Chung, W. Choi, and J. Yoon, "Linear correlation between inactivation of *E. coli* and OH radical concentration in TiO₂ photocatalytic disinfection," *Water Research*, vol. 38, no. 4, pp. 1069–1077, 2004.
- [64] A. G. Rincón, C. Pulgarin, N. Adler, and P. Peringer, "Interaction between *E. coli* inactivation and DBP-precursors—dihydroxybenzene isomers—in the photocatalytic process of drinking-water disinfection with TiO₂," *Journal of Photochemistry and Photobiology A*, vol. 139, no. 2-3, pp. 233–241, 2001.
- [65] A. G. Rincón and C. Pulgarin, "Field solar *E. coli* inactivation in the absence and presence of TiO₂: is UV solar dose an appropriate parameter for standardization of water solar disinfection?" *Solar Energy*, vol. 77, no. 5, pp. 635–648, 2004.
- [66] D. M. A. Alrousan, P. S. M. Dunlop, T. A. McMurray, and J. A. Byrne, "Photocatalytic inactivation of *E. coli* in surface water using immobilised nanoparticle TiO₂ films," *Water Research*, vol. 43, no. 1, pp. 47–54, 2009.
- [67] P. S. M. Dunlop, T. A. McMurray, J. W. J. Hamilton, and J. A. Byrne, "Photocatalytic inactivation of *Clostridium perfringens* spores on TiO₂ electrodes," *Journal of Photochemistry and Photobiology A*, vol. 196, no. 1, pp. 113–119, 2008.
- [68] O. Sunnotel, R. Verdoold, P. S. M. Dunlop et al., "Photocatalytic inactivation of *Cryptosporidium parvum* on nanostructured titanium dioxide films," *Journal of Water and Health*, vol. 8, no. 1, pp. 83–91, 2010.
- [69] S. Gelover, L. A. Gómez, K. Reyes, and M. Teresa Leal, "A practical demonstration of water disinfection using TiO₂ films and sunlight," *Water Research*, vol. 40, no. 17, pp. 3274–3280, 2006.
- [70] P. Fernández, J. Blanco, C. Sichel, and S. Malato, "Water disinfection by solar photocatalysis using compound parabolic collectors," *Catalysis Today*, vol. 101, no. 3-4, pp. 345–352, 2005.
- [71] C. Sichel, J. Tello, M. de Cara, and P. Fernández-Ibáñez, "Effect of UV solar intensity and dose on the photocatalytic disinfection of bacteria and fungi," *Catalysis Today*, vol. 129, no. 1-2, pp. 152–160, 2007.

- [72] N. Miranda-García, M. I. Maldonado, J. M. Coronado, and S. Malato, "Degradation study of 15 emerging contaminants at low concentration by immobilized TiO₂ in a pilot plant," *Catalysis Today*, vol. 151, no. 1-2, pp. 107–113, 2010.
- [73] J. W. J. Hamilton, J. A. Byrne, C. McCullagh, and P. S. M. Dunlop, "Electrochemical investigation of doped titanium dioxide," *International Journal of Photoenergy*, vol. 2008, Article ID 631597, 2008.
- [74] R. Asahi, T. Morikawa, T. Ohwaki, K. Aoki, and Y. Taga, "Visible-light photocatalysis in nitrogen-doped titanium oxides," *Science*, vol. 293, no. 5528, pp. 269–271, 2001.
- [75] Q. Li, M. A. Page, B. J. Mariñas, and K. S. Jian, "Treatment of coliphage MS2 with palladium-modified nitrogen-doped titanium oxide photocatalyst illuminated by visible light," *Environmental Science and Technology*, vol. 42, no. 16, pp. 6148–6153, 2008.
- [76] P. Wu, R. Xie, J. A. Imlay, and J. K. Shang, "Visible-light-induced photocatalytic inactivation of bacteria by composite photocatalysts of palladium oxide and nitrogen-doped titanium oxide," *Applied Catalysis B*, vol. 88, no. 3-4, pp. 576–581, 2009.
- [77] J. A. Rengifo-Herrera and C. Pulgarin, "Photocatalytic activity of N, S co-doped and N-doped commercial anatase TiO₂ powders towards phenol oxidation and *E. coli* inactivation under simulated solar light irradiation," *Solar Energy*, vol. 84, no. 1, pp. 37–43, 2010.

Research Article

Studying the Properties of RF-Sputtered Nanocrystalline Tin-Doped Indium Oxide

Abd El-Hady B. Kashyout,¹ Marwa Fathy,¹ and Moataz B. Soliman²

¹Advanced Technology and New Materials Research Institute, Mubarak City for Scientific Research and Technology Applications, New Borg El-Arab City, Alexandria 21934, Egypt

²Institute of Graduate Studies and Research, Alexandria University, 163 Horrya Avenue, P.O. Box 832, Shatby, Alexandria 21526, Egypt

Correspondence should be addressed to Abd El-Hady B. Kashyout, hady8@yahoo.com

Received 27 January 2011; Revised 28 February 2011; Accepted 31 March 2011

Academic Editor: Mohamed Sabry Abdel-Mottaleb

Copyright © 2011 Abd El-Hady B. Kashyout et al. This is an open access article distributed under the Creative Commons Attribution License, which permits unrestricted use, distribution, and reproduction in any medium, provided the original work is properly cited.

The ceramic target of Indium tin oxide (ITO) (90% In_2O_3 -10% SnO_2) has been used to prepare transparent semiconductive thin films on glass substrate by RF magnetron sputtering at room temperature. The properties of the thin films are affected by controlling the deposition parameters, namely, RF power values and deposition times. The structure, morphology, optical and electrical properties of the thin films are investigated using X-ray diffraction (XRD), field emission scanning electron microscope (FESEM), atomic force microscope (AFM), UV-Vis spectrophotometer, and four-point probe measurement. Nanoparticles of 10–20 nm are measured and confirmed using both FESEM and AFM. The main preferred orientations of the prepared thin films are (222) and (400) of the cubic ITO structure. The transparent semiconductive films have high transmittance within the visible range of values 80–90% and resistivity of about $1.62 \times 10^{-4} \Omega \cdot \text{cm}$.

1. Introduction

Indium-tin-oxide (ITO) thin film is n-type degenerated semiconductor with a wide band gap ($E_g \sim 3.3 \text{ eV}$) [1]. It has high photoelectrolytic properties: high transparence in the range of visible spectrum (>95%), high reflectance in the infrared (IR) range (>80%) because of its high density of free electrons in ITO conduction band, and high conductivity ($10^{-4} \Omega \cdot \text{cm}$) similar to a metallic material [1]. It is usually deposited at temperature above 200°C , since it is difficult to obtain a thin film with a resistivity below $2 \times 10^{-4} \Omega \cdot \text{cm}$ at a low substrate temperature. However, low-temperature deposition, below 100°C , is necessary to deposit films on plastic substrates that have poor heat resistance, such as polycarbonate [2] polyethylene terephthalate [3] and polyethersulfone [4]. ITO coatings are the most widely used as transparent conductive oxide (TCO) coatings in various applications such as transparent conducting electrode in flat-panel displays (FPDs) [5], organic light emitting diodes (OLEDs) [6], and photovoltaic solar cells because they have

high electrical conductivity, high optical transparency, and smooth surface morphology [7–10].

ITO thin films are prepared using various methods such as DC, pulsed DC, and RF magnetron sputtering [11–13], reactive evaporation [14], ion beam assisted deposition [15], sol-gel, co-precipitation [16, 17], chemical vapor deposition (CVD) [18], and spray pyrolysis [19]. Magnetron sputtering is one of the most versatile techniques for ITO thin films preparation. This technique provides a uniform fabrication of the reproduction of ITO thin films, which is advantageous for many applications in industry [20].

The optical and electrical properties of ITO coatings are sensitive to process parameters and depend on the control of films composition, structure, crystallinity, defect density, surface roughness, and dopant concentration [21, 22].

In this paper, the crystallization behavior of ITO thin films deposited at room temperature under Ar atmosphere by RF magnetron sputtering is examined as a function of RF power values and deposition time, aiming to determine the conditions that lead to the production of thin films with

an optical band gap (3.5 eV) and transparency ($\geq 90\%$) in the visible region and in some cases near IR region. Also, low resistivity, good surface uniformity, highly smooth and chemically stable surfaces in various environments are essential parameters that should be investigated.

2. Experimental Details

The ITO thin films were deposited on 1 mm thick soda lime glass by RF magnetron sputtering technique using the system (HUMMER 8.1) under an Ar atmosphere. $\text{SnO}_2\text{-In}_2\text{O}_3$ sintered disks of 10 cm in diameter were used as the target. Glass was precleaned with ethanol and acetone, respectively. The chamber was evacuated to a background pressure of 0.6 mTorr initially, and the working pressure during the film deposition was fixed to 7–10 mTorr by utilizing pure Ar (99.999%) gas. The RF power varied from 50 to 300 W, whereas the deposition time varied from 10 to 40 min. The deposition process is carried out at room temperature, that is, the substrate is not heated during the film deposition.

The film crystalline structure was investigated by X-ray diffractometer (Schimadzu-7000) using $\text{Cu-K}\alpha$ radiation target. The optical transmittance was measured using a UV-Vis double beam spectrophotometer (Ultrospec 2000-Pharmacia Biotech Co.) in the wavelength range from 200 nm to 1100 nm. The surface morphology of the films was observed with a field emission scanning electron microscope (JEOL 7600) and the average surface roughness is measured under ambient conditions with an atomic force microscope (AFM) JEOL-JSPM-5400 in the noncontact mode. The resistivity of the coatings is measured using a four-point probe technique (Sigma One) and the reported value was an average of three measurements over the sample.

3. Results and Discussion

3.1. Structural Properties. Figure 1 shows the X-ray diffraction patterns of the ITO thin films deposited with various RF power values at a constant working pressure, and the deposition time is fixed at 40 min. At low deposition power of 50 W (Figure 1(a)), the ITO thin film shows no diffraction peaks, which may indicate amorphous state of the deposited film. Increasing the deposition power to 100 W (Figure 1(b)), the deposited film shows the appearance of the (222) peak of the ITO cubic structure (JCPDS Card No. 06-0416).

Starting from a deposition power of 150 W, most of the typical ITO diffraction peaks of (222), (400), (440), and (622) are detected as shown in Figure 1(c). It has been observed that the (222) preferential orientation is highly dominant at the initial growth stage for any deposition condition. This is due to the fact that during the nucleation stage of ITO thin films, indium atoms on substrate are likely to aggregate into densely packed (111) planes which are close to (222) planes in the bixbyite structure. But the dominant nature changed from (222) to (400) when there is an increase in substrate temperature and also due to an increase in film thickness due to increasing the power value [23].

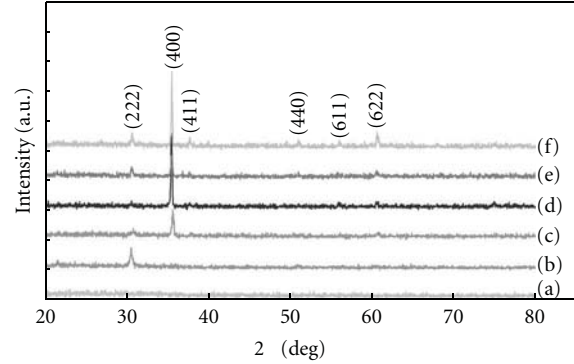


FIGURE 1: XRD patterns for ITO thin films deposited for 40 min deposition using various RF power, (a) 50, (b) 100, (c) 150, (d) 200, (e) 250 and (f) 300 W.

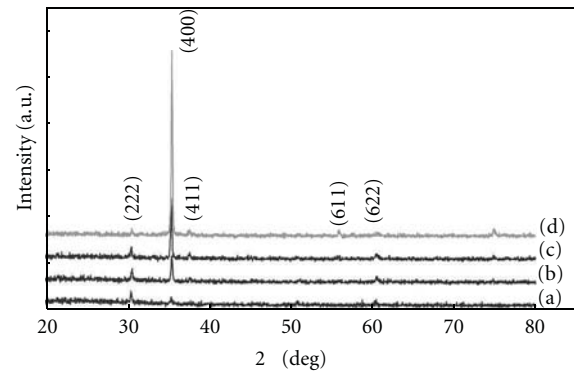


FIGURE 2: XRD patterns for ITO thin films deposited using RF power value of 200 W and various deposition time, (a) 10, (b) 20, (c) 30 and (d) 40 min.

A preferential orientation of (400) plane is observed as the deposition power is increased from 150 to 300 W as shown in Figure 1 ((c)–(f)). The data also shows that the peak position slightly shifts to a lower 2θ value as the power increases while the full width half maximum (FWHM) decreases, meaning that the film grain size increases [4]. It has also been noted that the intensity of the (222) diffraction peak does not increase significantly any more when the thickness is higher than a certain value, whereas the (400) diffraction intensity increases for thicker films. Thus, the growth of the (222) grains is suppressed when the thickness increases [24]. According to the literature, the predominant orientation changes from (222) to (400) as the oxygen incorporation in the structure decreases or as the deposition rate increases which is in good agreement with the presented results. On the other hand, the change in the orientation from (222) to (400) can also be influenced by the deposition rate because the (222-) oriented grains are less resistant against sputtering than the (400-) oriented grains [24].

Figure 2 shows the XRD patterns of the grown ITO thin films at a constant power of 200 W and various deposition times. The film deposited for 10 min (Figure 2(a)) reveals low-diffraction intensities of the ITO crystal structure (JCPDS Card No. 06-0416) with the preferred orientation of

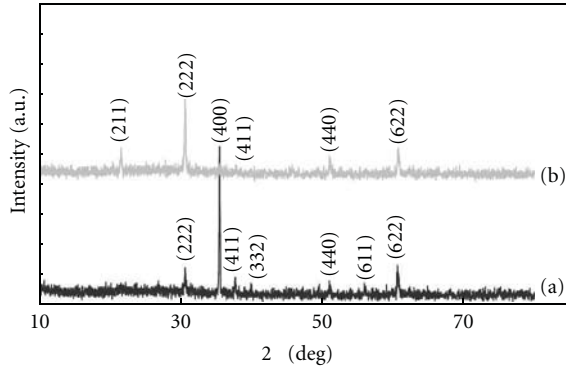


FIGURE 3: XRD patterns for ITO thin films deposited using RF power value 200 W for 40 min deposition time: (a) without, (b) with heat treatment at 400°C for 1 h.

the (222) plane, and changing the orientation to (400) plane will increase the deposition time to 20, 30, and 40 min (Figure 2 ((b), (c), and (d))). It is known that the thickness of the deposited film affects the X-ray spectra [24]. Thin crystallized film deposited for 10 min might represent the diffraction peak with very low intensity.

During deposition, plasma provides the sample with heat that increases temperature to about 150°C. This temperature is required in order to have a crystalline structure [6, 14, 15]. One aspect of the plasma-surface interactions is the transfer of energy. Energy transfer from plasma to solid surfaces occurs through optical radiation and fluxes of neutral particles and ions. In plasma, at a pressure below 1 Pa (7.5 mTorr), the degree of ionization is very high, the density of neutrals is much lower than that of ions, and the ions collisions are predominant [16]. During the ion bombardment, the dissipation of the kinetics and the vibration energy fractions of ions causes heating of the substrate [16]. Therefore, a deposition time up to 40 min resulted in good crystallization by the prolonged energetic bombardment, while insufficient energy for crystallization is transferred to the films when the deposition time is short [17].

Figure 3 illustrates the XRD patterns of the ITO-deposited thin films at a constant power (200 W) where the effect of heat treatment at 400°C for 1 hr is discussed. The nonheated film (Figure 3(a)) shows that the (400) plane is the preferred orientation which may indicate that the oxygen vacancies on these planes are accommodated. On the other hand, the postannealed ITO film (Figure 3(b)) shows that the (222) plane is a preferred one which is a close-packed plane in In_2O_3 body-centered cubic structure. This plane does not accommodate oxygen vacancies very well, and so it is stabilized [25].

Also, heat treatment causes a decrease in lattice constant (a) which is calculated using (1)

$$d_{hkl} = \frac{a}{\sqrt{h^2 + k^2 + l^2}}, \quad (1)$$

where d is the spacing between adjacent (hkl) lattice planes. It is decreased from 1.023 nm to 1.011 nm due to the attractive

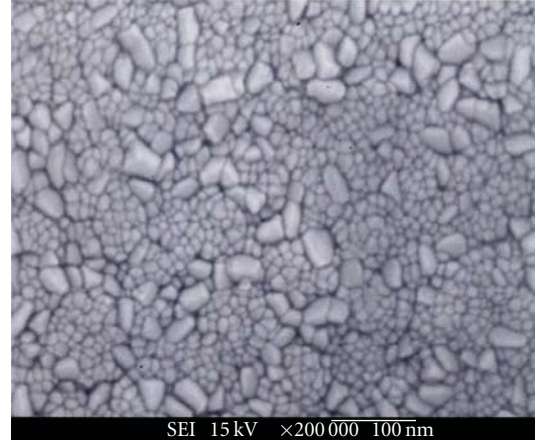


FIGURE 4: FESEM for ITO thin films deposited using RF power value of 200 W for 40 min deposition time.

force between the metal ions and the extra interstitial oxygen ions [26].

3.2. Morphological Properties. The FESEM and AFM of ITO thin films are shown in Figures 4 and 5, respectively, to show the film morphology and roughness. Figure 4 shows that the average grain size is about 10 nm with high density accompanied by large grains of 20–30 nm with low density is observed and may be explained as: for the thick film, a change from (222) to (400) orientation and columnar grains growing perpendicular to the substrate by increasing the deposition time to 40 min. It was previously reported that the morphology and orientation of ITO films depend on the energy of particles arriving to the substrate have been found.

Figure 5 shows the topography of the ITO thin film deposited at room temperature for 40 min. The average film roughness value calculated from this image is about 20 nm. According to the literature [27, 28], the average roughness increases with increasing the film thickness. In the same way, it has been reported for ITO films prepared by various techniques [29, 30] that the grain size enlargement is related with the increase of the film thickness.

3.3. Optical Properties. Several methods have been used to determine the optical constants of thin films based on the measurement of the intensity of the reflected, absorbed and/or transmitted light as a function of wavelength and/or the angle of incidence. Among these methods, the one given by Swanepoel is widely used because it is a simple method and does not need a complicated computer program [31].

T_M and T_m , which are the maximum and the minimum of the transmittance of the envelope of interference, are now considered to be continuous functions of λ . For any λ , T_M has a correspondent T_m value: The refractive index is calculated by Manificier et al. [32]

$$n = \left[N + (N^2 - S^2)^{1/2} \right]^{1/2}, \quad (2)$$

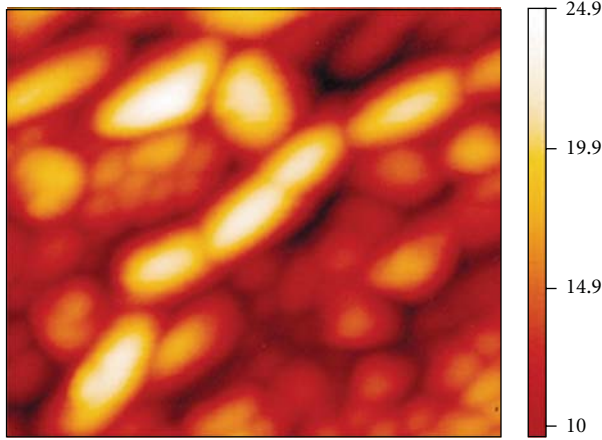


FIGURE 5: AFM for ITO thin films deposited using RF power value of 200 W for 40 min deposition time.

TABLE 1: Resistivity, thickness and refractive index of ITO thin films deposited using various RF power for 40 min deposition time.

RF power (W)	Thickness (μm)	Refractive index	Resistivity ($\Omega \cdot \text{cm}$)
50	0.50	1.48	77.15×10^{-4}
100	0.59	1.49	9.98×10^{-4}
150	0.63	1.5	3.96×10^{-4}
200	1.09	1.506	1.62×10^{-4}
250	1.17	1.505	2.32×10^{-4}
300	1.29	1.509	2.38×10^{-4}

where N is defined as

$$N = \frac{2S(T_M - T_m)}{T_M T_m} + \frac{(S^2 + 1)}{2}, \quad (3)$$

where S is the refractive index of the glass substrate.

If n_1 and n_2 are the refractive indices at two adjacent maxima (or minima) at λ_1 and λ_2 , according to the basic equation of interference fringes,

$$2nt = m\lambda, \quad (4)$$

the thickness t of the film is given by

$$t = \frac{\lambda_1 \lambda_2}{2(\lambda_1 n_2 - \lambda_2 n_1)}. \quad (5)$$

Table 1 shows an example of the calculated refractive indices and thicknesses of the ITO samples prepared with different RF power. With increasing the power value, the refractive index and the thickness are increased from 1.48 and $0.5 \mu\text{m}$ (power value = 50 W) to 1.509 and $1.29 \mu\text{m}$ (power value = 300 W), respectively, with increasing the deposition time, the refractive index and the thickness are increased from 1.499 and $0.46 \mu\text{m}$ (deposition time = 10 min) to 1.506 and $1.09 \mu\text{m}$ (deposition time = 40 min), respectively.

The measured optical transmittance as a function of the light wavelength is represented in Figures 6 and 7 for ITO

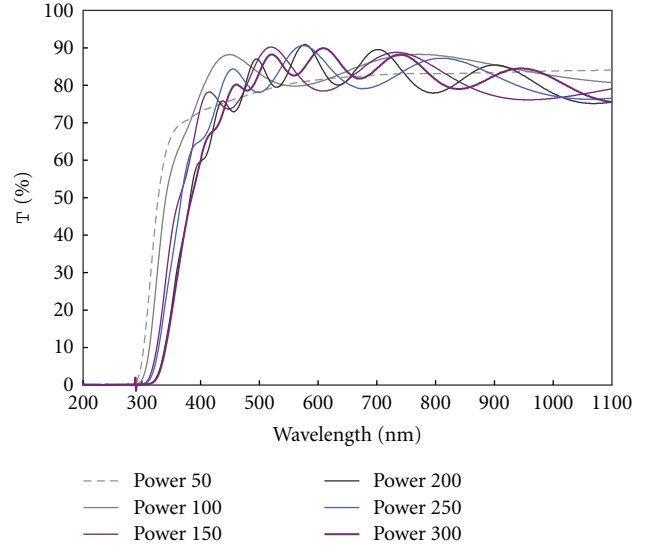


FIGURE 6: Optical transmittance for ITO thin films deposited for 40 min deposition time with various RF power.

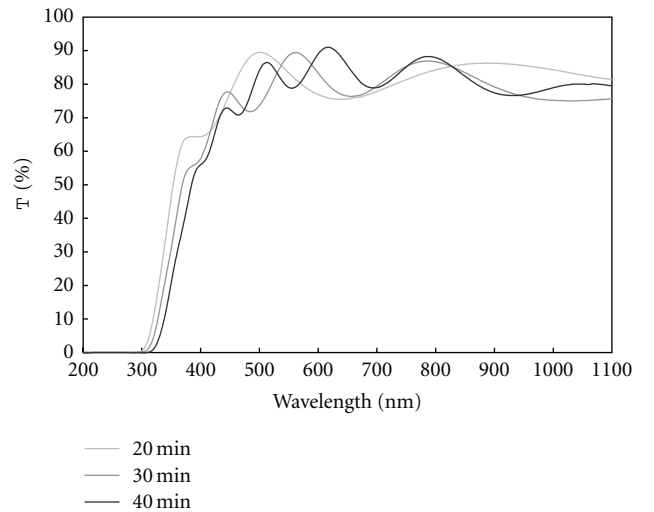


FIGURE 7: Optical transmittances for ITO thin films deposited using RF power value of 200 W and various deposition times.

thin films deposited as a function of RF deposition power and deposition time, respectively. From the results summarized in Figure 6 for various samples, it is observed that as the deposition power increases, the transmittance in the near infrared region decreases, which is explained by the increase of film's free electron absorption [4].

Also, the transmittance band edge is shifted to higher wavelengths as the RF power increases. Figure 7 shows the optical transmittance for the grown ITO thin films deposited at various deposition times. The optical transmission decreases as the ITO film thickness increases, which is attributed to the optical scattering arising from longer optical paths and also to the increased carrier concentration in the films [25, 27, 28]. The higher the carrier concentration value, the lower the ITO transmittance in the longer wavelength region.

TABLE 2: Resistivity, thickness and refractive index of ITO thin films deposited using RF deposition power value of 200 W for various deposition times.

Deposition time (min)	Thickness (μm)	Refractive index	Resistivity ($\Omega\cdot\text{cm}$)
10	0.46	1.499	5.18×10^{-4}
20	0.52	1.501	4.1×10^{-4}
30	0.63	1.503	1.92×10^{-4}
40	1.09	1.506	1.62×10^{-4}

Such higher free carrier density for thicker layers can be associated to the observed crystallite-size enhancement with increasing the film thickness that should reduce the number of donor sites trapped at the dislocations and grain boundaries [28].

3.4. Electrical Properties. Table 1 shows that the resistivity decreased from $77.15 \times 10^{-4} \Omega\cdot\text{cm}$ at 50 W to reach its minimum value of $1.62 \times 10^{-4} \Omega\cdot\text{cm}$ at 200 W then increased to $2.38 \times 10^{-4} \Omega\cdot\text{cm}$ at 300 W. Table 2 shows the resistivity of the ITO thin films deposited at a power of 200 W and various deposition times. At the deposition time of 10 min, the transmittance value is 79% with a high resistivity of $5.18 \times 10^{-4} \Omega\cdot\text{cm}$. At a high deposition time (40 min), the transmittance values increased to about 91%, and the resistivity decreased to $1.62 \times 10^{-4} \Omega\cdot\text{cm}$.

In the process of Ar sputtering (no oxygen), the oxygen concentration of the ITO film is lower than that of the target itself because a part of the oxygen sputtered from the target will not be incorporated into the film [17]. That is, the films without oxygen flow show metal-like characteristics with low transmittance, low resistivity, and higher oxygen vacancy concentration. On the other hand, as the power increases, the concentration of oxygen vacancies is drastically decreased resulting in a higher transmittance and resistivity like an oxide-insulating thin film [33, 34].

4. Conclusions

The ITO thin films are deposited by RF magnetron sputtering at room temperature. The film is in its amorphous state at low RF power. By increasing the deposition power and deposition time crystallization of the films was promoted because RF sputtering transfers the energy to the growing state by energetic bombardment and the activation energy for the crystallization of the film transferred during the deposition. To improve the electrical properties with low resistivity, ITO deposition should be processed under room temperature and low oxygen fraction. A tradeoff between low resistivity and high transmission exists due to the role that the oxygen vacancies have in the conduction and transmission. A higher number of oxygen vacancies facilitate conduction. The optical and electrical properties are strongly correlated to the preferred orientation of the films which is changed from (222) to (400) as the RF power increased (from 50 W to 300 W), and the deposition time increased from 10 to 40 min.

After heat treatment, the preferred orientation changed from (400) to (222) which is a result of the concentration of oxygen vacancy and the rearrangement of atoms in close-packed plane of In_2O_3 having a body-centered cubic structure.

References

- [1] Z. Ding, C. An, Q. Li et al., "Preparation of ITO nanoparticles by liquid phase coprecipitation method," *Journal of Nanomaterials*, vol. 2010, Article ID 543601, 5 pages, 2010.
- [2] Y. Hoshi and R. Ohki, "Low energy rf sputtering system for the deposition of ITO thin films," *Electrochimica Acta*, vol. 44, no. 21, pp. 3927–3932, 1999.
- [3] C. Guillén and J. Herrero, "Structural, optical and electrical characteristics of ITO thin films deposited by sputtering on different polyester substrates," *Materials Chemistry and Physics*, vol. 112, no. 2, pp. 641–644, 2008.
- [4] Y. Z. You, Y. S. Kim, D. H. Choi, H. S. Jang, J. H. Lee, and D. Kim, "Electrical and optical study of ITO films on glass and polymer substrates prepared by DC magnetron sputtering type negative metal ion beam deposition," *Materials Chemistry and Physics*, vol. 107, no. 2-3, pp. 444–448, 2008.
- [5] H. Lei, K. Ichikawa, Y. Hoshi, M. Wang, T. Uchida, and Y. Sawada, "A study of deposition of ITO films on organic layer using facing target sputtering in Ar and Kr gases," *Thin Solid Films*, vol. 518, no. 11, pp. 2926–2929, 2010.
- [6] C. J. Huang, Y. K. Su, and S. L. Wu, "The effect of solvent on the etching of ITO electrode," *Materials Chemistry and Physics*, vol. 84, no. 1, pp. 146–150, 2004.
- [7] A. B. Kashyout, M. Soliman, M. El Gamal, and M. Fathy, "Preparation and characterization of nano particles ZnO films for dye-sensitized solar cells," *Materials Chemistry and Physics*, vol. 90, no. 2-3, pp. 230–233, 2005.
- [8] A. B. Kashyout, M. Soliman, and M. Fathy, "Effect of preparation parameters on the properties of TiO_2 nanoparticles for dye sensitized solar cells," *Renewable Energy*, vol. 35, no. 12, pp. 2914–2920, 2010.
- [9] F. L. Wong, M. K. Fung, S. W. Tong, C. S. Lee, and S. T. Lee, "Flexible organic light-emitting device based on magnetron sputtered indium-tin-oxide on plastic substrate," *Thin Solid Films*, vol. 466, no. 1-2, pp. 225–230, 2004.
- [10] N. Naghavi, A. Rougier, C. Marcel, C. Guéry, J. B. Leriche, and J. M. Tarascon, "Characterization of indium zinc oxide thin films prepared by pulsed laser deposition using a $\text{Zn}_3\text{I}_2\text{O}_6$ target," *Thin Solid Films*, vol. 360, no. 1-2, pp. 233–240, 2000.
- [11] H. Y. Yeom, N. Popovich, E. Chason, and D. C. Paine, "A study of the effect of process oxygen on stress evolution in d.c. magnetron-deposited tin-doped indium oxide," *Thin Solid Films*, vol. 411, no. 1, pp. 17–22, 2002.
- [12] W. J. Lee, Y. K. Fang, J. J. Ho et al., "Optimizing indium tin oxide thin films with bipolar d.c.-pulsed magnetron sputtering for electrochromic device applications," *Journal of Materials Science*, vol. 13, no. 12, pp. 751–756, 2002.
- [13] T. C. Gorjanc, D. Leong, C. Py, and D. Roth, "Room temperature deposition of ITO using r.f. magnetron sputtering," *Thin Solid Films*, vol. 413, no. 1-2, pp. 181–185, 2002.
- [14] A. Kachouane, M. Addou, A. Bougrine et al., "Preparation and characterisation of tin-doped indium oxide films," *Materials Chemistry and Physics*, vol. 70, no. 3, pp. 285–289, 2001.
- [15] G. H. Takaoka, D. Yamazaki, and J. Matsuo, "High quality ITO film formation by the simultaneous use of cluster ion beam and laser irradiation," *Materials Chemistry and Physics*, vol. 74, no. 1, pp. 104–108, 2002.

- [16] M. J. Alam and D. C. Cameron, "Investigation of annealing effects on sol-gel deposited indium tin oxide thin films in different atmospheres," *Thin Solid Films*, vol. 420-421, pp. 76–82, 2002.
- [17] J. Vetrone and Y. W. Chung, "Organo-metallic chemical vapor deposition of tin oxide single crystal and polycrystalline films," *Journal of Vacuum Science and Technology A*, vol. 9, no. 6, pp. 3041–3047, 1991.
- [18] D. Yu, W. Yu, D. Wang, and Y. Qian, "Structural, optical, and electrical properties of indium tin oxide films with corundum structure fabricated by a sol-gel route based on solvothermal reactions," *Thin Solid Films*, vol. 419, no. 1-2, pp. 166–172, 2002.
- [19] S. H. Keshmiri, M. R. Roknabadi, and S. Ashok, "A novel technique for increasing electron mobility of indium-tin-oxide transparent conducting films," *Thin Solid Films*, vol. 413, no. 1-2, pp. 167–170, 2002.
- [20] C. H. Yang, S. C. Lee, T. C. Lin, and S. C. Chen, "Electrical and optical properties of indium tin oxide films prepared on plastic substrates by radio frequency magnetron sputtering," *Thin Solid Films*, vol. 516, no. 8, pp. 1984–1991, 2008.
- [21] H. Morikawa and M. Fujita, "Crystallization and electrical property change on the annealing of amorphous indium-oxide and indium-tin-oxide thin films," *Thin Solid Films*, vol. 359, no. 1, pp. 61–67, 2000.
- [22] M. Kamei, H. Enomoto, and I. Yasui, "Origin of the crystalline orientation dependence of the electrical properties in tin-doped indium oxide films," *Thin Solid Films*, vol. 392, no. 2, pp. 265–268, 2001.
- [23] R. Balasundaraprabhu, E. V. Monakhov, N. Muthukumarasamy, O. Nilsen, and B. G. Svensson, "Effect of heat treatment on ITO film properties and ITO/p-Si interface," *Materials Chemistry and Physics*, vol. 114, no. 1, pp. 425–429, 2009.
- [24] B.D. Cullity, *Elements of X-Ray Diffraction*, Addison-Wesley Publishing Company, Boston, Mass, USA, 2nd edition, 1978.
- [25] S.-I. Jun, T. E. McKnight, M. L. Simpson, and P. D. Rack, "A statistical parameter study of indium tin oxide thin films deposited by radio-frequency sputtering," *Thin Solid Films*, vol. 476, no. 1, pp. 59–64, 2005.
- [26] S. Seki, Y. Sawada, and T. Nishide, "Indium-tin-oxide thin films prepared by dip-coating of indium diacetate monohydroxide and tin dichloride," *Thin Solid Films*, vol. 388, no. 1-2, pp. 22–26, 2001.
- [27] C. Guillén and J. Herrero, "Polycrystalline growth and recrystallization processes in sputtered ITO thin films," *Thin Solid Films*, vol. 510, no. 1-2, pp. 260–264, 2006.
- [28] H. Kim, J. S. Horwitz, G. Kushto et al., "Effect of film thickness on the properties of indium tin oxide thin films," *Journal of Applied Physics*, vol. 88, no. 10, pp. 6021–6025, 2000.
- [29] G. Korotcenkov, V. Brinzari, A. Cerneavski et al., "The influence of film structure on In_2O_3 gas response," *Thin Solid Films*, vol. 460, no. 1-2, pp. 315–323, 2004.
- [30] Z. Qiao, R. Latz, and D. Mergel, "Thickness dependence of In_2O_3 : Sn film growth," *Thin Solid Films*, vol. 466, no. 1-2, pp. 250–258, 2004.
- [31] H.-N. Cui, V. Teixeira, and A. Monteiro, "Microstructure study of indium tin oxide thin films by optical methods," *Vacuum*, vol. 67, no. 3-4, pp. 589–594, 2002.
- [32] J. C. Manificier, J. Gasiot, and J. P. Fillard, "A simple method for the determination of the optical constants n, k and the thickness of a weakly absorbing thin film," *Journal of Physics E*, vol. 9, no. 11, pp. 1002–1004, 1976.
- [33] I. Baía, B. Fernandes, P. Nunes, M. Quintela, and R. Martins, "Influence of the process parameters on structural and electrical properties of r.f. magnetron sputtering ITO films," *Thin Solid Films*, vol. 383, no. 1-2, pp. 244–247, 2001.
- [34] C. G. Choi, K. No, W. J. Lee et al., "Effects of oxygen partial pressure on the microstructure and electrical properties of indium tin oxide film prepared by d.c. magnetron sputtering," *Thin Solid Films*, vol. 258, no. 1-2, pp. 274–278, 1995.

Research Article

Characterization of the Pore Filling of Solid State Dye Sensitized Solar Cells with Photoinduced Absorption Spectroscopy

Carol Olson, Dirk Veldman, Klaas Bakker, and Frank Lenzmann

Solar Energy, Energy Research Centre of the Netherlands (ECN), Westerduinweg 3, 1755 LE Petten, The Netherlands

Correspondence should be addressed to Carol Olson, olson@ecn.nl

Received 15 October 2010; Revised 26 April 2011; Accepted 16 May 2011

Academic Editor: Dinko Chakarov

Copyright © 2011 Carol Olson et al. This is an open access article distributed under the Creative Commons Attribution License, which permits unrestricted use, distribution, and reproduction in any medium, provided the original work is properly cited.

Near steady-state photoinduced absorption (PIA) and UV-Vis absorption spectroscopy are used to characterize the pore filling of spiro-MeOTAD (2,2',7,7'-tetrakis-(*N,N*-di-*p*-methoxyphenylamine)9,9'-spirobifluorene) into the nanoparticulate TiO₂ electrode of a solid-state dye-sensitized solar cell (ssDSC). The volumetric ratio of filled to unfilled pore volumes, as well as the optical signature of interacting chemical species, that is, the hole-transfer yield (HTY), are investigated. PIA spectroscopy is used to measure the HTY, relative to the amount of spiro-MeOTAD present, without needing to determine the extinction coefficients of the dye and spiro-MeOTAD cation species. The Beer-Lambert law is used to relate the relative PIA signal to the penetration length of the hole-conductor in the TiO₂ film. For the sample thickness range of 1.4–5 μm investigated here, the optimum characteristic penetration length is determined to be 3.1 + 0.46 μm, which is compared to 1.4 μm for the 200 mg mL⁻¹ concentration of spiro-MeOTAD conventionally used. Therefore, doubling the effective penetration of spiro-MeOTAD is necessary to functionalize all the dye molecules in a ssDSC.

1. Introduction

First generation dye sensitized solar cells (DSCs) are composed of a high surface area nanoparticulate TiO₂ electrode, onto which a ruthenium dye, such as the Z907 dye (*cis*-RuLL'(SCN)₂ (L = 4,4'-dicarboxylic acid-2,2'-bipyridine, L' = 4,4'-dinonyl-2,2'-bipyridine), [1, 2] is adsorbed, immersed in a liquid electrolyte, typically containing an I⁻/I₃⁻ redox couple, which conducts holes to a platinum counter electrode [3]. In the next generation of dye cells, however, replacement of the liquid electrolyte with a solid electrolyte is desirable. The liquid electrolyte presents sealing and module production challenges, especially because the I⁻/I₃⁻ redox couple is corrosive to metals such as Ag, the grid metal, and degradation products from the electrolyte block the activity of the Pt cathode [4]. The most widely investigated and successful [5] solid-state electrolyte material to date is the molecular hole-transporting spiro-MeOTAD [6, 7] but other possibilities for iodine-free

electrolytes [8], including inorganic and polymeric hole-transporting materials, have also been investigated.

The infiltration of a solid into a nanoporous electrode emerged as a challenging problem from the start [6, 7] and has remained [9–11] so in the making of ssDSCs. The primary characterization tool to date has been scanning electron microscopy (SEM) [10]. In the best cases, SEM images roughly indicate the homogeneity of the spiro-MeOTAD/TiO₂ composite at the exposed surface. Unlike transient absorption spectroscopy (TAS), it cannot quantitatively measure the percentage of dye molecules that are in effective contact with the hole transporter and therefore are regenerated, that is, the hole transfer yield (HTY). TAS optically identifies the signal of an oxidized species and quantifies it by use of the extinction coefficient.

TAS has been used to observe the kinetics of various electron transfer processes in the DSC [12–14] and to compare the HTY of various hole-conducting materials to spiro-MeOTAD [15]. However, it has not been possible

to isolate the separate absorption contributions from the charged dye and the spiro-MeOTAD in an assembled ssDSC within the spectral range of 500–1000 nm [16]. By comparing TAS results of both sides of a ssDSC sample, a concentration gradient in the filling of the spiro-MeOTAD is generally not observed, except for very low concentrations of spiro-MeOTAD or very thick TiO₂ films [15, 17, 18]. The strong absorption of the oxidized spiro-MeOTAD was unambiguously identified in the IR region, when TAS measurements were taken between 600–1500 nm [18].

Snaith et al. [18] proposed that the amount of spiro-MeOTAD in the pores of the TiO₂ is equal to the concentration of spiro-MeOTAD of the starting solution, c , plus an amount from the wet overlayer, resulting from the spin-coating, which is driven into the film by a concentration gradient setup during the process of evaporation. They defined a “filling fraction”, F , as the ratio of the thickness of the spiro-MeOTAD, t_{spiro} , divided by the equivalent thickness of the pores, equation (1a), where t_{spiro} depends on the thickness of the wet overlayer of spiro-MeOTAD solution, t_{WET} , the final dry spiro-MeOTAD “overlayer” thickness, t_{OL} , the thickness of the TiO₂ film, t_{TiO_2} , and the porosity of the titania, p , (1b)

$$F = \frac{t_{\text{spiro}}}{(p * t_{\text{TiO}_2})}, \quad (1a)$$

$$t_{\text{spiro}} = c * (t_{\text{WET}} + (p * t_{\text{TiO}_2})) - t_{\text{OL}}, \quad (1b)$$

T_{WET} is determined by spin-coating various concentrations of the spiro-MeOTAD onto flat substrates. After drying, the film thicknesses were measured with the SEM and the volume of the dry spiro-MeOTAD film was calculated. The wet volume results from dividing the dry volume of the spiro-MeOTAD by the % volume that the spiro-MeOTAD occupies in the starting solution (calculated from the density and the starting concentration). The focus is on the change in spun wet film thickness due to the change in solute concentration, which has been observed for many solutes and solvents [16]. Solvation effects are not considered here. Ding et al. [19] tested (1a) and (1b) with various characterization techniques, and they were the first to largely validate Snaith’s equation by quantifying the spiro-MeOTAD, desorbed out of the ssDSC, with UV-Vis absorption measurements.

In this work, we analyze the volume-based filling fraction by comparing calculated and experimental spiro-MeOTAD sample masses. From this analysis, an empirical correction factor is proposed to bring the filling fraction to more closely reflect the actual mass infiltrated into the pores. Observation of the filling fraction is complementary to the information gained with TAS, that is, the fraction of dye molecules that are (not) being regenerated by the spiro-MeOTAD.

We propose a method of using photoinduced absorption spectroscopy (PIA) to relatively determine the dye regeneration yield of an ssDSC, and we show its relationship to the filling fraction. After identifying the separate spectral contribution of the oxidized solid spiro-MeOTAD in a blend with phenyl-C71-butyric-acid-methyl ester ([70]PCBM) on TiO₂, we examine the PIA spectra of ssDSCs with various

filling fractions. We demonstrate that a single PIA measurement of a ssDSC at two different wavelengths can be used as a relative measure for the dye regeneration yield.

2. Experimental

2.1. Sample Preparation. The SnO₂:F coated glass substrates were cleaned with Extran MAO1, sodium hydroxide solution and ethanol and sintered at 450°C for 1 hour. The substrates were then coated with a compact layer of TiO₂ by aerosol spray pyrolysis deposition, at 0.9 bar and ~470°C, of titanium (IV) isopropoxide (1.56 g, Aldrich 97%), acetyl acetone (2.3 g), and ethanol (113.3 g). A total of 5 layers produced 80–100 nm of flat compact TiO₂ after sintering at 570°C for 30 min. TiO₂ paste (Dyesol screenprint paste DSR 18R-T, 3 g) was diluted with ethanol (3 mL) for 4 micron thick films this paste was further diluted with ethanol for thinner films, and was doctor bladed onto the substrates. They were then dried (20 min at 80°C) and sintered at a rate of 900°C/h until 450°C where they remained for 30 minutes. After the substrates were cooled down to approximately 40°C they were immersed in aqueous TiCl₄ solution (40 mM), kept at 70°C for 30 min, and subsequently rinsed with deionized water and ethanol. They were sintered again at 450°C for 30 minutes. Directly out of the oven, the TiO₂ films were sensitized overnight in a solution of Z907 Dyesol DNH2 (0.28 mM) in a 1:1 mixture of CH₃CN : tBuOH, and subsequently rinsed with CH₃CN. The spiro-MeOTAD solution (Merck SHT-263) was dissolved overnight at 70°C in chlorobenzene at concentrations of 25, 45, 90, 100, 180, and 200 mg mL⁻¹. Before spin-coating, TBP (0.1 μL per mg spiro-MeOTAD) and Li-FSI solution (175 mg/mL Li-FSI in Acetonitrile; 0.21 μL per mg spiro-MeOTAD) was added to this solution. The solution was heated again to 70°C and then was spin-coated (180 μL or 20 μL/cm²) onto the TiO₂ films that had been heated on a hotplate for 90 seconds at 70°C. Spin-coating was done with a Laurell Technologies Corp. spin coater (Model WS-400B-6NPP/LITE) programmed to wait 1 minute, accelerate to 2300 rpm for 30 sec, and decelerate to 800 rpm for 30 seconds. After the spiro-MeOTAD was applied, 100 nm thick gold contacts were thermally evaporated on top of the spiro-MeOTAD overlayer with a rate of 0.15 nm/s at a pressure of 1×10^{-6} mbar.

The spectra of the dye alone was obtained from a TiO₂ film sensitized with Z907 dye as described above but without spin-coating and gold evaporation.

The sample with a blend of [70]PCBM and spiro-MeOTAD on TiO₂ was made using [70]PCBM ([6,6]-phenyl C71-butyric acid methyl ester, Solenne B.V., used as received, 6.9 g) and dissolved at 70°C in chlorobenzene (100 μL). After the [70]PCBM was fully dissolved, a solution (100 μL of 180 mg mL⁻¹ spiro-MeOTAD in chlorobenzene) was added. This [70]PCBM/spiro solution was then spin-coated as described above on a TCO substrate coated with 80 nm of compact TiO₂.

The total thickness (TiO₂ + spiro MeOTAD overlayer) of the ssDSC was measured using a Dektak Profiler after

a scratch with a scalpel was made in the nonactive region between the gold contacts.

2.2. IV Measurements. Current-voltage measurements of the ssDSC were performed using a continuous solar simulator (Wacom) with a 5 kW Xe lamp (Type WXS-300S-50). The measurements were performed at STC (Standard Test Conditions: 1000 W m^{-2} , 25°C and AM1.5 spectrum, inclusive of a spectral mismatch correction, designed for the liquid DSC with Z907, utilizing a monocrystalline silicon solar cell with KG3 filter (Fraunhofer ISE RS-ID 2)) using a home-made measurement system which included a Keithley 2400 Source meter. The mismatch factor was not tailored to the ssDSC. Our experience with Z907 informs us of an error of about 5%.

2.3. Desorption Measurements. UV-Vis spectra were taken using a HP 8453 spectrometer and cuvettes from Hellma type 117.100-QS. The area of the cut samples was determined with the aid of a computerized optical microscope (Leica MZ7.5 Microsystems). Desorption of the samples was done in a closed flask filled with a known volume of chlorobenzene for 1 hour.

2.4. Density of Spiro-MeOTAD. A quartz cuvette with an opening of $4 \times 10 \text{ mm}$ was filled to the rim with water to determine the total inner volume of the cuvette. The volume was calculated by subtracting the weight of the full cuvette with that of the empty cuvette. To determine the volume of spiro-MeOTAD, this procedure was done on both an empty cuvette and a cuvette containing spiro-MeOTAD. After the volume of the empty cuvette was determined, the cuvette was filled with a 200 mg/mL spiro solution and heated to 70°C for 24 hours to evaporate the chlorobenzene. The weight of the spiro-MeOTAD was then determined by subtracting the weight of the cuvette before and after it was filled with spiro MeOTAD.

2.5. Photoinduced Absorption. Near steady-state photoinduced absorption spectra were recorded between 0.5 and 2.5 eV by excitation at 458 (2.71 eV) or 514 nm (2.41 eV) with a mechanically modulated (275 Hz) continuous wave argon ion laser pump beam and by measuring the change in transmission of a tungsten-halogen probe beam through the sample (ΔT) with a phase sensitive lock-in amplifier after dispersion with a monochromator and detection using Si, InGaAs, and cooled InSb detectors. The pump power was typically 50 mW with a beam diameter of 2 mm. The signal intensity ($\Delta T T^{-1}$) was corrected for the photoluminescence, which was recorded in a separate experiment. Samples were measured in ambient atmosphere (290 K). The error is estimated to be $<5\%$, but depends on the signal intensity and the transmission of the sample. Any error in the overlap of the beams is cancelled out by dividing the signals taken at different wavelengths.

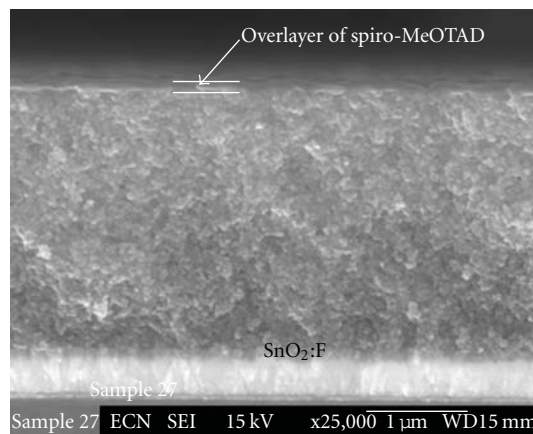


FIGURE 1: SEM cross-section of a ssDSC: the overlayer of the spiro-MeOTAD is visible on the top of the TiO_2 film.

3. Results and Discussion

3.1. SEM Characterization and Filling Fraction Analysis. A typical example of an ssDSC cross-section is shown in Figure 1. The $\text{SnO}_2:\text{F}$ layer on the conducting glass is clearly visible. The degree of the penetration of the spiro-MeOTAD into the TiO_2 is visually often not apparent and the composite often appears as a monolithic layer. The spiro-MeOTAD overlayer however is evident and measurable in the SEM image. ssDSC cross-sections showing a range of overlayer thicknesses are shown in Figure 2. The images A and B in Figure 2 have relatively thick spiro-MeOTAD overlayers, with visible striations apparently produced in the spin-coating process step. While the upper edge in Image C of Figure 2 is smooth, it is not resolvable whether there is a continuous spiro-MeOTAD overlayer or not. The existence of this layer was only deduced by the electrical measurements described below. The topmost edge of the sample in Image D appears to have a rougher surface, with particles clearly visible, indicating that there is no overlayer present, or that the overlayer may be shortened by the particles sticking up.

In order to calculate the filling fraction in (1a) and (1b), the thicknesses of the spiro-MeOTAD overlayer and of the TiO_2 film were measured by SEM. The porosity was taken to be 68% [19], which is typical for unsensitized TiO_2 films. The influences on the porosity due to sample variation, the presence of the dye, double layer or solvation effects, were not taken into account here. The focus is to identify the influential parameters and the trends observed in the pore filling due to the variation of spiro-MeOTAD concentration. Figure 3 shows the range of filling fractions, as calculated using (1a) and (1b), plotted as a function of the concentration of spiro-MeOTAD in solution, for the ssDSC samples in this study. The relationship of t_{WET} to the spiro-MeOTAD concentration is plotted in Figure 4(a).

3.2. I-V Characteristics. The short circuit currents and fill factors are plotted in Figure 4(b) for some samples with spiro-MeOTAD concentrations of 100 and 200 mg mL^{-1} . Cells having no overlayer (as for all samples with

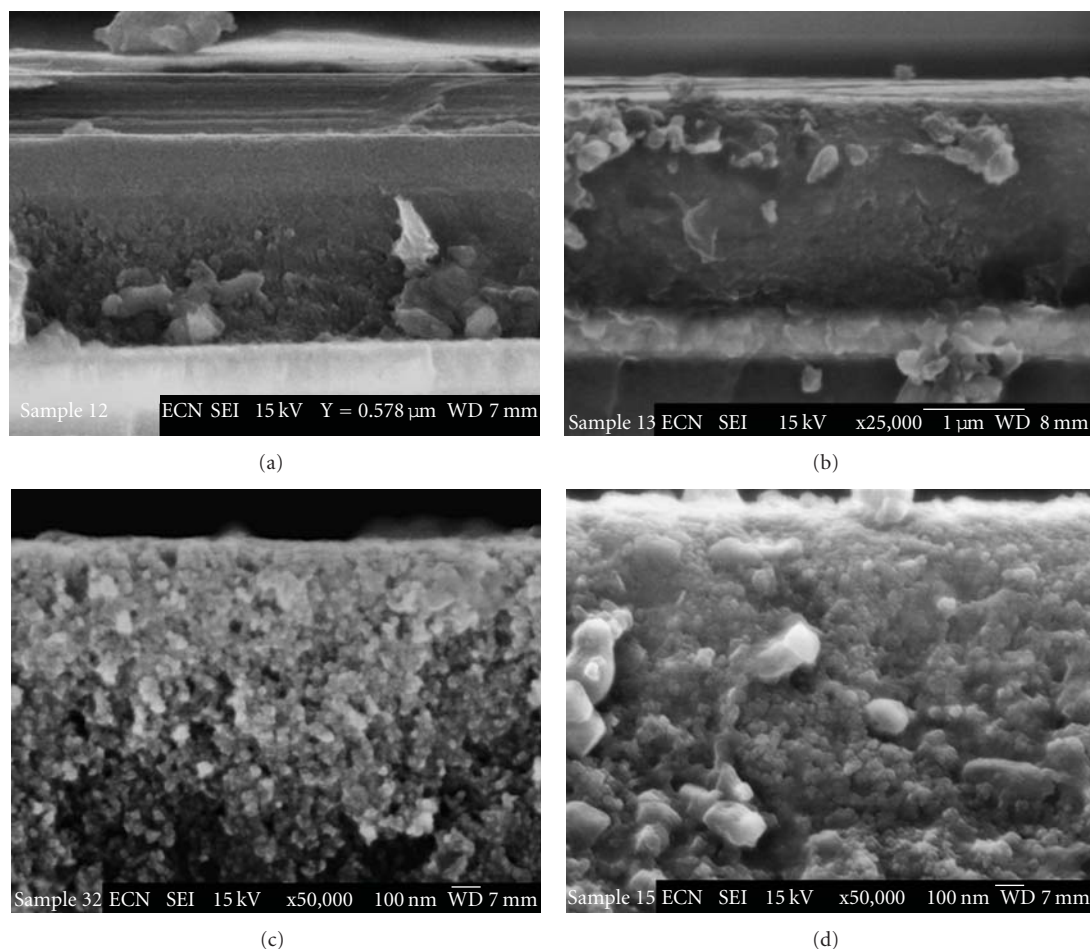


FIGURE 2: SEM cross-sections of ssDSCs with overlayers of (a) 580 nm; (b) 190 nm (c) ~10 nm and (d) 0 nm.

25 mg mL⁻¹ spiro-MeOTAD) are short circuited due to the direct connection between the TiO₂ electrode and the counter electrode. It is interesting to note, however, that the sample with an overlayer of only ~10 nm (as shown in Figure 2(c)) performs with roughly the same efficiency as those cells with much thicker overlayers. (See supplementary material available at doi: 10.1155/2011/513089).

3.3. Desorption to Measure Mass. After dissolving the ssDSC in chlorobenzene for 1 hour, the concentration of spiro-MeOTAD was determined using Beer's law, as pioneered by Ding et al. [19]. The change in UV-vis absorption, at 390 nm, of the desorbed sample was measured spectroscopically and compared to the optical densities, at the same wavelength, of solutions with known spiro-MeOTAD concentrations. Lambert-Beer's law was experimentally verified to be valid in the range of 25–300 mg mL⁻¹.

3.4. Calculated Mass. As an alternative to using the desorption measurements to determine the spiro-MeOTAD mass, the mass was calculated using (2), which involves using three measured parameters: the thicknesses of the TiO₂ and the overlayer, t_{TiO_2} and t_{OL} , (to express volumes with assumed

areas of 1 mm²), and the density, ρ ; one parameter retrieved from the literature, the porosity, p ; the parameter of interest, the filling fraction, F .

$$\begin{aligned} \text{spiro}_{\text{calc mass}} &= ((t_{\text{TiO}_2} \cdot 1 \text{ mm}^2) \cdot p \cdot F + (t_{\text{OL}} \cdot 1 \text{ mm}^2)) \cdot \rho. \end{aligned} \quad (2)$$

The calculated mass *in the pores* is the quantity expressed in (2) minus the second term, that is, the contribution of the overlayer. The density of spiro-MeOTAD was determined to be 1 ± 0.1 g/cm³, as detailed in the experiment section.

The observed desorbed mass agrees with the calculated total mass of spiro-MeOTAD (2) at low concentrations, but is significantly lower at higher concentrations (Figure 5). One explanation is that the films infiltrated with higher spiro-MeOTAD concentrations may require a longer desorption time than 1 hour to completely desorb all the spiro-MeOTAD. The desorbed TiO₂ films were examined spectroscopically, but were too scattering to give meaningful data. On the other hand, Ding et al. [19] also used desorption times of one hour and confirmed the total desorption of the spiro MeOTAD by XPS. Another possibility that is explored below, is that the calculated mass does not take into account

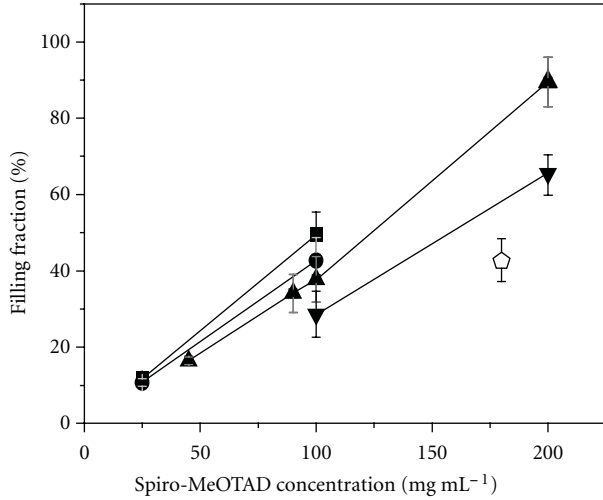


FIGURE 3: Filling fraction versus spiro-MeOTAD concentration, calculated according (1a) and (1b), for samples with TiO_2 thicknesses of: $1.4 \mu\text{m}$ (■); $1.7 \mu\text{m}$ (●); $2 \mu\text{m}$ (▲); $3 \mu\text{m}$ (▼); $5 \mu\text{m}$ (○).

the effect of increased viscosity at higher spiro-MeOTAD solution concentrations, which lowers the capillary force to draw the liquid into the oxide matrix (see (6) below).

3.5. Characteristic Penetration Length. By multiplying the filling fraction by the thickness of the TiO_2 film, a characteristic penetration length (CPL) may be determined:

$$\text{CPL} = F * t_{\text{TiO}_2}. \quad (3)$$

The term “characteristic penetration length” may suggest that the solution penetrates the film from top to bottom, infiltrating all the porous spaces equally, but this is not realistic considering the experimental evidence that there is typically no concentration gradient across the ssDSC [15, 17, 18]. The TiO_2 particulate film is composed of pores of various diameters which randomly branch and neck, and the primary infiltration mechanism is thought to be capillary action [19], which depends on the pore diameter. Nevertheless, it is a way of comparing the relative filling of one film with another. The CPL is found to be a constant, for all ssDSCs of a given spiro-MeOTAD concentration, independent of film thickness. (Please see supporting information for electrical characteristics.)

The mass, m , is related to the CPL through (4), using the volume (area, A , times length, CPL), porosity, p , and density, ρ .

$$\begin{aligned} m &= A * \text{CPL} * \rho * p \\ &= 1 \text{ mm}^2 * (t_{\text{TiO}_2} * F) * \rho * p. \end{aligned} \quad (4)$$

Equation (4) is the same as (2) minus the overlayer. In Figure 5, the experimentally desorbed mass (which includes the overlayer) for ssDSCs of different spiro-MeOTAD concentrations are compared to the calculated total mass, as well as the calculated mass in the pores (or equivalently, the

CPL times porosity). The filling fraction used in the calculated quantities overestimates the mass of spiro-MeOTAD infiltrated in the pores. (Equivalently, we could have used the desorbed mass (see supplementary materials) and (2) to compare empirical filling fractions to filling fractions calculated with (1a) and (1b), with the latter similarly overestimating the experimental.) While the filling fraction allows for variations in wet overlayer thicknesses, t_{WET} , it does not account for the effect of viscosity on the capillary infiltration force. Therefore a correction based on viscosity is proposed to bring the CPL, and the filling fraction, F , more in line with the observed desorbed mass.

The relationship between t_{WET} and the spiro-MeOTAD concentration is an exponential one, as shown in Figure 4(a), suggesting that the higher concentrations have a higher viscosity, requiring more centrifugal force to be spun off than lower concentrations of spiro-MeOTAD. The film thickness, as determined by spin-coating at a fixed speed, is a balance between the drying rate and the radial shear force on the solution. The viscosity of the solution is the resistance of the solution to deformation by the shear force. For many materials, up to concentrations of 50%, the viscosity of solution increases for higher concentrations of solute [16]. The results show that spiro-MeOTAD in chlorobenzene also follows this trend.

An empirical correction factor may be proposed to account for the exponentially thicker layer at higher concentrations. Extrapolating the exponential function to a concentration of 0 mg mL^{-1} gives a $t_{\text{WET}0}$ of 3.5 microns, the value at which the CPL-based calculation agrees well with the calculated mass. The data shows that an increase in the viscosity with concentration has an inverse impact on the penetration length. Therefore the CPL may be adjusted with the ratio of $t_{\text{WET}0}/t_{\text{WET}}$ to account for this effect. Indeed, an improved characteristic length which is more in line with the experimental results is obtained, as indicated in (5), and plotted in Figure 5

$$\text{CPL}_{\text{corr}} = \text{CPL} * \frac{t_{\text{WET}0}}{t_{\text{WET}}}, \quad F_{\text{corrected}} = F * \frac{t_{\text{WET}0}}{t_{\text{WET}}}. \quad (5)$$

This may be useful to estimate the extent of filling of spiro-MeOTAD in the pores of a TiO_2 nanoparticulate film. The penetration of a solution into a wetted capillary, or porous medium, is described by the Lucas-Washburn [20–22] equation, in which ℓ is the penetration length, r_{eff} is the effective hydrodynamic pore radius, γ is the surface tension, η is the viscosity, θ is the contact angle, and t is the time, as given in (4)

$$\ell^2 = \left(\frac{\gamma \cos \theta}{\eta} \right) r_{\text{eff}} t. \quad (6)$$

Equation (6) shows that the penetration length is a function of the viscosity of the penetrating solution. The application of this equation requires a determination of the effective radius in the tortuous particulate TiO_2 film, which, for example, has been performed for alumina packed beds [21]. It clearly shows the relationship of viscosity to penetration length and may be the focus of future work in understanding

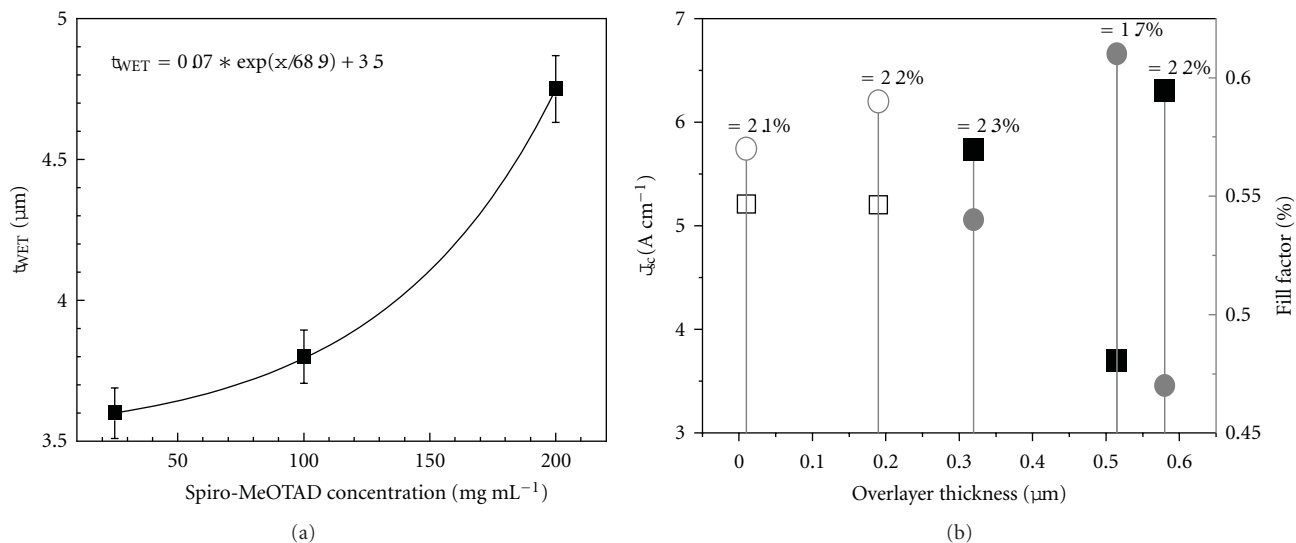


FIGURE 4: (a) Wet layer thickness (t_{WET}) as a function of the spiro-MeOTAD concentration, fitted with an exponential. (b) Short circuit currents (squares) and fill factors (circles) for ssDSCs as a function of spiro-MeOTAD overlayer thicknesses, for spiro-MeOTAD concentrations of 100 mg mL^{-1} (open symbols) and of 200 mg mL^{-1} (closed symbols).

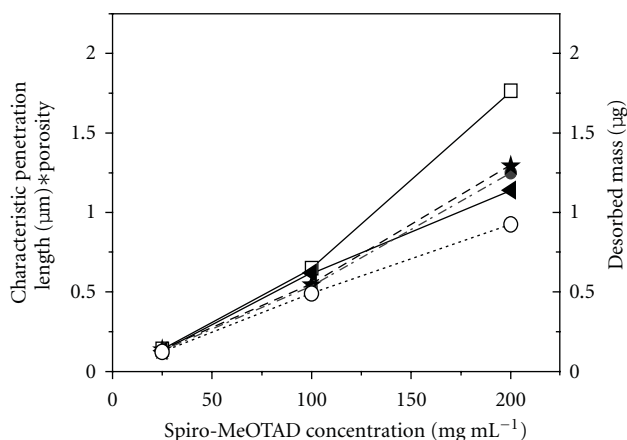


FIGURE 5: The scale of the CPL (μm), times the porosity (%), is the same as the one for the desorbed mass (μg) for spiro-OMeTAD with a density of 1 g/cm^3 (see text). Average calculated and experimental values of the mass are plotted versus spiro-MeOTAD concentration. The experimentally determined mass desorbed from the samples (▲) is much lower than the calculated total mass (□) and should be greater than the calculated mass in the pores (★) because the former also includes the overlayer. The uncorrected CPL (●) is equal to the calculated mass in the pores (★). These values indicate that the filling fraction overestimates the amount of spiro-MeOTAD which actually infiltrates the pores. The correction for viscosity effects (○) for higher concentrations of spiro-MeOTAD gives an improved value for the CPL, or calculated mass in the pores. (The standard deviation of all CPL and desorbed mass values is $<0.12 \mu\text{m}$.)

and optimizing the infiltration of a hole conductor into a TiO_2 film. Understanding the pore filling mechanism reflected by the filling fraction is a key to optimizing the pore filling. References to the CPL in this paper from this point on

will refer to the CPL_{corr} , which is corrected for the effects of viscosity.

3.6. Photoinduced Absorption Spectroscopy: Relation to Filling Fraction. The photoinduced absorption spectroscopy technique allows optical detection of excited species generated by photoexcitation, such as the oxidized states of the dye, Z907, and the hole conductor, spiro-MeOTAD, in a ssDSC. After injection of the electron by the dye into the conduction band of the TiO_2 , the dye cation is normally regenerated to its neutral state by an electron from the spiro-MeOTAD after a period ranging from less than ps to greater than ns [6]. In the absence of a hole conductor, an electron from the TiO_2 recombines with the oxidized dye cation after a period of hundreds of microseconds [2], during which the absorption spectrum of the oxidized dye may be observed.

When spiro-MeOTAD perfectly infiltrates the sensitized TiO_2 film and regenerates the dye, the photoinduced absorption features of the oxidized dye are replaced with that of oxidized spiro-MeOTAD [6, 7, 15, 17, 18]. In the extended visible spectral range (400–1000 nm), many signals may overlap due to contributions of the oxidized dye (absorption and bleaching bands) [23], electrons in TiO_2 [24, 25], and oxidized spiro-MeOTAD [18]. This confluence of signals in the visible region makes it very difficult to analyze spectra. Even when the separate spectral features of the oxidized dye and spiro-MeOTAD are known, near steady state photoinduced absorption spectra in the spectral range of 400–1000 nm cannot always be fitted with a linear addition of the independent oxidized dye or hole-conductor, because the electron density of the TiO_2 surface may lead to spectral shifts in the ground state absorption of dyes and thereby to additional spectral variations near the bleaching band [17]. Alternatively, the observation window may be extended to the near infrared region of the spectrum, where

oxidized spiro-MeOTAD shows a broad absorption band and the oxidized ruthenium dyes do not absorb. This strategy was used by Snaith et al. in a qualitative analysis of their photoinduced absorption spectra [18].

The PIA spectrum of only the dye Z907 on TiO₂ reveals a positive ΔTT^{-1} signal (i.e., bleaching) with a maximum at 515 nm, and a negative signal (i.e., absorption) peaking between 750–800 nm. (Figure 6(a)). The spectral shape is very similar to that reported for TiO₂ films sensitized with the well-studied and structurally similar dyes N3 (*cis*-Ru(dcbpy)₂(NCS)₂) [12–14, 26] and N719 (its bis-deprotonated analog) [27]. Therefore, we can safely attribute the positive signal to the bleaching band of Z907 and the negative signal to the absorption band of oxidized Z907. Additionally, a weak absorption tail of electrons in TiO₂⁻ is present in the visible to near infrared region [24, 25].

Although steady-state spectra of chemically oxidized spiro-MeOTAD in solution [28, 29] as well as spectroelectrical studies [29] of spiro-MeOTAD in TiO₂ films are available, spectral near steady-state PIA features of optically oxidized spiro-MeOTAD in the solid state may provide slightly different absorption features. Therefore [70]PCBM was used as a photosensitizer to generate a photoinduced absorption spectrum (Figure 6(a)) of oxidized spiro-MeOTAD in a solid composite blend with [70]PCBM on TiO₂ and in the absence of dye Z907. [70]PCBM is used because it can be photoexcited and accept electrons from spiro-MeOTAD [29–31], as a result of its strong ground state absorption in the visible region and strong electron accepting properties [32]. The PIA spectrum of the [70]PCBM:spiro-MeOTAD mixture in TiO₂ reveals two absorption bands in the visible region at ca. 515 nm (2.41 eV) and 700 nm (1.68 eV), and one in the near infrared at 1500 nm (0.83 eV) as shown in Figure 6(a). These three bands are attributed to oxidized spiro-MeOTAD, because of good agreement with previously reported spectra that were obtained by stepwise chemical oxidation [28, 29] or in spectroelectrical studies [29, 33]. In dichloromethane solution, Struijk found two absorption bands in the visible, a strong band at 521 nm and a less intense band at 678 nm, and one in the near infrared, at 1514 nm, after stepwise chemical oxidation [28]. A 5–25 nm shift is typically observed when comparing the spectra of a photoactive species in solution to one in the solid state and is due to molecular interaction with the local environment.

Having established the separate contributions of oxidized Z907 and spiro-MeOTAD, it is possible to analyze PIA spectra of TiO₂ films containing both Z907 and spiro-MeOTAD. For ssDSCs, the PIA spectrum strongly changes with increasing spiro-MeOTAD concentration from 25 to 180 mg mL⁻¹ (Figure 6(b)). For the lowest concentration, the absorption maximum at 780 nm and the presence of a bleaching band below 600 nm (Figure 6(b)) are signatures of oxidized Z907. Contributions of oxidized spiro-MeOTAD are visible from the band at 1450 nm, and from its absorption between 550 and 800 nm. This latter absorption peak overlaps with the bleaching band of the dye and thereby causes an altered form of the positive ΔTT^{-1} band below 600 nm, as compared to the dyed film without spiro-MeOTAD (Figure 6(a)). For the highest concentration of spiro-MeOTAD the absorption

maxima of the bands are 515, 730, and 1450 nm, in good correspondence to the spectrum obtained for the film using [70]PCBM as photosensitizer. This indicates that at the highest concentration, the major part of the dye is regenerated by spiro-MeOTAD. However, comparison of the spectrum of the ssDSC, with 180 mg mL⁻¹ spiro-MeOTAD, with that of the spiro-MeOTAD/PCBM blend (Figure 6(c)) shows that even for the highest concentration of spiro-MeOTAD (triangles), there is still some oxidized dye present (visible by the bleaching band at 565 nm and the additional absorption around 750 nm). Furthermore, the additional absorption in the region 850–1200 nm may be explained with the absorption of free electrons in TiO₂ [24].

Overall, with increasing spiro-MeOTAD concentration, two major spectral changes occur: (1) between 750 and 850 nm the ΔTT^{-1} signal intensity reduces (relative to the 1450 nm peak) and (2) between 525 and 600 nm the positive (i.e., bleaching) signal turns into a negative (i.e., absorption) signal (Figure 6(b)). With increasing spiro-MeOTAD content, both absorption changes are due to lower contribution of the strong absorption (around 800 nm) and bleaching (around 565 nm) of oxidized Z907, relative to oxidized spiro-MeOTAD. By plotting the absorbance at 565 nm versus that at 825 nm, as in Figure 7(a), a linear relation is found with increasing spiro-MeOTAD concentration, when the spectra is normalized at the spiro-MeOTAD 1450 nm peak. This indicates that the spectral changes are due to the same photoexcited species, which we conclude is the oxidized dye.

Plotting all the data gives a slope of -2.0 , but the PIA signal (ΔTT^{-1}) of those samples with the lowest concentration of spiro-MeOTAD are much more scattering than the rest of the samples. They are a bilayer, in which the effective refractive index of one layer is the average of spiro-MeOTAD, TiO₂ and air and the other layer is only an average of TiO₂ and air, and is consistent with other observations of concentration gradients in samples with low concentrations of spiro-MeOTAD [17]. These samples clearly scatter the light differently than a single composite layer of spiro-MeOTAD, TiO₂ and air. Highly scattering samples may dramatically influence the accuracy of the PIA measurement by lowering the magnitude of both ΔT and T^{-1} , introducing a large error in their ratio. When these points are disregarded, the linear fit has a slope of -2.2 . A line with a slope of -2.4 is also plotted to show that this slope is also within the accuracy of the measurement and/or the fit. A slope of -2.4 is expected because the ratio of PIA signal intensities at 565 nm to 825 nm for the dye on TiO₂ alone, without spiro-MeOTAD, is -2.4 . (Figure 6(a)). The ratio of the dye cation absorption peak at 825 nm, or at 565 nm, to the spiro-MeOTAD cation peak at 1450 nm may be used to extract the relative dye cation concentration from the absorption spectrum of the ssDSC.

The PIA signal intensities for the 565 nm and 825 nm peaks, relative to the 1450 nm spiro-MeOTAD peak, are plotted as a function of filling fraction in the inset of Figure 7(b). Because the filling fraction is a nondimensional measure of concentration, it has an exponential relationship to the transmitted light intensity, as predicted by the Beer-Lambert law, given in (7), where I is intensity, ϵ_i is

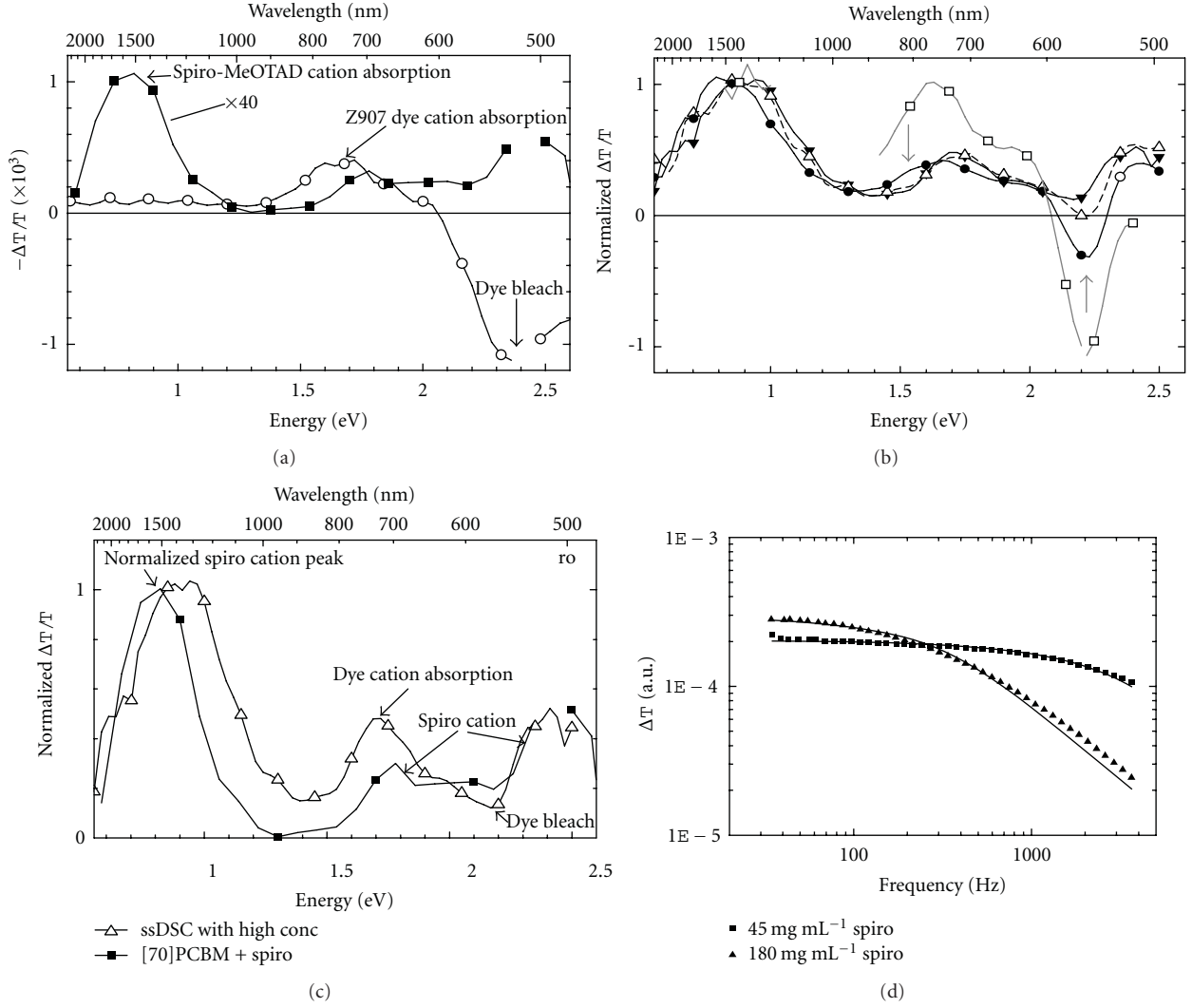


FIGURE 6: Photoinduced absorption spectra of (a) dye Z907 in TiO_2 (\circ), and [70]PCBM blended with spiro-MeOTAD on TiO_2 (\blacksquare , multiplied with a factor of 40); (b) TiO_2 sensitized with dye Z907, with spiro-MeOTAD, normalized at the peak at 1400–1500 nm (0.83–0.89 eV), using spiro-MeOTAD concentrations of 25 (\square), 45 (\bullet), 90 (\triangle), and 180 (\blacktriangledown) mg mL^{-1} ; (c) spectrum of a ssDSC: sensitized TiO_2 infiltrated with a high concentration of spiro-MeOTAD (200 mg mL^{-1}), (\triangle); compared with the spectrum of the spiro-MeOTAD/PCBM blend, (\blacksquare). Spectra were recorded using excitation wavelengths of 514 nm (a, c) and 458 nm (b, c). (d) Frequency-dependent PIA intensities for TiO_2 samples sensitized with dye Z907, infiltrated with 45 (\blacksquare) or 180 (\blacktriangle) mg mL^{-1} spiro-MeOTAD solution. The measurements were recorded at 1.05 eV (1180 nm). The solid lines are fits to the data (13) and result in steady-state lifetimes of 115 and 995 μs for the low and the high spiro-MeOTAD concentration, respectively.

the extinction coefficient of species i , c_i is the concentration of species i and l is path length.

$$\log\left(\frac{I_0}{I}\right) = \sum \varepsilon_i c_i l$$

$$= \varepsilon_{\text{dye cation}} c_{\text{dye cation}} l + \varepsilon_{\text{spiro MeOTAD}} c_{\text{spiro MeOTAD}} l. \quad (7)$$

Normalizing the data at the spiro-MeOTAD peak at 1450 has two effects: (i) the observed signal at the 825 nm peak is now a ratio of the signals at the 825 and 1450 nm peaks and (ii) the expression $(\varepsilon_{\text{spiro}^+}^{1450} * c_{\text{spiro}^+}^{1450} * l)$ is set to a magnitude of one. The Beer-Lambert law for the normalized data may be written as shown in (8) and simplified with the introduction

of constants for the ratio of the extinction coefficients for the respective peaks, as shown in (9)

$$\frac{\log(\Delta I)_{825}}{\log(\Delta I)_{1450}}$$

$$= \frac{(\varepsilon_{\text{spiro}^+}^{825} c_{\text{spiro}^+} l + \varepsilon_{\text{dye}^+}^{825} c_{\text{dye}^+} l)}{\varepsilon_{\text{spiro}^+}^{1450} c_{\text{spiro}^+} l} \quad (8)$$

$$= \frac{\varepsilon_{\text{spiro}^+}^{825}}{\varepsilon_{\text{spiro}^+}^{1450}} + \frac{\varepsilon_{\text{dye}^+}^{825} c_{\text{dye}^+} l}{\varepsilon_{\text{spiro}^+}^{1450} c_{\text{spiro}^+} l}$$

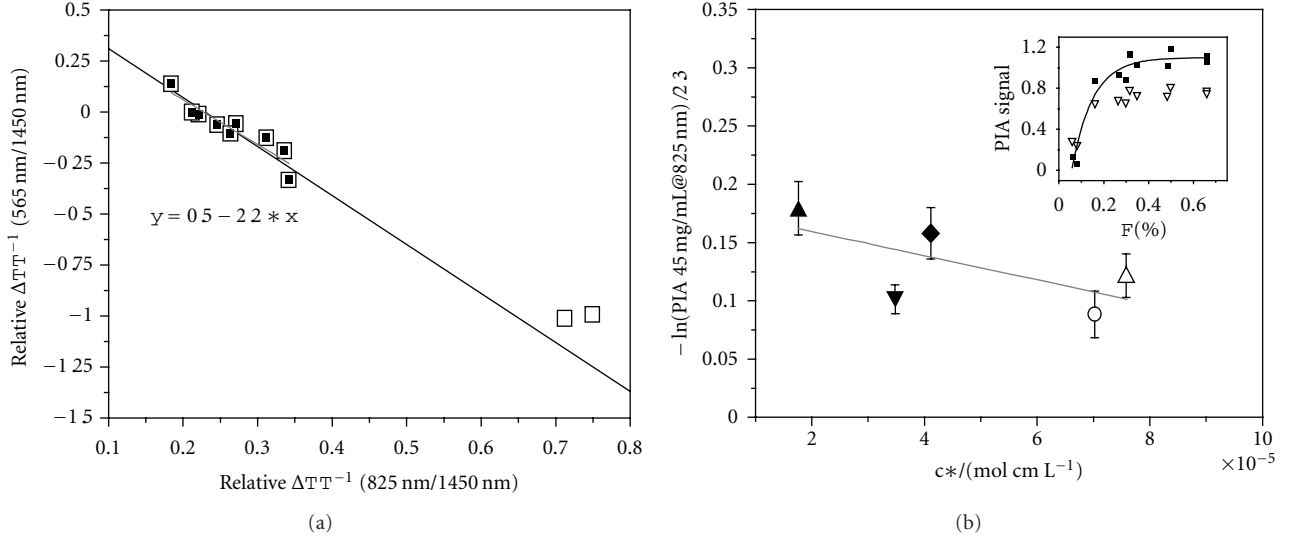


FIGURE 7: (a) ΔTT^{-1} signal intensities relative to the peak at 1450 nm, for 565 nm ($(\Delta T_{565 \text{ nm}} T_{565 \text{ nm}}^{-1})/(\Delta T_{1450 \text{ nm}} T_{1450 \text{ nm}}^{-1})$, y -axis) compared to 825 nm ($(\Delta T_{825 \text{ nm}} T_{825 \text{ nm}}^{-1})/(\Delta T_{1450 \text{ nm}} T_{1450 \text{ nm}}^{-1})$, x -axis). The solid line is a linear fit to the data, excluding the highly scattering points at the lowest concentration: $y = -2.2x + 0.5$. The dashed line shows $y = -2.4x + 0.55$. (b) The $\ln(\text{relative PIA signal at } 825 \text{ nm})/2.3$ is plotted against the concentration times length (mol cm L^{-1}). The spiro-MeOTAD concentrations are 45 (\blacktriangle), 90 (\blacktriangledown), 100 (\blacklozenge) mg mL^{-1} ; 180 (\circ) mg mL^{-1} ; 200 (\triangle) mg mL^{-1} . Inset: ΔTT^{-1} signal intensity relative to the peak at 1450 nm, for 825 nm ($(\Delta T_{825 \text{ nm}} T_{825 \text{ nm}}^{-1})/(\Delta T_{1450 \text{ nm}} T_{1450 \text{ nm}}^{-1})$, \blacksquare) and for 565 nm ($(\Delta T_{565 \text{ nm}} T_{565 \text{ nm}}^{-1})/(\Delta T_{1450 \text{ nm}} T_{1450 \text{ nm}}^{-1})$, ∇) compared to the filling fraction obtained in Section 2.1. The data are fitted with exponential functions: $y = -2 * \exp(-x/0.1) + 1.1$ (solid line) and $-1 * \exp(-x/0.1) + 0.75$.

$$= B + A * \left(\frac{c_{\text{dye}^+}}{c_{\text{spiro}^+}} \right), \quad \text{where } A = \left(\frac{\epsilon_{\text{dye}^+}^{825}}{\epsilon_{\text{spiro}^+}^{1450}} \right), \quad B = \left(\frac{\epsilon_{\text{spiro}^+}^{825}}{\epsilon_{\text{spiro}^+}^{1450}} \right). \quad (9)$$

If the extinction coefficients and the concentrations of the dye and spiro MeOTAD cations are known, then (9) is quite useful. But, it is also possible to reformulate (8) so that the normalized PIA signal provides a measure of the dye cation population, relative to the concentration of spiro-MeOTAD present, without knowledge of the respective extinction coefficients or cation concentrations. It is quite evident that the dye cation population, that is, those dyes that are not regenerated by the hole conductor, is related to the concentration of the hole conductor, and so we can let the ratio of the dye cation density to the spiro-cation density be a function of the spiro-MeOTAD concentration, as expressed in (10). Now, a relationship between the normalized PIA signal and the concentration of spiro-MeOTAD can be written using an effective extinction coefficient as shown in (11)

$$\text{let } \frac{c_{\text{dye}^+}}{c_{\text{spiro}^+}} = f(c_{\text{spiro}}) = \xi * c_{\text{spiro}}, \quad (10)$$

$$\text{let } \epsilon'_{\text{effective}} = \frac{\epsilon_{\text{dye}^+}^{825}}{\epsilon_{\text{spiro}^+}^{1450}} * \frac{\xi}{l},$$

$$\frac{\log(\Delta I)_{825}}{\log(\Delta I)_{1450}} = B + \epsilon'_{\text{effective}} * c_{\text{spiro}} * l. \quad (11)$$

It is interesting to apply (11) to the PIA data, using the CPL (i.e., $F * t_{\text{TiO}_2}$) in (12), to calculate the effective extinction coefficient, with units of $\text{M}^{-1} \text{cm}^{-1}$, of the relative intensity signal at 825 nm, as plotted in Figure 7(b).

$$\begin{aligned} \text{cl} \left[\frac{\text{mol cm}}{L} \right] &= \frac{\rho}{M_{\text{spiroMeOTAD}}} * p * F * t_{\text{TiO}_2} \\ &= \frac{1000 \text{ g/L}}{1230 \text{ g/mol}} * 0.68 * \text{CPL} [\mu\text{m}] * \frac{\text{cm}}{10^4 \mu\text{m}}. \end{aligned} \quad (12)$$

Figure 7(b) shows that the data may be linearly fitted for all concentrations higher than 25 mg mL^{-1} . The error bars are based upon the deviation of a group of three measurements, and the line has an intercept of 0.16 ± 0.02 and the slope, -814 ± 120 . The slope of this line is the effective extinction coefficient for this system. Here, as in the linear fit of the optical data plotted in Figure 7(a), the data points for the very low concentrations of spiro-MeOTAD were not included in the linear fit. Furthermore, in the event of a bi-layer ($\text{TiO}_2 + \text{spiro-MeOTAD} + \text{air} | \text{TiO}_2 + \text{air}$), the relationship between the spiro-MeOTAD concentrations and the dye and oxidized spirocations, assumed in (10), would break down. Indeed, as the concentration of spiro-MeOTAD approaches zero, so will the concentration of spiro-MeOTAD cation, and the expression for ξ will become undefined and very near to this singularity, the relationship becomes superlinear. Despite these considerations, employing this relationship is useful for interpreting the data in the range of concentrations from 45 mg mL^{-1} up through at least 300 mg mL^{-1} .

It is possible to estimate the magnitude of $c * l$ that is necessary to eliminate the dye cation signal. By extrapolating the linear fit in Figure 7(b) to the case where there is no signal from the dye cation, that is, to $y = 0$, the abscissa, $c * l$, is equal to $1.71 \times 10^{-4} \pm 2.6 \times 10^{-5}$ M cm, which can be converted to a CPL of $3.1 \pm 0.46 \mu\text{m}$ using (12). The average (corrected) CPL of the samples with spiro-MeOTAD concentrations of 200 mg mL^{-1} is 1.4. Comparison of these two values shows that a doubling of the characteristic penetration length of spiro MeOTAD is required, than currently achieved, in order to be able to regenerate, and thus functionalize, all the dye molecules in a conventionally sensitized ssDSC.

A sample may have a filling fraction of 90% but if the 10% of the remaining pore space (i.e., narrow pores) contain a third of the dye molecules then the filling is not optimum. Usually high filling fractions can be only achieved with films not greater than 2–2.5 microns. Thicker films would lead to higher light absorption, higher currents, and higher efficiencies. Indeed, the liquid electrolyte DSC's are routinely made to be 8–10 microns thick. Equation (6) shows that the penetration depth of the capillary force depends on viscosity, wetting and the pore radius. (We can assume, as did Snaith et al. [18] that the chlorobenzene completely wets the TiO_2 .) In this case, optimization of the pore filling should address the viscosity of the concentrated spiro-MeOTAD and/or the effective pore radius of the TiO_2 film, to optimize the amount of spiro-MeOTAD which can infiltrate into the pores by capillary action.

The PIA measurements in this work were made at a frequency of 275 Hz, very near the crossover point of the two curves in Figure 6(d), at which there is little variation of signal intensity with spiro MeOTAD concentration, and appropriate for a measurement relative to a constant spiro MeOTAD contribution and the analysis used above. However, to quantitatively determine the number of [non]regenerated cations, or the HTY, the extinction coefficients of the two species must be independently known, and the effect of lifetime upon the measurement must be taken into account. The magnitude of the PIA signal is proportional to g , the efficiency of generation of the photoinduced species; I , the pump intensity; τ_s , the lifetime of a photoexcitation under steady-state conditions, and $\alpha = (2\nu\tau_s)^{-1}$.

$$-\Delta T \propto \frac{gI\tau_s\alpha \tanh \alpha}{(\alpha + \tanh \alpha)}. \quad (13)$$

This equation can be used to detect τ_s from chopper frequency-dependent PIA measurements. This results in steady-state lifetimes of $\tau_s = 115 \mu\text{s}$ for a low spiro-MeOTAD concentration of 45 mg mL^{-1} and to $\tau_s = 995 \mu\text{s}$ for a four times higher spiro-MeOTAD concentration. Such nonequal lifetimes with different hole conductor concentrations complicate quantitative determination of hole transfer yields using near steady-state photoinduced absorption spectra, because the lifetimes are shorter than the period of the chopper ($\nu^{-1} = 3.6 \text{ ms}$). In this case, an increase in lifetime leads to an increase in PIA intensity. For lifetime-independent and hence more quantitative detection using near-state PIA

measurements, much higher frequencies would be required. For example, when measuring at 10 kHz, an increase in lifetime from 0.1 to 1 ms would lead to an increase in PIA intensity as a result of the increased lifetime of only 4%.

This analysis shows that a single PIA measurement at two different wavelengths (825 nm and 1450 nm) can be used as a measure for the hole transfer yield (HTY). Furthermore, this method is more robust than the previous method described by Kroeze et al. [15] In that the quantification may be obtained from a single measurement set, therefore it is not necessary to measure the ssDSC before and after filling with the hole conductor which requires that the light intensities and sample repositioning must be as identical as possible.

4. Conclusions

We prepared ssDSCs with a range of TiO_2 thicknesses and filling fractions. The calculated mass based on the filling fraction, as proposed by Snaith, was greater than the experimentally desorbed mass. Because the effects of viscosity were observed in the thicknesses of the spiro MeOTAD films spun on flat substrates, a correction factor was proposed for the filling fraction to account for the effects of viscosity in capillary infiltration. According to the Beer-Lambert law, it was shown that PIA signal is related to the filling fraction, and the CPL, through an effective extinction coefficient, which was determined for this material system, allowing the relative dye cation density to be deduced. The optimum value of the CPL, for the sample range of 1.4 to $5 \mu\text{m}$ investigated here, was determined to be 3.1 ± 0.46 microns which is roughly double the average CPL for the samples used in this study (see supplementary material). This suggests that a solution with a higher concentration of hole conductor and a lower viscosity and/or a greater effective pore radius in the TiO_2 film is necessary to minimize the thickness of the overlayer, increase the penetration length of the spiro-MeOTAD and to optimally functionalize all the dye molecules in an ssDSC. In other words, for the solid electrolyte to achieve the same intimate contact with the dye molecules as a liquid electrolyte, the infiltration conditions must be engineered so that a more concentrated solution will enter the pores, either by altering the viscosity of the spiro-MeOTAD solution and/or by altering the pore radii of the TiO_2 film.

Acknowledgments

The authors kindly acknowledge Professor Dr. Rene Janssen (TU/e) for allowing us to work with their PIA setup. They are also kindly acknowledge Jan Kroon for helpful discussions. Thanks due to Esther Cobussen for evaporating the gold contacts and to Sjoerd Veenstra for providing the [70]PCBM. Thanks due to G. Boschloo for introducing us to their PIA set-up at Uppsala University. The funding for this work was provided by the Dutch Ministry of Economic Affairs.

References

- [1] P. Wang, B. Wenger, R. Humphry-Baker et al., "Charge separation and efficient light energy conversion in sensitized mesoscopic solar cells based on binary ionic liquids," *Journal of the American Chemical Society*, vol. 127, no. 18, pp. 6850–6856, 2005.
- [2] P. Wang, S. M. Zakeeruddin, J. E. Moser, M. K. Nazeeruddin, T. Sekiguchi, and M. Grätzel, "A stable quasi-solid-state dye-sensitized solar cell with an amphiphilic ruthenium sensitizer and polymer gel electrolyte," *Nature Materials*, vol. 2, no. 6, pp. 402–407, 2003.
- [3] B. O'Regan and M. Grätzel, "A low-cost, high-efficiency solar cell based on dye-sensitized colloidal TiO₂ films," *Nature*, vol. 353, pp. 737–740, 1991.
- [4] E. Figgemeier and A. Hagfeldt, "Are dye-sensitized nanostructured solar cells stable? An overview of device testing and component analyses," *International Journal of Photoenergy*, vol. 6, no. 3, pp. 127–140, 2004.
- [5] H. J. Snaith, A. J. Moule, C. Klein, K. Meerholz, R. H. Friend, and M. Grätzel, "Efficiency enhancements in solid-state hybrid solar cells via reduced charge recombination and increased light capture," *Nano Letters*, vol. 7, no. 11, pp. 3372–3376, 2007.
- [6] U. Bach, Y. Tachibana, J. E. Moser et al., "Charge separation in solid-state dye-sensitized heterojunction solar cells," *Journal of the American Chemical Society*, vol. 121, no. 32, pp. 7445–7446, 1999.
- [7] U. Bach, D. Lupo, P. Comte et al., "Solid-state dye-sensitized mesoporous TiO₂ solar cells with high photon-to-electron conversion efficiencies," *Nature*, vol. 395, no. 6702, pp. 583–585, 1998.
- [8] Y. Shozo, Y. Youhai, and M. Kazuhiro, "Iodine/iodide-free dye-sensitized solar cells," *Accounts of Chemical Research*, vol. 42, no. 11, pp. 1827–1838, 2009.
- [9] H. J. Snaith and L. Schmidt-Mende, "Advances in liquid-electrolyte and solid-state dye-sensitized solar cells," *Advanced Materials*, vol. 19, no. 20, pp. 3187–3200, 2007.
- [10] L. Schmidt-Mende and M. Grätzel, "TiO₂ pore-filling and its effect on the efficiency of solid-state dye-sensitized solar cells," *Thin Solid Films*, vol. 500, no. 1-2, pp. 296–301, 2006.
- [11] J. H. Yum, P. Chen, M. Grätzel, and M. K. Nazeeruddin, "Recent developments in solid-state dye-sensitized solar cells," *ChemSusChem*, vol. 1, no. 8-9, pp. 699–707, 2008.
- [12] J. R. Durrant, S. A. Haque, and E. Palomares, "Towards optimisation of electron transfer processes in dye sensitised solar cells," *Coordination Chemistry Reviews*, vol. 248, no. 13-14, pp. 1247–1257, 2004.
- [13] H. Van't Spijker, B. O'Regan, and A. Goossens, "Quantitative study of electron losses in nanoporous anatase using transient absorption spectroscopy," *Journal of Physical Chemistry B*, vol. 105, no. 30, pp. 7220–7226, 2001.
- [14] N. Kopidakis, K. D. Benkstein, J. van de Lagemaat, and A. J. Frank, "Transport-limited recombination of photocarriers in dye-sensitized nanocrystalline TiO₂ solar cells," *Journal of Physical Chemistry B*, vol. 107, no. 41, pp. 11307–11315, 2003.
- [15] J. Kroeze, N. Hirata, L. Schmidt-Mende et al., "Parameters influencing charge separation in solid-state dye-sensitized solar cells using novel hole conductors," *Advanced Functional Materials*, vol. 16, no. 14, pp. 1832–1836, 2006.
- [16] M. Kunitz, "An empirical formula for the relation between viscosity of solution and volume of solute," *Journal of General Physiology*, vol. 9, no. 6, pp. 715–725, 1926.
- [17] U. B. Cappel, E. A. Gibson, A. Hagfeldt, and G. Boschloo, "Dye regeneration by Spiro-MeOTAD in solid state dye-sensitized solar cells studied by photoinduced absorption spectroscopy and spectroelectrochemistry," *Journal of Physical Chemistry C*, vol. 113, no. 15, pp. 6275–6281, 2009.
- [18] H. J. Snaith, R. Humphry-Baker, P. Chen, I. Cesar, S. M. Zakeeruddin, and M. Grätzel, "Charge collection and pore filling in solid-state dye-sensitized solar cells," *Nanotechnology*, vol. 19, no. 42, Article ID 424003, 2008.
- [19] I.-K. Ding, N. Tétreault, J. Brillet et al., *Adv. Funct. Mater.*, vol. 19, pp. 2431–2436, 2009.
- [20] E. W. Washburn, "The dynamics of capillary flow," *Physical Review*, vol. 17, no. 3, pp. 273–283, 1921.
- [21] D. Patro, S. Bhattacharyya, and V. Jayaram, "Flow kinetics in porous ceramics: understanding with non-uniform capillary models," *Journal of the American Ceramic Society*, vol. 90, no. 10, pp. 3040–3046, 2007.
- [22] N. Fries, K. Odic, M. Conrath, and M. Dreyer, "The effect of evaporation on the wicking of liquids into a metallic weave," *Journal of Colloid and Interface Science*, vol. 321, no. 1, pp. 118–129, 2008.
- [23] J. E. Moser, D. Noukakis, U. Bach et al., "Comment on "measurement of ultrafast photoinduced electron transfer from chemically anchored Ru-dye molecules into empty electronic states in a colloidal anatase TiO₂ film""," *Journal of Physical Chemistry B*, vol. 102, no. 18, pp. 3649–3650, 1998.
- [24] G. Boschloo and D. Fitzmaurice, "Electron accumulation in nanostructured TiO₂ (anatase) electrodes," *Journal of Physical Chemistry B*, vol. 103, no. 37, pp. 7860–7868, 1999.
- [25] Y. Tachibana, J. E. Moser, M. Grätzel, D. R. Klug, and J. R. Durrant, "Subpicosecond interfacial charge separation in dye-sensitized nanocrystalline titanium dioxide films," *Journal of Physical Chemistry*, vol. 100, no. 51, pp. 20056–20062, 1996.
- [26] G. Boschloo and A. Hagfeldt, "Photoinduced absorption spectroscopy of dye-sensitized nanostructured TiO₂," *Chemical Physics Letters*, vol. 370, no. 3-4, pp. 381–386, 2003.
- [27] G. Boschloo and A. Hagfeldt, "Photoinduced absorption spectroscopy as a tool in the study of dye-sensitized solar cells," *Inorganica Chimica Acta*, vol. 361, no. 3, pp. 729–734, 2008.
- [28] M. P. Struijk, *High-spin through bond and space*, Ph.D. thesis, TU Eindhoven, 2001, chapter 7.
- [29] U. Bach, *Solid-state dye-sensitized mesoporous TiO₂ solar cells*, Ph.D. thesis, EPFL Lausanne, 2000, chapter 4.
- [30] D. Veldman, *Charge generation in molecular materials*, Ph.D. thesis, TU Eindhoven, 2008, chapter 8.
- [31] The band gap and reduction potential of [70]PCBM are similar to those of C60-PCBM,^[25] hence the oxidation potential of is [70]PCBM must also be similar to that of C60-PCBM ($E_{ox} = +1.08$ V vs. Fc/Fc⁺),^[23] which is nearly 1 V higher than that of spiro-MeOTAD ($E_{ox} = +0.118$ V vs. Fc/Fc⁺).^[22] This allows efficient electron transfer from photoexcited [70]PCBM to spiro-MeOTAD.
- [32] M. M. Wienk, J. M. Kroon, W. J. H. Verhees et al., "Efficient methano[70]fullerene/MDMO-PPV bulk heterojunction photovoltaic cells," *Angewandte Chemie International Edition*, vol. 42, no. 29, pp. 3371–3375, 2003.
- [33] The absorption of the radical anion of [70]PCBM is likely to be obscured by the radical cation absorption of spiro-MeOTAD. This is also the case for MDMO-PPV:[70]PCBM blends.^[25]

Research Article

Synthesis and Application of New Ruthenium Complexes Containing β -Diketonato Ligands as Sensitizers for Nanocrystalline TiO₂ Solar Cells

Ashraful Islam,^{1,2,3} Surya Prakash Singh,^{1,2} and Liyuan Han^{1,2}

¹ International Center for Materials Nanoarchitectonics (MANA), National Institute for Materials Science (NIMS), 1-2-1 Sengen, Tsukuba, Ibaraki 305-0047, Japan

² Advanced Photovoltaics Center, National Institute for Materials Science (NIMS), 1-2-1 Sengen, Tsukuba, Ibaraki 305-0047, Japan

³ Center of Excellence for Research in Engineering Materials (CEREM), College of Engineering, King Saud University, Riyadh 11421, Saudi Arabia

Correspondence should be addressed to Ashraful Islam, islam.ashraful@nims.go.jp

Received 30 March 2011; Accepted 4 May 2011

Academic Editor: Mohamed Sabry Abdel-Mottaleb

Copyright © 2011 Ashraful Islam et al. This is an open access article distributed under the Creative Commons Attribution License, which permits unrestricted use, distribution, and reproduction in any medium, provided the original work is properly cited.

Five heteroleptic ruthenium complexes having different β -diketonato ligands, [Ru(tctpy)(dppd)(NCS)] (1), [Ru(tctpy)(pd)(NCS)] (2), [Ru(tctpy)(tdd)(NCS)] (3), [Ru(tctpy)(mepd)(NCS)] (4), and [Ru(tctpy)(tmhd)(NCS)] (5), where tctpy = 4,4',4''-tricarboxy-2,2':6',2''-terpyridine, pd = pentane-2,4-dione, mepd = 3-methylpentane-2,4-dione, tmhd = 2,2,6,6-tetramethylheptane-3,5-dione, tdd = tridecane-6,8-dione, and dppd = 1,3-diphenylpropane-1,3-dione, were synthesized and characterized. These heteroleptic complexes exhibit a broad metal-to-ligand charge transfer absorption band over the whole visible range extending up to 950 nm. The low-energy absorption bands and the $E(\text{Ru}^{3+/2+})$ oxidation potentials in these complexes could be tuned to about 15 nm and 110 mV, respectively, by choosing appropriate β -diketonato ligands. Molecular orbital calculation of complex 1 shows that the HOMO is localized on the NCS ligand and the LUMO is localized on the tctpy ligand, which is anchored to the TiO₂ nanoparticles. The β -diketonato-ruthenium(II)-polypyridyl sensitizers, when anchored to nanocrystalline TiO₂ films for light to electrical energy conversion in regenerative photoelectrochemical cells, achieve efficient sensitization to TiO₂ electrodes with increasing activity in the order $5 < 4 < 3 \approx 2 < 1$. Under standard AM 1.5 sunlight, the complex 1 yielded a short-circuit photocurrent density of 16.7 mA/cm², an open-circuit voltage of 0.58 V, and a fill factor of 0.64, corresponding to an overall conversion efficiency of 6.2%. A systematic tuning of HOMO energy level shows that an efficient sensitizer should possess a ground-state redox potential value of $> +.53$ V versus SCE.

1. Introduction

Dye-sensitized solar cells (DSCs) have attracted a great deal of attention as one of the promising solar-to-electricity power conversion devices because of their high efficiency and their potential of low-cost production [1–6]. The properties of photosensitizers are one of the most important factors that influence the solar cell performance. Two outstanding Ru(II) polypyridyl sensitizers for nanocrystalline TiO₂ solar cells so far reported are [Ru(dcbpy)₂(NCS)₂]{(C₄H₉)₄N}₂] and [Ru(tctpy)(NCS)₃]{(C₄H₉)₄N}₃], where dcbpy is 4,4'-dicarboxy-2,2'-bipyridine and tctpy is 4,4',4''-tricarboxy-2,2':6',2''-terpyridine, yielding solar to electric power conversion efficiency of over 11% under standard AM 1.5

condition [5, 7–9]. To get an efficient solar cell performance, the sensitizer should fulfill several requirements, including that (i) the dye's absorption spectrum should overlap with the solar spectrum to get maximum power conversion, (ii) the excited state should have enough thermodynamic driving force for the injection of electrons into the conduction band, and (iii) the redox potential should be sufficiently positive so that the neutral sensitizer can be regenerated via electron donation from the redox electrolyte. Molecular design of new sensitizers for nanocrystalline TiO₂ solar cells that can absorb all solar radiation is a challenging task. The highest occupied molecular orbital (HOMO) and lowest unoccupied molecular orbital (LUMO) have to be maintained at the levels where photoinduced electron transfers into the TiO₂

conduction band. Moreover, the regeneration of the dye by iodide can take place practically at 100% yield is another challenge [10].

We have reported a series of ruthenium polypyridyl complexes where the LUMO energy level of the sensitizer is systematically tuned, and we show that a sensitizer should possess excited-state oxidation potential of -0.8V versus SCE for efficient charge injection [11–17]. So far, terpyridine ruthenium(II) complex having one triphenylamine-substituted β -diketonato chelating ligand exhibits a broad absorption spectrum covering the visible and near-IR regions and a high molar extinction coefficient [14]. However, there is no report of systematic tuning of the HOMO energy level to elucidate the threshold ground-state redox potential for efficient dye regeneration. Thus we developed novel sensitizers, where we have systematically tuned the HOMO energy level by changing the electron donor ability of the β -diketonato ligands such as pentane-2,4-dione (pd), 3-methylpentane-2,4-dione (mepd), 2,2,6,6-tetramethylheptane-3,5-dione (tmhd), tridecane-6,8-dione (tdd), and 1,3-diphenylpropane-1,3-dione (dppd) compared to our previous complex [Ru(4,4',4''-tricarboxy-2,2':6',2''-terpyridine)(1,1,1-trifluoropentane-2,4-dionato)(NCS)](**R1**) as a reference [13]. The molecular structures of the five new terpyridine-ruthenium(II) complexes [Ru(tctpy)(dppd)(NCS)] (**1**), [Ru(tctpy)(pd)(NCS)] (**2**), [Ru(tctpy)(tdd)(NCS)] (**3**), [Ru(tctpy)(mepd)(NCS)] (**4**), and [Ru(tctpy)(tmhd)(NCS)] (**5**) are shown in Figure 1. The photovoltaic performance and the threshold ground-state redox potential for efficient dye regeneration in DSCs are discussed.

2. Experimental Details

2.1. Materials. The following chemicals were purchased and used without further purification: hydrated ruthenium trichloride (from Aldrich), ammonium thiocyanate (from TCI), pentane-2,4-dione (pd), 3-methylpentane-2,4-dione (mepd), 2,2,6,6-tetramethylheptane-3,5-dione (tmhd), tridecane-6,8-dione (tdd), and 1,3-diphenylpropane-1,3-dione (dppd; from Aldrich). Solvents used in synthesis were of reagent grade. Chromatographic purification was performed by gel permeation on Sephadex LH-20 (from Sigma). Ru(4,4',4''-trimethoxycarbonyl-2,2':6',2''-terpyridine)Cl₃ [7] was synthesized using literature procedures.

2.1.1. Synthesis of [Ru(tctpy)(dppd)(NCS)] (1**).** To a solution of complex Ru(4,4',4''-trimethoxycarbonyl-2,2':6',2''-terpyridine)Cl₃ (307 mg, 0.5 mmol) in methanol (100 mL) were added dppd (448 mg, 2.0 mmol) and Et₃N (0.5 mL). The reaction mixture was refluxed for 8 h, and the solvent was allowed to evaporate on a rotary evaporator. The crude complex Ru(4,4',4''-trimethoxycarbonyl-2,2':6',2''-terpyridine)(dppd)Cl was purified on a Sephadex LH-20 column using methanol as eluent. The green color band was collected and the solvent was allowed to evaporate on a rotary evaporator. The solid mass obtained was dissolved in 30 mL of DMF under nitrogen. To this solution 5 mL of an aqueous solution of NaSCN (300 mg, 3.7 mmol) was added.

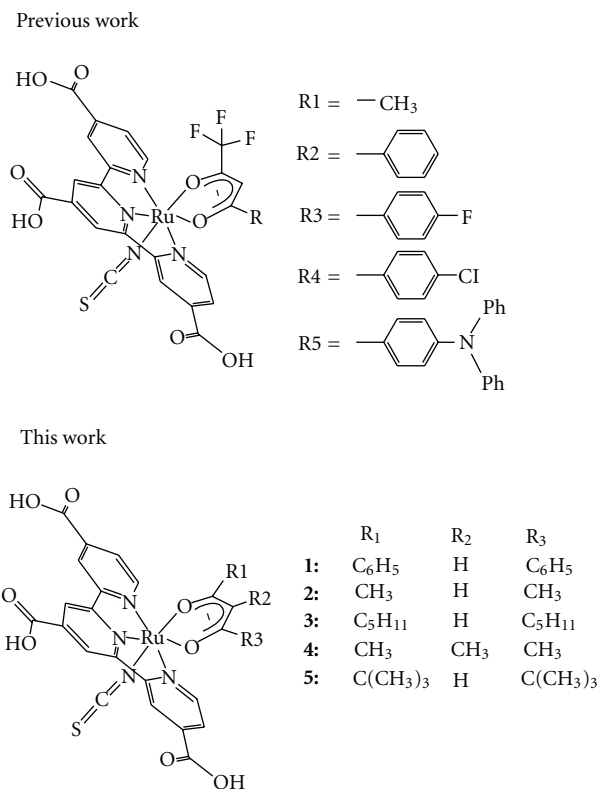


FIGURE 1: Molecular structures of complexes **1**–**5** (this work) and complexes R1–R5 (previous work).

After refluxing for 8 h, 10 mL of Et₃N was added and the solution refluxed for a further 24 h to hydrolyze the ester groups on the terpyridine ligand. The reaction mixture was allowed to cool and the solvent volume reduced on a rotary evaporator to around 5 mL. Water was added to the flask and the insoluble solid was filtered and dried under vacuum. The complex Ru(tctpy)(dppd)(NCS) was further purified by loading onto a Sephadex LH-20 column with water as eluent. Yield 65%. MS (ESIMS): m/z : 248.2 (M-3H)³⁻, 372.6 (M-2H)²⁻. ¹H NMR (300 MHz, D₂O-NaOD): δ 8.56 (4H, s), 8.53 (2H, d), 8.02 (2H, d), 7.69 (2H, d), 7.51 (H, d), 7.41 (2H, t), 7.39 (H, t), 6.92 (4H, sm), 6.34 (H, s). Anal. Calcd for C₃₄H₂₂N₄O₈SRu·(H₂O): C, 53.33; H, 3.16; N, 7.32. Found: C, 53.03; H, 3.20; N, 7.40.

2.1.2. Synthesis of [Ru(tctpy)(pd)(NCS)] (2**).** Complex **2** was synthesized by the method used for **1** using ligand pentane-2,4-dione (pd). The title compound was obtained as a dark green powder. [Ru(tctpy)(pd)(NCS)] (**2**). Yield was 60%. MS (ESIMS): m/z : 206.7 (M-3H)³⁻, 310.4 (M-2H)²⁻. ¹H NMR (300 MHz, D₂O-NaOD): δ 8.59 (2H, s), 8.58 (2H, d), 8.51 (2H, d), 7.77 (2H, d), 5.45 (H, s), 2.31 (3H, s), 1.25 (3H, s). Anal. Calcd for C₂₄H₁₈N₄O₈SRu·(H₂O)₂: C, 43.70; H, 3.36; N, 8.49. Found: C, 43.20; H, 3.45; N, 8.50.

2.1.3. Synthesis of [Ru(tctpy)(tdd)(NCS)] (3**).** Complex **3** was synthesized by the method used for **1** using ligand tridecane-6,8-dione (tdd). The title compound was obtained as a dark

green powder. [Ru(tctpy)(tdd)(NCS){ $(C_4H_9)_4N$ }] (**3**). Yield was 56%. MS (ESIMS): m/z : 244.1 (M-3H) $^{3-}$, 367.4 (M-2H) $^{2-}$. 1H NMR (300 MHz, D_2O -NaOD): δ 8.41 (4H, s), 8.31 (2H, d), 7.63 (2H, d), 5.21 (H, s), 2.33 (2H, t), 1.60 (2H, m), 1.29 (2H, t), 1.18 (4H, m), 0.65 (2H, t), 0.51 (3H, m), 0.38 (2H, m), 0.13 (2H, t), 0.02 (3H, m). Anal. Calcd for $C_{32}H_{35}N_4O_8SRu$: C, 52.17; H, 4.79; N, 7.60. Found: C, 51.85; H, 4.81; N, 7.85.

2.1.4. Synthesis of [Ru(tctpy)(mepd)(NCS)] (4**).** Complex **4** was synthesized by the method used for **1** using ligand 3-methylpentane-2,4-dione (mepd). The title compound was obtained as a dark green powder. [Ru(tctpy)(mepd)(NCS)] (**4**). Yield was 35%. MS (ESIMS): m/z : 211.8 (M-3H) $^{3-}$, 313.3 (M-2H) $^{2-}$. 1H NMR (300 MHz, D_2O -NaOD): δ 8.60 (2H, s), 8.58 (2H, d), 7.78 (2H, d), 2.45 (3H, s), 1.78 (3H, s), 1.32 (3H, s). Anal. Calcd for $C_{25}H_{20}N_4O_8SRu$: C, 47.09; H, 3.16; N, 8.79. Found: C, 46.74; H, 3.23; N, 8.86.

2.1.5. Synthesis of [Ru(tctpy)(tmhd)(NCS)] (5**).** Complex **5** was synthesized by the method used for **1** using ligand 2,2,6,6-tetramethylheptane-3,5-dione (tmhd). The title compound was obtained as a dark green powder. [Ru(tctpy)(tmhd)(NCS)] (**5**). Yield was 55%. MS (ESIMS): m/z : 234.6 (M-3H) $^{3-}$, 352.7 (M-2H) $^{2-}$, 707.0 (M-H) $^{-}$. 1H NMR (300 MHz, D_2O -NaOD): δ 8.26 (4H, s), 8.13 (2H, d), 7.44 (2H, d), 5.40 (H, s), 1.03 (9H, s), 0.00 (9H, s). Anal. Calcd for $C_{30}H_{31}N_4O_8SRu \cdot (H_2O)$: C, 49.65; H, 4.44; N, 7.72. Found: C, 49.77; H, 4.62; N, 7.89.

2.2. Spectroscopic Measurements. UV-visible spectra were recorded on a Shimadzu UV-3101PC spectrophotometer. Steady-state emission spectra were recorded using a grating monochromator (Triax 1900) and a CCD image sensor. The spectral sensitivity of the spectrophotometer was calibrated using a bromine lamp (Ushio IPD100 V 500 WCS). The emission lifetimes were measured by exciting the sample with a ~ 7 ns pulse at 500 nm from an optical parametric oscillator (Surelite OPO) pumped at 355 nm by a Nd:YAG laser (Continuum Surelite II). The emission decay was followed on a Tektronix TDS680C digitizing signal analyzer, having used a Hamamatsu R928 photomultiplier to convert the light signal to a voltage signal. Dewar vessel was used for the measurements at 77 K. 1H NMR spectra were recorded by a Varian 300 BB spectrometer. Electrospray ionization mass spectra (ESIMS) were obtained on a Micromass Quattro II mass spectrometer.

2.3. Electrochemical Measurements. The redox potential of the complexes was measured using a standard three-electrode apparatus. The counter electrode was a platinum wire, the working electrode was a ruthenium-complex-adsorbed conducting nanocrystalline TiO_2 film, and the reference electrode was an Ag/AgCl (saturated aqueous KCl) in contact with a KCl salt bridge. Cyclic voltammograms were collected using an electrochemical analyzer. Scan rates were 0.05–0.5 Vs^{-1} . Acetonitrile was used as solvent and the supporting electrolyte was 0.1 M tetrabutylammonium

perchlorate. Electrode potential values were calibrated to the saturated calomel electrode (SCE).

2.4. Preparation of TiO_2 Electrode. Nanocrystalline TiO_2 photoelectrodes of around 20 μm thickness (area: 0.25 cm^2) were prepared using a variation of a method reported by Nazeeruddin et al. [7]. Fluorine-doped tin oxide-coated glass electrodes (Nippon Sheet Glass Co., Japan) with a sheet resistance of 8–10 Ωm^{-2} and an optical transmission of >80% in the visible range were used. Anatase TiO_2 colloids (particle size ~ 13 nm) were obtained from commercial sources (Ti-Nanoxide D/SP, Solaronix). The nanocrystalline TiO_2 thin films of approximately 20 μm thickness were deposited onto the conducting glass by screen-printing. The film was then sintered at 500°C for 1 h. The film thickness was measured with a Surfcom 1400 A surface profiler (Tokyo Seimitsu Co. Ltd.). The electrodes were impregnated with a 50 mM titanium tetrachloride solution and sintered at 500°C. The dye solutions (2×10^{-4} M) were prepared in 1:1 acetonitrile and *tert*-butyl alcohol solvents. Deoxycholic acid as a coadsorbent was added to the dye solution at a concentration of 20 mM. The electrodes were immersed in the dye solutions and then kept at 25°C for 20 h to adsorb the dye onto the TiO_2 surface.

2.5. Fabrication of Dye-Sensitized Solar Cell. Photovoltaic measurements were performed in a two-electrode sandwich cell configuration. The dye-deposited TiO_2 film was used as the working electrode, and a platinum-coated conducting glass was used as the counter electrode. Two electrodes were separated by a surlyn spacer (40 μm thick) and sealed up by heating the polymer frame. The electrolyte was composed of 0.6 M dimethylpropyl-imidazolium iodide (DMPII), 0.05 M I_2 , and 0.1 M LiI in acetonitrile (AN).

2.6. Photovoltaic Characterization. The working electrode was illuminated through a conducting glass. The current-voltage characteristics were measured by using the previously reported method [18] with a solar simulator (AM-1.5, 100 mW/cm^2 , WXS-155S-10: Wacom Denso Co. Japan). Monochromatic incident photon-to-current conversion efficiency (IPCE) for the solar cell, plotted as a function of excitation wavelength, was recorded on a CEP-2000 system (Bunkoh-Keiki Co. Ltd.). Incident photon-to-current conversion efficiency (IPCE) at each incident wavelength was calculated from (1), where I_{sc} is the photocurrent density at short circuit in $mA cm^{-2}$ under monochromatic irradiation, q is the elementary charge, λ is the wavelength of incident radiation in nm, and P_0 is the incident radiative flux in $W m^{-2}$

$$IPCE(\lambda) = 1240 \left(\frac{I_{sc}}{q\lambda P_0} \right). \quad (1)$$

3. Results and Discussion

3.1. Photophysical Properties. The absorption, emission, and electrochemical properties of complexes **1–5** and reference

TABLE 1: Absorption, luminescence, and electrochemical properties of the ruthenium complexes.

Sensitizer	Absorption, $^a\lambda_{\max}/\text{nm}$ ($\epsilon/10^3 \text{ M}^{-1} \text{ cm}^{-1}$)	Emission $\lambda_{\max}^b / \text{nm}$		Emission τ^b/ns		$E(\text{Ru}^{3+/2+})^c$ /versus SCE	$E^*(\text{Ru}^{3+/2+})^d$ /versus SCE
		298 K	77 K	298 K	77 K		
1	294 (34.7), 329 (41.7), 440 (16.8), 615 (7.2)	990	930	13	225	+0.57	-0.89
2	293 (22.8) 330 (19.2), 433 (9.8), 622 (4.9)	995	950	11	170	+0.54	-0.89
3	293 (23.9), 331 (23.1), 438 (13.4), 629 (6.5)	1010	960	10	150	+0.53	-0.88
4	293 (32.0), 331 (18.7), 433 (12.2), 620 (5.5)	1010	960	8	147	+0.49	-0.91
5	293 (19.0), 332 (18.7), 435 (9.7), 630 (5.0)	1010	970	~7	130	+0.46	-0.92
R1^e	293 (27.6), 331 (22.7), 422 (14.7), 606 (7.0)	940		16		+0.68	

^a Measured in 4 : 1 v/v ethanol:methanol at room temperature.

^b The emission spectra and emission lifetime were obtained by exciting into the lowest MLCT band in 4 : 1 v/v ethanol:methanol.

^c Half-wave potentials assigned to the $\text{Ru}^{3+/2+}$ couple for ruthenium sensitizers bound to nanocrystalline TiO_2 film, measured in 0.1 M LiClO_4 acetonitrile solution.

^d Calculated from $E^*(\text{Ru}^{3+/2+}) = E(\text{Ru}^{3+/2+}) - E^{0-0}$; E^{0-0} values were estimated from the 5% intensity level of the emission spectra at 77 K.

^e Data taken from [13].

complex $[\text{Ru}(4,4',4''\text{-tricarboxy-2,2':6',2''-terpyridine})(1,1,1\text{-trifluoropentane-2,4-dionato})(\text{NCS})]$ (**R1**) are summarized in Table 1. The absorption spectra of complexes **1**, **3**, **5**, and **R1** in ethanol-methanol solution are shown in Figure 2. The absorption spectra of the sensitizers **1–5** are dominated in the visible region by absorption between 433 and 630 nm, and in the UV region between 293 and 332 nm. The bands in the visible region are assigned to metal-to-ligand charge-transfer transitions (MLCT) and in the UV region to ligand $\pi-\pi^*$ transitions of 4,4',4''-tricarboxy-2,2':6',2''-terpyridine [19]. In complexes **1–5**, the molar extinction coefficient of the lowest energy MLCT band shows in the range of 5000–7200 $\text{M}^{-1} \text{ cm}^{-1}$. The low-energy MLCT absorption bands of complexes **1–5** are red-shifted from that of **R1** complex. The lower energy MLCT band maximum of complex **1** is observed at 615 nm, which is red-shifted by around 9 nm compared to that of complex **R1**. The molar absorption coefficient of this low-energy band is 7200 $\text{M}^{-1} \text{ cm}^{-1}$ and can absorb entire visible range of solar emission wavelengths. Substitution of the 1,1,1-trifluoropentane-2,4-dionato (tfac) ligand with the 1,3-diphenylpropane-1,3-dione (dppd) in complex **1** destabilizes the ground state by electron donation to Ru, causing an increase in the energy of the t_{2g} metal orbital compared to that of complex **R1** and thus red-shifts the lowest-energy MLCT band. When compared to the complex **1**, which shows a maximum at 615 nm, the lowest MLCT band of complex **5** is red-shifted by around 15 nm because of the stronger electron-donating nature of the methyl groups present in the 2,2,6,6-tetramethylheptane-3,5-dione ligand of complex **5**.

In this study, we have tuned the low-energy MLCT absorption band of the complexes **1–5** around 25 nm compared to **R1** with variation of the diketonato ligands having different electron-donating strengths (Table 1). The donor properties of the diketonato ligand decreases in the following order $\text{tmhd} > \text{mepd} > \text{pd} \approx \text{tdd} > \text{dppd} > \text{tfac}$. In the red-light region, the diketonato complexes **1–5** show a distinct shoulder at around 720 nm, which is assigned to metal-to-ligand charge transfer (MLCT) transition (Figure 2) [20]. The enhanced red absorption of these complexes renders

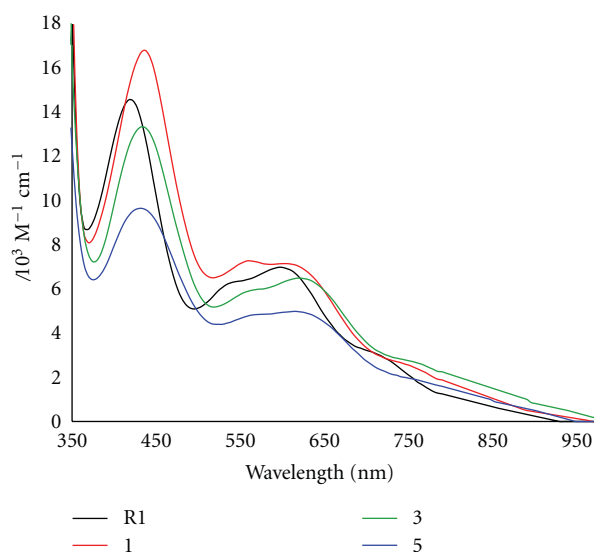


FIGURE 2: UV-vis absorption spectra of complexes **1**, **3**, **5**, and **R1** in ethanol-methanol (4 : 1) solution.

them attractive candidates as panchromatic charge transfer sensitizers for DSCs.

It is well known that the excited-state responsible for the luminescence of the $\text{Ru}(\text{II})$ -polypyridine compounds is the lowest-energy triplet metal-to-ligand charge-transfer ($^3\text{MLCT}$) state [21]. When excited at the charge transfer absorption band, complexes **1–5** show an intense emission at the 77 K ethanol-methanol glass matrix with a maximum between 930 and 970 nm. In degassed ethanol-methanol solution at 298 K, the emission spectra become weak and broad with a small shift to the lower-energy end. All complexes **1–5** show an emission at 298 K with a maximum between 990 nm and 1010 nm. The blue shift that occurs for all of the complexes in the transition from fluid solution to frozen solvent glass is a common rigidochromic effect observed in many metal diamine complexes [21, 22]. The emission spectra of complex **1** in ethanol-methanol mixed solvents at 77 and 298 K are presented in Figure 3. At 298 K,

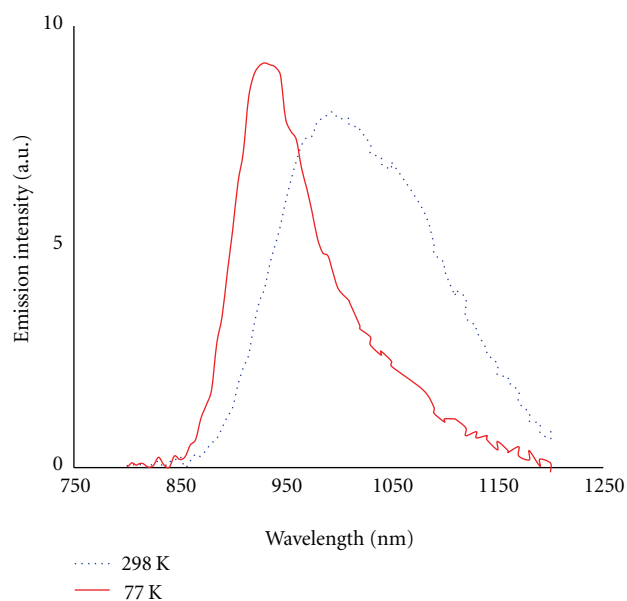


FIGURE 3: Emission spectra of complex 1 in ethanol-methanol (4 : 1) solution at 77 K (a) and 298 K (b).

complex 1 exhibits an emission maximum at 990 nm, which is 50 nm red-shifted compared to that of the **R1** emission and consistent with the shift in the lowest-MLCT absorption band. The luminescence data are gathered in Table 1. At 77 K, complexes 1–5 displayed excited-state lifetimes ranging from 225 to 130 ns. The lifetimes decrease significantly with the increase in temperature, to 7–13 ns in fluid solution at 298 K. The very short-lived excited state in fluid solution may be caused by efficient nonradiative decay via low-lying ligand-field excited states [21]. The excited-state lifetime of all the complexes is long enough for the process of electron injection into the conduction band of the TiO₂ electrode to make it efficient enough [23, 24]. To become a suitable sensitizer in DSCs, the band structure of the metal complex should match the conduction band of the semiconductor electrode and the redox potential of the electrolyte. The electrochemical data of the complexes measured in methanol solution are summarized in Table 1. All the complexes exhibit quasireversible oxidation wave for the Ru^{3+/2+} couple ranging from +0.46 to +0.57 V versus SCE. The formation of an MLCT excited state of these complexes formally involves the oxidation of a HOMO having metal t_{2g} orbital character and reduction of a diimine-based LUMO. Table 1 shows that the ground-state oxidation potentials (Ru^{3+/2+}) of the β -diketonato complexes 1–5 are more negative than those of the complex **R1**. In these complexes, the energy of the acceptor orbital (LUMO) remains nearly constant and the decrease in MLCT transition energy arises mainly from the increase in the energy of the metal t_{2g} orbital (HOMO).

The excited-state oxidation potential, E^* (Ru^{3+/2+}), is a measure of the loss of the electron that is placed in the π^* (terpyridine) LUMO upon excitation. For complexes 1–5, E^* (Ru^{3+/2+}) values are estimated using equation (2), where E (Ru^{3+/2+}) is the oxidation potential of the ground state and E^{0-0} is the energy difference between the lowest

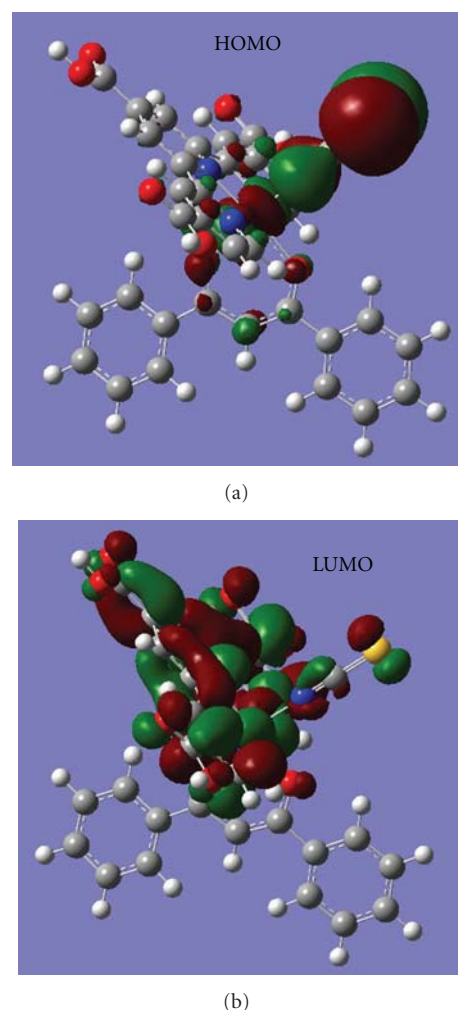


FIGURE 4: Graphic representation of the frontier molecular orbitals of complex 1.

excited and ground states. The resulting E^* (Ru^{3+/2+}) values are shown in Table 1. The excited states of complexes 1–5 lie above the conduction band edge (−0.82 V versus SCE) of the nanocrystalline TiO₂ [2]. Efficient electron injection into the conduction band of the TiO₂ is thus possible for all of complexes 1–5. The oxidation potential values of the complexes 1–5 lie above the I₃[−]/I[−] redox couple (0.07 V versus SCE) [25]

$$E^* (\text{Ru}^{3+/2+}) = E^* (\text{Ru}^{3+/2+}) - E^{0-0}. \quad (2)$$

To get an insight into the electron distribution of this new series of complexes for better understanding of the charge injection and dye regeneration process, the highest occupied molecular orbital (HOMO) and the lowest unoccupied molecular orbital (LUMO) of complex 1 were calculated by using Gaussian-03 program package (Figure 4). The HOMO of complex 1 is delocalized on Ru metal and NCS ligand, and the amplitude is primarily delocalized on the sulfur atom within the NCS ligand. The NCS group pointing in the direction of the electrolyte may facilitate reduction of the oxidized dye (Ru³⁺) through reaction with

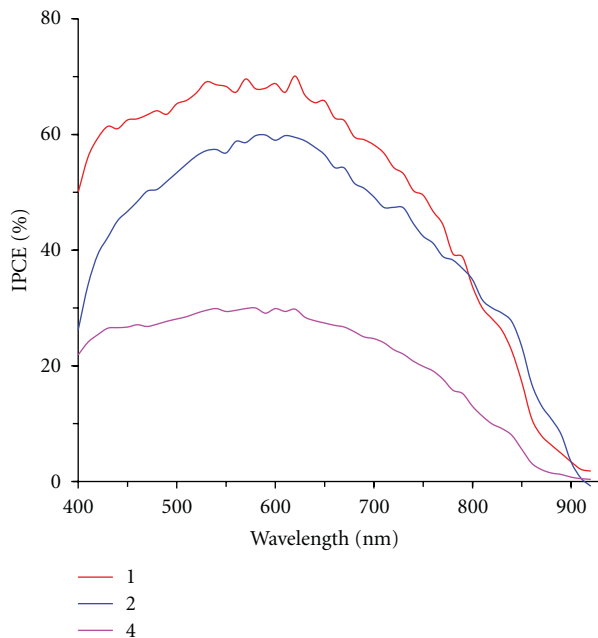


FIGURE 5: Photocurrent action spectra obtained with complexes **1** (a), **2** (b), and **4** (c) attached to nanocrystalline TiO₂ film. The incident photon-to-current conversion efficiency is plotted as a function of wavelength. A sandwich type sealed cell configuration was used to measure this spectrum. The electrolyte composition was 0.6 M DMPII, 0.05 M I₂, and 0.1 M LiI in acetonitrile.

I⁻. The β -diketonato ligand has a negligible contribution to HOMO. The LUMO has homogeneous amplitudes on the terpyridine ligand, facilitating the electron injection from the photoexcited sensitizer to the TiO₂ semiconductor.

3.2. Photovoltaic Properties. The photovoltaic performance of complexes **1–5** on nanocrystalline TiO₂ electrode was studied under standard AM 1.5 irradiation (100 mW cm⁻²) using an electrolyte with a composition of 0.6 M dimethylpropyl-imidazolium iodide (DMPII), 0.05 M I₂, and 0.1 M LiI in acetonitrile. Figure 5 shows the photocurrent action spectra for complexes **1**, **2**, and **4** where the incident photon to current conversion efficiency (IPCE) values is plotted as a function of wavelength. The maximum IPCE values of complexes **1–5** are listed in Table 2. Complexes **1–3** achieved efficient sensitization of nanocrystalline TiO₂ over the whole visible range extending into the near IR region. The most efficient sensitizer in this series was complex **1** that shows an IPCE value of 70% in the plateau region. Taking into account the reflection and absorption losses by the conducting glass, the photon-to-current conversion efficiency in this range reaches around 85%. One of the possible explanations for this low IPCE value of complex **1** is the aggregation of sensitizer molecules on TiO₂ surface. The red response was improved by replacing dppd with tdd while injection efficiencies were very low throughout the visible region (Figure 5). The maximum IPCE values of these β -diketonato complexes **1–5** decreases with the decrease in the ground-state oxidation potentials (Ru^{3+/2+}) values. Complexes **4** and **5** showed a drastically reduced IPCE value

TABLE 2: Photovoltaic properties of ruthenium polypyridyl sensitizers^a.

Sensitizer	IPCE _{max}	J _{sc} (mA cm ⁻²)	V _{oc} (V)	FF	η (%)
1	70	16.7	0.58	0.64	6.2
2	61	14.2	0.57	0.66	5.3
3	54	13.0	0.58	0.70	5.3
4	30	7.6	0.56	0.70	3.0
5	24	6.2	0.45	0.71	2.0
R1 ^b	70	18.3	0.57	0.64	6.7

^a Conditions: sealed cells; coadsorbate, DCA 40 mM; photoelectrode, TiO₂ (20 μ m thickness and 0.25 cm²); electrolyte, 0.6 M DMPII, 0.1 M LiI, 0.05 M I₂ in AN; irradiated light, AM 1.5 solar light (100 mW cm⁻²). J_{sc}, short-circuit photocurrent density; V_{oc}, open-circuit photovoltage; FF, fill factor; η , total power conversion efficiency; IPCE, incident photon-to-current conversion efficiency.

^b Data taken from [13].

(i.e., <30%) in the plateau region, and this reduction may be due to the decrease in the dye regeneration rate after tuning the ground-state oxidation potential toward more negative range. The recombination rate of injected electrons with the oxidized dye is an important factor that affects the electron collection efficiency. The recombination rates will increase by changing the oxidation values toward more negative potential. After electron injection, a competition is setup between charge recombination and iodide oxidation by oxidized dye. Considering the relative driving force of these complexes, the charge recombination rates will increase in the order of **1** < **2** \approx **3** < **4** \approx **5**. The low injection efficiencies (IPCE_{max} = 24–30%) of the complexes **4–5** compared to the complexes **1–3** can be explained by the fact that these complexes have more negative Ru^{3+/2+} ground state oxidation potential compared to those of the complexes **1–3** and the back reaction of injected electrons with Ru(III) competes to regeneration of Ru(II) through reaction with iodide. The ground-state potential of complex **3** (+0.53 V versus SCE) offers a minimum limit for the ground-state redox potential of the dye in the current configuration of the electrochemical cell and redox couple.

Figure 6 shows the photocurrent-voltage curves obtained under AM1.5 simulated illumination of the various dye coated TiO₂ electrode systems studied in this work. The short-circuit photocurrent density (J_{sc}), open-circuit voltage (V_{oc}), fill factors (FF), and overall cell efficiencies (η) for each dye-TiO₂ electrode are summarized in Table 2. The dppd complex **1** shows the best performance in this series. The solar cell sensitized with complex **1** showed a photocurrent density of 16.7 mA cm⁻², an open circuit potential of 0.58 V, and a fill factor of 0.64, corresponding to an overall conversion efficiency (η) of 6.2%. The complexes **4–5** showed poor cell performance (η < 3%) compare to those of complexes **1–3**. The low injection efficiencies (IPCE_{max} = 24–30%) of complexes **4–5** decrease the short-circuit photocurrent density (J_{sc}), and thus the decrease of overall cell efficiencies.

Thus, this class of diketonato ruthenium complexes serves as a basis for further design of new potential sensitizers by introducing suitable substituents on the diketonato ligand

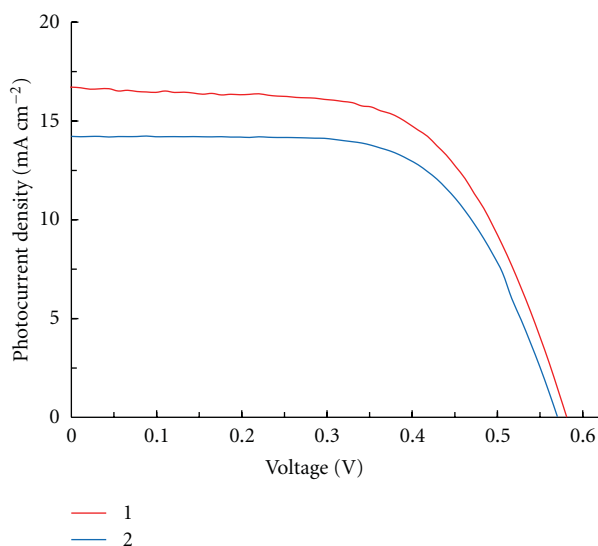


FIGURE 6: Photocurrent voltage characteristics of DSCs sensitized with the complexes 1 (a) and 2 (b) at AM 1.5 illuminations (light intensities: 100 mW cm^{-2}). The redox electrolyte consisted of a solution of 0.6 M DMPII, 0.05 M I_2 , and 0.1 M LiI in acetonitrile.

to adjust a desired electronic environment on the metal center for efficient dye regeneration. Since the modifications of electronic and steric environments in the sensitizing molecules are possible by changing the substituents on the diketonate ligand, further improvement in the solar cell efficiency will be accomplished in the near future.

4. Conclusions

Five new panchromatic photosensitizers based on 4,4',4''-tricarboxy-2,2':6',2''-terpyridine-ruthenium(II) complexes with one β -diketonato chelating ligand, pentane-2,4-dione (pd), 3-methylpentane-2,4-dione (mepd), 2,2,6,6-tetramethylheptane-3,5-dione (tmhd), tridecane-6,8-dione (tdd), or 1,3-diphenylpropane-1,3-dione (dppd) were developed, and systematically characterized using electrochemical and spectroscopic methods. The low-energy MLCT transitions in these complexes have been tuned by increasing the donor strength of the β -diketonato ligand to extend the spectral response of nanocrystalline TiO_2 electrodes to a range of longer wavelengths. The decrease in MLCT transition energy arises mainly from the negative shift in the ground state oxidation potential, that is, the energy of the metal t_{2g} orbital (HOMO). The complexes achieved efficient sensitization of nanocrystalline TiO_2 over the whole visible range extending into the near IR region (ca. 950 nm). The photovoltaic data of these new complexes shows 6.2% power conversion efficiency under standard AM 1.5 irradiation (100 mW cm^{-2}). Though complexes 4 and 5 have superior panchromatic light-harvesting properties compared to the complex 1, they show poor overall photovoltaic performance. A sluggish halide oxidation rate and a fast recombination of injected electron with the oxidized dye due to unfavorable HOMO energy level are perhaps responsible for the low cell efficiency of these complexes.

References

- [1] B. O'Regan and M. Grätzel, "A low-cost, high-efficiency solar cell based on dye-sensitized colloidal TiO_2 films," *Nature*, vol. 353, no. 6346, pp. 737–740, 1991.
- [2] A. Hagfeld and M. Grätzel, "Light-induced redox reactions in nanocrystalline systems," *Chemical Reviews*, vol. 95, no. 1, pp. 49–68, 1995.
- [3] M. Grätzel, "Conversion of sunlight to electric power by nanocrystalline dye-sensitized solar cells," *Journal of Photochemistry and Photobiology A*, vol. 164, no. 1–3, pp. 3–14, 2004.
- [4] A. Hagfeldt and M. Grätzel, "Molecular photovoltaics," *Accounts of Chemical Research*, vol. 33, no. 5, pp. 269–277, 2000.
- [5] M. K. Nazeeruddin, A. Kay, I. Rodicio et al., "Conversion of light to electricity by *cis*- X_2 bis(2,2'-bipyridyl-4,4'-dicarboxylate)ruthenium(II) charge-transfer sensitizers ($\text{X} = \text{Cl}^-$, Br^- , I^- , CN^- , and SCN^-) on nanocrystalline TiO_2 electrodes," *Journal of the American Chemical Society*, vol. 115, no. 14, pp. 6382–6390, 1993.
- [6] K. Hara, H. Sugihara, Y. Tachibana et al., "Dye-sensitized nanocrystalline TiO_2 solar cells based on ruthenium(II) phenanthroline complex photosensitizers," *Langmuir*, vol. 17, no. 19, pp. 5992–5999, 2001.
- [7] M. K. Nazeeruddin, P. Péchy, T. Renouard et al., "Engineering of efficient panchromatic sensitizers for nanocrystalline TiO_2 -based solar cells," *Journal of the American Chemical Society*, vol. 123, no. 8, pp. 1613–1624, 2001.
- [8] M. K. Nazeeruddin, F. D. Angelis, S. Fantacci et al., "Combined experimental and DFT-TDDFT computational study of photoelectrochemical cell ruthenium sensitizers," *Journal of the American Chemical Society*, vol. 127, no. 48, pp. 16835–16847, 2005.
- [9] Y. Chiba, A. Islam, Y. Watanabe, R. Komiya, N. Koide, and L. Han, "Dye-sensitized solar cells with conversion efficiency of 11.1%," *Japanese Journal of Applied Physics*, vol. 45, no. 25, pp. L638–L640, 2006.
- [10] A. Islam, H. Sugihara, and H. Arakawa, "Molecular design of ruthenium(II) polypyridyl photosensitizers for efficient nanocrystalline TiO_2 solar cells," *Journal of Photochemistry and Photobiology A*, vol. 158, no. 2–3, pp. 131–138, 2003.
- [11] A. Islam, F. A. Chowdhury, Y. Chiba et al., "Synthesis and characterization of new efficient tricarboxyterpyridyl (β -diketonato) ruthenium(II) sensitizers and their applications in dye-sensitized solar cells," *Chemistry of Materials*, vol. 18, no. 22, pp. 5178–5185, 2006.
- [12] A. Islam, F. A. Chowdhury, Y. Chiba et al., "Ruthenium(II) tricarboxyterpyridyl complex with a fluorine-substituted β -diketonato ligand for highly efficient dye-sensitized solar cells," *Chemistry Letters*, vol. 34, no. 3, pp. 344–345, 2005.
- [13] A. Islam, H. Sugihara, M. Yanagida et al., "Efficient panchromatic sensitization of nanocrystalline TiO_2 films by β -diketonato ruthenium polypyridyl complexes," *New Journal of Chemistry*, vol. 26, no. 8, pp. 966–968, 2002.
- [14] S. Gao, A. Islam, Y. Numata, and L. Han, "A β -diketonato ruthenium(II) complex with high molar extinction coefficient for panchromatic sensitization of nanocrystalline TiO_2 film," *Applied Physics Express*, vol. 3, no. 6, Article ID 062301, 3 pages, 2010.
- [15] S. P. Singh, A. Islam, M. Yanagida, and L. Han, "Development of a new class of thiocyanate-free cyclometallated ruthenium(II) complex for sensitizing nanocrystalline TiO_2 solar cells," *International Journal of Photoenergy*, vol. 2011, p. 5, 2011.

- [16] A. Islam, S. P. Singh, M. Yanagida, R. Karim, and L. Han, "Amphiphilic ruthenium(II) terpyridine sensitizers with long alkyl chain substituted β -diketonato ligands: An efficient coadsorbent free dye-sensitized solar cells," *International Journal of Photoenergy*, vol. 2011, p. 7, 2011.
- [17] A. Islam, S. P. Singh, and L. Han, "Thiocyanate-free, panchromatic ruthenium(II) terpyridine sensitizer having a tridentate diethylenetriamine ligand for near-IR sensitization of nanocrystalline TiO_2 ," *Functional Materials Letters*, vol. 4, no. 1, pp. 21–24, 2011.
- [18] N. Koide and L. Han, "Measuring methods of cell performance of dye-sensitized solar cells," *Review of Scientific Instruments*, vol. 75, no. 9, pp. 2828–2831, 2004.
- [19] A. Mamo, A. Juris, G. Calogero, and S. Campagna, "Near-infrared luminescence at room temperature of two new osmium(II) terdentate polypyridine complexes," *Chemical Communications*, no. 10, pp. 1225–1226, 1996.
- [20] Y. Takahashi, H. Arakawa, H. Sugihara et al., "Highly efficient polypyridyl-ruthenium(II) photosensitizers with chelating oxygen donor ligands: β -diketonato-bis(dicarboxybi-pyridine)ruthenium," *Inorganica Chimica Acta*, vol. 310, no. 2, pp. 169–174, 2000.
- [21] A. Islam, N. Ikeda, A. Yoshimura, and T. Ohno, "Nonradiative transition of phosphorescent charge-transfer states of ruthenium(II)-to-2,2'-biquinoline and ruthenium(II)-to-2,2':6',2''-terpyridine in the solid state," *Inorganic Chemistry*, vol. 37, no. 12, pp. 3093–3098, 1998.
- [22] A. Juris, V. Balzani, F. Barigelletti, S. Campagna, P. Belser, and A. Zelewsky, "Ru(II) polypyridine complexes: photophysics, photochemistry, electrochemistry, and chemiluminescence," *Coordination Chemistry Reviews*, vol. 84, no. C, pp. 85–277, 1988.
- [23] Y. Tachibana, S. A. Haque, I. P. Mercer, J. R. Durrant, and D. R. Klug, "Electron injection and recombination in dye sensitized nanocrystalline titanium dioxide films: a comparison of ruthenium bipyridyl and porphyrin sensitizer dyes," *Journal of Physical Chemistry B*, vol. 104, no. 6, pp. 1198–1205, 2000.
- [24] J. M. Rehm, G. L. McLendon, Y. Nagasawa, K. Yoshihara, J. Moser, and M. Grätzel, "Femtosecond electron-transfer dynamics at a sensitizing dye-semiconductor (TiO_2) interface," *Journal of Physical Chemistry*, vol. 100, no. 23, pp. 9577–9578, 1996.
- [25] G. Oskam, B. V. Bergeron, G. J. Meyer, and P. C. Searson, "Pseudohalogens for dye-sensitized TiO_2 photoelectrochemical cells," *Journal of Physical Chemistry B*, vol. 105, no. 29, pp. 6867–6873, 2001.

Research Article

Development of a New Class of Thiocyanate-Free Cyclometalated Ruthenium(II) Complex for Sensitizing Nanocrystalline TiO₂ Solar Cells

Surya Prakash Singh, Ashraful Islam, Masatoshi Yanagida, and Liyuan Han

Photovoltaic Materials Unit, National Institute for Materials Science (NIMS), 1-2-1 Sengen, Tsukuba, Ibaraki 305-0047, Japan

Correspondence should be addressed to Liyuan Han, han.liyuan@nims.go.jp

Received 26 January 2011; Accepted 23 February 2011

Academic Editor: Mohamed Sabry Abdel-Mottaleb

Copyright © 2011 Surya Prakash Singh et al. This is an open access article distributed under the Creative Commons Attribution License, which permits unrestricted use, distribution, and reproduction in any medium, provided the original work is properly cited.

We designed and developed a new class of thiocyanate-free cyclometalated ruthenium sensitizers for sensitizing nanocrystalline TiO₂ solar cells. This complex shows appreciably broad absorption range. Anchoring to nanocrystalline TiO₂ films for light to electrical energy conversion in regenerative photoelectrochemical cells achieves efficient sensitization to TiO₂ electrode. With this new sensitizer, there were a power conversion efficiency of 4.76%, a short-circuit photocurrent density of 11.21 mA/cm², an open-circuit voltage of 0.62 V, and a fill factor of 0.68 obtained under standard AM 1.5 sunlight.

1. Introduction

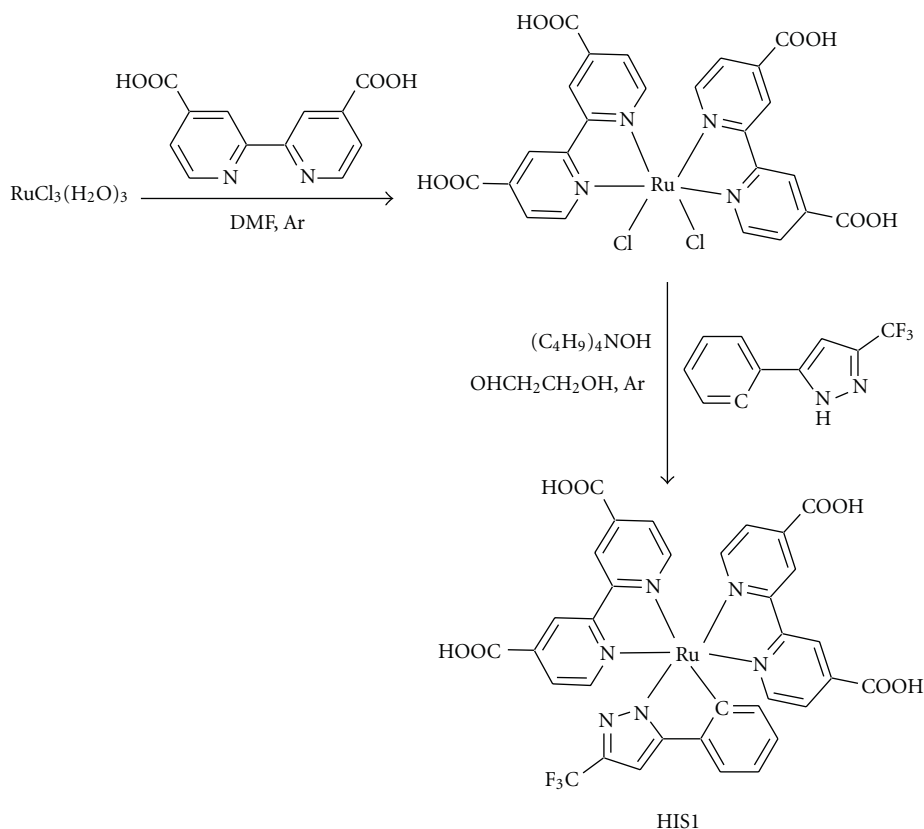
A molecular system that consists of a wideband gap semiconductor photoanode, typically TiO₂, an anchored molecular photosensitizer, a redox electrolyte, and a platinized photocathode is called dye-sensitized solar cells (DSCs) [1–5]. Among these elements, the sensitizers play a vital role in DSC. A lot of Ru-complex sensitizers [6–16] and organic sensitizers have been developed in DSC [17]. So far, sensitizers such as black dye, N719, and N3 are known as best sensitizers in DSC. Black dye sensitized nanocrystalline TiO₂ solar cells yielding solar to electric power conversion efficiency of over 11% under standard AM 1.5 conditions [12, 13]. Much effort has been made to increase photovoltaic performance (stability) of a device, towards the development of sensitizers, electrode, and photoanode material. A way to improve the stability is the development of a dye without thiocyanate (SCN) donor ligands because monodentate SCN is believed to provide the weakest dative bonding within the metal complexes, making the sensitizer unstable. Few efforts have been made to replace the SCN donor ligands with effective pyridyl pyrazolate chelating chromophores [18] and 2,4-difluorophenyl pyridinato ancillary ligands [19]. More recently, cycloruthenated compounds have been used

as sensitizers for efficient DSC devices [19–24]. Although the preliminary attempts gave only limited success [20–24], a superior power conversion efficiency is now achieved with a novel thiocyanate-free cyclometalated sensitizer [19]. However, further development of new sensitizer is still a challenging issue for DSC to improve the efficiency. Here, we report on the new class of thiocyanate-free cyclometalated ruthenium(II) complex for sensitizing nanocrystalline TiO₂ solar cells.

2. Experimental

2.1. Materials. All the solvents and chemicals were of reagent grade and used as received unless otherwise noted. Chromatographic purification was performed by gel permeation on Sephadex LH-20 (from Sigma).

Synthesis of Complex HIS1. *cis*-Dichlorobis (4,4'-dicarboxy-2,2'-bipyridine)ruthenium (180 mg, 0.27 mmol) and 5-phenyl-3-(trifluoromethyl)-1H-pyrazole (117 mg, 0.55 mmol) were dissolved in ethylene glycol (30 mL), and the reaction mixture was heated to 170°C under argon for 2 h. Then tetrabutyl ammonium hydroxide (1.1 g, 1.37 mmol) was added to the reaction mixture and further heated to 170°C under argon for 2 h. After evaporating the solvent,



SCHEME 1: Synthetic route for Bis(4,4'-dicarboxy-2,2'-bipyridine) 5-phenyl-3-(trifluoromethyl)-1H-pyrazole Ruthenium (II).

the resulting solid was dissolved in water (15 mL) and was titrated with 0.2 M HNO_3 to pH 3.8. The reaction mixture was kept in a refrigerator overnight and allowed to warm to 25°C. The resulting precipitation was collected on a sintered glass crucible by suction filtration. The solid was dissolved in a basic water solution (pH 10-11) and purified on a Sephadex LH-20 column by eluting with water. The yield, 167 mg. ^1H NMR (CD_3OD with a drop of NaOD): δ 9.04–8.86 (m, 5H), 8.06 (d, 1H), 7.9 (d, 1H), 7.89 (d, 1H), 7.8 (d, 1H), 7.67 (d, 2H), 7.55 (d, 2H), 7.27 (t, 2H), 7.13 (t, 1H), and 6.92 (s, 1H).

2.2. Fabrication of Dye-Sensitized Solar Cell. A nanocrystalline TiO_2 photoelectrode of 20 μm thickness (area: 0.25 cm^2) was prepared by screen printing on conducting glass as previously described [25]. The films were further treated with 0.05 M TiCl_4 and 0.1 M HCl aqueous solutions before examination [26]. Coating of the TiO_2 film was carried out by immersing for 45 h in a sensitizer solution of 3×10^{-4} M acetonitrile/*tert*-butyl alcohol (1/1, *v/v*) solution. Deoxycholic acid (20 mM) was added to the dye solution as a coadsorbent to prevent aggregation of the dye molecules [27, 28]. Photovoltaic measurements were performed in a two-electrode sandwich cell configuration. The dye-deposited TiO_2 film and a platinum-coated conducting glass were used as the working electrode and the counterelectrode, respectively. The two electrodes were separated by a surlyn spacer

(40 μm thick) and sealed by heating the polymer frame. The electrolyte was composed of 0.6 M dimethylpropylimidazolium iodide (DMPII), 0.05 M I_2 , TBP 0.3 M, and 0.1 M LiI in acetonitrile.

3. Results and Discussion

Scheme 1 shows the synthetic approach for the synthesis of thiocyanate-free cyclometalated ruthenium (II) complex HIS1.

The absorption spectrum of the complex HIS1 is dominated by metal to ligand charge transfer transitions (MLCTs) and shows MLCT bands in the visible region at 546 nm with a molar extinction coefficient of $12 \times 10^3 \text{ M}^{-1} \text{ cm}^{-1}$. There are high-energy bands at 380 nm due to ligand π - π^* charge transitions. A comparison of UV-vis spectra of the HIS1 and N719 complexes is displayed in Figure 1.

To get an insight into the electron distribution of this new series of complexes for better understanding of the charge injection and dye regeneration process, the highest occupied molecular orbital (HOMO) and the lowest unoccupied molecular orbital (LUMO) of complex HIS1 were calculated using Gaussian-09 program package (Figure 2). The HOMO of cyclometalated complexes of type $[\text{Ru}(\text{N}^{\wedge}\text{N}^{\wedge}\text{N})\text{Ru}(\text{N}^{\wedge}\text{N}^{\wedge}\text{C})]$ and $[\text{Ru}(\text{N}^{\wedge}\text{N}^{\wedge})_2(\text{C}^{\wedge}\text{N}^{\wedge})^+]$ is typically extended over the metal and, to a lesser extent, the anionic portion of the cyclometalating ligand [29]. The LUMO typically resides

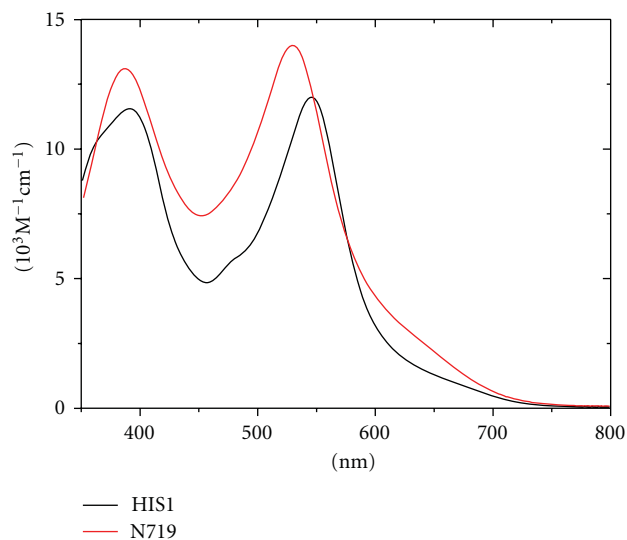
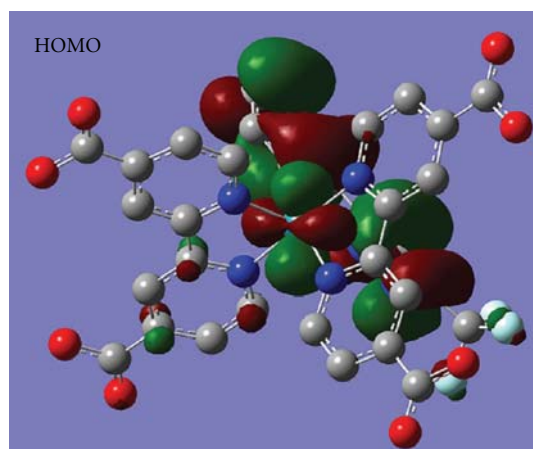
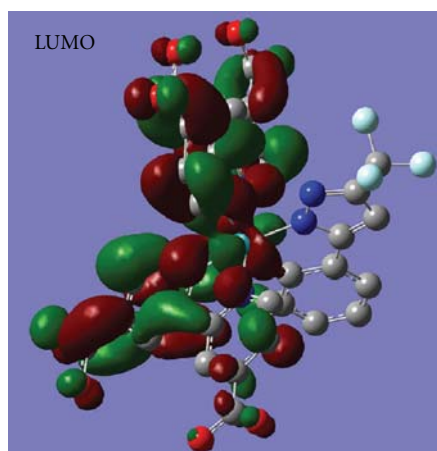


FIGURE 1: UV-vis absorption spectra of complex HIS1 (black line) and N719 (red line), measured in ethanol solution.



(a)



(b)

FIGURE 2: Graphic representation of frontier molecular orbital of complex HIS1.

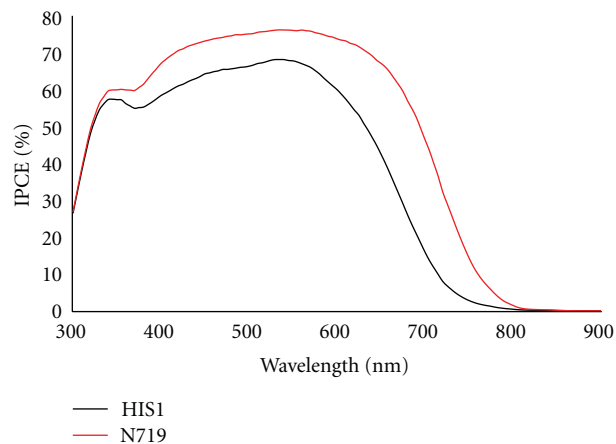


FIGURE 3: Incident photon-to-current conversion efficiency (IPCE) spectra of complex HIS1 (black line) and N719 (red line).

on the neutral polypyridyl ligands along with low-lying excited states delocalized over the polypyridyl portion(s) cyclometalating ligand (Figure 2).

Ionization potential of complex HIS1 bound to nanocrystalline TiO_2 film was determined using a photoemission yield spectrometer (Riken Keiki, AC-3E). The ground-state oxidation potentials ($\text{Ru}^{3+/2+}$) value of -5.95 eV obtained for sensitizer HIS1 was low enough for efficient regeneration of the oxidized dye through reaction with iodide. The excited-state oxidation potential, E^* ($\text{Ru}^{3+/2+}$), of sensitizer HIS1 was estimated to be -4.18 eV.

Monochromatic incident photon-to-current conversion efficiency (IPCE) for the solar cell, plotted as a function of excitation wavelength, was recorded on a CEP-2000 system (Bunkoh-Keiki Co. Ltd.). IPCE at each incident wavelength was calculated from (1), where I_{sc} is the photocurrent density at short circuit in mA cm^{-2} under monochromatic irradiation, q is the elementary charge, λ is the wavelength of incident radiation in nm, and P_0 is the incident radiative flux in Wm^{-2} ,

$$\text{IPCE}(\lambda) = 1240 \left(\frac{I_{sc}}{q\lambda P_0} \right). \quad (1)$$

The photocurrent density-voltage curves and incident photon-to-current efficiency (IPCE) spectra of the cells based on sensitizer HIS1 under the illumination of air mass (AM) 1.5 sunlight (100 mW/cm^2 , WXS-155S-10: Wacom Denso Co., Japan). Figure 3 shows the action spectra of monochromatic incident photon-to-current conversion efficiency (IPCE) for DSC composed of complex HIS1 sensitized nanocrystalline TiO_2 electrode and an iodine/triiodide redox electrolyte with reference to N719-based DSC constructed under comparable conditions. Although complex HIS1 shows somewhat lower IPCE values, this problem could be solved using structural modification of complex HIS1, a subject for future research. We observed an IPCE of 68% in complex HIS1, while in the case of N719, the IPCE was 76%. The dye-sensitized solar cell based on sensitizer

HIS1 achieves a conversion efficiency (η) of 4.76%, a short-circuit photocurrent density of 11.21 mA/cm², an open-circuit voltage of 0.62 V, and a fill factor of 0.68 obtained under standard AM 1.5 sunlight. N719-sensitized solar cell under the same cell fabrication and efficiency measuring procedures achieves a conversion efficiency (η) of 7.56%, a short-circuit photocurrent density of 15.83 mA/cm², an open-circuit voltage of 0.65 V, and a fill factor of 0.73. The photo-induced voltage (V_{oc}) is determined by the difference between the quasi-Fermi level of TiO₂ and redox potential of the electrolyte and is able to be enhanced as a slow recombination process of injected electrons in TiO₂ with oxidized species and a negative shift of band edge. *tert*-butylpyridine (TBP) is known to increase V_{oc} of DSC due to an enhanced electron lifetime and a negative shift of band edge [30, 31]. Hence, the higher V_{oc} with electrolyte containing 0.3 M TBP is (0.62 V) and without TBP 0.50 V observed.

4. Conclusions

In summary, a new class of thiocyanate-free cyclometalated ruthenium-based dye HIS1 was strategically designed and synthesized. This complex shows appreciably broad absorption range. Anchoring to nanocrystalline TiO₂ films for light to electrical energy conversion in regenerative photoelectrochemical cells achieves efficient sensitization to TiO₂ electrode. With this new sensitizer power, there were a conversion efficiency of 4.76%, a short-circuit photocurrent density of 11.21 mA/cm², an open-circuit voltage of 0.62 V, and a fill factor of 0.68 obtained under standard AM 1.5 sunlight. Further improvement in the solar cell efficiency as well as the dynamic study of electron injection and recombination in complex HIS1 sensitized nanostructured TiO₂ is currently on progress in our lab and will be disclosed in due course.

References

- [1] B. O'Regan and M. Grätzel, "A low-cost, high-efficiency solar cell based on dye-sensitized colloidal TiO₂ films," *Nature*, vol. 353, no. 6346, pp. 737–740, 1991.
- [2] A. Hagfeldt and M. Grätzel, "Light-induced redox reactions in nanocrystalline systems," *Chemical Reviews*, vol. 95, no. 1, pp. 49–68, 1995.
- [3] A. Hagfeldt and M. Grätzel, "Molecular photovoltaics," *Accounts of Chemical Research*, vol. 33, no. 5, pp. 269–277, 2000.
- [4] M. Grätzel, "Solar energy conversion by dye-sensitized photovoltaic cells," *Inorganic Chemistry*, vol. 44, no. 20, pp. 6841–6851, 2005.
- [5] M. Grätzel, "Conversion of sunlight to electric power by nanocrystalline dye-sensitized solar cells," *Journal of Photochemistry and Photobiology A*, vol. 164, no. 1–3, pp. 3–14, 2004.
- [6] A. Islam, H. Sugihara, and H. Arakawa, "Molecular design of ruthenium(II) polypyridyl photosensitizers for efficient nanocrystalline TiO₂ solar cells," *Journal of Photochemistry and Photobiology A*, vol. 158, no. 2–3, pp. 131–138, 2003.
- [7] A. Hagfeldt, G. Boschloo, L. Sun, L. Kloo, and H. Pettersson, "Dye-sensitized solar cells," *Chemical Reviews*, vol. 110, no. 11, pp. 6595–6663, 2010.
- [8] T. Funaki, M. Yanagida, N. Onozawa-Komatsuzaki, K. Kasuga, Y. Kawanishi, and H. Sugihara, "Efficient panchromatic sensitization of nanocrystalline TiO₂-based solar cells using 2-pyridinecarboxylate-substituted Ruthenium(II) complexes," *Chemistry Letters*, vol. 38, no. 1, pp. 62–63, 2009.
- [9] A. Islam, F. A. Chowdhury, Y. Chiba et al., "Synthesis and characterization of new efficient tricarboxyterpyridyl (β -diketonato) ruthenium(II) sensitizers and their applications in dye-sensitized solar cells," *Chemistry of Materials*, vol. 18, no. 22, pp. 5178–5185, 2006.
- [10] M. K. Nazeeruddin, P. Péchy, T. Renouard et al., "Engineering of efficient panchromatic sensitizers for nanocrystalline TiO₂-based solar cells," *Journal of the American Chemical Society*, vol. 123, no. 8, pp. 1613–1624, 2001.
- [11] A. Islam, F. A. Chowdhury, Y. Chiba et al., "Ruthenium(II) tricarboxyterpyridyl complex with a fluorine-substituted β -diketonato ligand for highly efficient dye-sensitized solar cells," *Chemistry Letters*, vol. 34, no. 3, pp. 344–345, 2005.
- [12] Y. Chiba, A. Islam, Y. Watanabe, R. Komiya, N. Koide, and L. Han, "Dye-sensitized solar cells with conversion efficiency of 11.1%," *Japanese Journal of Applied Physics*, vol. 45, no. 25, pp. L638–L640, 2006.
- [13] Q. Wang, S. Ito, M. Grätzel et al., "Characteristics of high efficiency dye-sensitized solar cells," *Journal of Physical Chemistry B*, vol. 110, no. 50, pp. 25210–25221, 2006.
- [14] A. Islam, H. Sugihara, M. Yanagida et al., "Efficient panchromatic sensitization of nanocrystalline TiO₂ films by β -diketonato ruthenium polypyridyl complexes," *New Journal of Chemistry*, vol. 26, no. 8, pp. 966–968, 2002.
- [15] S. Gao, A. Islam, Y. Numata, and L. Han, "A β -diketonato ruthenium(II) complex with high molar extinction coefficient for panchromatic sensitization of nanocrystalline TiO₂ film," *Applied Physics Express*, vol. 3, no. 6, Article ID 062301, 2010.
- [16] A. Islam, S. P. Singh, M. Yanagida, M. R. Karim, and L. Han, "Amphiphilic ruthenium(II) terpyridine sensitizers with long alkyl chain substituted β -diketonato ligands: an efficient coadsorbent free dye-sensitized solar cells," *International Journal of Photoenergy*, vol. 2011, Article ID 757421, 7 pages, 2011.
- [17] A. Mishra, M. K. R. Fischer, and P. Buerle, "Metal-free organic dyes for dye-sensitized solar cells: from structure: property relationships to design rules," *Angewandte Chemie: International Edition*, vol. 48, no. 14, pp. 2474–2499, 2009.
- [18] K.-L. Wu, H.-C. Hsu, K. Chen et al., "Development of thiocyanate-free, charge-neutral Ru(II) sensitizers for dye-sensitized solar cells," *Chemical Communications*, vol. 48, pp. 5124–5126, 2010.
- [19] T. Bessho, E. Yoneda, J. H. Yum et al., "New paradigm in molecular engineering of sensitizers for solar cell applications," *Journal of the American Chemical Society*, vol. 131, no. 16, pp. 5930–5934, 2009.
- [20] S. H. Wadman, J. M. Kroon, K. Bakker et al., "Cyclometalated ruthenium complexes for sensitizing nanocrystalline TiO₂ solar cells," *Chemical Communications*, no. 19, pp. 1907–1909, 2007.
- [21] S. H. Wadman, M. Lutz, D. M. Tooke et al., "Consequences of N, C, N' - and C, N, N' -coordination modes on electronic and photophysical properties of cyclometalated aryl ruthenium(II) complexes," *Inorganic Chemistry*, vol. 48, no. 5, pp. 1887–1900, 2009.
- [22] P. G. Bomben, K. C. D. Robson, P. A. Sedach, and C. P. Berlinguette, "On the viability of cyclometalated Ru(II) complexes for light-harvesting applications," *Inorganic Chemistry*, vol. 48, no. 20, pp. 9631–9643, 2009.

- [23] B. D. Koivisto, K. C. D. Robson, and C. P. Berlinguette, "Systematic manipulation of the light-harvesting properties for tridentate cyclometalated ruthenium(II) complexes," *Inorganic Chemistry*, vol. 48, no. 20, pp. 9644–9652, 2009.
- [24] S. H. Wadman, J. M. Kroon, K. Bakker, R. W. A. Havenith, G. P. M. Van Klink, and G. Van Koten, "Cyclometalated organoruthenium complexes for application in dye-sensitized solar cells," *Organometallics*, vol. 29, no. 7, pp. 1569–1579, 2010.
- [25] M. K. Nazeeruddin, P. Péchy, T. Renouard et al., "Engineering of efficient panchromatic sensitizers for nanocrystalline TiO₂-based solar cells," *Journal of the American Chemical Society*, vol. 123, no. 8, pp. 1613–1624, 2001.
- [26] Z. S. Wang, T. Yamaguchi, H. Sugihara, and H. Arakawa, "Significant efficiency improvement of the black dye-sensitized solar cell through protonation of TiO₂ films," *Langmuir*, vol. 21, no. 10, pp. 4272–4276, 2005.
- [27] M. Ikeda, N. Koide, L. Han, A. Sasahara, and H. Onishi, "Scanning tunneling microscopy study of black dye and deoxycholic acid adsorbed on a rutile TiO₂(110)," *Langmuir*, vol. 24, no. 15, pp. 8056–8060, 2008.
- [28] Z. S. Wang, Y. Cui, Y. Dan-oh, C. Kasada, A. Shinpo, and K. Hara, "Thiophene-functionalized coumarin dye for efficient dye-sensitized solar cells: electron lifetime improved by coadsorption of deoxycholic acid," *Journal of Physical Chemistry C*, vol. 111, no. 19, pp. 7224–7230, 2007.
- [29] P. G. Bomben, B. D. Koivisto, and C. P. Berlinguette, "Cyclometalated Ru complexes of type [Ru^{II}(N[^]N)₂(C[^]N)]^z: physicochemical response to substituents installed on the anionic ligand," *Inorganic Chemistry*, vol. 49, no. 11, pp. 4960–4971, 2010.
- [30] S. Y. Huang, G. Schlichthörl, A. J. Nozik, M. Grätzel, and A. J. Frank, "Charge recombination in dye-sensitized nanocrystalline TiO₂ solar cells," *Journal of Physical Chemistry B*, vol. 101, no. 14, pp. 2576–2582, 1997.
- [31] G. Boschloo, L. Häggman, and A. Hagfeldt, "Quantification of the effect of 4-tert-butylpyridine addition to I⁻/I₃⁻ redox electrolytes in dye-sensitized nanostructured TiO₂ solar cells," *Journal of Physical Chemistry B*, vol. 110, no. 26, pp. 13144–13150, 2006.

Research Article

Nanostructured Mesoporous Titanium Dioxide Thin Film Prepared by Sol-Gel Method for Dye-Sensitized Solar Cell

Yu-Chang Liu, Yun-Fang Lu, Yz-Zhen Zeng, Chi-Hung Liao, Jen-Chieh Chung, and Tsong-Yang Wei

Institute of Nuclear Energy Research, AEC, Taoyuan County 32546, Taiwan

Correspondence should be addressed to Yu-Chang Liu, eddyliu@iner.gov.tw

Received 17 February 2011; Accepted 8 April 2011

Academic Editor: Mohamed Sabry Abdel-Mottaleb

Copyright © 2011 Yu-Chang Liu et al. This is an open access article distributed under the Creative Commons Attribution License, which permits unrestricted use, distribution, and reproduction in any medium, provided the original work is properly cited.

Titanium dioxide (TiO_2) paste was prepared by sol-gel and hydrothermal method with various precursors. Nanostructured mesoporous TiO_2 thin-film back electrode was fabricated from the nanoparticle colloidal paste, and its performance was compared with that made of commercial P25 TiO_2 . The best performance was demonstrated by the DSSC having a $16\ \mu\text{m}$ -thick TTIP- TiO_2 back electrode, which gave a solar energy conversion efficiency of 6.03%. The ability of strong adhesion on ITO conducting glass substrate and the high surface area are considered important characteristics of TiO_2 thin film. The results show that a thin film with good adhesion can be made from the prepared colloidal paste as a result of alleviating the possibility of electron transfer loss. One can control the colloidal particle size from sol-gel method. Therefore, by optimizing the preparation conditions, TiO_2 paste with nanoparticle and narrow diameter distribution was obtained.

1. Introduction

Titanium dioxide (TiO_2) has attracted tremendous attention from researchers worldwide due to its potential applications in environmental protection and energy generation [1]. It has demonstrated unique properties such as high adsorption ability and good photocatalytic activity. Recently, TiO_2 has been applied largely in dye-sensitized solar cell (DSSC) due to its nanocrystalline mesopore nature that translates to high surface area for dye adsorption. The adsorbed dye molecules can then be excited by the solar energy to generate electron-hole pairs that are subsequently separated and transported within the lattice of TiO_2 [2]. Burnside et al. [3] reported a dye-sensitized solar cell that comprises a black-dye-adsorbed TiO_2 working electrode, which achieved a high solar energy conversion efficiency (η) of 10.4% [4]. The nanoparticle film is $16\ \mu\text{m}$ thick, and the anatase TiO_2 was prepared by the hydrolysis of titanium(IV) isopropoxide.

The TiO_2 film working electrode is an important part of DSSC. It can be prepared by various methods such as sol-gel [5–7], chemical vapor deposition (CVD) [8, 9], and sputtering [10–12]. Sol-gel process is a favorable method for

preparing TiO_2 nanoparticles since the composition, particle size, film thickness, and porosity of TiO_2 can be easily controlled by adjusting parameters such as sol concentration, hydrothermal growth temperature, and sintering condition. Hydrolysis of titanium(IV) isopropoxide in acidic solution was performed by Dolmatov et al. [13] and Jerman et al. [14]. The process produced several types of $\text{Ti}(\text{OH})_x(4-x)^+$ hydroxocomplexes in equilibrium with $x < 4$. The value of x changed with reactant concentration, pH, and temperature. When temperature was increased, particle size of TiO_2 increased, leading to the formation of precipitate. Yoldas [15] has studied the gelatination process of titanium dioxide. The influence of reactant on hydrolysis and condensation was discussed. They discovered that when an alkyl, as the reactant, was increased, the hydrolytic reaction and the diffusion rate were both slowed down. As a result, the gelatination product formed was smaller, which contained lower concentration of oxide compound.

The addition of some acidic compounds, such as HCl, HNO_3 , and CH_3COOH in $\text{Si}(\text{OR})_4$, may be used to control the speed of hydrolysis [16]. Some literature on solar cells [17–20] has mentioned the ideal nanocrystal sizes, ranging

TABLE 1: Comparison of different preparation methods for titanium dioxide nanoparticle colloidal paste from TiCl_4 .

Sample	Hardness	BET surface area (m^2/g)	Pore diameter (\AA)	Pore volume (cm^3/g)	d_{BET}	d_{SEM}
P25	HB~F	51.69	104.71	0.17	29.1	—
ETIP-TiO ₂	6H	60.54	129.29	0.19	24.8	28
H-ETIP-TiO ₂	HB	52.78	74.32	0.13	28.4	45
TTIP-TiO ₂	H	71.40	136.92	0.21	21.0	30
H-TTIP-TiO ₂	F	72.05	232.01	0.13	20.8	30
TiCl_4 -TiO ₂	HB	83.10	125.49	0.26	—	105

from 10 to 25 nm, in achieving high cell efficiency. During the preparation of TiO_2 powder, primary single-crystal particles may agglomerate to form secondary polycrystalline particles of various sizes, and such process is dependent on the synthesis routes. Shen et al. [21] had conducted a series of studies on the optical absorption and electron transfer of TiO_2 with different particle and pore sizes. TiO_2 powder with large pores as well as small particle sizes seemed to show high efficiency.

The dye adsorption and charge transport of TiO_2 nanoparticle thin film coated with a substrate (e.g., ITO-or FTO-coated glass) have been studied extensively in recent years. The transport of photogenerated electrons or efficiency of device will be dependent on the adhesion of TiO_2 thin film. In this study, pencil hardness technique was adopted to test the adhesion of TiO_2 film prepared. Furthermore, nanocrystallites will beneficially influence the photocatalytic properties of TiO_2 film by increasing the number of active sites, which reduces the risks of charge carrier recombination. In order to efficiently separate and collect photogenerated electrons and holes, TiO_2 thin film must offer an environment that has high electron-transferring rate and less carrier traps. According to the results of recent studies on dye-sensitized solar cell, metal oxide is the main constituent for making the thin film. Among the various metal oxides, titanium dioxide is most often selected [22, 23].

Here, three types of precursors were used in the sol-gel method to prepare TiO_2 working photoelectrode. The purpose is to control the film thickness and produce a mesoporous TiO_2 film. The previously reported mesoporous films were only few micrometers thick. Such thin films provide insufficient surface areas for dye adsorption. On the other hand, a thick film with large BET surface areas will harvest more light, which translates to higher efficiency. The TiO_2 film prepared in this study was sensitized by commercial N_3 dye and was applied as the photoelectrode in dye-sensitized solar cell.

2. Experimental

2.1. Materials. P-25 TiO_2 (70% anatase, 30% rutile, primary particle size 30 nm, Degussa) powder purchased from Aldrich was used for comparison purpose. Titanium(IV) isopropoxide (TTIP, 97%, Aldrich), titanium(IV) ethoxide (TTIE, ACROS), and titanium tetrachloride (TiCl_4 , Merck) were precursors for preparing titanium dioxide by sol-gel

method. The adjustment of pH was done by adding reagent grade NaOH (Merck). Triton X-100 (Merck) and polyethylene glycol (PEG M.W = 20,000, Fluka) were used as binders, and N3 dye (Ruthenium 533 bis-TBA, Solaronix) was used as the sensitizer. The R150 redox electrolyte was purchased from the Solaronix Commercials. Acetic acid and ethanol were purchased from Merck. All other solvents and reagents were analytical-grade quality, purchased commercially, and used without any further purification.

ITO-conducting glass ($20\sim 30\ \Omega/\text{cm}^2$, Merck, Co., Ltd.) was selected as the substrate for TiO_2 film. Wolff-wilborn hardness pencil test was adopted for the TiO_2 film adhesion test. The crystalline property of TiO_2 film was modified using the hydrothermal method with a bomb-type autoclave. In order to avoid the contamination of colloidal paste and protect the autoclave, a teflon beaker was lined in the stainless steel bomb.

2.2. Preparation Methods and Measurement

2.2.1. Sol-Gel and Hydrothermal Preparation Methods. A series of TiO_2 nanoparticles were prepared by sol-gel method using acetic acid and nitric acid as the catalytic agent. The sol-gel was prepared from three precursors including titanium(IV) isopropoxide (TTIP), titanium(IV) ethoxide (TTIE), and titanium tetrachloride (TiCl_4). The solvent used was ethanol to give a solvent/precursor molar ratio of 1/1. High-purity helium (99.99%) was flowed through the reactor. This solution was added dropwise to the mixture containing 5.2 moles of acetic acid and 50 moles of DI water (deionized water) cooled at 5°C under helium gas purging and vigorous stirring. In order to increase the stability of TTIP and control the particle size [24], the sol-gel was prepared at 5°C under helium gas purge. Fresh sol-gel solution was transparent without any precipitate. After hydrolysis and condensation, the mixture was heated at 80°C in a water bath for 8 h. After that, the temperature was gradually decreased to room temperature. The resulting sol-gel was placed into an autoclave to undergo the hydrothermal process, which heated the mixture at 190°C for 12 h. After hydrothermal process, the mixture became thick and concentrated. TiO_2 catalysts prepared were denoted as Y- TiO_2 , where Y represents the precursor of titanium added. To further study the effect of acid used during hydrolysis, acetic acid was replaced by HNO_3 , and the catalysts prepared were denoted as X-Y- TiO_2 . The preparation conditions of TiO_2 photocatalysts are listed in Table 1.

2.2.2. Characterization. The mesoporous TiO_2 thin film was characterized by nitrogen sorption, Nano-ZS, XRD, SEM, and UV-vis. The efficiencies of photoelectrodes fabricated by these TiO_2 thin films were also tested with a solar simulator.

Particle size distribution of the colloidal paste was measured by a nanoparticle analyzer (Malvern zetasizer Nano-ZS).

Powder X-ray diffraction (XRD) measurements were taken using a Bruker-D8-ADVANCE powder diffractometer with $\text{Cu-K}\alpha$ radiation (40 kV, 30 mA). The sample was scanned over the 2θ range of $20\text{--}60^\circ$ at a rate of $0.05^\circ \text{min}^{-1}$ to identify the crystalline structure. Sample for XRD was prepared as a thin layer on a sample holder.

BET surface areas were obtained by physisorption of nitrogen at -197°C using a micromeritics ASAP-2020 instrument. Prior to measurement, the samples were degassed to 0.1 Pa at 100°C . The surface areas were calculated in a relative pressure range $0.05 < p/p_0 < 0.2$ assuming a cross-sectional area of 0.162 nm^2 for the N_2 molecules.

Scanning electron microscopy (SEM) images were obtained with a Hitachi 4800 field emission microscope using an acceleration voltage of 20 kV. Samples were placed on a stage especially made for SEM. They were coated with Pt prior to analysis and imaged directly. SEM images were recorded at magnification that ranged from 50000 X to 110000 X. The magnification was calibrated in pixel/nm on the camera. The chemical composition of the sample was determined by scanning electron microscopy-X-ray energy-dispersive spectrum (SEM-EDS) with accelerating voltage of 20 kV.

The diffuse reflectance UV-vis spectra were measured with a UV 3101PC UV-visible spectrophotometer. Powder samples were loaded in a quartz cell with suprasil windows, and spectra were collected in the range from 300 nm to 800 nm against quartz standard.

2.2.3. Preparation and Analysis of Mesoporous Titania Film Working Photoelectrode. Dye-sensitized solar cell prepared was consisted of a TiO_2 working electrode coated with ITO conducting glass, a counter electrode, and electrolyte dispersed in between. TiO_2 film working electrodes prepared from different titanium precursors (e.g., TTIP- TiO_2 , TTIE- TiO_2 , and TiCl_4 - TiO_2) were coated on ITO glass ($20 \text{ mm} \times 10 \text{ mm}$) by doctor-blade method [25]. The thickness of TiO_2 film after calcination was measured by Tencor α -step profiler, which gave more reliable results than those in previous report [26]. The size and thickness of solar cell were controlled by 3 M tape. The area of photoelectrode was about 0.25 cm^2 ($0.5 \text{ cm} \times 0.5 \text{ cm}$), and the thickness was about $15 \mu\text{m}$ before calcination. The N_3 dye was adsorbed onto the working electrode by soaking TiO_2 film in 0.2 M dye solution using ethanol as the solvent. The amount of N_3 dye adsorbed on TiO_2 film was determined by UV-vis spectrophotometer, where the chemisorbed dye on TiO_2 film was desorbed by adding a mixture of NaOH and ethanol (1:1), and the resulting solution was measured.

Counter electrode was made by sputtering a layer of platinum on ITO glass. The photovoltaic property of the cell

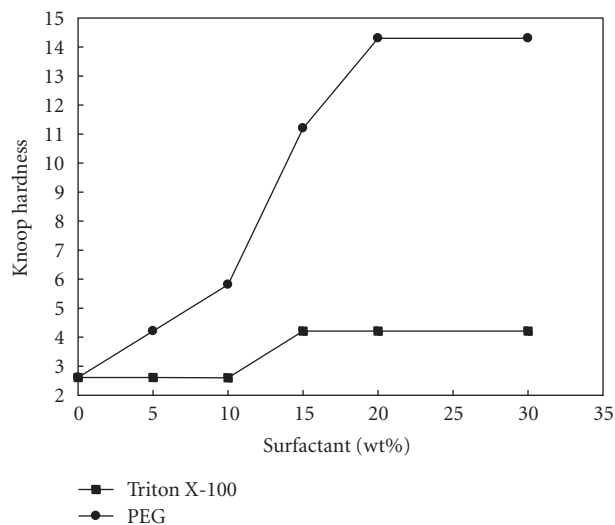


FIGURE 1: Effect of surfactant addition on the P25 thin film hardness.

was measured by solar simulator (i.e., AM 1.5, 100 mW/cm^2 , YAMASHITA YSS-80A). The light intensity of solar simulator was calibrated by standard silicon solar cell (223 mV).

3. Results and Discussion

3.1. Structural and Morphological Characteristics of TiO_2 Thin Film. For dye-sensitized solar cell (DSSC), the adhesion of titania film on ITO glass is an important criterion that will impact the cell performance. This is because cracking of titania film tends to influence the interfacial transfer of charge carriers [27]. To prevent such phenomenon from happening, a surfactant such as PEG and triton X-100 was added to improve the adhesion of TiO_2 thin film. In addition, PEG could also increase the thickness of TiO_2 thin film and further enhance its light-absorbing ability [28, 29].

Figure 1 shows the effect of surfactant addition on the hardness of P25 thin film. From the figure, it is noted that TiO_2 film with 20 wt% PEG demonstrated the best adhesion property. On the other hand, the addition of triton X-100 showed insignificant effect in improving the adhesion of TiO_2 film. The formation of fine bubbles observed while mixing TiO_2 paste with triton X-100 might be the reason for the poor adhesion.

Furthermore, adding surfactant has the effect of increasing the thickness of TiO_2 film. This will prevent film cracking since thin film tends to crack more easily due to the shrinkage effect, that is, the change of TiO_2 volume due to evaporation and decomposition of organic substances, which induces considerable stress on the film [30].

Since the alkoxide titanium will quickly react with water to generate titanium hydroxide, the reaction was kept at 5°C during hydrolysis and followed by the acidification reaction. The acidification reaction can enhance the crystalline property of the nanoparticle. The mixture at the moment was not considered a paste since the particle size and solvent constituent must be further conditioned by the hydrothermal

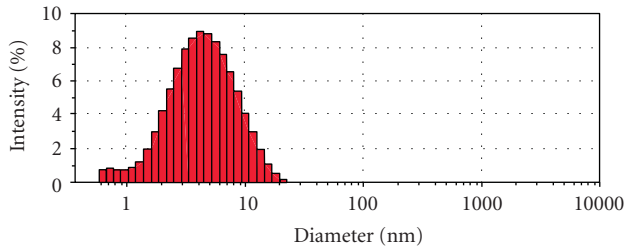


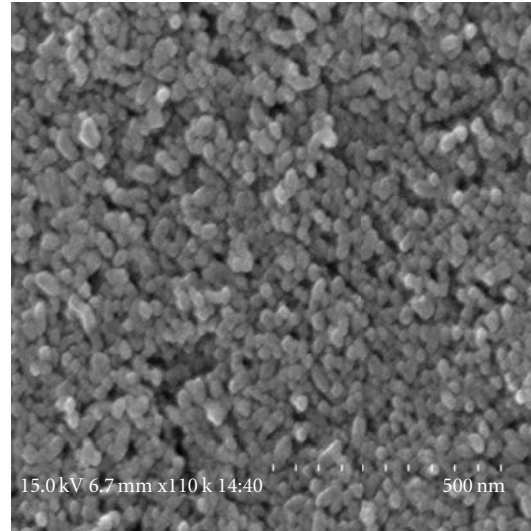
FIGURE 2: Colloidal nanoparticle size distribution before hydrothermal treatment.

treatment at a temperature of 190°C. Dominant factors that will influence the characteristics of the thin film include particle size, particle morphology, and solvent constituent of the paste [31, 32]. The experimental results show that TTIE-TiO₂ colloidal paste with the controllable particle size from 1 to 10 nm can be obtained with good reproducibility. Figure 2 indicates the typical particle size distribution of TTIE-TiO₂ sol-gel before hydrothermal treatment, which is similar to that of the original sol-gel colloidal solution. A mixture of alcohol and water is a suitable dispersion solution for measuring nanoparticle size distribution. Originally, the particle size of colloidal solution was below 10 nm. However, both the particle size and the crystallinity of the colloid were increased after carrying out the hydrothermal treatment.

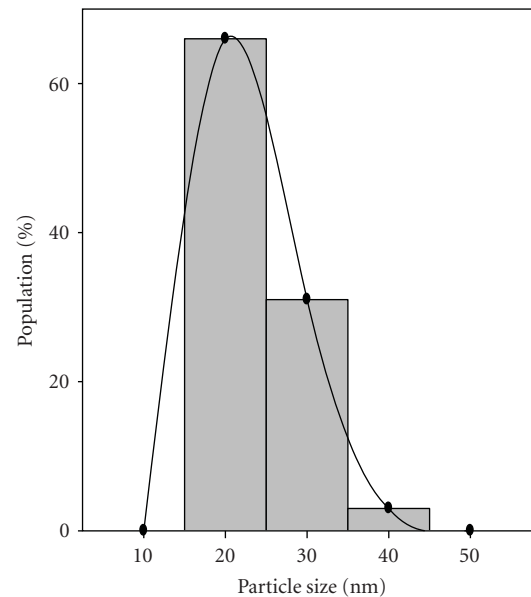
3.2. SEM. The SEM images in Figures 3, 4, 5, 6, and 7 show the average diameter of TiO₂ particles, which is about 28, 30, 105, 30 and 45 nm for TTIE-TiO₂, TTIP-TiO₂, TiCl₄-TiO₂, H-TTIP-TiO₂, and H-TTIE-TiO₂, respectively. The BET surface area of P25 is 51.69 m²/g. However, from the result of nitrogen adsorption-desorption isotherm, the prepared TiO₂ paste showed higher surface area than that of commercial P25 powder.

The differences in morphology and particle size among the prepared TiO₂ paste were observed by SEM. Nanoparticles of both TTIE-TiO₂ and TTIP-TiO₂ displayed spherical shape with apparent boundary. In contrast, nanoparticles of TiCl₄-TiO₂ had a rod-like shape. Obviously, differences in morphology or shape of the TiO₂ nanoparticles prepared with different precursors and acids were observed. The porous structure of TiO₂ film was clearly observed from the SEM images.

As shown in Table 1, the BET surface area of TTIP-TiO₂ and TTIE-TiO₂ is 71.4 m²/g and 60.54 m²/g, respectively, whereas that of TTIP-TiO₂ and TTIE-TiO₂ prepared with HNO₃ is 72.05 m²/g and 52.78 m²/g, respectively. Assuming the particles are spherical and nonporous, the average particle size can be estimated by the following equation: $\bar{d}(nm) = (6/S_{BET}\rho) \times 10^3$, where S_{BET} is the surface area and ρ is the density of a particle using the value of 4.0 g/cm³ (the density of titania). The average particle size calculated from BET surface area is 21 nm, 24.8 nm, 20.8 nm, and 28.4 nm for TTIP-TiO₂, TTIE-TiO₂, H-TTIP-TiO₂, and H-TTIE-TiO₂, respectively. The results indicated that all particles are in nanoscale. It should be noted that the average particle size was overestimated because the catalyst under measurement



(a)



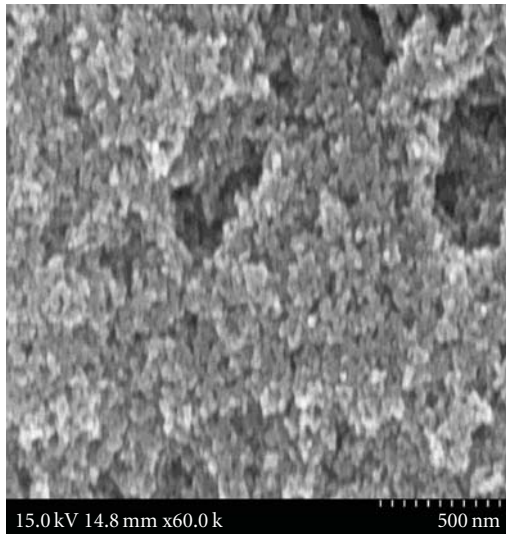
(b)

FIGURE 3: TTIE-TiO₂ thin film morphology after annealing at 500°C.

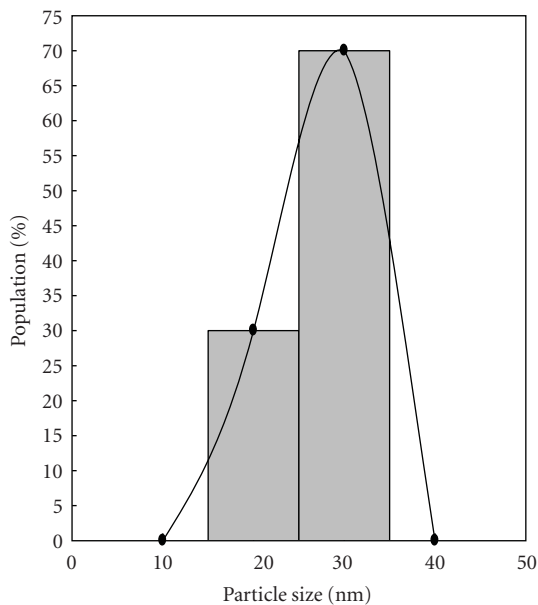
was pretreated at 120°C before nitrogen sorption, which could cause metal sintering to some extent.

3.3. XRD. All TiO₂ films prepared in this study have nanosize particles. Figure 8 shows the XRD pattern of the TiO₂ film that was coated on ITO glass by doctor blending followed by calcination at 500°C for 1 h.

The XRD patterns of different samples prepared under temperature of 190°C are shown in Figure 8. Only anatase peaks at 2θ of around 25, 38, 48, and 55° were observed. Therefore, the selection of different precursor (TTIE and TTIP) for preparing TiO₂ will not affect its crystalline structure.



(a)

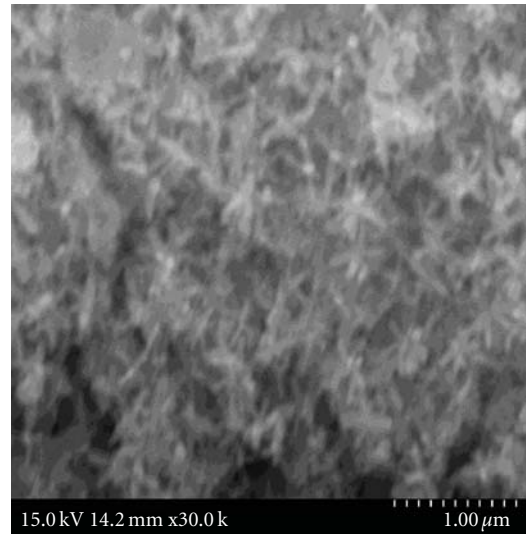


(b)

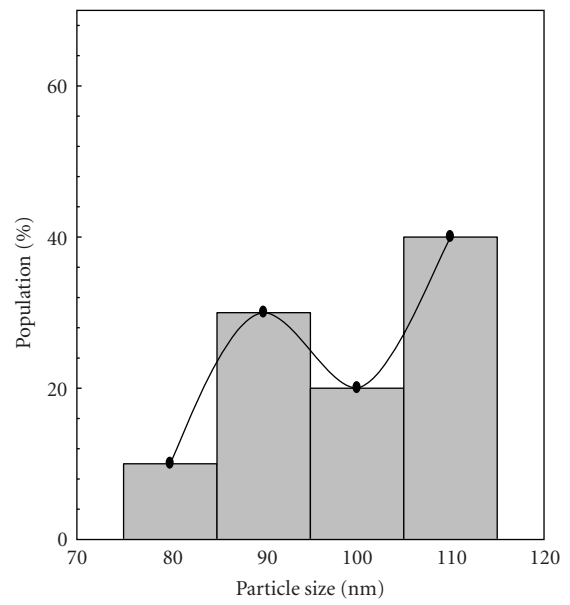
FIGURE 4: TTIP-TiO₂ thin film morphology after annealing at 500°C.

The XRD results show that TTIP-TiO₂ (500) and TTIE-TiO₂ (500) were composed of both anatase and rutile phases. The rutile phase was formed during high-temperature calcination at 500°C. The main peaks of TTIP-TiO₂ and TTIE-TiO₂ became sharper as the calcination temperature was increased, indicating an increase in its crystallinity. The XRD patterns of TiCl₄-TiO₂ (500) show both rutile and anatase phases; however, no change in peak sharpness has been observed. Nevertheless, the XRD patterns show that these TiO₂ have the structure with short-range mesophase order, which is a typical characteristic of TiO₂ [24].

3.4. Photoelectrode Characteristics. The photoconversion efficiency of solar cells fabricated from various TiO₂ working



(a)



(b)

FIGURE 5: TiCl₄-TiO₂ thin film morphology after annealing at 500°C.

electrodes were investigated in this study. The thickness of TiO₂ film after calcination was estimated to be 8~9 nm. The photocurrent generated by the solar cell is directly proportional to the amount of dye adsorbed on TiO₂ film [19] which can be seen in Figure 9. It is noted that the amount of dye adsorbed on TiO₂ increases with the film thickness. This is also in agreement with the increase in BET surface area as shown in Table 1.

The amount of dye chemisorbed on H-TTIP-TiO₂ film electrode was tested. Despite the fact that H-TTIP-TiO₂ exhibited high surface area, its dye adsorption behavior was very poor. This can be explained by the small pore volume of H-TTIP-TiO₂ (0.13 cm³/g) as shown in Table 1 which limits its dye adsorption ability.

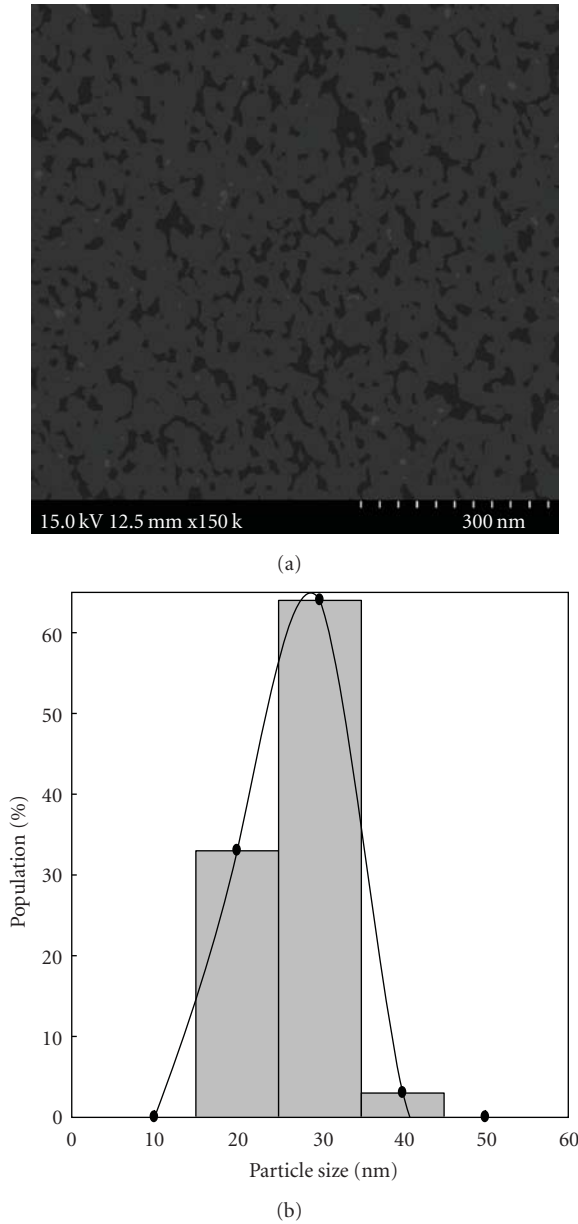


FIGURE 6: H-TTIP-TiO₂ thin film morphology after annealing at 500°C.

The H-TTIE-TiO₂ film prepared was composed mostly of spherical primary particles and some ellipse-like secondary particles. The use of TTIP precursor to react with different solvent and reactant will change the rate of hydrolysis and primary particle growth [33]. In other words, the primary and secondary particle size, surface morphology, composition, and porosity of TiO₂ will be influenced by the concentration and type of precursor used.

Figure 10 shows photocurrent voltage characteristics of the cell made from various TiO₂ calcined at 500°C for 0.5 h. It is noted that the resistance of ITO conducting glass after calcination was increased to about 85~110 Ω. This will cause a big impact on the efficiency of the solar cell since ITO

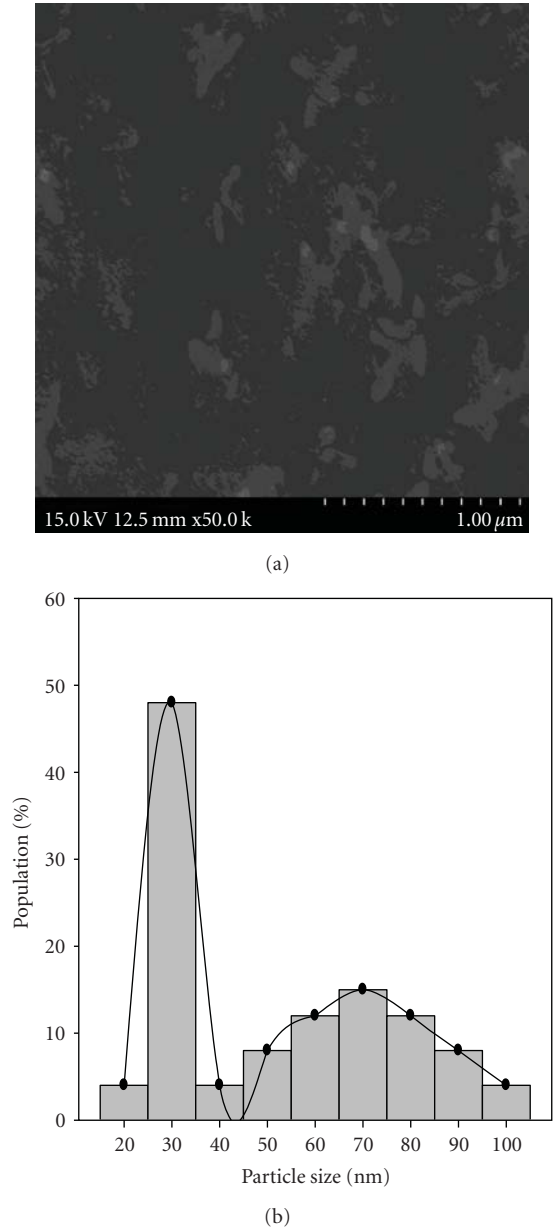


FIGURE 7: H-TTIE-TiO₂ thin film morphology after annealing at 500°C.

functions to transfer electrons that are photogenerated from dye-incorporated TiO₂. From Table 2, it is obvious that the solar cell made from TTIP-TiO₂ thin film produces the largest short-circuit current (J_{sc}).

High photocurrent could be generally related to high surface area, which results in an increase in the amount of dye adsorbed if the film thickness and light irradiation intensity were kept constant. It might also be due to the presence of more anatase TiO₂, which facilitates the electron transport [34]. This can be explained by the large pore size and high surface area of TTIP-TiO₂ electrode as revealed by SEM and BET analyses. In Tanaka's study, as the titania particle gets bigger, the chance of electron/hole recombination gets lower

TABLE 2: Performances of various TiO₂ thin film electrodes for DSSC.

Sample	Thickness (μm)	Jsc (mA/cm^2)	Voc (V)	Fill factor	η (%)
P25	10-11 \pm 0.5	6.25	0.64	52.64	2.19
TTIE-TiO ₂	8-9 \pm 0.5	5.63	0.70	62.18	2.45
H-TTIE-TiO ₂	8-9 \pm 0.5	4.25	0.69	68.45	1.90
TTIP-TiO ₂	8-9 \pm 0.5	13.13	0.76	44.96	4.45
H-TTIP-TiO ₂	8-9 \pm 0.5	5.13	0.65	68.15	2.25
TiCl ₄ -TiO ₂	8-9 \pm 0.5	2.13	0.64	74.09	0.99
TTIP/TTIP*	15-16 \pm 0.5	15.50	0.67	57.89	6.03

* Double layer of TTIP-TiO₂ for efficiency test.

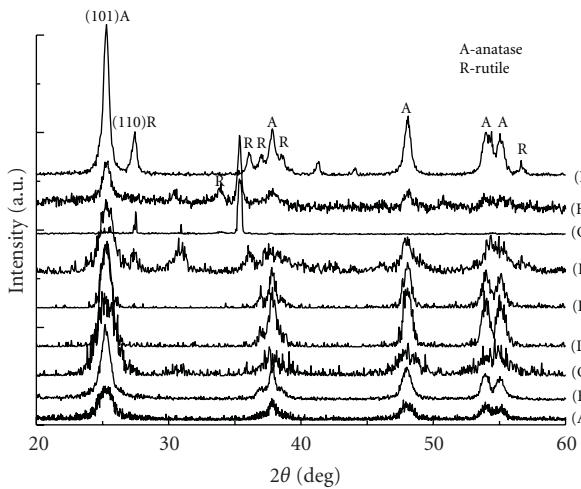


FIGURE 8: XRD patterns of TiO₂ synthesized hydrothermally at 190°C for 12 h and calcinated at 500°C for 0.5 h (A: TTIP (190), B: TTIE (190), C: H-TTIP (190), D: TTIP (500), E: TTIE (500), F: H-TTIP (500), G: H-TTIE (500), H: TiCl₄ (500), I: P25).

[35]. The cell performance depends on the thickness of the TiO₂ film. Therefore, we have made a double-layer TTIP-TiO₂ thin film electrode that has a thickness of 16 μm [4]. By incorporating this double-layer electrode into a solar cell, a photoconversion efficiency as high as 6.03% can be reached. The sufficient film thickness will create large pore size and enough space which allow more redox electrolyte to diffuse into the film.

TiCl₄-TiO₂ shows the highest surface area; however, its solar energy conversion efficiency is only 0.99% with low Jsc of 2.13 mA/cm^2 . It is attributed to the poor adhesion of TiO₂ on ITO glass observed. The pH of TiCl₄-TiO₂ paste is around 1~2, which might cause a corrosion problem on ITO conducting glass. Furthermore, TiCl₄-TiO₂ film showed poor adhesion when immersed in the iodine electrolyte after calcination. Although TiCl₄-TiO₂ showed poor performance, it displayed nanotube-like structure. If the adhesion problem can be eliminated, low-cost and high-efficiency solar cell may be fabricated.

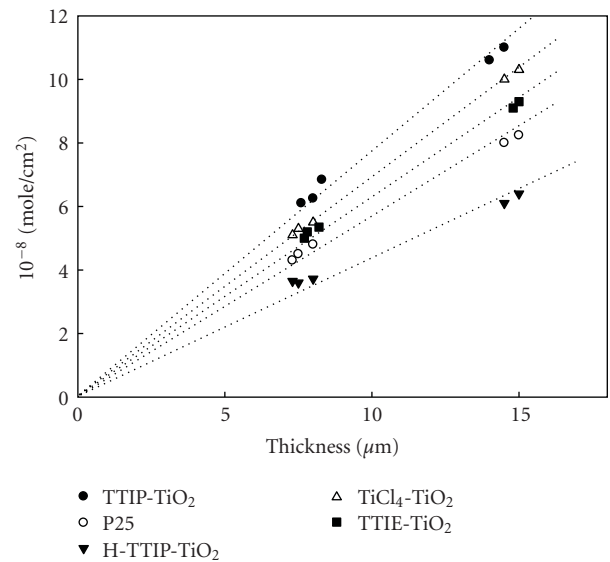


FIGURE 9: The amount of chemisorbed dye on the different thicknesses.

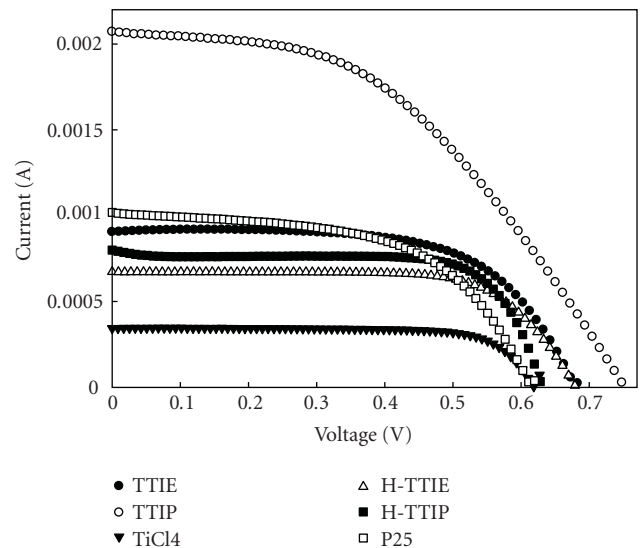


FIGURE 10: Photocurrent voltage characteristics of nanocrystalline TiO₂ films prepared with different precursors.

4. Conclusion

In this study, various TiO₂ pastes were prepared with different precursors and acids. There are many factors that will influence the performance of DSSC, for instance, the nature of dye, semiconductor electrode, and activity of redox electrolyte, and so forth. In DSSC, TiO₂ is the key component in determining the device efficiency. TiO₂ prepared by sol-gel and hydrothermal method has the advantage of tuning its composition, particle size, and pore size distribution. The criteria of making an effective TiO₂ working electrode include high surface area, appropriate band gap, and good adhesion [36]. TiO₂ working electrode having high anatase content can facilitate electron transport due to its superior conductivity [34]. It is essential to increase the surface area of TiO₂ nanoparticles in order to increase the amount of dye adsorbed. In this study, a double-layer TTIP-TiO₂ working electrode with a thickness of 16 μm has been presented. The solar cell incorporating such double-layer working electrode has demonstrated a photoconversion efficiency as high as 6.03%.

References

- [1] L. Saadoun, J. A. Ayllon, J. Jimenez-Becerril, J. Peral, X. Domenech, and R. Rodriguez-Clemente, "Synthesis and photocatalytic activity of mesoporous anatase prepared from tetrabutylammonium-titania composites," *Materials Research Bulletin*, vol. 35, no. 2, pp. 193–202, 2000.
- [2] B. O'Regan and M. Gratzel, "A low-cost, high-efficiency solar cell based on dye-sensitized colloidal TiO films," *Nature*, vol. 353, no. 6346, pp. 737–740, 1991.
- [3] S. D. Burnside, V. Shklover, C. Barbé et al., "Self-organization of TiO nanoparticles in thin films," *Chemistry of Materials*, vol. 10, no. 9, pp. 2419–2425, 1998.
- [4] M. K. Nazeeruddin, P. Péchy, T. Renouard et al., "Engineering of efficient panchromatic sensitizers for nanocrystalline TiO-based solar cells," *Journal of the American Chemical Society*, vol. 123, no. 8, pp. 1613–1624, 2001.
- [5] T. Yoko, A. Yuasa, K. Kamiya, and S. Sakka, "Sol-gel-derived TiO film semiconductor electrode for photocleavage of water. Preparation and effects of postheating treatment on the photoelectrochemical behavior," *Journal of the Electrochemical Society*, vol. 138, no. 8, pp. 2279–2285, 1991.
- [6] K. A. Vorotilov, E. V. Orlova, and V. I. Petrovsky, "Sol-gel TiO films on silicon substrates," *Thin Solid Films*, vol. 207, no. 1-2, pp. 180–184, 1992.
- [7] V. J. Nagpal, R. M. Davis, and S. B. Desu, "Novel thin films of titanium dioxide particles synthesized by a sol-gel process," *Journal of Materials Research*, vol. 10, no. 12, pp. 3068–3078, 1995.
- [8] K. S. Yeung and Y. W. Lam, "A simple chemical vapour deposition method for depositing thin TiO films," *Thin Solid Films*, vol. 109, no. 2, pp. 169–178, 1983.
- [9] J. -P. Lu, J. Wang, and R. Raj, "Solution precursor chemical vapor deposition of titanium oxide thin films," *Thin Solid Films*, vol. 204, no. 1, pp. L13–L17, 1991.
- [10] S. Schiller, G. Beister, W. Sieber, G. Schirmer, and E. Hacker, "Influence of deposition parameters on the optical and structural properties of TiO films produced by reactive d.c. plasmatron sputtering," *Thin Solid Films*, vol. 83, no. 2, pp. 239–245, 1981.
- [11] M. H. Suhail, G. M. Rao, and S. Mohan, "Dc reactive magnetron sputtering of titanium-structural and optical characterization of TiO films," *Journal of Applied Physics*, vol. 71, no. 3, pp. 1421–1427, 1992.
- [12] K. Okimura, N. Maeda, and A. Shibata, "Characteristics of rutile TiO films prepared by r.f. magnetron sputtering at a low temperature," *Thin Solid Films*, vol. 281-282, no. 1-2, pp. 427–430, 1996.
- [13] Yu. D. Dolmatov, Zh. Priklad et al., "Changes of state of titanium (TV) during its hydrolysis in sulfuric acid," *Zhurnal Prikladnoi Khimii*, vol. 42, no. 8, pp. 1725–1732, 1969.
- [14] Z. Jerman et al., "Gas/diffusion flow injection determination of ammonium ions in river and waste waters by conductometry," *Collection of Czechoslovak Chemical Communications*, vol. 31, no. 12, p. 3280, 1966.
- [15] B. E. Yoldas, "Hydrolysis of titanium alkoxide and effects of hydrolytic polycondensation parameters," *Journal of Materials Science*, vol. 21, no. 3, pp. 1087–1092, 1986.
- [16] K. Kamiya and S. Sakka, "Thermal expansion of TiO₂SiO₂ and TiO₂GeO₂ glasses," *Journal of Non-Crystalline Solids*, vol. 52, no. 1-3, pp. 357–363, 1982.
- [17] Z. Zhang, C. C. Wang, R. Zakaria, and J. Y. Ying, "Role of particle size in nanocrystalline TiO_i-based photocatalysts," *Journal of Physical Chemistry B*, vol. 102, no. 52, pp. 10871–10878, 1998.
- [18] A. J. Maira, K. L. Yeung, C. Y. Lee, P. L. Yue, and C. K. Chan, "Size effects in gas-phase photo-oxidation of trichloroethylene using nanometer-sized TiO catalysts," *Journal of Catalysis*, vol. 192, no. 1, pp. 185–196, 2000.
- [19] S. Ito, S. Inoue, H. Kawada, M. Hara, M. Iwasaki, and H. Tada, "Low-temperature synthesis of nanometer-sized crystalline TiO particles and their photoinduced decomposition of formic acid," *Journal of Colloid and Interface Science*, vol. 216, no. 1, pp. 59–64, 1999.
- [20] J. F. Porter, Y. G. Li, and C. K. Chan, "Effect of calcination on the microstructural characteristics and photoreactivity of degussa P-25 TiO," *Journal of Materials Science*, vol. 34, no. 7, pp. 1523–1531, 1999.
- [21] Q. Shen, T. Toyoda et al., "Studies of optical absorption and electron transport in nanocrystalline TiO electrodes," *Thin Solid Films*, vol. 438-439, pp. 167–170, 2003.
- [22] Y. Li, J. Hagen, W. Schaffrath, P. Otschik, and D. Haarer, "Titanium dioxide films for photovoltaic cells derived from a sol gel process," *Solar Energy Materials and Solar Cells*, vol. 56, no. 2, pp. 167–174, 1999.
- [23] U. Diebold, "The surface science of titanium dioxide," *Surface Science Reports*, vol. 48, no. 5–8, pp. 53–229, 2003.
- [24] Yu. Jianguo, Yu. Huogen, B. Cheng, Z. Xiujuan, and Z. Qingjie, "Preparation and photocatalytic activity of mesoporous anatase TiO nanofibers by a hydrothermal method," *Journal of Photochemistry and Photobiology A: Chemistry*, vol. 182, no. 2, pp. 121–127, 2006.
- [25] A. A. Belhekar, S. V. Awate, and R. Anand, "Photocatalytic activity of titania modified mesoporous silica for pollution control," *Catalysis Communications*, vol. 3, no. 10, pp. 453–458, 2002.
- [26] M. Adachi, I. Okada, S. Ngamsinlapasathian, Y. Murata, and S. Yoshikawa, "Dye-sensitized solar cells using semiconductor thin film composed of ceramic nanotubes," *Electrochemistry*, vol. 70, pp. 449–452, 2002.
- [27] S. Ngamsinlapasathian, S. Sakulkhaemaruehai, S. Pava-supree et al., "Highly efficient dye-sensitized solar cell using

- nanocrystalline titania containing nanotube structure,” *Journal of Photochemistry and Photobiology A*, vol. 164, no. 1-3, pp. 145–151, 2004.
- [28] K. Srikanth, M. M. Rahman, H. Tanaka et al., “Investigation of the effect of sol processing parameters on the photoelectrical properties of dye-sensitized TiO_2 solar cells,” *Solar Energy Materials and Solar Cells*, vol. 65, no. 1, pp. 171–177, 2001.
- [29] E. Stathatos, P. Lianos, and C. Krontiras, “Dye-sensitized photoelectrochemical cell using a nanocomposite SiO_2/Poiy (ethylene glycol) thin film as electrolyte support. Characterization by time-resolved luminescence and conductivity measurements,” *Journal of Physical Chemistry B*, vol. 105, no. 17, pp. 3486–3492, 2001.
- [30] K. Kajihara and T. Yao, “Macroporous morphology of the titania films prepared by a sol-gel dip-coating method from the system containing poly(ethylene glycol). IV. general principle of morphology formation and effect of heat treatment,” *Journal of Sol-Gel Science and Technology*, vol. 17, no. 2, pp. 173–184, 2000.
- [31] M. Wu, G. Lin, D. Chen et al., “Sol-hydrothermal synthesis and hydrothermally structural evolution of nanocrystal titanium dioxide,” *Chemistry of Materials*, vol. 14, no. 5, pp. 1974–1980, 2002.
- [32] A. Tolvanen, M.S. thesis, Helesinki University of Technology, Finland, 2003.
- [33] C. Longo and M.-A. De Paoli, “Dye-sensitized solar cells: a successful combination of materials,” *Journal of the Brazilian Chemical Society*, vol. 14, no. 6, pp. 889–901, 2003.
- [34] N. G. Park, J. Van De Lagemaat, and A. J. Frank, “Comparison of dye-sensitized rutile-and anatase-based TiO_2 solar cells,” *Journal of Physical Chemistry*, vol. 104, no. 38, pp. 8989–8994, 2000.
- [35] K. Tanaka, M. F. V. Capule, and T. Hisanaga, “Effect of crystallinity of TiO_2 on its photocatalytic action,” *Chemical Physics Letters*, vol. 187, no. 1-2, pp. 73–76, 1991.
- [36] T. Ma, K. Inoue, H. Noma, K. Yao, and E. Abe, “Ionization potential studies of organic dye adsorbed onto TiO_2 electrode,” *Journal of Materials Science Letters*, vol. 21, no. 13, pp. 1013–1014, 2002.

Research Article

TiO₂-Based Organic Hybrid Solar Cells with Mn⁺² Doping

Zühal Alparslan,¹ Arif Kösemen,^{1,2} Osman Örnek,^{1,3} Yusuf Yerli,¹ and S. Eren San¹

¹Organic Electronics Research Group, Department of Physics, Gebze Institute of Technology, 41400 Gebze, Turkey

²Department of Physics, Muş Alparslan University, 49100 Muş, Turkey

³Department of Physics, Sakarya University, 54187 Sakarya, Turkey

Correspondence should be addressed to Yusuf Yerli, yusufyerli@gmail.com

Received 22 February 2011; Revised 9 April 2011; Accepted 24 April 2011

Academic Editor: Mohamed Sabry Abdel-Mottaleb

Copyright © 2011 Zühal Alparslan et al. This is an open access article distributed under the Creative Commons Attribution License, which permits unrestricted use, distribution, and reproduction in any medium, provided the original work is properly cited.

A hybrid solar cell is designed and proposed as a feasible and reasonable alternative, according to acquired efficiency with the employment of TiO₂ (titanium dioxide) and Mn-doped TiO₂ thin films. In the scope of this work, TiO₂ (titanium dioxide) and Mn:TiO₂ hybrid organic thin films are proposed as charge transporter layer in polymer solar cells. Poly(3-hexylthiophene):phenyl-C61-butyric acid methyl ester (P3HT:PCBM) is used as active layer. When the Mn-doped TiO₂ solar cells were compared with pure TiO₂ cells, Mn-doped samples revealed a noteworthy efficiency enhancement with respect to undoped-TiO₂-based cells. The highest conversion efficiency was obtained to be 2.44% at the ratio of 3.5% (wt/wt) Mn doping.

1. Introduction

Main criteria in choosing material for photovoltaic devices are feasibility and environmental convenience, as well as compatibility to solar spectra and easy and cheap production [1]. Organic-based materials are promising for photovoltaic applications [2–4] with advantageous features such as low cost, easy production, and flexible application. Therefore, organic solar cells are serious candidates in place of silicon solar cells [5]. Although organic-based materials are satisfying with most of these mentioned criteria, charge transport properties of these materials are not so good and their efficiency is still quite low. To overcome this problem, in recent studies, bulk heterojunction structure of the n-type PCBM and p-type P3HT materials was used [6–9] and 4–5% efficiencies were obtained [10]. The PEDOT:PSS used as an anode buffer layer in this kind of cells is acidic and hygroscopic. Also, ITO is quite susceptible against the acidic corruptions [11]. Therefore, PEDOT:PSS-based solar cells are known to be unstable in air conditions and under light illumination [12–14]. Moreover, in these devices, electron collecting a metal cathode (e.g., Al, Ca) with low work function must be used but they are easily oxidized and lead to deterioration in performance. In order to get rid of these

problems, inverted solar cells have been used with inorganic materials [15–18]. In inverted organic solar cells, the anode is an air-stable high-work-function metal collecting holes such as Ag. The ITO is also used as the cathode to collect electrons. Previous works reveal that conventional solar cells could merely endure for 4 days while inverted solar cells still preserve almost 80% of their efficiency even 40 days later [19]. However, power conversion efficiencies of inverted solar cells are less than those of the conventional organic solar cells. One of the reasons is the bad quality of interface in these inverted designs. These worse interface conditions deteriorate exciton formation and separation [20]. There are various studies to cope with mentioned interface problems [21].

When the polymer active layer in organic solar cell is exposed to the light, excitons begin to form. Excitons diffuse to donor-acceptor interface. In here, they dissociate to form bound electron-hole pair. To separate this pairs into free holes and electrons, there should be an electric field. With the effect of the electric field produced by the work function difference of both electrodes, these free charges are transported to positive and negative electrodes. Since the polymer has a disordered structure, there exists charge carrier loss during transportation through polymer skeleton.

Inorganic materials are used with organics so that ordered continuous paths are provided to charge transfer. This kind of designs are called hybrid systems, and for this aim, various inorganic materials are used in solar cells such as ZnO [22], CdTe [23], PbS [24], and so forth. TiO_2 [20, 25, 26] is also an attractive alternative among these materials. Usage of TiO_2 electrode in dye-based solar cell by Gratzel et al. could be given as a successful application of this material [27]. There are various works to understand the structural changes occurred when TiO_2 is doped by metal ions. In particular, photocatalytic and magnetic properties were investigated by [28, 29]. In the result of such investigations, it was understood that photoreactivity, charge carrier recombination rates, and interfacial electron transfer rates were changed by metal ion doping [30]. Doped TiO_2 is widely used in solar cell applications, and there are several comparative works. In one of them, it has been reported that power conversion efficiency was achieved to be 8% with the dye-based solar cells prepared by nitrogen-doped TiO_2 while 6% efficiency with pure TiO_2 [31]. Also, K. H. Ko et al. performed another work in which TiO_2 was doped with Al and W elements for dye-based solar cells. In Al-doped cells, while open-circuit voltage (V_{OC}) has increased, short-circuit current (I_{SC}) has decreased. As for W-doped cells, a behavior opposite to Al-doped cells was observed [32].

In this work, hybrid solar cells were produced and characterized with ITO/ TiO_2 /P3HT:PCBM/Ag configuration. The novelty and goal of this work comes from the employment of Mn^{+2} ions for the first time with this configuration, in which different amounts of Mn were incorporated to TiO_2 and cell parameters were investigated in terms of doping amount. It was explicitly observed that solar cell efficiency was being improved with Mn doping until a certain doping amount, which is 3.5%. One of the inspirations of choosing Mn^{+2} ion in our aim comes from some works such as [33], which reveals the fact that although the Mn^{+2} ion is slightly larger than Ti^{+4} , the general crystal structure is not changed with doping but light interaction of modified TiO_2 .

2. Experimental

P3HT (Aldrich) and PCBM (Aldrich) were used in the structure of active layer without any further purification. Their chemical formulas are given in Figure 1. P3HT and PCBM were firstly mixed in chlorobenzene with 1:0.8 (wt/wt) ratio at 60°C for a night. In order to prepare TiO_2 sol-gel mixture, titanium n-butoxide, ethanol, isopropanol alcohol, and acetic acid were mixed with (1:20:20:0.15) molar ratio, respectively, for two days at room temperature. Also, MnCl_2 was added into a solution containing a mixture of ethanol, isopropanol alcohol, and acetic acid. This solution of mixture was stirred for two hours at room temperature, and then titanium n-butoxide was added to this sol-gel mixture so that Mn-doped TiO_2 sample was prepared. Ti amount in the solution of mixture is proportional to the amount of Mn, at ratio of their weights. The Mn amounts in samples were prepared as 0.5%, 1.5%, 3.5%, 8.5%, 15%, and 25%.

In regard to the solar cell fabrication process, ITO-coated glass was firstly subject to a standard cleaning process

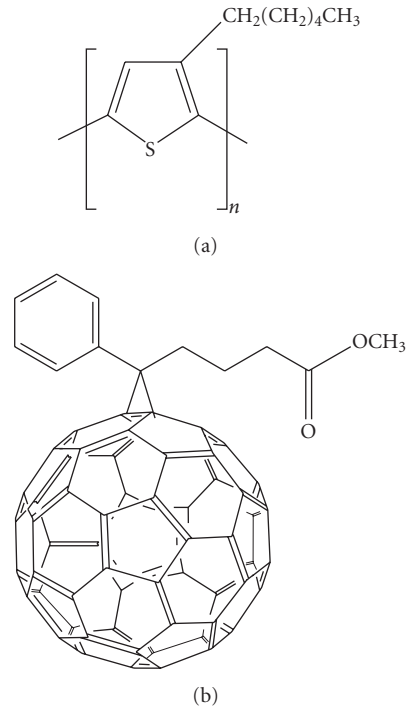


FIGURE 1: Chemical formulas of (a) P3HT and (b) PCBM.

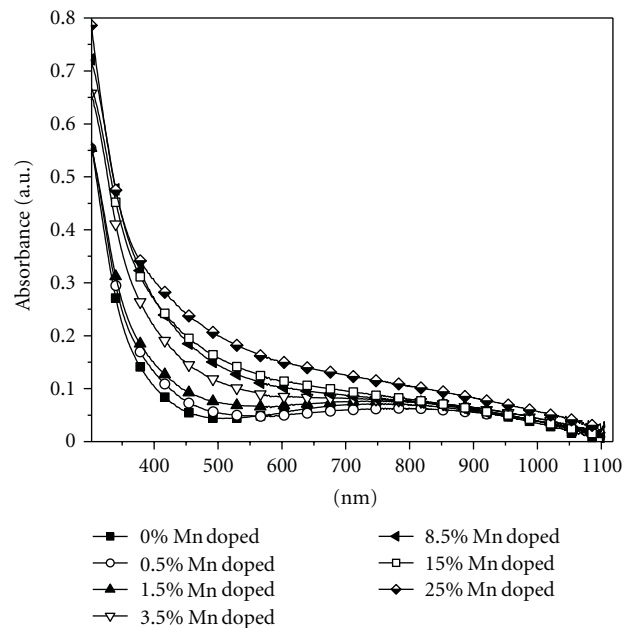


FIGURE 2: Absorption spectra of pure, 0.5%, 1.5%, 3.5%, 8.5%, 15%, and 25% doped TiO_2 films.

with acetone, ethanol, and distilled water in ultrasonic bath for 15 minutes to each cleaning agent. Later, TiO_2 - and Mn-doped TiO_2 gels were coated with spin coater at 3500 rpm. These thin films were annealed at 400°C for 30 min, which was reached in steps of $10^\circ\text{C}/\text{min}$. The solar cells were designed with ITO/ TiO_2 /P3HT:PCBM/Ag and ITO/ TiO_2 :Mn/P3HT:PCBM/Ag configuration. TiO_2

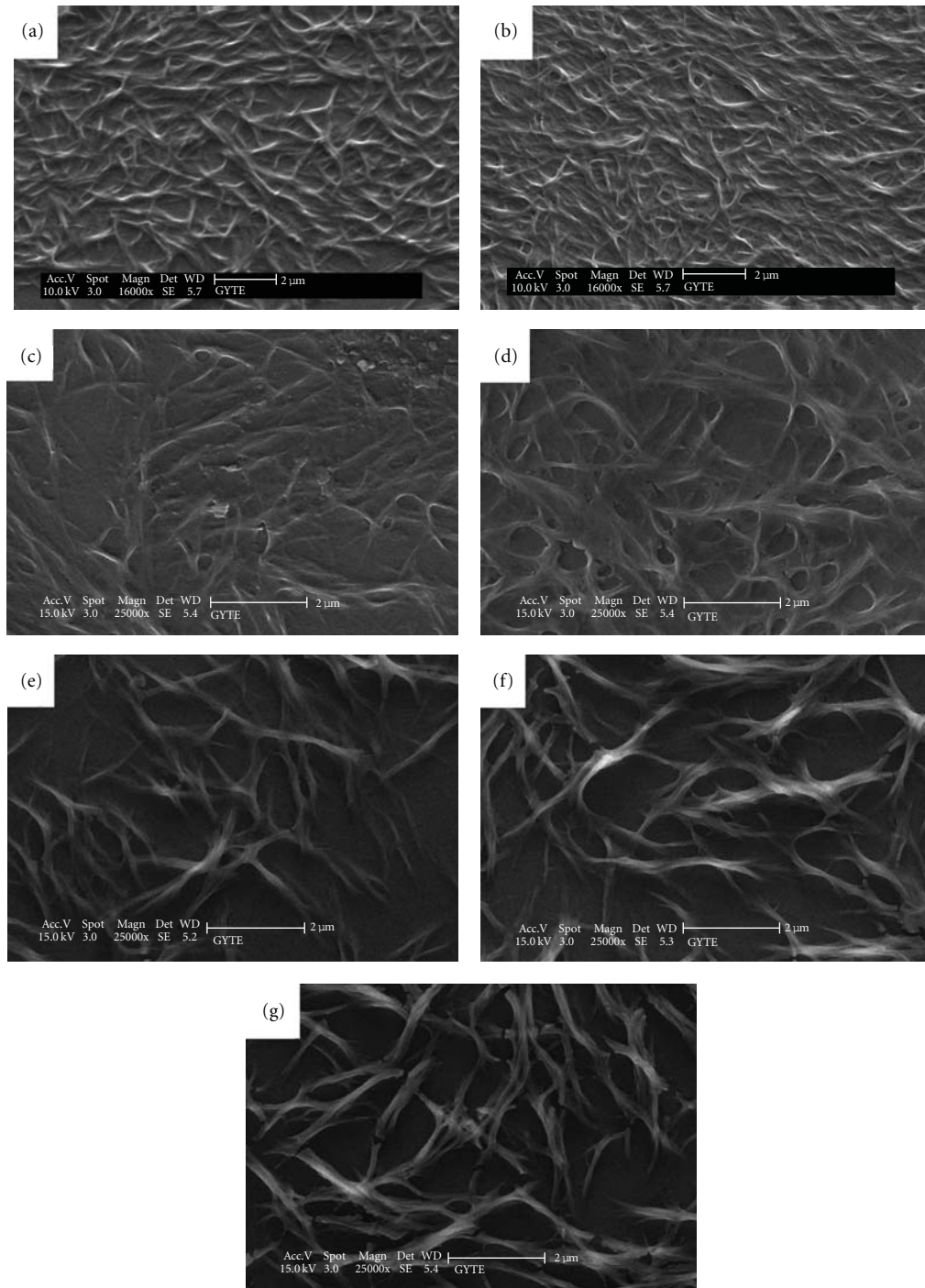


FIGURE 3: SEM pictures of pure (a), 0.5% (b), 1.5% (c), 3.5% (d), 8.5% (e), 15% (f), and 25% (g) doped TiO₂ films.

and doped TiO₂ films were coated with the mixture of P3HT:PCBM as active layer at 2500 rpm. After this, Ag contact layers were deposited at approximately thickness of 100 nm with thermal evaporator. Current-voltage characteristics of the samples were analyzed with (Keithley 4200 SCS) semiconductor characterization system and (Thermo Oriel) Solar Simulator under AM1.5 G (100 mW/cm²) standard characterization regulations. Solar Simulator was calibrated with reference photodiode.

3. Result and Discussion

Figure 2 depicts the UV-Vis absorbance spectra of TiO₂- and Mn-doped TiO₂ films. As the doping percentage of Mn increases, the absorbance curves shift to visible region. In fact, it is supposed that this shift is caused by the diffusion of Mn atoms into TiO₂ lattice. The shift implies that the energy levels of Mn atoms placed in TiO₂ lattice are between the band gap of TiO₂ and the contribution to the light-induced

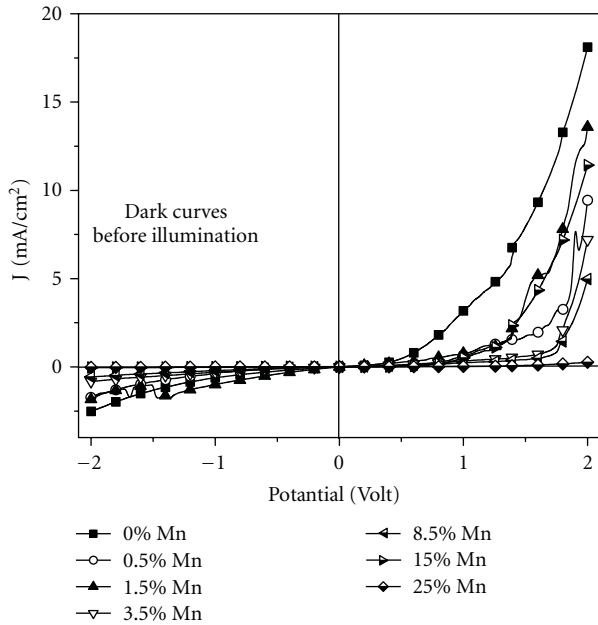


FIGURE 4: J-V characteristic curves for TiO₂- and Mn-doped TiO₂ solar cells under dark circumstances (before any illumination process).

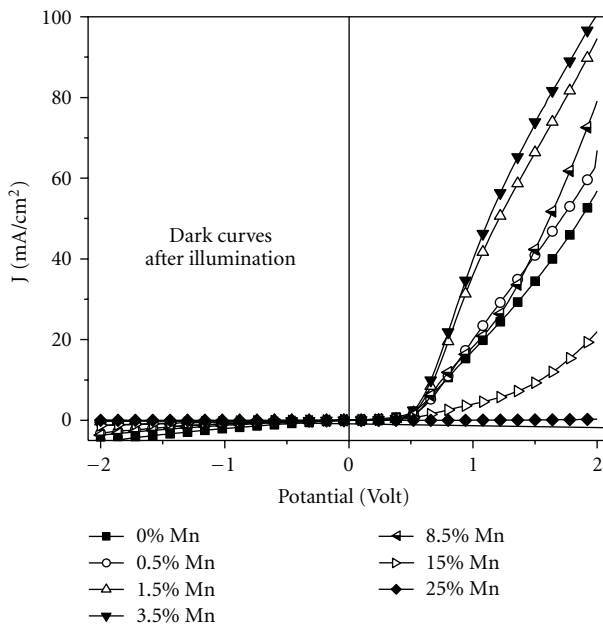


FIGURE 5: J-V characteristic curves for TiO₂- and Mn-doped TiO₂ solar cells under dark circumstances (after 60-minute illumination).

charge transfer [34]. Also, these kinds of red shifts are related to the charge transfer between d-electrons of metal ions and valance or conduction band of TiO₂ [35]. The SEM pictures of TiO₂- and Mn-doped TiO₂ films are given in Figure 3. The SEM pictures show the growing of weak skeletons in the case of Pure TiO₂ as shown in Figure 3(a). As the Mn doping percentage is further increased, branches of the skeleton are getting stronger and these stronger branches are yielding an

obvious fiber structures particularly as seen in Figures 3(f) and 3(g).

Figure 4 shows the dark J-V characteristic curves of solar cells prepared by Mn-doped and pure TiO₂ films. The forward bias current of pure-TiO₂-based cells is bigger than that of the Mn-based cells. That is, injection current is more in pure TiO₂ cells. This indicates the presence of an injection barrier imposed by Mn doping. The same cells are subject to the same measurements under dark conditions again, but this time these cells are exposed to illumination for 60 minutes before dark J-V measurements (Figure 5). This time, the obtained results are entirely different from previous measurements. Forward bias current has increased in all cells, but this increase is much more in 0.5%, 1.5%, 3.5%, and 8.5% doping percentages. In the case of 15% and 25% Mn-doped TiO₂ cells, the increasing tendency of the forward bias current is disrupted. This indicates that there is a threshold value of the Mn doping in our solar cell design. When the cells are exposed to illumination, both photoexcitation and thermal-excitation play an important role in increasing the number of charge carriers in (P3HT : PCBM) active layer and highly photoreactive TiO₂ layers. This could be recognized to be the cause of the increase in current. Also, the injection barrier mentioned for the Mn-doped cells is eliminated when the cells are waited under illumination, so forward bias currents are becoming more with respect to the pure TiO₂ based cells.

The highest forward bias current and maximum power conversion efficiency were observed in 3.5% Mn-doped solar cell. The J-V plots of pure TiO₂ and Mn-doped TiO₂-based solar cells under illuminated conditions are shown in Figure 6. The power conversion efficiency parameters obtained from these graphs are given in Table 1. There is no improvement in the pure TiO₂ solar cell when the cell is subject to a light illumination even if forward bias current slightly changes due to the heating of the cell. Whereas, even very little amount of Mn doping, for example 0.5%, causes an S-shape in reverse bias in the J-V curves, as soon as illumination starts. In this study as the solar cells were exposed to continuous illumination, the S-shape disappears. After two minutes, it converted conventional solar cell shape for % 0.5 Mn doped. This was observed in all Mn-doped TiO₂ cells. In a work, this kind of S-shape curves was previously explained with electrical dipoles occurred at the interface [36]. In another study, it is expressed that the reason for S-shaped curve is charge accumulation near one of the electrodes [37]. As for our cells, the reason for S-shaped curve (Figure 6) was the accumulation of the charge occurring in TiO₂ due to Mn doping.

ITO/TiO₂/P3HT:PCBM/Ag solar cells are actually the inverted structures, and light is absorbed in P3HT active layer. The excitons, which are produced in polymer active layer, are separated at P3HT/PCBM interface, and free electrons are diffused to ITO side by passing through TiO₂ while the free holes are diffused to Ag side as represented in Figure 7. It is obvious that the reason of S-shaped curve is the Mn(II) ions, since there is no such a shape in pure-TiO₂-containing cells, as seen in Figure 6. In regard to possible mechanism of this event, one can think that either the

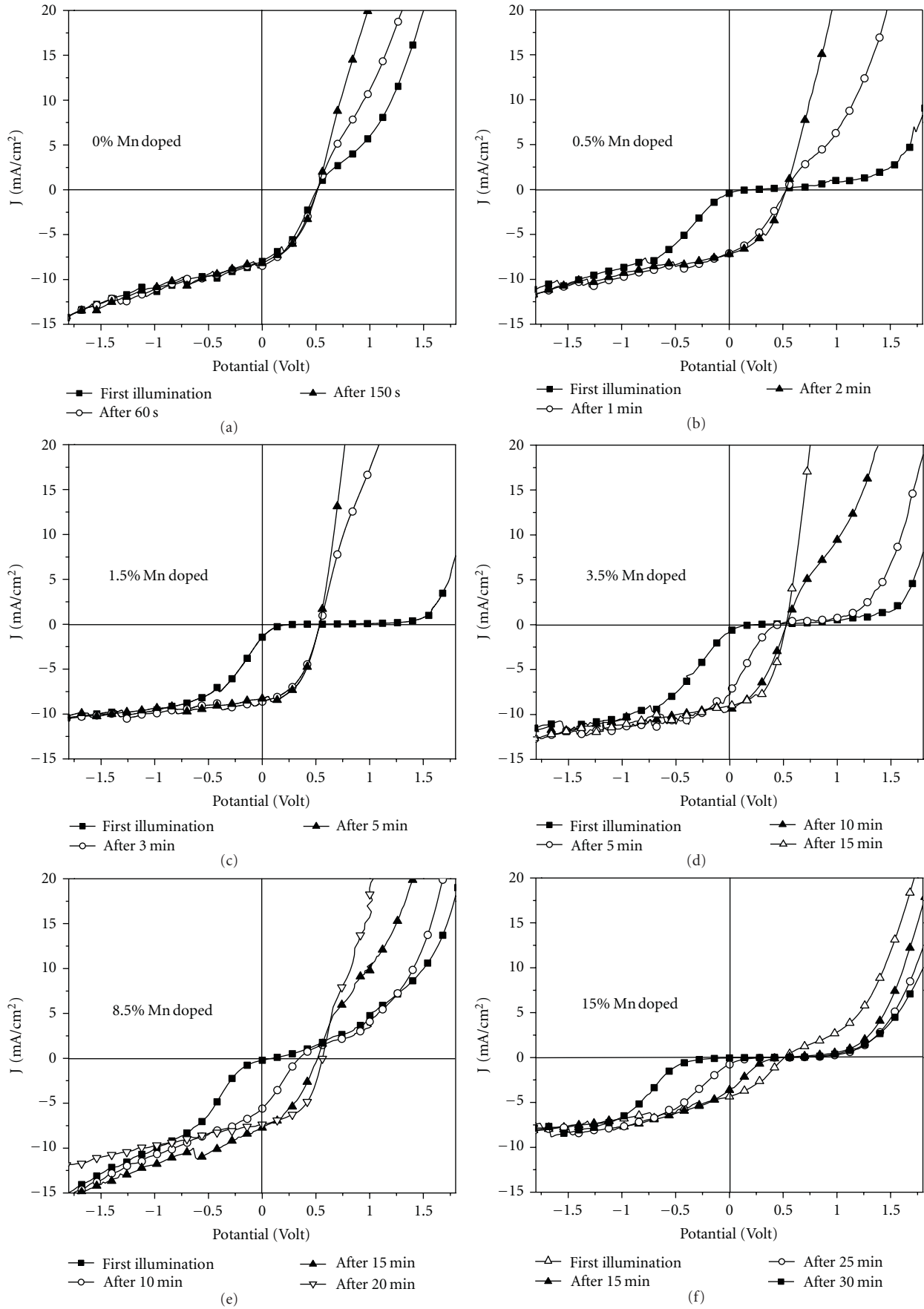


FIGURE 6: Continued.

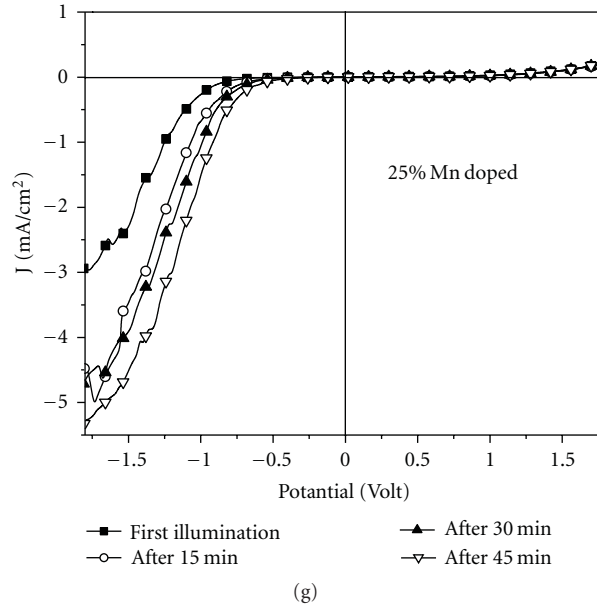


FIGURE 6: J-V characteristic curves for TiO₂- and Mn-doped TiO₂ solar cells under illumination.

TABLE 1: Designed solar cells power conversion parameters.

Mn doped	FF (%)	V _{OC} (Volt)	I _{SC} (mA/cm ²)	η (%)
0% Mn	41	0.51	8.18	1.71
0.5% Mn	45	0.53	7.19	1.74
1.5% Mn	51	0.53	8.41	2.27
3.5% Mn	51	0.53	9.03	2.44
8.5% Mn	50	0.56	7.37	2.06
15% Mn	36	0.50	4.34	0.78
25% Mn	—	—	—	—

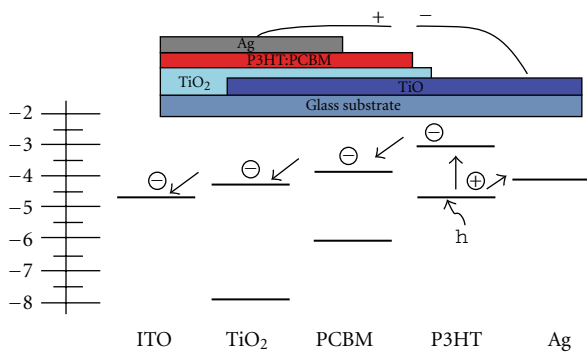
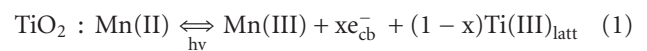


FIGURE 7: Schematic representation of the energy levels in our solar cell design (inset: the proposed solar cell assembly).

production of an electric dipole at the TiO₂/P3HT:PCBM interface or energy levels of Mn(II) ions are close to the valance band in the band gap of TiO₂ [38].

As the light illumination time is prolonged, this S shape disappears and the power conversion efficiency reaches 2.44% in 3.5% Mn²⁺-doped sample. Also dependency of the increase of the stabilization period on Mn amount reveals the

presence of a reaction between Ti and Mn atoms. Actually Saponjic and his coworkers propose the following reaction for this event [33]:



For this reason, the injection barrier of the TiO₂/P3HT:PCBM interface disappears and those electrons produced in active layer diffuse to TiO₂. However, there exists a decrease in conversion efficiency in the case of 8.5% Mn doping, although the light exposure duration is at the order of 20 minutes. Consistently, 15% Mn doping amount causes further decrease in the efficiency even after 30 minutes of the light exposure duration and solar cell parameters were lost in 25% Mn-doped sample.

In terms of dependence on the doping amount and light exposure, reasons of the S-shaped curve were tried to be clarified by inspirations from previous works done for both Mn and TiO₂ for other purposes. In regard to the evaluation of them in our case, the Mn(II) ions, embedded in the TiO₂ lattice, are excited by light resulting in that Mn(II) is converted to Mn(III). Then, the excited electrons are trapped producing in Ti(III). In this solar cell device, we can suppose that the electrons produced in active layer follow a path from

the TiO₂ to the ITO. As the light falls on the cell, the Mn (III) traps in the TiO₂ lattice occur for the electrons from the active layer. These electrons should pass to ITO side, but Mn (III) traps in the TiO₂ lattice capture them. The real reason of the observed S-shaped curve can be these Mn (III) traps. As long as the device is waited under the light illumination, electrons fill these trap levels. After the filling of the trap levels, the electrons transfer towards ITO effectively. In our opinion, the use of transition metal ions in hybrid solar cell is a serious candidate for the applications according to the results obtained experimentally.

4. Conclusion

The goal of this work is to exploit transition metal ions in hybrid organic solar cell. The Mn(II) ions were successfully adapted to TiO₂-based solar cells for the first time.

The S-like shape, which is observed occasionally, in the proposed solar cells, is attained in the scope of our hybrid design. The S-like shape is dependent on the Mn doping amounts and light exposure time (it disappears after long exposure time) for yielding an efficient solar cell. Maximum power conversion efficiency was obtained to be $\eta = 2.44\%$ for 3.5% Mn-doped TiO₂ solar cell. I_{sc} value is considered to be 9.03 mA/cm², which is a maximum in this efficient cell and Voc value is 0.53 V, which is a constant in all cells. This efficient cell reaches stability after 10-minute illumination. But further doping with Mn(II) ions resulted in decaying of the efficiency despite having longer stability periods. 25% Mn-doped cell could not reach desired stability and the cell parameters could not be measured for it even after 45-minute illumination.

References

- [1] A. P. Zoombelt, M. Fonrodona, M. M. Wienk, A. B. Sieval, J. C. Hummelen, and R. A. J. Janssen, "Photovoltaic performance of an ultrasmall band gap polymer," *Organic Letters*, vol. 11, no. 4, pp. 903–906, 2009.
- [2] C. J. Brabec, N. S. Sariciftci, and J. C. Hummelen, "Plastic solar cells," *Advanced Functional Materials*, vol. 11, no. 1, pp. 15–26, 2001.
- [3] S. Günes, H. Neugebauer, and N. S. Sariciftci, "Conjugated polymer-based organic solar cells," *Chemical Reviews*, vol. 107, no. 4, pp. 1324–1338, 2007.
- [4] H. Spanggaard and F. C. Krebs, "A brief history of the development of organic and polymeric photovoltaics," *Solar Energy Materials and Solar Cells*, vol. 83, no. 2-3, pp. 125–146, 2004.
- [5] J. Kalowekamo and E. Baker, "Estimating the manufacturing cost of purely organic solar cells," *Solar Energy*, vol. 83, no. 8, pp. 1224–1231, 2009.
- [6] N. S. Sariciftci, L. Smilowitz, A. J. Heeger, and F. Wudl, "Photoinduced electron transfer from a conducting polymer to buckminsterfullerene," *Science*, vol. 258, no. 5087, pp. 1474–1476, 1992.
- [7] M. M. Wienk, M. G. R. Turbiez, M. P. Struijk, M. Fonrodona, and R. A. J. Janssen, "Low-band gap poly(di-2-thienylthienopyrazine): fullerene solar cells," *Applied Physics Letters*, vol. 88, no. 15, Article ID 153511, 2006.
- [8] N. Camaioni, G. Ridolfi, G. Casalbore-Miceli, G. Possamai, and M. Maggini, "The effect of a mild thermal treatment on the performance of poly(3-alkylthiophene)/fullerene solar cells," *Advanced Materials*, vol. 14, no. 23, pp. 1735–1738, 2002.
- [9] J. K. J. van Duren, X. Yang, J. Loos et al., "Relating the morphology of poly(p-phenylene vinylene)/methanofullerene blends to solar-cell performance," *Advanced Functional Materials*, vol. 14, no. 5, pp. 425–434, 2004.
- [10] M. Reyes-Reyes, K. Kim, and D. L. Carroll, "High-efficiency photovoltaic devices based on annealed poly(3-hexylthiophene) and 1-(3-methoxycarbonyl)-propyl-1-phenyl-(6,6)C₆₁ blends," *Applied Physics Letters*, vol. 87, no. 8, Article ID 083506, 3 pages, 2005.
- [11] H. Yan, P. Lee, N. R. Armstrong et al., "High-performance hole-transport layers for polymer light-emitting diodes. Implementation of organosiloxane cross-linking chemistry in polymeric electroluminescent devices," *Journal of the American Chemical Society*, vol. 127, no. 9, pp. 3172–3183, 2005.
- [12] K. Kawano, R. Pacios, D. Poplavskyy, J. Nelson, D. D. C. Bradley, and J. R. Durrant, "Degradation of organic solar cells due to air exposure," *Solar Energy Materials and Solar Cells*, vol. 90, no. 20, pp. 3520–3530, 2006.
- [13] N. Koch, A. Vollmer, and A. Elschner, "Influence of water on the work function of conducting poly(3,4-ethylenedioxythiophene)/poly(styrenesulfonate)," *Applied Physics Letters*, vol. 90, no. 4, Article ID 043512, 2007.
- [14] M. P. de Jong, L. J. van Ijendoorn, and M. J. A. de Voigt, "Stability of the interface between indium-tin-oxide and poly(3,4-ethylenedioxythiophene)/poly(styrenesulfonate) in polymer light-emitting diodes," *Applied Physics Letters*, vol. 77, no. 14, pp. 2255–2257, 2000.
- [15] A. C. Arango, L. R. Johnson, V. N. Bliznyuk, Z. Schlesinger, S. A. Carter, and H. H. Hörhold, "Efficient titanium oxide/conjugated polymer photovoltaics for solar energy conversion," *Advanced Materials*, vol. 12, no. 22, pp. 1689–1692, 2000.
- [16] Y. Liu, M. A. Summers, C. Edder, J. M. J. Fréchet, and M. D. McGehee, "Using resonance energy transfer to improve exciton harvesting in organic-inorganic hybrid photovoltaic cells," *Advanced Materials*, vol. 17, no. 24, pp. 2960–2964, 2005.
- [17] J. Owen, M. S. Son, K. H. Yoo, B. D. Ahn, and S. Y. Lee, "Organic photovoltaic devices with Ga-doped ZnO electrode," *Applied Physics Letters*, vol. 90, no. 3, Article ID 033512, 2007.
- [18] C. Waldauf, M. Morana, P. Denk et al., "Highly efficient inverted organic photovoltaics using solution based titanium oxide as electron selective contact," *Applied Physics Letters*, vol. 89, no. 23, Article ID 233517, 2006.
- [19] S. K. Hau, H. L. Yip, N. S. Baek, J. Zou, K. O'Malley, and A. K. Y. Jen, "Air-stable inverted flexible polymer solar cells using zinc oxide nanoparticles as an electron selective layer," *Applied Physics Letters*, vol. 92, no. 25, Article ID 253301, 2008.
- [20] W. H. Baek, I. Seo, T. S. Yoon, H. H. Lee, C. M. Yun, and Y. S. Kim, "Hybrid inverted bulk heterojunction solar cells with nanoimprinted TiO₂ nanopores," *Solar Energy Materials and Solar Cells*, vol. 93, no. 9, pp. 1587–1591, 2009.
- [21] S. K. Hau, H. L. Yip, O. Acton, N. S. Baek, H. Ma, and A. K. Y. Jen, "Interfacial modification to improve inverted polymer solar cells," *Journal of Materials Chemistry*, vol. 18, no. 42, pp. 5113–5119, 2008.
- [22] Y. Hames, Z. Alpaslan, A. Kösemen, S. E. San, and Y. Yerli, "Electrochemically grown ZnO nanorods for hybrid solar cell applications," *Solar Energy*, vol. 84, no. 3, pp. 426–431, 2010.

- [23] Y. Kang, N. G. Park, and D. Kim, "Hybrid solar cells with vertically aligned CdTe nanorods and a conjugated polymer," *Applied Physics Letters*, vol. 86, no. 11, Article ID 113101, 2005.
- [24] S. Günes, K. P. Fritz, H. Neugebauer, N. S. Sariciftci, S. Kumar, and G. D. Scholes, "Hybrid solar cells using PbS nanoparticles," *Solar Energy Materials and Solar Cells*, vol. 91, no. 5, pp. 420–423, 2007.
- [25] Q. Qiao, Y. Xie, and J. T. McLeskey Jr., "Organic/inorganic polymer solar cells using a buffer layer from all-water-solution processing," *Journal of Physical Chemistry C*, vol. 112, no. 26, pp. 9912–9916, 2008.
- [26] L. Shena, X. D. Zhang, W. B. Guo, C. X. Liu, W. Dong, and S. P. Ruan, "Performance improvement of inverted polymer solar cells using V_2O_5 as an anode buffer layer," *Materials Science Forum*, vol. 663–665, pp. 865–868, 2011.
- [27] B. O'Regan and M. Grätzel, "A low-cost, high-efficiency solar cell based on dye-sensitized colloidal TiO_2 films," *Nature*, vol. 353, no. 6346, pp. 737–740, 1991.
- [28] K. Zhang, W. Xu, X. Li, S. Zheng, and G. Xu, "Effect of dopant concentration on photocatalytic activity of TiO_2 film doped by Mn non-uniformly," *Central European Journal of Chemistry*, vol. 4, no. 2, pp. 234–245, 2006.
- [29] J. P. Xu, Y. B. Lin, Z. H. Lu et al., "Enhanced ferromagnetism in Mn-doped TiO_2 films during the structural phase transition," *Solid State Communications*, vol. 140, no. 11–12, pp. 514–518, 2006.
- [30] W. Choi, A. Termin, and M. R. Hoffmann, "The role of metal ion dopants in quantum-sized TiO_2 : correlation between photoreactivity and charge carrier recombination dynamics," *Journal of Physical Chemistry*, vol. 98, no. 51, pp. 13669–13679, 1994.
- [31] Y. Wang, Y. Hao, H. Cheng et al., "Photoelectrochemistry of transition metal-ion-doped TiO_2 nanocrystalline electrodes and higher solar cell conversion efficiency based on Zn^{2+} -doped TiO_2 electrode," *Journal of Materials Science*, vol. 34, no. 12, pp. 2773–2779, 1999.
- [32] K. H. Ko, Y. C. Lee, and Y. J. Jung, "Enhanced efficiency of dye-sensitized TiO_2 solar cells (DSSC) by doping of metal ions," *Journal of Colloid and Interface Science*, vol. 283, no. 2, pp. 482–487, 2005.
- [33] Z. V. Saponjic, N. M. Dimitrijevic, O. G. Poluektov et al., "Charge separation and surface reconstruction: a Mn^{2+} doping study," *Journal of Physical Chemistry B*, vol. 110, no. 50, pp. 25441–25450, 2006.
- [34] W. Choi, A. Termin, and M. R. Hoffmann, "The role of metal ion dopants in quantum-sized TiO_2 : correlation between photoreactivity and charge carrier recombination dynamics," *Journal of Physical Chemistry*, vol. 98, no. 51, pp. 13669–13679, 1994.
- [35] J. Moser, M. Grätzel, and R. Gally, "Inhibition of electron-hole recombination in substitutionally doped colloidal semiconductor crystallites," *Helvetica Chimica Acta*, vol. 70, pp. 1596–1604, 1987.
- [36] A. Kumar, S. Sista, and Y. Yang, "Dipole induced anomalous S-shape I-V curves in polymer solar cells," *Journal of Applied Physics*, vol. 105, no. 9, Article ID 094512, 2009.
- [37] D. Gupta, M. Bag, and K. S. Narayan, "Correlating reduced fill factor in polymer solar cells to contact effects," *Applied Physics Letters*, vol. 92, no. 9, Article ID 093301, 2008.
- [38] T. Umeyayashi, T. Yamaki, H. Itoh, and K. Asai, "Analysis of electronic structures of 3d transition metal-doped TiO_2 based on band calculations," *Journal of Physics and Chemistry of Solids*, vol. 63, no. 10, pp. 1909–1920, 2002.

Research Article

Amphiphilic Ruthenium(II) Terpyridine Sensitizers with Long Alkyl Chain Substituted β -Diketonato Ligands: An Efficient Coadsorbent-Free Dye-Sensitized Solar Cells

Ashraful Islam,^{1,2} Surya Prakash Singh,¹ Masatoshi Yanagida,¹
Mohammad Rezaul Karim,² and Liyuan Han¹

¹International Center for Materials Nanoarchitectonics (MANA) and Advanced Photovoltaics Center,
National Institute for Materials Science (NIMS), 1-2-1 Sengen, Tsukuba, Ibaraki 305-0047, Japan

²Center of Excellence for Research in Engineering Materials (CEREM), College of Engineering, King Saud University,
Riyadh 11421, Saudi Arabia

Correspondence should be addressed to Ashraful Islam, islam.ashraful@nims.go.jp

Received 16 October 2010; Accepted 3 December 2010

Academic Editor: Mohamed Sabry Abdel-Mottaleb

Copyright © 2011 Ashraful Islam et al. This is an open access article distributed under the Creative Commons Attribution License, which permits unrestricted use, distribution, and reproduction in any medium, provided the original work is properly cited.

Three alkyl-substituted β -diketonato-ruthenium(II)-polypyridyl sensitizers with different alkyl chain lengths, [Ru(tctpy)(tfpd)(NCS)] (**A1**), [Ru(tctpy)(tfdd)(NCS)] (**A2**), and [Ru(tctpy)(tfid)(NCS)] (**A3**), were designed and synthesized for dye-sensitized solar cells (DSCs) to investigate the effect of bulky alkyl chain substituents on the photovoltaic performances (where tctpy = 4,4',4''-tricarboxy-2,2':;6',2''-terpyridine, tfpd = 1,1,1-trifluoropentane-2,4-dione, tfdd = 1,1,1-trifluorodecane-2,4-dione, and tfid = 1,1,1-trifluoroicosane-2,4-dione). These complexes exhibit a broad metal-to-ligand charge transfer absorption band over the whole visible range extending up to 950 nm. All complexes were examined in the presence and absence of the coadsorbent deoxycholic acid (DCA) in dye-bath solutions. These sensitizers, when anchored to nanocrystalline TiO₂ films, achieve efficient sensitization to TiO₂ electrodes. Under standard AM 1.5 sunlight, the complex **A3** containing long alkyl chain length of C₁₆ yielded a short-circuit photocurrent density of 18.0 mA/cm², an open-circuit voltage of 0.64 V, and a fill factor of 0.66, corresponding to an overall conversion efficiency of 7.6% in the absence of DCA. The power conversion efficiency of **A1** sensitized DSCs was significantly increased upon the addition of DCA as compared to that in the absence of DCA. However, the photovoltaic performance of **A3** was not dependent on DCA at all, probably due to the inherent structural nature of the **A3** molecule.

1. Introduction

In general, dye-sensitized solar cells (DSCs) comprise a nanocrystalline titanium dioxide (TiO₂) electrode modified with a dye and fabricated on a transparent conducting oxide TCO, a platinum counter electrode, and an electrolyte solution with a dissolved iodide ion/triiodide (I⁻/I₃⁻) redox couple between the electrodes [1–5]. Among these elements, the photosensitizer plays a vital role for the light harvesting efficiency. Many sensitizers, including organic sensitizers [6] and transition metal complexes [7–16], have been employed in DSCs. Ru(II) polypyridyl sensitized nanocrystalline TiO₂ solar cells yielding solar to electric power conversion efficiency of over 11% under standard AM 1.5 condition [13, 14]. This is because of their intense

charge-transfer (CT) absorption in the whole visible range, and the absorption properties can be tuned by changing the donor-acceptor properties of the ligand in a controlled manner. Photoexcitation of the charge-transfer (CT) excited states of the adsorbed dye leads to an efficient injection of electrons into the conduction band of the TiO₂.

Ru(II) 4,4',4''-tricarboxy-2,2':6',2''-terpyridine based dyes show efficient panchromatic sensitization of nanocrystalline TiO₂ solar cell that make these class of sensitizers as potential candidates for near-IR dye development [7, 9, 13, 15, 16]. We have reported a series of Ru(II) 4,4',4''-tricarboxy-2,2':6',2''-terpyridine based dye containing β -diketonato ligand that efficiently sensitized nanocrystalline TiO₂ over the whole visible range extending into the near IR region [10, 12, 15, 16]. An important feature of

β -diketonato ligand is its structural versatility due to presence of three substituents on the ligand. Therefore, a desired electronic environment on the metal center, improvement of light harvesting efficiency by extending π -conjugated system, and also introduction of bulky substituent to suppress dye aggregation on TiO₂ surface is possible by molecular designing of the three substituents on the β -diketonato ligand.

Coadsorbents are usually added in the dye solutions to suppress aggregate formation resulting in an improved performance of DSCs through increasing both the short-circuit photocurrent density (J_{sc}) and the open-circuit voltage (V_{oc}) [10, 12, 13, 15–23]. Such aggregate formation has been suggested to promote unwanted intermolecular energy transfer or nonradiative decay pathways, thus reducing the electron injection efficiency. Organic dyes have been found to be more susceptible to aggregate formation compared to Ru-polypyridine based dye [19–23]. Conversely, Ru-bipyridyl based dye has been shown not to form aggregates and addition of coadsorbent in dye-bath solutions only yields a modest or no increase in photocurrents [8, 14]. Although Ru(II) 4,4',4''-tricarboxy-2,2':6',2''-terpyridine based panchromatic sensitizers containing NCS and/or β -diketonato ligand show potential candidates for further improvement of device efficiency, they are susceptible to aggregate formation resulting in a poor device performance without additive in dye-bath solutions [7, 9–13, 15, 16]. In addition, some works showed that the power conversion efficiency of DSCs can be further improved by introducing bulky alkyl chains into the dye structure to obtain an insulating effect of dye layer on the TiO₂ surface [19, 24–27]. Considering the high potentiality of efficient DSCs based on Ru(II)-terpyridine dyes, a strategic structural modification of these dyes is an effective approach to improve light harvesting efficiency in the near-IR region and also suppression of aggregate formation resulting in a coadsorbent-free efficient device processing. Recently we have reported that a β -diketonato ruthenium(II)-tricarboxy-2,2':6',2''-terpyridine sensitizer with extended π -conjugated system by introducing a triphenylamine substituted β -diketonato ligand shows efficient sensitization of nanocrystalline TiO₂ over the whole visible range extending up to 1000 nm [16]. Here we report the synthesis and characterization of terpyridine-ruthenium(II) complexes with β -diketonato ligands having different substituted alkyl chain lengths 1,1,1-trifluoropentane-2,4-dione (tfpd), 1,1,1-trifluorodecane-2,4-dione (tfdd), and 1,1,1-trifluoroicosane-2,4-dione (tfid) and investigated their effects on DSCs performance in the presence and absence of deoxycholic acid (DCA) as a coadsorbent, with the aid of photophysical, and photoelectrochemical measurements. The molecular structures of the complexes [Ru(tctpy)(tfpd)(NCS)] (**A1**), [Ru(tctpy)(tfdd)(NCS)] (**A2**), and [Ru(tctpy)(tfid)(NCS)] (**A3**), and DCA are shown in Figure 1.

2. Experimental Details

2.1. Materials. The following chemicals were purchased and used without further purification: hydrated ruthenium trichloride (from Aldrich), ammonium thiocyanate

(from TCI), 1,1,1-trifluoropentane-2,4-dione (tfpd) (from Aldrich), and LH-20 Sephadex gel (from Sigma). 1,1,1-trifluorodecane-2,4-dione (tfdd) [28], 1,1,1-trifluoroicosane-2,4-dione (tfid) [28] and Ru(H₃tctpy)Cl₃ [11] were synthesized using the literature procedures. Complexes [Ru(tctpy)(tfpd)(NCS)] (**A1**) and [Ru(tctpy)(tfid)(NCS)] (**A3**) were prepared using the literature procedure [15].

*Synthesis of [Ru(tctpy)(tfdd)(NCS)] (**A2**).* Using the same conditions as for complex **A1**, and starting from ligand 1,1,1-trifluorodecane-2,4-dione (tfdd), the title compound was obtained as a dark green powder, [Ru(tctpy)(tfdd)(NCS)] (**A2**). Yield was 60%: MS (ESIMS): m/z : 249.3 (M-3H)³⁻, 374.5 (M-2H)²⁻. ¹H NMR (300 MHz, D₂O-NaOD): δ 8.76 (2H, s), 8.72 (2H, d), 8.52 (H, d), 8.46 (H, d), 7.85 (H, d), 7.78 (H, d), 5.84 (0.5H, s), 5.82 (0.5H, s), 2.53 (2H, m), 1.55–0.80 (8H, m), 0.50 (3H, m), Anal. Calcd for C₂₉H₂₈F₃N₄O₈RuS·(H₂O)₂: C, 44.27; H, 4.10; N, 7.12, found: C, 45.01; H, 4.21; N, 6.88.

2.2. Analytical Measurements. UV-visible spectra were recorded on a Shimadzu UV-3101PC spectrophotometer. Steady-state emission spectra were recorded using a grating monochromator (Triax 1900) with a CCD image sensor. The redox potential of the complexes was measured using a standard three-electrode apparatus.

2.3. Preparation of TiO₂ Electrode and Dye-Loading Measurements. Nanocrystalline TiO₂ photoelectrodes of about 20 μ m thickness (area: 0.25 cm²) were prepared using a variation of a method reported by Nazeeruddin et al. for solar cells measurements [11]. We also prepared transparent TiO₂ film of 7 μ m thicknesses to check the adsorption properties of the complexes on to TiO₂ film using the same method. The dye-loading measurement on TiO₂ films was carried out by desorbing the dye into 0.1 M NaOH, solution in CH₃OH and the dye load on the TiO₂ film was estimated by means of an ultraviolet-visible absorption spectroscopy.

2.4. Fabrication of Dye-Sensitized Solar Cell. Two-electrode sandwich cell configurations were used for photovoltaic measurements. The dye-deposited TiO₂ film was used as the working electrode and a platinum-coated conducting glass as the counter electrode. The two electrodes were separated by a surlyn spacer (40 μ m thick) and sealed up by heating the polymer frame. The electrolyte was composed of 0.6 M dimethylpropyl-imidazolium iodide (DMPII), 0.05 M I₂, and 0.1 M LiI in acetonitrile (AN).

3. Results and Discussion

3.1. Photophysical Properties. The absorption, emission, and electrochemical properties of complexes **A1**, **A2**, and **A3** are summarized in Table 1. All the complexes show similar absorption spectra in ethanol-methanol solution as shown in Figure 2. The bands in the visible region are assigned to metal-to-ligand charge-transfer (MLCT) transitions and in the UV region to ligand π - π^* transitions

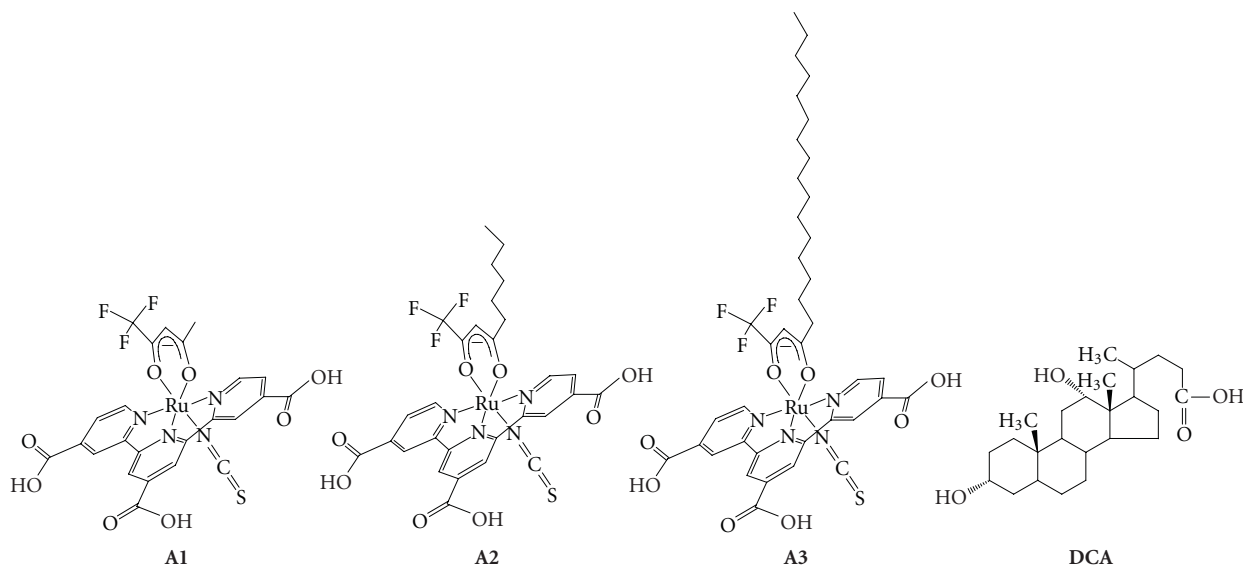
FIGURE 1: Molecular structures of complexes **A1**, **A2**, **A3**, and **DCA**.

TABLE 1: Absorption, luminescence, and electrochemical properties of the ruthenium complexes.

Sensitizer	Absorption, $^a\lambda_{\max}/\text{nm}$ ($\epsilon/10^3 \text{ M}^{-1} \text{ cm}^{-1}$)	Emission $\lambda_{\max}^b/\text{nm}$		Emission τ^b/ns		$E(\text{Ru}^{3+/2+})^c /$ versus SCE	$E^*(\text{Ru}^{3+/2+})^d /$ versus SCE
		298 K	77 K	298 K	77 K		
A1	280 (27.6), 331 (22.7), 422 (14.7), 606 (7.0)	940	905	16	160	+0.68	-0.90
A2	280 (28.2), 331 (23.1), 418 (13.6), 605 (7.1)	945	900	15	214	+0.70	-0.95
A3	280 (30.0), 331 (23.6), 422 (14.7), 606 (7.0)	950	910	16	152	+0.70	-0.95

^a Measured in 4 : 1 v/v ethanol : methanol at room temperature.

^b The emission spectra and emission lifetime were obtained by exciting into the lowest MLCT band in 4 : 1 v/v ethanol : methanol.

^c Half-wave potentials assigned to the $\text{Ru}^{3+/2+}$ couple for ruthenium sensitizers bound to nanocrystalline TiO_2 film, measured in 0.1 M LiClO_4 acetonitrile solution.

^d Calculated from $E^*(\text{Ru}^{3+/2+}) = E(\text{Ru}^{3+/2+}) - E^{0-0}$; E^{0-0} values were estimated from the 5% intensity level of the emission spectra at 77 K.

of 4,4',4''-tricarboxy-2,2':6',2''-terpyridine [29]. The low-energy MLCT band maximum of complex **A1** is observed at 606 nm with the molar extinction coefficient of about $7000 \text{ M}^{-1} \text{ cm}^{-1}$. The emission spectra of complex **A3** in ethanol-methanol mixed solvents at 77 and 298 K are presented in Figure 3. The luminescence data are displayed in Table 1. At 77 K, complexes **A1**, **A2**, and **A3** displayed excited-state lifetimes ranging from 152 to 214 ns. The lifetimes decreased significantly with increasing temperature, to 15-16 ns in fluid solution at 298 K. The very short-lived excited state in fluid solution may be caused by efficient nonradiative decay via low-lying ligand-field excited states [30]. The excited-state lifetime of all the complexes is long enough for the process of electron injection into the conduction band of the TiO_2 electrode to be efficient [31]. To be a suitable sensitizer in DSCs, the band structure of the metal complex should match the energy level of the semiconductor anode and the redox electrolyte or the hole conductor. The electrochemical data of the complexes measured in methanol solution are summarized in Table 1. All the complexes exhibit quasireversible oxidation wave for the $\text{Ru}^{3+/2+}$ couple ranging from +0.68 to +0.70 V versus SCE. The formation of an

MLCT excited state of these complexes formally involves the oxidation of a HOMO having metal t_{2g} orbital character and reduction of a terpyridine-based LUMO.

3.2. Dye Adsorption Behavior. Figure 4 shows the absorption spectra of complexes **A1**, **A2**, and **A3** adsorbed onto a nanocrystalline $7 \mu\text{m}$ thick TiO_2 film. All the complexes show almost similar absorption spectra on TiO_2 film but the absorbance decreases with increasing alkyl chain length of the substituted β -diketonato ligands. We compare the UV-vis absorption spectra for the **A1** dye-loaded TiO_2 films, with and without the addition of DCA during the dye-loading process. When DCA was added in the dye solution, the dye-sensitized TiO_2 film cografed along with DCA and showed a similar absorption spectrum. The absorbance at around 570 nm decreased by 18% compared with that of without DCA. The competition of DCA with the dye for binding to the TiO_2 surface is responsible for the decrease in dye adsorption. The adsorbed amount of dye on the TiO_2 film with and without DCA was listed in Table 2. It was noticed that the amount of dye adsorbed onto the TiO_2 surface was

TABLE 2: Adsorbed amount of dye and cell performance^a of **A1**, **A2**, and **A3** sensitizers with and without DCA.

Sensitizer	DCA (mM)	IPCE _{max}	J_{sc} (mA cm ⁻²)	V_{oc} (V)	FF	η (%)	Dye load ^b (10 ⁻⁸ mol cm ⁻²)
A1	0	67	15.9	0.53	0.63	5.31	11.5
	15	74	18.5	0.56	0.64	6.63	7.6
A2	0	69	17.2	0.57	0.63	6.18	9.4
	15	72	18.1	0.58	0.65	6.82	7.2
A3	0	72	18.0	0.64	0.66	7.60	7.3
	15	70	17.4	0.64	0.67	7.46	6.6

^aConditions: sealed cells; coadsorbate, DCA 0 or 15 mM; photoelectrode, TiO₂ (20 μm thickness and 0.25 cm²); electrolyte, 0.6 M DMPII, 0.1 M LiI, 0.05 I₂ in AN; irradiated light, AM 1.5 solar light (100 mW cm⁻²). J_{sc} : short-circuit photocurrent density; V_{oc} : open-circuit photovoltage; FF: fill factor; η : total power conversion efficiency; IPCE: incident photon-to-current conversion efficiency.

^bSurface concentration of the dye molecules on TiO₂ film.

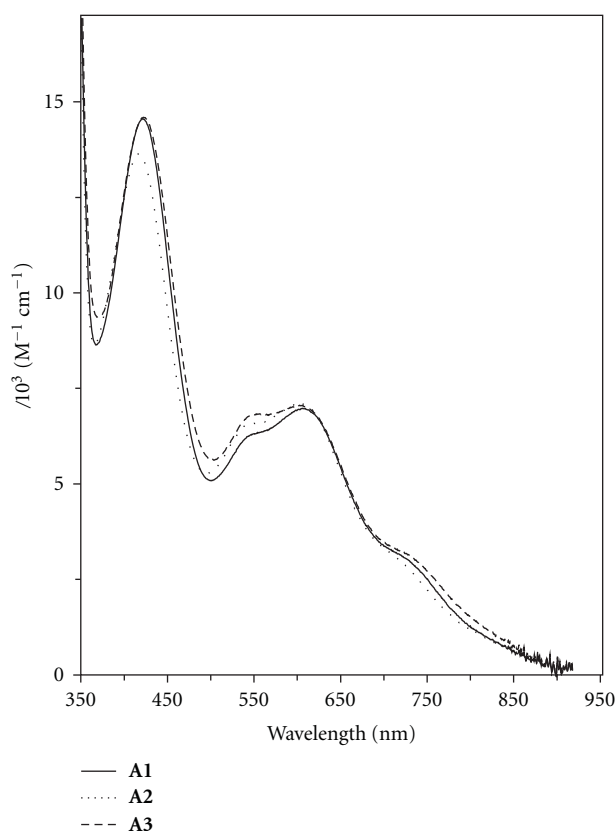


FIGURE 2: UV-vis absorption spectra of complexes **A1**, **A2**, and **A3** in ethanol-methanol (4 : 1) solution.

reduced in the presence of DCA, as compared to that without DCA in the dye bath. For complex **A1**, the difference between the amount of dye adsorbed onto the TiO₂ surface in the presence and absence of DCA in the dye bath is 34%. This is maybe due to the suppression of dye aggregation in the presence of DCA. For complex **A3**, having long alkyl chain length, the amount of dye adsorbed onto the TiO₂ surface in the absence of DCA decreases compared to that of **A1**. There was a small decrease in dye load when DCA was added into the dye bath. The amount of complex **A3** adsorbed onto the TiO₂ surface decreased by only 9% in the presence of DCA,

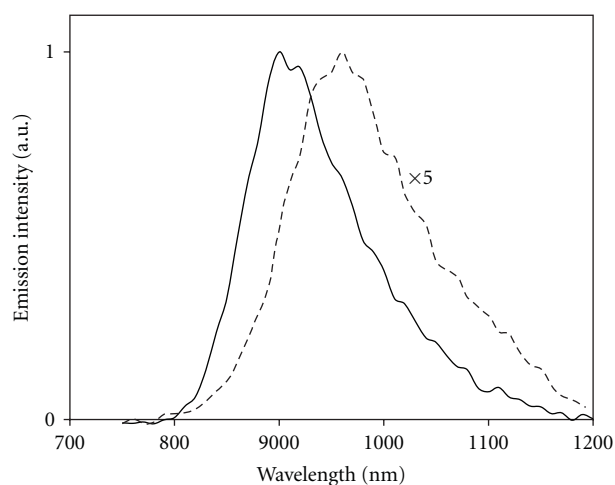


FIGURE 3: Emission spectra of complex **A3** in ethanol-methanol (4 : 1) solution at 77 K (—) and 298 K (---).

whereas the complex **A1** load was reduced about 34%. The long alkyl chain present on complex **A3**, may be suppress the aggregate formation onto the TiO₂ surface and works like DCA. It is suggested that **A3** form an ordered dye layer on TiO₂ surface and binds more strongly to the TiO₂ surface than DCA.

3.3. Photovoltaic Properties. The photovoltaic performance of complexes **A1**, **A2**, and **A3** on nanocrystalline TiO₂ electrode was studied under standard AM 1.5 irradiation (100 mW cm⁻²) using an electrolyte with a composition of 0.6 M dimethylpropyl-imidazolium iodide (DMPII), 0.05 MI₂, and 0.1 M LiI in acetonitrile in the presence and absence of DCA in the dye bath. The short-circuit photocurrent density (J_{sc}), open-circuit voltage (V_{oc}), fill factors (FF), and overall cell efficiencies (η) for each dye-TiO₂ electrode are summarized in Table 2. Figure 5 shows the photocurrent action spectra for complexes **A1** and **A3** in the presence and absence of DCA, where the incident photon to current conversion efficiency (IPCE) values is plotted as a function of wavelength. All complexes achieved efficient sensitization of nanocrystalline TiO₂ over the whole visible

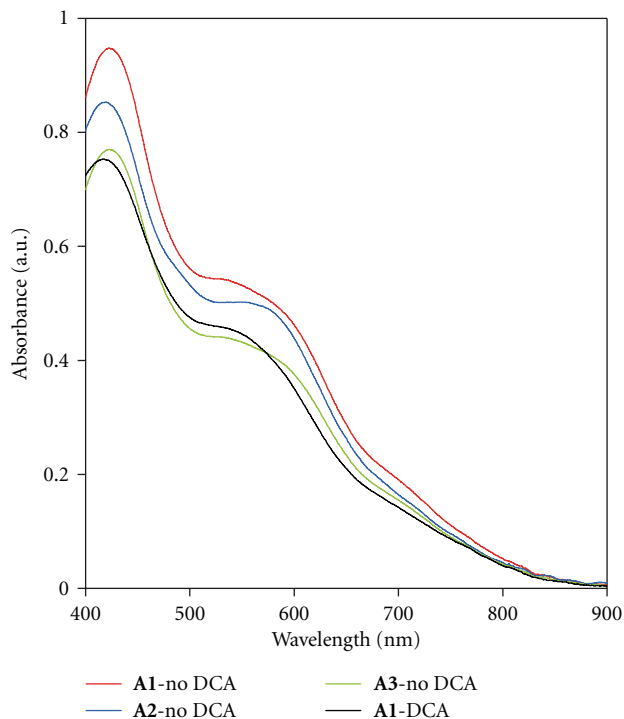


FIGURE 4: Absorption spectra of complexes **A1**, **A2**, and **A3** adsorbed onto a nanocrystalline $7\ \mu\text{m}$ thick TiO_2 film.

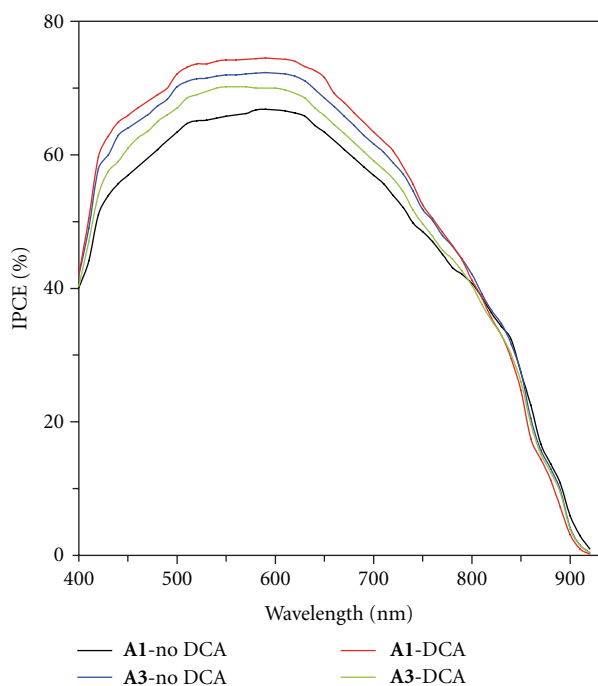


FIGURE 5: Photocurrent action spectra obtained with complexes **A1** and **A3** with and without **DCA** addition during the sensitization process. Incident photon-to-current conversion efficiency is plotted as a function of wavelength. A sandwich type sealed cell configuration was used to measure this spectrum. The electrolyte composition was $0.6\ \text{M DMPII}$, $0.05\ \text{M I}_2$, and $0.1\ \text{M LiI}$ in acetonitrile.

range extending into the near IR region. The maximum IPCE values of complexes **A1**–**A3** are given in Table 2.

As shown in Table 2, a solar cell containing complex **A1** yielded a short-circuit photocurrent density (J_{sc}) of $15.9\ \text{mA cm}^{-2}$, an open-circuit photovoltage (V_{oc}) of $0.53\ \text{V}$, and a fill factor (FF) of 0.63 , corresponding to an overall conversion efficiency (η) of 5.3% in the absence of **DCA**. The addition of **DCA** gave a pronounced efficiency enhancement up to 6.6% with a short-circuit photocurrent density of $18.5\ \text{mA cm}^{-2}$ and an open-circuit photovoltage of $0.56\ \text{V}$. Although the amount of complex **A1** adsorbed on the TiO_2 film decreased to 34% with the addition of **DCA** during the dye-loading process, the values of J_{sc} , V_{oc} , and, thus, the efficiency were increased as compared to the case without **DCA** addition. As shown in Figure 5, complex **A1** shows the IPCE value of 67% in the plateau region in the absence of **DCA**, and the maximum IPCE value increased up to 74% with the addition of **DCA** during the dye-loading process. The observed changes in J_{sc} agreed well with the corresponding IPCE spectra for **A1**-sensitized DSCs with and without the addition of **DCA**. The main possible explanation is that the coadsorption of **DCA** prevents dye aggregation, which can cause intermolecular energy transfer and sequentially result in the excited-state quenching of the dyes [19]. As a result, the reduction of dye load on the TiO_2 surface in the presence of **DCA** consequently results in more efficient electron injection from the excited dyes to the TiO_2 conduction band [19]. A more efficient electron injection thus compensates for the less amount of dye adsorption.

It is interesting to find that **A3**-sensitized DSCs having a long alkyl chain, in the absence of **DCA**, give a high overall conversion efficiency of 7.6% with a short-circuit photocurrent density of $18.0\ \text{mA cm}^{-2}$ and an open-circuit photovoltage of $0.64\ \text{V}$. The photovoltaic performance of **A3**-sensitized DSCs is higher than that of **A3**-sensitized DSCs with the addition of **DCA** during the dye-loading process. This indicates that the photovoltaic performance of bulky alkyl chain substituted sensitizer **A3** was not dependent on additive **DCA**. It is expected that the injection of electron into the TiO_2 conduction band and the recombination of electrons in the TiO_2 film with the oxidized species in the redox electrolyte is unaffected in **A3**-sensitized DSCs with and without **DCA** addition. As shown in Table 2, the amount of adsorbed **A3** on TiO_2 surface with and without **DCA** addition is almost the same and also shows similar photovoltaic performance which suggest a self-assembly property of complex **A3** due to the presence of a bulky alkyl chain substitute in the structure. A self-assembly property of the dye during the sensitization of TiO_2 film is important to obtain efficient surface coverage and efficient electron injection and thus obtain high photovoltaic performance of DSCs [19]. Figure 1 showed that the **A3** sensitizer contains long alkyl chain in the β -diketonato ligand which may produce surface blocking through steric hindrance, preventing the access of electrons to the redox electrolyte, which will be in favor of higher V_{oc} . On the other hand, this bulky alkyl group may not only facilitate the ordered molecular arrangement on the TiO_2 surface but also keep dye molecules at a distance, which may suppress

possibly intermolecular dye interaction, favoring higher J_{sc} [19]. The protection by the alkyl chain is proven to be more efficient as compared to the coadsorption of DCA under the examined conditions. However, the less efficient surface protection in **A1** sensitizer resulted in poor photovoltaic performance. In conclusion, higher power conversion efficiencies were obtained for DSCs based on **A3** with bulky alkyl substituent due to the inherent properties of the dye molecule.

As illustrated in Figure 1, **A2** sensitizer has an alkyl chain length of C_6 on the β -diketonato ligand which is shorter than **A3** sensitizer (C_{16}). Thus, an expected intermediate performance for **A2**-sensitized DSCs was obtained in comparison with **A1** and **A3** under both conditions, with and without the DCA addition. From Table 2, it is clear that the dye load of **A2** dropped by about 23% due to the addition of DCA in the dye bath. However, the value of J_{sc} increased with decreasing dye coverage, probably due to the same reason as mentioned for **A1**.

The **A3** sensitizer having long alkyl chain substituent on the β -diketonato ligand shows the best performance in this series. Thus, this class of diketonato ruthenium complexes serves as a basis for further design of new potential sensitizers by introducing suitable substituents on the diketonato ligand to prevent surface aggregation of the sensitizer for efficient injection efficiencies and furthermore to enhance the molar extinction coefficient of the sensitizer.

4. Conclusions

Three panchromatic photosensitizers **A1**, **A2**, and **A3** based on 4,4',4''-tricarboxy-2,2':6',2''-terpyridine-ruthenium(II) complexes with one β -diketonato chelating ligand containing different bulky alkyl chain lengths between C_1 – C_{16} were developed and systematically characterized using electrochemical and spectroscopic methods. The complexes achieved efficient sensitization of nanocrystalline TiO_2 over the whole visible range extending into the near IR region (ca. 950 nm). These dyes showed gradually enhanced photovoltaic performance with increasing the alkyl chain length. The photovoltaic data of these new complexes show 7.6% power conversion efficiency under standard AM 1.5 irradiation (100 mW cm^{-2}). To understand the effect of the bulky substituent on the photovoltaic performance of DSCs, we investigated the photovoltaic performances of **A1**-, **A2**-, and **A3**-sensitized DSCs with and without DCA addition in the dye bath. We notice that the photovoltaic performance of **A3**-sensitized DSCs containing bulky alkyl chain length of C_{16} was independent of the DCA, while the **A2** bearing alkyl chains length of C_6 and **A1** without alkyl chain showed 10% and 24%, respectively, improvement in photovoltaic performance in the presence of the DCA. Without DCA, **A3**-based DSCs were still superior to both **A1** and **A2** in the presence of DCA. This is probably due to the inherently structural nature of **A3** molecule, functionalized with bulky alkyl chain substituent, which resulted in excellent photovoltaic performance.

References

- [1] B. O'Regan and M. Grätzel, "A low-cost, high-efficiency solar cell based on dye-sensitized colloidal TiO_2 films," *Nature*, vol. 353, no. 6346, pp. 737–740, 1991.
- [2] A. Hagfeldt and M. Grätzel, "Light-induced redox reactions in nanocrystalline systems," *Chemical Reviews*, vol. 95, no. 1, pp. 49–68, 1995.
- [3] A. Hagfeldt and M. Grätzel, "Molecular photovoltaics," *Accounts of Chemical Research*, vol. 33, no. 5, pp. 269–277, 2000.
- [4] M. Grätzel, "Solar energy conversion by dye-sensitized photovoltaic cells," *Inorganic Chemistry*, vol. 44, no. 20, pp. 6841–6851, 2005.
- [5] M. Grätzel, "Conversion of sunlight to electric power by nanocrystalline dye-sensitized solar cells," *Journal of Photochemistry and Photobiology A*, vol. 164, no. 1–3, pp. 3–14, 2004.
- [6] A. Mishra, M. K. R. Fischer, and P. Buerle, "Metal-Free organic dyes for dye-sensitized solar cells: from structure: property relationships to design rules," *Angewandte Chemie*, vol. 48, no. 14, pp. 2474–2499, 2009.
- [7] A. Islam, H. Sugihara, and H. Arakawa, "Molecular design of ruthenium(II) polypyridyl photosensitizers for efficient nanocrystalline TiO_2 solar cells," *Journal of Photochemistry and Photobiology A*, vol. 158, no. 2–3, pp. 131–138, 2003.
- [8] A. Hagfeldt, G. Boschloo, L. Sun, L. Klöö, and H. Pettersson, "Dye-sensitized solar cells," *Chemical Reviews*, vol. 110, no. 11, pp. 6595–6663, 2010.
- [9] T. Funaki, M. Yanagida, N. Onozawa-Komatsuzaki, K. Kasuga, Y. Kawanishi, and H. Sugihara, "Efficient panchromatic sensitization of nanocrystalline TiO_2 -based solar cells using 2-pyridinecarboxylate-substituted Ruthenium(II) complexes," *Chemistry Letters*, vol. 38, no. 1, pp. 62–63, 2009.
- [10] A. Islam, F. A. Chowdhury, Y. Chiba et al., "Synthesis and characterization of new efficient tricarboxyterpyridyl (β -diketonato) ruthenium(II) sensitizers and their applications in dye-sensitized solar cells," *Chemistry of Materials*, vol. 18, no. 22, pp. 5178–5185, 2006.
- [11] M. K. Nazeeruddin, P. Péchy, T. Renouard et al., "Engineering of efficient panchromatic sensitizers for nanocrystalline TiO_2 -based solar cells," *Journal of the American Chemical Society*, vol. 123, no. 8, pp. 1613–1624, 2001.
- [12] A. Islam, F. A. Chowdhury, Y. Chiba et al., "Ruthenium(II) tricarboxyterpyridyl complex with a fluorine-substituted β -diketonato ligand for highly efficient dye-sensitized solar cells," *Chemistry Letters*, vol. 34, no. 3, pp. 344–345, 2005.
- [13] Y. Chiba, A. Islam, Y. Watanabe, R. Komiya, N. Koide, and L. Han, "Dye-sensitized solar cells with conversion efficiency of 11.1%," *Japanese Journal of Applied Physics, Part 2*, vol. 45, no. 24–28, pp. L638–L640, 2006.
- [14] Q. Wang, S. Ito, M. Grätzel et al., "Characteristics of high efficiency dye-sensitized solar cells," *Journal of Physical Chemistry B*, vol. 110, no. 50, pp. 25210–25221, 2006.
- [15] A. Islam, H. Sugihara, M. Yanagida et al., "Efficient panchromatic sensitization of nanocrystalline TiO_2 films by β -diketonato ruthenium polypyridyl complexes," *New Journal of Chemistry*, vol. 26, no. 8, pp. 966–968, 2002.
- [16] S. Gao, A. Islam, Y. Numata, and L. Han, "A β -diketonato ruthenium(II) complex with high molar extinction coefficient for panchromatic sensitization of nanocrystalline TiO_2 film," *Applied Physics Express*, vol. 3, no. 6, Article ID 062301, 2010.

- [17] A. Morandeira, I. López-Duarte, B. O'Regan et al., "Ru(II)-phthalocyanine sensitized solar cells: the influence of coadsorbents upon interfacial electron transfer kinetics," *Journal of Materials Chemistry*, vol. 19, no. 28, pp. 5016–5026, 2009.
- [18] Z. Zhang, N. Evans, S. M. Zakeeruddin, R. Humphry-Baker, and M. Grätzel, "Effects of ω -guanidinoalkyl acids as coadsorbents in dye-sensitized solar cells," *Journal of Physical Chemistry C*, vol. 111, no. 1, pp. 398–403, 2007.
- [19] X. Jiang, T. Marinado, E. Gabrielsson, D. P. Hagberg, L. Sun, and A. Hagfeldt, "Structural Modification of organic dyes for efficient coadsorbent-free dye-sensitized solar cells," *Journal of Physical Chemistry C*, vol. 114, no. 6, pp. 2799–2805, 2010.
- [20] H. Chen, H. Huang, X. Huang et al., "High molar extinction coefficient branchlike organic dyes containing Di(*p*-tolyl)phenylamine donor for dye-sensitized solar cells applications," *Journal of Physical Chemistry C*, vol. 114, no. 7, pp. 3280–3286, 2010.
- [21] X. Ren, Q. Feng, G. Zhou, C. H. Huang, and Z. S. Wang, "Effect of cations in coadsorbate on charge recombination and conduction band edge movement in dye-sensitized solar cells," *Journal of Physical Chemistry C*, vol. 114, no. 15, pp. 7190–7195, 2010.
- [22] T. Marinado, M. Hahlin, X. Jiang et al., "Surface molecular quantification and photoelectrochemical characterization of mixed organic dye and coadsorbent layers on TiO₂ for dye-sensitized solar cells," *Journal of Physical Chemistry C*, vol. 114, no. 27, pp. 11903–11910, 2010.
- [23] J. H. Yum, S. J. Moon, R. Humphry-Baker et al., "Effect of coadsorbent on the photovoltaic performance of squaraine sensitized nanocrystalline solar cells," *Nanotechnology*, vol. 19, no. 42, Article ID 424005, 2008.
- [24] S. Ito, H. Miura, S. Uchida et al., "High-conversion-efficiency organic dye-sensitized solar cells with a novel indoline dye," *Chemical Communications*, no. 41, pp. 5194–5196, 2008.
- [25] C. Kim, H. Choi, S. Kim et al., "Molecular engineering of organic sensitizers containing *p*-phenylene vinylene unit for dye-sensitized solar cells," *Journal of Organic Chemistry*, vol. 73, no. 18, pp. 7072–7079, 2008.
- [26] H. Choi, S. Kim, S. O. Kang et al., "Stepwise cosensitization of nanocrystalline TiO₂ films utilizing Al₂O₃ layers in dye-sensitized solar cells," *Angewandte Chemie*, vol. 47, no. 43, pp. 8259–8263, 2008.
- [27] N. Koumura, Z. S. Wang, S. Mori, M. Miyashita, E. Suzuki, and K. Hara, "Alkyl-functionalized organic dyes for efficient molecular photovoltaics," *Journal of the American Chemical Society*, vol. 128, no. 44, pp. 14256–14257, 2006.
- [28] J. C. Sloop, C. L. Bumgardner, and W. D. Loehle, "Synthesis of fluorinated heterocycles," *Journal of Fluorine Chemistry*, vol. 118, no. 1-2, pp. 135–147, 2002.
- [29] A. Mamo, A. Juris, G. Calogero, and S. Campagna, "Near-infrared luminescence at room temperature of two new osmium(II) terdentate polypyridine complexes," *Chemical Communications*, no. 10, pp. 1225–1226, 1996.
- [30] A. Islam, N. Ikeda, A. Yoshimura, and T. Ohno, "Nonradiative transition of phosphorescent charge-transfer states of ruthenium(II)-to-2,2'-biquinoline and ruthenium(II)-to-2,2':6',2''-terpyridine in the solid state," *Inorganic Chemistry*, vol. 37, no. 12, pp. 3093–3098, 1998.
- [31] Y. Tachibana, S. A. Haque, I. P. Mercer, J. R. Durrant, and D. R. Klug, "Electron injection and recombination in dye sensitized nanocrystalline titanium dioxide films: a comparison of ruthenium bipyridyl and porphyrin sensitizer dyes," *Journal of Physical Chemistry B*, vol. 104, no. 6, pp. 1198–1205, 2000.

Research Article

Metal-Free Counter Electrode for Efficient Dye-Sensitized Solar Cells through High Surface Area and Large Porous Carbon

Pavuluri Srinivasu,¹ Surya Prakash Singh,² Ashraful Islam,^{2,3} and Liyuan Han²

¹International Center for Young Scientists, International Center for Materials Nanoarchitectonics, National Institute for Materials Science, 1-1 Namiki, Tsukuba, Ibaraki 305-0044, Japan

²Advanced Photovoltaics Center, National Institute for Materials Science, 1-2-1 Sengen, Tsukuba, Ibaraki 305-0047, Japan

³Center of Excellence for Research in Engineering, Materials (CEREM), College of Engineering, King Saud University, Riyadh 11421, Saudi Arabia

Correspondence should be addressed to Pavuluri Srinivasu, pavuluri.srini@gmail.com

Received 10 March 2011; Accepted 8 May 2011

Academic Editor: Mohamed Sabry Abdel-Mottaleb

Copyright © 2011 Pavuluri Srinivasu et al. This is an open access article distributed under the Creative Commons Attribution License, which permits unrestricted use, distribution, and reproduction in any medium, provided the original work is properly cited.

Highly efficient, large mesoporous carbon is fabricated as a metal-free counter electrode for dye-sensitized solar cells. The mesoporous carbon shows very high energy conversion efficiency of 7.1% compared with activated carbon. The mesoporous carbon is prepared and characterized by nitrogen adsorption, scanning electron microscopy (SEM), and transmission electron microscopy (TEM). The nitrogen adsorption data reveals that the material possesses BET specific surface area ca.1300 m²/g and pore diameter 4.4 nm. Hexagonal rod-like morphology and ordered pore structure of mesoporous carbon are confirmed by electron microscopy data. The better performance of this carbon material is greatly benefited from its ordered interconnected mesoporous structure and high surface area.

1. Introduction

Global energy demand is likely to increase with the expansion of economy, even though great efforts are made to increase the energy utilization efficiency. In recent years, fuel cells and solar cells have contributed remarkably for the development of renewable energy technologies. Photovoltaic cells such as dye-sensitized solar cells (DSCs) have attracted much attention as an alternative energy source for future requirements [1], which composed of porous nanostructured oxide film with adsorbed dye molecules as a dye-sensitized anode, an electrolyte containing iodide/triiodide redox couple, and a platinized fluorine-doped tin oxide (FTO) glass as the counter electrode [2–4]. DSCs have advantages over traditional Si-solar cells due to low cost, easy fabrication, and high energy conversion efficiency [5, 6]. For additional improvement in energy efficiency and commercialization of DSCs [7, 8], further cost reduction is necessary. Therefore, efforts have been made to lower the production cost of DSCs

by using flexible ITO-coated polyester film, metal foil [9], and organic dyes or metalorganic complex dyes [10]. In DSCs the platinum counter electrode is very crucial towards catalytic reduction of tri-iodine. But the platinum is an expensive metal and takes large portion of fabrication cost of DSCs, which retards commercialization of the process. To reduce to the cost of DSCs process various carbon materials such as carbon black [11], activated carbon [12], carbon nanotubes, porous carbon [13], and graphite [14] have been investigated as counter electrode. However, energy conversion efficiency of reported carbon counter electrode of DSCs is still low. Therefore, further enhancement of efficiency is necessary. Among the other carbon materials, mesoporous carbon materials have received much attention due to their large internal surface area and pore volume, tunable and narrow pore diameter [15, 16]. Templated synthesis method of mesoporous carbon, which is also known as “nanocasting” has been extensively used due to the obtained material possesses uniform and interconnected

pores. This synthetic technique involves impregnation of silica templates with an appropriate carbon source, carbonization of carbon precursor, and subsequent removal of silica. The resulting carbon is inverse replica of ordered mesoporous silica. Herein, ordered high specific surface area and large porous carbon is synthesized using large porous silica as a template and dye-sensitized solar cells properties of synthesized carbon are investigated as a metal-free counter electrode.

2. Experimental

2.1. Preparation of Large Porous Carbon (LPC) Counter Electrode. Ordered mesoporous carbon material referred to as LPC is synthesized by pyrolysis of sucrose inside the large porous silica (LPS) synthesized at 130°C using P123 surfactant. In a typical synthesis of mesoporous carbon, 1 g of LPS is added to a solution obtained by dissolving 0.75 g of sucrose and 5.0 g of water, and keeping the mixture in an oven for 6 h at 100°C. Subsequently, the oven temperature was raised to 160°C for another 6 h. In order to obtain fully polymerized and carbonized sucrose inside the pores of silica template, 0.5 g of sucrose, 0.06 g of H₂SO₄, and 5.0 g of water are again added to the pretreated sample, and the mixture is again subjected to thermal treatment as described above. Carbonization is performed at 900°C for 5 h under N₂-atmosphere. The resulting carbon/silica composite is treated with HF acid (5 wt%) at room temperature to selective removal of silica. The finally obtained mesoporous carbon paste is coated on FTO glass using doctor blade technique [17, 18].

2.2. Fabrication of Dye-Sensitized Solar Cell. A nanocrystalline TiO₂ photoelectrodes of 20 μm thickness (area: 0.25 cm²) were prepared by screen printing on conducting glass as previously described [19]. The films were further treated with 0.05 M TiCl₄ and 0.1 M HCl aqueous solutions before examination [20]. Coating of the TiO₂ film was carried out by immersing for 45 h in a sensitizer solution (N719) of 3 × 10⁻⁴ M acetonitrile/*tert*-butyl alcohol (1/1, *v/v*) solution. Deoxycholic acid (20 mM) was added to the dye solution as a coadsorbent to prevent aggregation of the dye molecules [21, 22]. Photovoltaic measurements were performed in a two-electrode sandwich cell configuration. The dye-deposited TiO₂ film and a large pore mesoporous carbon on conducting glass were used as the working electrode and the counter electrode, respectively. The two electrodes were separated by a surlyn spacer (40 μm thick) and sealed by heating the polymer frame. The electrolyte was composed of 0.6 M dimethylpropyl-imidazolium iodide (DMPII), 0.05 M I₂, TBP 0.5 M, and 0.1 M LiI in acetonitrile.

3. Results and Discussion

The unit cell parameters for the LPC and LPS materials are evaluated from the XRD data, which are summarized in Table 1. The hexagonal unit cell a_0 parameter is calculated using the formula $a_0 = 2d_{100}/\sqrt{3}$. It was observed that the

TABLE 1: Textural parameters of large pore silica and carbon materials.

Sample	a_0/nm	$A_{\text{BET}}/\text{m}^2 \cdot \text{g}^{-1}$	$V_p (\text{cm}^3/\text{g})$	dp, BJH (nm) adsorption
LPC	9.02	1317	1.31	4.4
LPS	10.42	530	1.17	10.3

unit cell constant of these LPC material decreases to 9.02 nm compare with unitcell constant of 10.42 for LPS due to structural pore shrinkage after removal of the template. Nitrogen adsorption-desorption isotherms are measured at 77 K on a Quantachrome Autosorb 1 volumetric adsorption analyzer. Before the adsorption measurements, all samples are out gassed at 250°C in the port of the adsorption analyzer. The position of the maximum on pore size distribution is referred to as the pore diameter, which was calculated from adsorption branches by Barrett-Joyner-Halenda (BJH) method. The nitrogen adsorption-desorption isotherm of LPC along with BJH pore size distribution (inset) is shown in Figure 1(a). The isotherm is of type IV and exhibited a H2 type hysteresis loop. As the relative pressure increases ($P/P_0 > 0.4$), the isotherm exhibits a sharp capillary condensation step of nitrogen within uniform mesopores, where the P/P_0 position of the inflection point is correlated to the diameter of the mesopore. The BET specific surface area was obtained from adsorption branches in the relative pressure range of 0.05–0.20. The total pore volume was estimated from the amount of nitrogen gas adsorbed at a relative pressure of 0.98. The position of the maximum on pore size distribution is referred to as the pore diameter, which was calculated from adsorption branch by Barrett-Joyner-Halenda (BJH) method. The specific surface area amounts to 530 m²/g for LPS and increases to 1317 m²/g for LPC, while the specific pore diameter decreases from 10.3 nm to 4.4 nm for the same samples. The large pore carbon LPC material possesses pore volume 1.31 cm³/g, which is higher than large pore silica LPS material. The specific surface area and specific pore volume are higher for LPC than the LPS template, which facilitates for application in dye-sensitized solar cells. It is interesting to note that structural order is retained even after the removal of the template by acid treatment. The HRTEM images are obtained with JEOL JEM-2100F. Hitachi S-4800 HR-FESEM is used to observe the morphology of the material. SEM image in Figure 1(b) reveals that the LPC has hexagonal rod like morphology, which is similar to the morphology of mesoporous silica. Highly ordered linear array of pore channels and pore structure of LPC was confirmed by high resolution transmission electron microscopy (Figures 1(c) and 1(d)).

Monochromatic incident photon-to-current conversion efficiency (IPCE) for the solar cell, plotted as a function of excitation wavelength, was recorded on a CEP-2000 system (Bunkoh-Keiki Co. Ltd.). IPCE at each incident wavelength was calculated from (1), where I_{sc} is the photocurrent density at short circuit in mA cm⁻² under monochromatic irradiation, q is the elementary charge, λ is the wavelength of

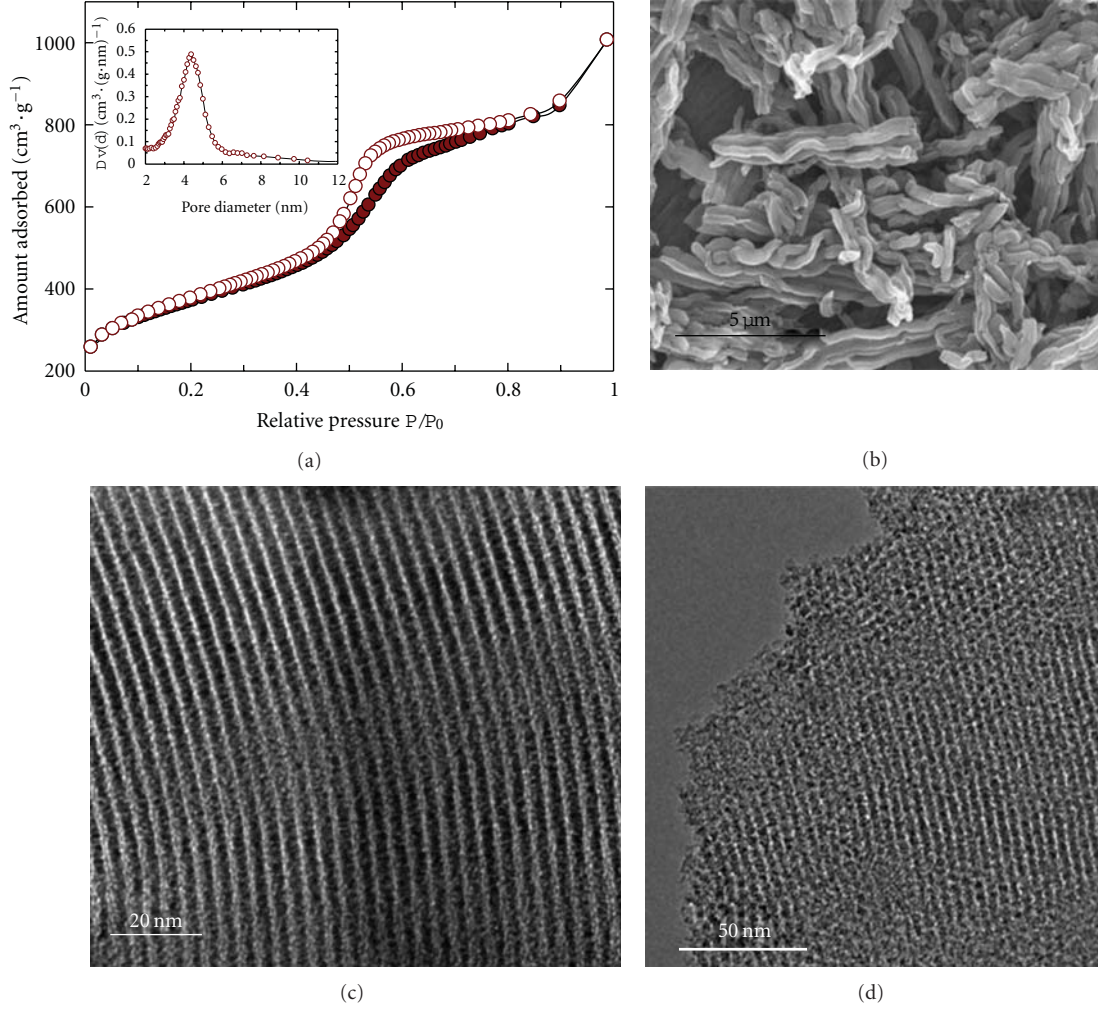


FIGURE 1: (a) Nitrogen adsorption isotherm (\bullet adsorption, \circ desorption) and BJH pore-size distribution (in set) of LPC material. (b) SEM image of LPC material. (c, d) TEM images of LPC.

incident radiation in nm, and P_0 is the incident radiative flux in Wm^{-2}

$$\text{IPCE}(\lambda) = 1240 \left(\frac{I_{\text{sc}}}{q\lambda P_0} \right). \quad (1)$$

The photocurrent density-voltage curves and incident photon-to-current efficiency (IPCE) spectra of the cells are based on N719 dye under the illumination of air mass (AM) 1.5 sunlight (100 mW/cm^2 , WXS-155S-10; Wacom Denso Co. Japan).

Photovoltaic performances of DSCs based on the mesoporous carbon and activated charcoal are shown in Figure 2. The short circuit current (J_{sc}), the open-circuit voltage (V_{oc}), the fill factor (FF), and the overall conversion efficiency (η) are summarized in Table 2. The results indicate that the activated charcoal shows poor performance compare with mesoporous carbon. The LPC counter electrode shows J_{sc} of 12.07 mA/cm^2 , V_{oc} of 0.80 V and FF of 0.66% superior over J_{sc} of 12.07 mA/cm^2 , and V_{oc} of 0.76 V and FF of 0.15% of activated charcoal material. The overall conversion efficiency

TABLE 2: Photovoltaic parameters of DSCs based on mesoporous carbon and activated carbon electrodes.

Sample	$J_{\text{sc}}/\text{mA cm}^{-2}$	V_{oc}/V	FF%	$\eta/\%$
LPC	13.41	0.80	0.66	7.1
AC	12.07	0.76	0.15	1.4

achieved is 7.1% and 1.44% for LPC and AC, respectively. The higher FF and η indicate that LPC is more efficient than AC material.

4. Conclusions

High surface area and large mesoporous carbon LPC with ordered pore structure has been explored as the metal-free counter electrode for DSCs. Nitrogen adsorption isotherm measurement indicates that LPC material shows very high surface area and large pore volume than mesoporous silica LPS material. SEM and TEM analyses confirm that LPC material retain morphology and order pore structure of

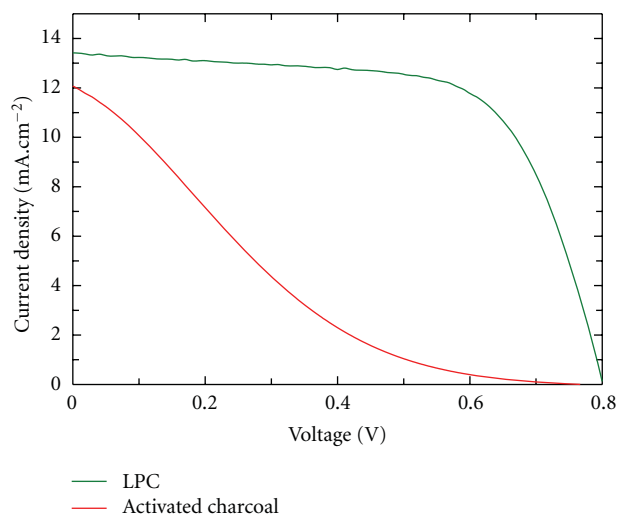


FIGURE 2: Photocurrent-voltage characteristics of dye-sensitized solar cells of LPC and activated charcoal materials.

the template LPS even after acid treatment. Large porous structure of LPC helps for the penetration of electrolyte and high-specific surface area of ca. $1300 \text{ m}^2/\text{g}$, interconnected pore structure facilitate for high energy conversion efficiency than activated charcoal.

Acknowledgments

The author P. Srinivasu thanks the International Center for Young Scientists (ICYS) and International Center for Materials Nanoarchitectonics (MANA) at National Institute for Materials Science, Tsukuba, Japan for financial support.

References

- [1] M. S. Dresselhaus and I. L. Thomas, "Alternative energy technologies," *Nature*, vol. 414, no. 6861, pp. 332–337, 2001.
- [2] M. Grätzel, "Photoelectrochemical cells," *Nature*, vol. 414, no. 6861, pp. 338–344, 2001.
- [3] J. Bisquert, D. Cahen, G. Hodes, S. Rühle, and A. Zaban, "Physical chemical principles of photovoltaic conversion with nanoparticulate, mesoporous dye-sensitized solar cells," *Journal of Physical Chemistry B*, vol. 108, no. 24, pp. 8106–8118, 2004.
- [4] A. B. F. Martinson, T. W. Hamann, M. J. Pellin, and J. T. Hupp, "New architectures for dye-sensitized solar cells," *Chemistry: A European Journal*, vol. 14, no. 15, pp. 4458–4467, 2008.
- [5] M. K. Nazeeruddin, A. Kay, I. Rodicio et al., "Conversion of light to electricity by cis-X2bis(2,2'-bipyridyl-4,4'-dicarboxylate)ruthenium(II) charge-transfer sensitizers (X = Cl⁻, Br⁻, I⁻, CN⁻, and SCN⁻) on nanocrystalline TiO₂ electrodes," *Journal of the American Chemical Society*, vol. 115, no. 14, pp. 6382–6390, 1993.
- [6] Y. Chiba, A. Islam, Y. Watanabe, R. Komiya, N. Koide, and L. Han, "Dye-sensitized solar cells with conversion efficiency of 11.1%," *Japanese Journal of Applied Physics*, vol. 45, no. 24-28, pp. L638–L640, 2006.
- [7] S. Ito, P. Liska, P. Comte et al., "Control of dark current in photoelectrochemical (TiO₂/I⁻-I₃⁻) and dye-sensitized solar cells," *Chemical Communications*, no. 34, pp. 4351–4353, 2005.
- [8] M. A. Green, "Recent developments in photovoltaics," *Solar Energy*, vol. 76, no. 1-3, pp. 3–8, 2004.
- [9] M. Dürr, A. Schmid, M. Obermaier, S. Rosselli, A. Yasuda, and G. Nelles, "Low-temperature fabrication of dye-sensitized solar cells by transfer of composite porous layers," *Nature Materials*, vol. 4, no. 8, pp. 607–611, 2005.
- [10] D. P. Hagberg, T. Edvinsson, T. Marinado, G. Boschloo, A. Hagfeldt, and L. Sun, "A novel organic chromophore for dye-sensitized nanostructured solar cells," *Chemical Communications*, no. 21, pp. 2245–2247, 2006.
- [11] T. N. Murakami, S. Ito, Q. Wang et al., "Highly efficient dye-sensitized solar cells based on carbon black counter electrodes," *Journal of the Electrochemical Society*, vol. 153, no. 12, pp. A2255–A2261, 2006.
- [12] S. R. Jang, R. Vittal, and K. J. Kim, "Incorporation of functionalized single-wall carbon nanotubes in dye-sensitized TiO₂ solar cells," *Langmuir*, vol. 20, no. 22, pp. 9807–9810, 2004.
- [13] G. Wang, L. Wang, and S. Zhu, "Improvement of the photovoltaic performance of dye-sensitized solar cells by using mesoporous carbon in polyvinylidene fluoride/1-methyl-3-hexylimidazolium iodide gel electrolyte," *Advanced Materials Research*, vol. 156-157, pp. 1078–1081, 2011.
- [14] K. Imoto, K. Takahashi, T. Yamaguchi, T. Komura, J. I. Nakamura, and K. Murata, "High-performance carbon counter electrode for dye-sensitized solar cells," *Solar Energy Materials and Solar Cells*, vol. 79, no. 4, pp. 459–469, 2003.
- [15] R. Ryoo, S. H. Joo, M. Kruk, and M. Jaroniec, "Ordered mesoporous carbons," *Advanced Materials*, vol. 13, no. 9, pp. 677–681, 2001.
- [16] S. Jun, S. H. Joo, R. Ryoo et al., "Synthesis of new, nanoporous carbon with hexagonally ordered mesostructure," *Journal of the American Chemical Society*, vol. 122, no. 43, pp. 10712–10713, 2000.
- [17] I. M. Arabatzis, T. Stergiopoulos, M. C. Bernard, D. Labou, S. G. Neophytides, and P. Falaras, "Silver-modified titanium dioxide thin films for efficient photodegradation of methyl orange," *Applied Catalysis B*, vol. 42, no. 2, pp. 187–201, 2003.
- [18] R. E. Mistler, "Tape casting. The basic process for meeting the needs of the electronics industry," *American Ceramic Society Bulletin*, vol. 69, no. 6, pp. 1022–1026, 1990.
- [19] M. K. Nazeeruddin, P. Péchy, T. Renouard et al., "Engineering of efficient panchromatic sensitizers for nanocrystalline TiO₂-based solar cells," *Journal of the American Chemical Society*, vol. 123, no. 8, pp. 1613–1624, 2001.
- [20] Z. S. Wang, T. Yamaguchi, H. Sugihara, and H. Arakawa, "Significant efficiency improvement of the black dye-sensitized solar cell through protonation of TiO₂ films," *Langmuir*, vol. 21, no. 10, pp. 4272–4276, 2005.
- [21] M. Ikeda, N. Koide, L. Han, A. Sasahara, and H. Onishi, "Scanning tunneling microscopy study of black dye and deoxycholic acid adsorbed on a rutile TiO₂(110)," *Langmuir*, vol. 24, no. 15, pp. 8056–8060, 2008.
- [22] Z.-S. Wang, Y. Cui, Y. Dan-oh, C. Kasada, A. Shinpo, and K. Hara, "Thiophene-functionalized coumarin dye for efficient dye-sensitized solar cells: electron lifetime improved by coadsorption of deoxycholic acid," *Journal of Physical Chemistry C*, vol. 111, no. 19, pp. 7224–7230, 2007.

Research Article

Conversion of Dagang Vacuum Residue into Oxygen-Containing Organic Compounds by Photo-Oxidation with H₂O₂ over TiO₂

Heng-Shen Xie,^{1,2} Zhi-Min Zong,¹ Qing Wei,¹ Tong Liu,¹ Jian-Jun Zhao,¹ Pei-Zhi Zhao,¹ Shi-Hua Zhang,¹ and Xian-Yong Wei^{1,3}

¹Key Laboratory of Coal Processing and Efficient Utilization (Ministry of Education),
China University of Mining and Technology, Xuzhou, Jiangsu 221008, China

²Division of Science & Technology, Xuzhou Institute of Architectural Technology, Xuzhou, Jiangsu 221116, China

³Hubei Coal Conversion and New Carbon Materials Key Laboratory, Wuhan University of Science and Technology,
Wuhan, Hubei 430081, China

Correspondence should be addressed to Xian-Yong Wei, wei_xianyong@163.com

Received 26 October 2010; Revised 19 January 2011; Accepted 21 April 2011

Academic Editor: J. Anthony Byrne

Copyright © 2011 Heng-Shen Xie et al. This is an open access article distributed under the Creative Commons Attribution License, which permits unrestricted use, distribution, and reproduction in any medium, provided the original work is properly cited.

The photocatalytic depolymerization of Dagang vacuum residue (DVR) was carried out with H₂O₂ over TiO₂ in a photochemical reactor. Most of the organic matter in DVR was converted into oxygen-containing organic compounds. The yields of carboxylic acids, oxalates, epoxy compounds, and hydroxyl compounds from DVR oxidation are 40.6%, 36.4%, 17.86%, and 13.5%, respectively. In addition, the oxidation causes significant decrease in viscosity and chromaticity of DVR. The related reaction mechanisms are discussed according to the experimental results.

1. Introduction

Heavy oil becomes more and more important with rapid reduction of light oil and drastic increase of liquid fuels [1–5]. As typical heavy oil in China, Dagang vacuum residue (DVR) has high viscosity and chromaticity [6].

Photo-catalytic oxidation (PCO) has been widely applied to many aspects such as solar energy transformation, environmental protection and the syntheses of coating, cosmetic and printing ink, food-packaging materials, gas sensors and functional ceramics [7–15]. Almost all the organic matter (OM) in aqueous solution can be converted into carbon dioxide and water by PCO; hydroxyl oxidation and electron-hole pair oxidation are principal processes in the course of oxidation [16–18]. However, selective PCO of heavy oil in organic solvent has not been reported to our knowledge. In the present study, we found that OM in DVR can be converted into oxygen-containing organic compounds (OCOCs), which can be used as industrial raw materials for the synthesis of dyes and medicines. Particularly, dialkyl oxalates in the OCOCs are reactive intermediates for preparing chemical cold light source [19–22].

2. Experimental Section

2.1. Samples and Reagents. DVR, the residue of crude oil vacuum distilled later and collected from Dagang Oil Field, Tianjin Municipality, China, was preserved in sealed condition. Table 1 shows the elementary properties and ultimate analysis of DVR. Cyclohexane, acetone, and hydrogen peroxide (30% wt) are commercial purchased analytical reagents, and all organic solvents used in the experiment were distilled prior to use. Titanium dioxide as photocatalyst was prepared by Sol-Gel method and characterized by ultraviolet visible (UV-VIS), X-ray diffraction (XRD), and transmission electron microscopy (TEM) (as shown in Figures SI-1, 2, 3, and 4 and Table SI-1, see Supplementary Materials available at doi:10.1155/2011/869589), implying the homemade powders are anatase nanometer particles, and its particle radius is no more than 20 nm, and its properties are similar to the commercial reagent P-25 [23].

2.2. Instruments and Equipment. The SGY-1 multifunctions photochemistry reactor with the function of rotating and with 500 W low-pressure mercury lamp as light source, which can emit around 85% ultraviolet light with wavelength

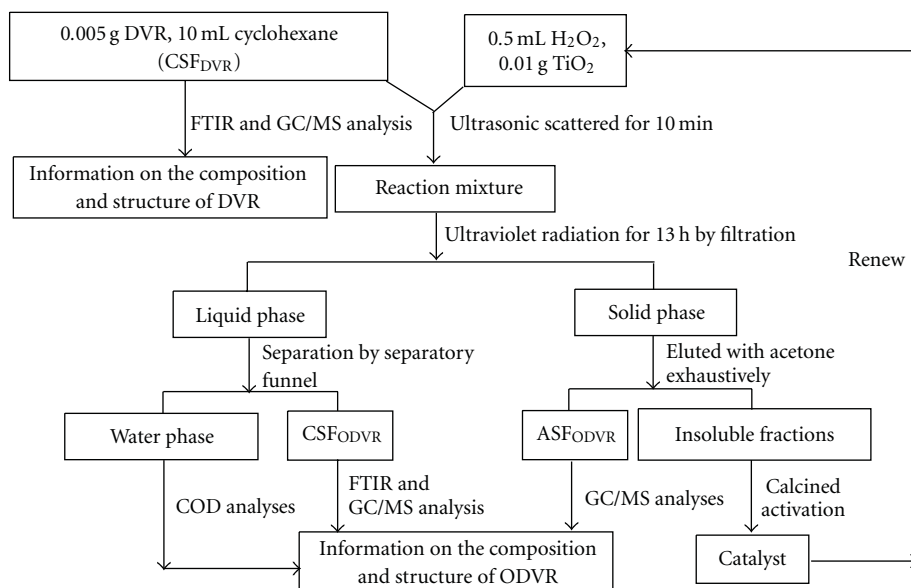


FIGURE 1: Procedure for DVR oxidation, subsequent treatment, and products analysis.

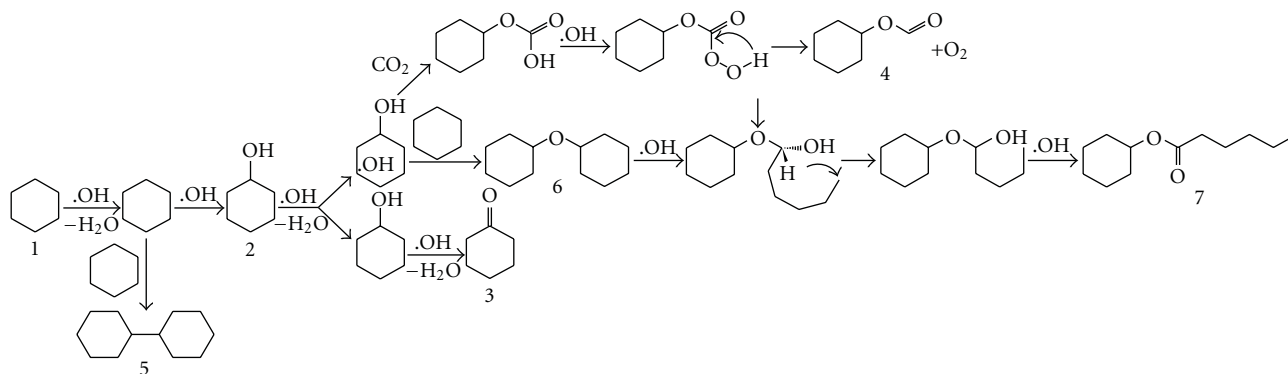
of 365 nm (its energy distribution as shown in Table SI-8), was made in Nanjing Sidongke Electric Equipment Co. of China. The reactor was used to study the quantum yield of photochemistry reaction, especially the synthesis of new materials or the degradation of organic contaminations (as Figure SI-7). The instruments for analyses of products are a Nicolet Magna IR-560 Fourier transform infrared (FTIR) and a Hewlett-Packard 6890/5973 gas chromatography/mass spectrometer (GC/MS) equipped with a capillary column coated with HP-5 (cross-link 5% PH ME siloxane, 30 m × 0.25 mm i.d., 0.25 μm film thickness) and a quadrupole analyzer and operated in electron impact (70 eV) mode.

2.3. Photochemical Treatment and Analyses Method. As shown in Figure 1, 0.005 g of DVR was dissolved in 10 mL cyclohexane and mixed with TiO₂ (amount of 0.01 g) and H₂O₂ (ca. 0.5 mL). The mixtures were dispersed under ultrasonic for 10 min and illuminated with 500 watt low-pressure ultraviolet mercury lamp for 13 hours in electromagnetic stirring. Then the reaction mixture was filtered and separated and eluted with cyclohexane and acetone, respectively. The cyclohexane-soluble fraction (CSF_{ODVR}) and the acetone-soluble fraction (ASF_{ODVR}) were analyzed with GC-MS or FTIR. The residue was calcined to obtain the service life of catalyst. The chemical oxygen demand (COD) of the aqueous soluble was determined using titration with potassium dichromate. In addition to the model compounds such as liquid paraffin, decahydronaphthene and tetrahydronaphthalene were oxidized by UV light to analyze the depolymerization mechanism of DVR photo-catalytic oxidation under the same condition. The reaction results of model compounds were shown in Tables SI 3, 4 and 5. And the reaction results of DVR were also discussed with FTIR analyses.

3. Results and Discussion

3.1. Analysis of Cyclohexane Photo-Oxidation. Different solvents have different polarity and stability, especially when they are illuminated by UV light. DVR mainly consists of low-polarity alkyl saturated hydrocarbon. Hence, cyclohexane with lower polarity and stability to UV light is selected as solvent in PCO according to similar dissolve mutually theory. Of course, the products from the PCO of cyclohexane may have effect on the analysis result of ODVR. So in order to eliminate the interference, the cyclohexane was oxidized alone by photo-catalytic oxidation and with GC/MS analyses. The result is exhibited in Figure 2, the oxidation products are listed in Table SI-2. As shown Figure 2, in total six products were identified, including cyclohexanol, cyclohexanone, cyclohexyl formate, cyclohexylcyclohexane, (cyclohexyloxy)cyclohexane, and cyclohexyl hexanoate. Among the oxidation products the relative contents of compound 6 ((cyclohexyloxy)cyclohexane) and compound 2 (cyclohexanol) are higher and account for 14.30% and 5.76%, respectively. However, no 1-cyclohexylcyclohex-1-ene, cyclohexene, and cyclohexylidene-cyclohexane were detected, implying active hydrogens in cyclohexane ring can be substituted partly by hydroxyl radicals to form cyclohexane derivatives, but the derivatives are difficult to eliminate and to form the products of cyclohexane ring opening or unsaturated compounds. The mechanism of product formation is represented in Scheme 1. Where the solvent is not oxidized under the mild conditions, present selection of solvent is more appropriate.

3.2. Effect of TiO₂ on DVR Oxidation by FTIR Analysis. As shown in Figure 3, no absorbance at 3480 cm⁻¹ was observed in E_I (the system of DVR cyclohexane solution) and E_{II} (the system of DVR cyclohexane solution oxidized with



SCHEME 1: Mechanism for the degradation of cyclohexane in PCO.

TABLE 1: Property and ultimate analyses of DVR.

DVR property				Elemental composition (wt%, daf)				
RC (%)	<i>D</i> (g cm ⁻³)	<i>V</i> (mPas)	MM	C	H	N	S	O*
17.02	0.9796	2074	1008	85.91	11.43	0.61	0.24	1.81

RC: residual carbon; *D*: density; *V*: viscosity; MM: molecular mass; *by difference.

TABLE 2: Alkenes detected in the products from CSF_{DVR} and ASF_{ODVR}.

Peak	Alkene	Detected in	
		CSF _{DVR}	ASF _{ODVR}
54	(E)-icos-7-ene	2.2	
68	Octadec-1-ene		1.0
71	Docos-1-ene		0.2
76	(E)-octadec-7-ene	1.2	
86	(E)-heneicos-10-ene		0.7
93	Nonadec-1-ene	3.8	0.5
104	Squalene	8.0	

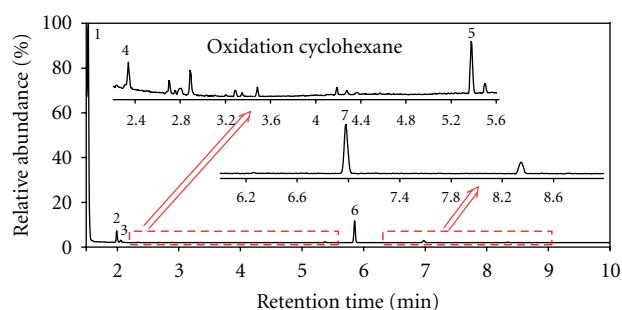


FIGURE 2: Total ion chromatograms of oxidation cyclohexane.

H₂O₂), but a broad absorption band in E_{III} (the system of DVR cyclohexane soluble oxidized with H₂O₂ over TiO₂), which suggests that the concentration of hydroxyls produced by the synergistic effect of TiO₂ and H₂O₂ is higher. The absorbance at 1730 cm⁻¹ is found in E_{II}, and E_{III} and the peak is stronger in E_{III} than in E_{II}, indicating C=O as a functional group in oxidation products, and the oxidation effect is obvious in E_{III}. This shows that oxidation of DVR

requires both TiO₂ and peroxide for successful oxidation. Peaks at 3480 cm⁻¹, 2930 cm⁻¹, 2860 cm⁻¹, 1370 cm⁻¹, and 1460 cm⁻¹ are very strong, only with different strength, suggesting that -CH₃ and =CH₂ exist in CSF_{DVR}, CSF_{ODVR}, and ASF_{ODVR} and with different contents. It proved the formation of -OH, and the existence of hydroxyl oxidation was included in E_{II} and in E_{III}. As far as two systems, the absorbances at 1730 cm⁻¹ were attributed to the carbonyl compounds, but the intensity in E_{III} is stronger than in E_{II}, indicating higher concentration of carbonyl groups and the oxidation effect of DVR more obviously. The absorbance at 2380, 2330 cm⁻¹ in cyclohexane and E_I, but not in E_{II}, was found, illustrating that C=C has been converted into saturation hydrocarbon or other OOCs. Hence, most of OMs in DVR have been converted into high-polarity compounds. Especially, the conversion in E_{III} is the most effective because of the synergistic effect. The conclusion also depends on GC/MS analyses and verification.

3.3. GC/MS Analysis of DVR and Oxidation Products. The compounds detected in CSF_{DVR}, CSF_{ODVR}, and ASF_{ODVR} were listed in Tables 2–11 and Tables SI-3 and 4. The total ion chromatograms (TICs) were presented in Figures SI-5 and 6. 27 species compounds in CSF_{DVR}, 21 species compounds in CSF_{ODVR}, and 73 species compounds in ASF_{ODVR} were detected. Their parent compounds can be classified normal alkanes (NAs), branched-chain alkanes (BAs), esters, carbonyl acids, alkenes, arenes, ketones, alcohols, phenols and epoxy compounds (ECs). Compounds 99, 51, and 5 are the most abundant in CSF_{DVR}, CSF_{ODVR}, and ASF_{ODVR}, respectively; they are dotriacontane, allyl tetradecyl oxalate, and 4-oxopentanoic acid, in sequence accounting for 10.02%, 13.47%, and 25.14%. As shown in Figures SI-5 and 6 and Tables 2–10, OMs in CSF_{DVR} were converted into polar OOCs in CSF_{ODVR} or in ASF_{ODVR} via PCO.

TABLE 3: Monobasic acid esters detected in the products from ASF_{ODVR}.

Peak	Monobasic acid ester	Detected in
14	Dihydro-4-hydroxyfuran-2(3H)-one	2.1
17	Dihydro-5-(hydroxymethyl)furan-2(3H)-one	1.2
19	2-hydroxycyclohexyl acetate	0.7
24	4-hydroxycyclohexyl acetate	0.6
31	(3Z,11Z)-octadeca-3,11-dienyl acetate	0.3
35	4-methylpentyl pentanoate	5.2
36	Octan-4-yl hexanoate	2.0
38	5,6-dihydro-4-(2-methylprop-1-enyl)pyran-2-one	0.2
48	Sec-butyl phenyl carbonate	0.1
72	Heptadecyl 2,2,2-trifluoroacetate	0.4
79	Etradec-13-enyl acetate	0.2

TABLE 4: Dialkyl alkanedioates in the products from CSF_{ODVR} and ASF_{ODVR}.

Peak	Dialkyl alkanedioate	Detected in	
		CSF _{ODVR}	ASF _{ODVR}
22	Trans-cyclohexane-1,4-diyl-diacetate		0.4
49	Dodecyl isobutyl oxalate	7.2	
51	Allyl tetradecyl oxalate	13.5	
58	Cyclobutyl octadecyl oxalate	4.7	
63	Dicyclohexyl malonate		1.0
73	Cyclobutyl pentadecyl oxalate	3.7	
77	Isobutyl pentadecyl oxalate	5.7	
84	Hexadecyl isobutyl oxalate	5.8	

As listed in Table SI-3, in total 18 NAs (C₁₄–C₃₆) were affirmed in CSF_{DVR}, CSF_{ODVR}, and ASF_{ODVR}. As Figures SI-5 and 6 show the TICs spectra of CSF_{DVR}, CSF_{ODVR}, and ASF_{ODVR}, 16 NAs were identified in CSF_{DVR}, accounting for 65.67%, indicating DVR mainly composed of NAs. It is considered that it is difficult for NAs to oxidize in mild condition, but the RC of NAs in CSF_{ODVR} and ASF_{ODVR} was reduced dramatically. Only 8 NAs in CSF_{ODVR} and 5 NAs in ASF_{ODVR} were detected, accounting for 41.55% and 2.1%, respectively. So we assumed that the NAs have been converted into other OOCs in the experiment. Through the photo-catalytic oxidation degradation of model compounds, liquid paraffin indicates that NAs can be converted into OOCs including alcohols and α -unsaturated chain hydrocarbons.

As shown in Tables SI-4 and 5 BAs, accounting for 12.22%, were detected in CSF_{DVR}. After PCO about a quarter BAs were reduced in CSF_{ODVR} in relative to in CSF_{DVR}, less than 2% BAs was detected in ASF_{ODVR}. These data indicate that BAs participated in the reaction of photo-oxidation. BAs with large amounts of active hydrogen were subject to

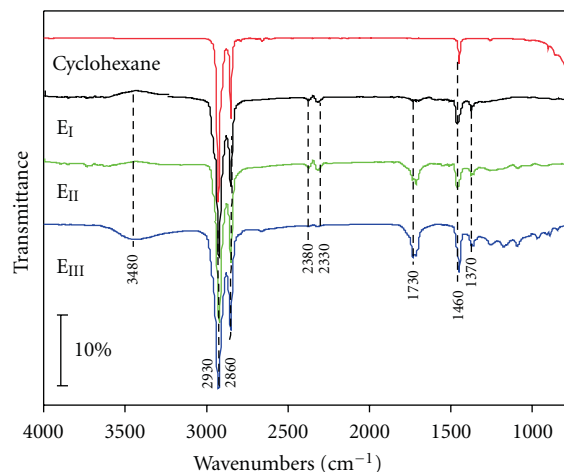


FIGURE 3: FTIR spectra of cyclohexane and DVR oxidized before and later.

substituting by hydroxyl free radicals formation hydroxyl compounds (HCs) or eliminating dehydration by electron-hole pairs in the process of PCO. It is obvious that part BAs may be formed in the course of PCO degradation, so BAs can be detected in CSF_{ODVR} and ASF_{ODVR} though they are easy to be degraded.

As shown in Table 2, alkenes is a vital component in CSF_{DVR}, only 4 alkenes, accounting for 15.19%, were detected. The RC of alkenes in ASF_{ODVR} was 2.4% though 4 alkenes were determined, while no alkenes were observed in CSF_{ODVR}. The analysis result of GC/MS indicate that these alkenes with high-polarity in contrast to cyclohexane are unstable under UV light irradiation, they participate in photo-oxidation degradation reaction by two processes of the oxidation of hydroxyl radicals and Michael' addition reaction.

As shown in Tables 3–5, in total 23 esters were determined in CSF_{ODVR} and ASF_{ODVR} and no OEs was detected in CSF_{DVR}, suggesting that OEs are the main oxidation products. In them, 6 OEs (including dodecyl isobutyl oxalate, allyl tetradecyl oxalate, cyclobutyl octadecyl oxalate, cyclobutyl pentadecyl oxalate, isobutyl pentadecyl oxalate, and hexadecyl isobutyl oxalate) were identified in CSF_{ODVR}, and the total RC is 40.55%, indicating the formation of oxalate functional groups in PCO (as shown in Figure 4, the mass spectra of the oxalic esters). In addition, 16.34% of 17 OEs were also detected in ASF_{ODVR}, indicating that heavy oil has been converted successfully by PCO. Because of the existence of carbonyl acids (CAs) and alcohols as shown in Tables 8 and 9, OEs are possibly generated through the esterification of acids and alcohols. It is unlikely generation from the openingring of ACs' hydroxylation derivatives because the photo-catalytic oxidation degradation of model compounds did not discover the open-loop product (as shown in Tables SI-5 and 6 PCOs of decahydronaphthene and tetrahydronaphthalene). And the formation of OEs proved that DVR can be converted into OOCs successfully through several methods. OEs, as terminal OOCs, are easy to isolate from nonpolar materials, so they are important

TABLE 5: Dialkyl phthalates detected in the products from ASF_{ODVR}.

Peak	Dialkyl phthalate	Detected in	Peak	Dialkyl phthalate	Detected in
52	Diethyl phthalate	0.5	74	Butyl octyl phthalate	0.4
57	Diisobutyl phthalate	0.9	91	Bis(6-methylheptyl)phthalate	0.1

TABLE 6: Acids detected in the products from ASF_{ODVR}.

Peak	Acid	Detected in	Peak	Acid	Detected in
2	Hexanoic acid	0.4	33	Oxepane-2,7-dione	3.7
5	4-oxopentanoic acid	25.1	40	Dodecanoic acid	0.2
12	5-oxohexanoic acid	1.6	45	Tridecanoic acid	0.3
13	3-(ethoxycarbonyl)propanoic acid	0.8	47	Tetradecanoic acid	0.4
15	1,3-dioxol-2-one	0.4	56	Pentadecanoic acid	0.3
23	Succinic acid	0.1	64	n-hexadecanoic acid	0.3
27	Glutaric acid	3.0	65	Palmitic acid	0.3

TABLE 7: Alcohols detected in the products from CSF_{DVR}, CSF_{ODVR} and ASF_{ODVR}.

Peak	Alcohol	Detected in		
		CSF _{DVR}	CSF _{ODVR}	ASF _{ODVR}
6	(1R,2R)-cyclohexane-1,2-diol			2.9
11	2,2-dimethyloctan-3-ol			5.9
16	4-methylheptan-3-ol			1.0
29	2,5-dimethylhex-4-en-3-ol			0.2
30	Tridecan-7-ol			0.4
39	2-octadecylpropane-1,3-diol		0.7	
60	Hexadecane-1,2-diol			0.2
62	2-methyl-5,5-diphenylpenta-3,4-dien-2-ol			0.3
90	2-(octadecyloxy)ethanol	2.0	1.9	

TABLE 8: Phenols detected in the products from ASF_{ODVR}.

Peak	Phenol	Detected in
3	Phenol	0.1
88	2,4-bis(2-phenylpropan-2-yl)phenol	1.4

industrial raw materials. Among them, oxalates always are considered as a main intermediate to make the cold light illuminator or other military supplies. Hence, the conversion of compounds in PCO provides an effective approach to make the DVR utilization effective.

As listed in Table 6, CAs are one of the OOCs and merely detected in ASF_{ODVR}, suggesting that CAs as final products are strongly polarity matters. As Figure 5 has shown that the RC of CAs is 36.4%, and compound 5 (shown in Figure SI-6 and in Figure 5) is the most abundant account for 25.58% in ASF_{ODVR}. OKs and ACs were also detected only in ASF_{ODVR}, as shown in Tables 9 and 10, and the RC of them is 8.79% and 1.13%, respectively, indicating that carbonyl compounds have been formed in the reaction, and the primary products can react continuously with each other through the addition reaction cyclopolymerization. From the upper analysis result, we suppose that the solvent participated in the reaction but without the formation of ring opening components. The

formation of compounds containing cyclohexane provided a proof that the active hydrogens were attacked by hydroxyls and obtained the production of cyclohexyl free radicals.

As illustrated in Tables 7 and 8, in total 10 HCs (including alcohols and phenols) were detected, among them, one HC in CSF_{DVR}, 2 HCs in CSF_{ODVR} and 7 HCs in ASF_{ODVR}. In ASF_{ODVR} 2,2-dimethyloctan-3-ol (compound 11 in Figure SI-6) is the most abundant, accounting for ~5.94% of OMs, while ~1.86% of OMs in CSF_{ODVR}. The formation of (1R,2R)-cyclohexane-1,2-diol suggests that OMs in DVR can be oxidized by hydroxyl substitution besides cyclohexane. These facts indicate that hydroxyl oxidation is a main step in photo-oxidation process. It must be considered as the mechanism causing the ring-opening reaction of cyclohexane, but the products of ring opening were almost not detected in the products of pure cyclohexane oxidation, so it is sure that active hydrogen in DVR has been substituted by hydroxyl free radicals and led to the formation of these HCs. The RC of HCs in CSF_{ODVR} is less than that in ASF_{ODVR}, indicating the HCs with high polar. In addition, one HC exists in CSF_{DVR}, and it is unsteady and easy to depolymerization.

As listed in Table 11, in total 11 ECs were detected 2-((dodecyloxy)methyl)oxirane appeared both in CSF_{DVR} and CSF_{ODVR} simultaneously, whereas 10 ECs were detected in

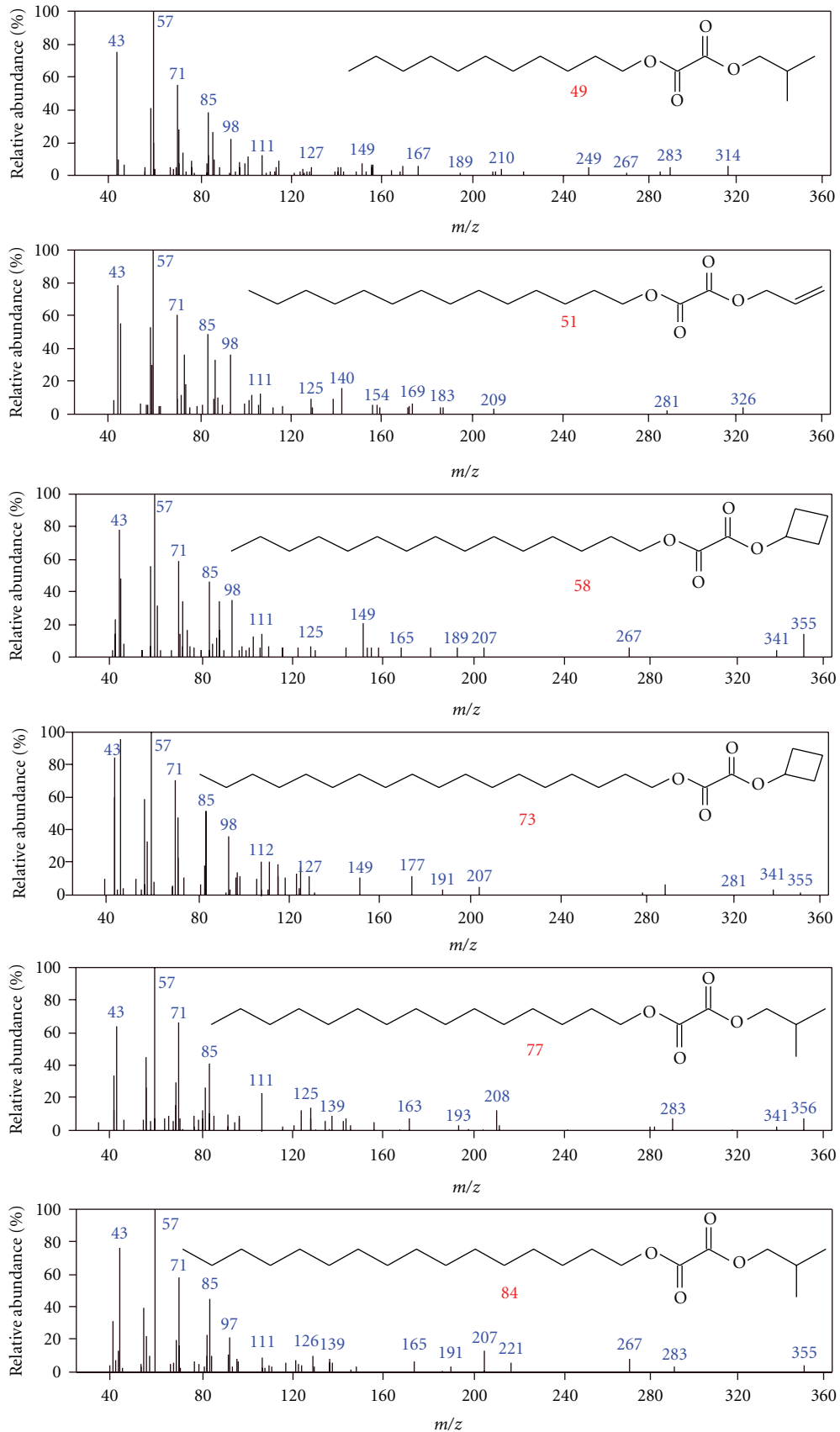
FIGURE 4: Mass spectra of the dialkyl oxalates detected in CSF_{ODVR}.

TABLE 9: Ketones detected in the products from ASF_{ODVR}.

Peak	Ketone	Detected in	Peak	Ketone	Detected in
1	Cyclohex-2-enone	0.6	32	3-hydroxycyclohexanone	7.2
8	Cyclohexane-1,4-dione	0.3	38	5,6-dihydro-4-(2-methylprop-1-enyl)pyran-2-one	0.2
10	4-hydroxycyclohexanone	0.3	75	Anthracene-9,10-dione	0.6

TABLE 10: ACs detected in the products from ASF_{ODVR}.

Peak	AC	Detected in	Peak	AC	Detected in
9	(4as,8as)-decahydronaphthalene	0.7	55	Phenanthrene	0.1
53	Anthracene	0.2	81	9,10-dichloroanthracene	0.1

TABLE 11: ECs detected in the products from CSF_{DVR}, CSF_{ODVR} and ASF_{ODVR}.

Peak	Epoxy compound	Detected in		
		CSF _{DVR}	CSF _{ODVR}	ASF _{ODVR}
4	dihydrofuran-2,5-dione			6.7
7	2-propylfuran			0.4
18	3,4-dimethylfuran-2,5-dione			0.3
21	4,5-dimethyl-2-pentadecyl-1,3-dioxolane			0.4
25	tetrahydro-3-methyl-5-oxofuran-2-carboxylic			5.8
26	isobenzofuran-1,3-dione			1.5
28	tetrahydro-5-oxofuran-2-carboxylic acid			0.5
34	5-heptyl-dihydrofuran-2(3H)-one			1.4
46	dihydro-5-(hydroxymethyl)furan-2(3H)-one			0.5
87	3-(tetrahydro-5-oxofuran-2-yl)propanoic			0.3
97	2-((dodecyloxy)methyl)oxirane	4.9	6.3	

ASF_{ODVR} and most of them are rich with pentaheterocycles (such as furan, lactone, and acid anhydrides). The reason is that the electron pair in hydroxyl oxygen atoms attacked the active hydrogen in the same link and formed a ring and then formed the stable structure in organic molecular on account of losing the proton. This is the electrophilic substitution reaction. Furthermore, the relative content of penta-heterocycles is the highest (account for 17.82%) mainly because of the small ring strain and the stable ring structure [24].

3.4. Mass Spectra Analyses of Oxalate in CSF_{ODVR}. As exhibited in Figure 4, six oxalates in CSF_{ODVR} were identified with large number of RC. These compounds in peaks 49, 51, 58, 73, 77, and 84 (as shown in Figure SI-5) seem to be oxalate containing because of the fragments at m/z 207. The molecular ions M⁺ at m/z 356 are compounds 73 and 77, and compound 49 is at m/z 314 and compound 51 is at m/z 326, but the molecular ions of the compounds 58 and 84 disappear. If the peak at m/z 207 was considered as column loss or other impurity peaks, the mass spectra shape of oxalates should be similar to that of NAs. However, the oxalates were determined with GC/MS analyses and acquired processes using Chemstation software with NIST05 library data. In addition, the structure of compounds 58 and 73 is cis-, but the structures of compounds 49, 51, 77, and 84 are trans-, indicating the cis-formation of oxalates

with cyclobutane as branched-chain more stable than the corresponding trans-forms. However, the transformation of oxalates with branched chain alkanes or unsaturated is more stable than the corresponding trans-forms. The possible reason is that the substitutions meet with different steric hindrance. The stereohindrance effect of cyclobutane and the repulsion force between a pair of electrons cause the carbon-carbon bond formation in oxalate rotation.

3.5. Mechanics of Photo-Oxidation Degrading DVR. As shown in Figure 5, five species OMs in CSF_{DVR} were converted into five species of OMs in CSF_{ODVR} and nine species of OMs in ASF_{ODVR}, presenting the diversified products formed. Key steps of the products transformation are as follows. Firstly, the active hydrogen from methyl or methylene in NAs, BAs or branched-chain aromatics could be substituted by the hydroxyls generated on the surface of TiO₂ with H₂O₂ in the process priority, and lead to form HCs. Some HCs eliminate water molecular to form UCs, and UCs in ASF_{ODVR} product easily undergo Michael addition reaction and generate lactone rings or cyclic ethers (such as furan or acid anhydrides). In addition, some HCs or UCs can also be converted into OKs or CAs and other OEs by hydroxyl radicals attack. The facts proved that alkanes, not only BAs or ACs with branched chain, can be oxidized in the processes. Secondly, the biomarkers through bond breaking, ring opening, and small molecules eliminated could be

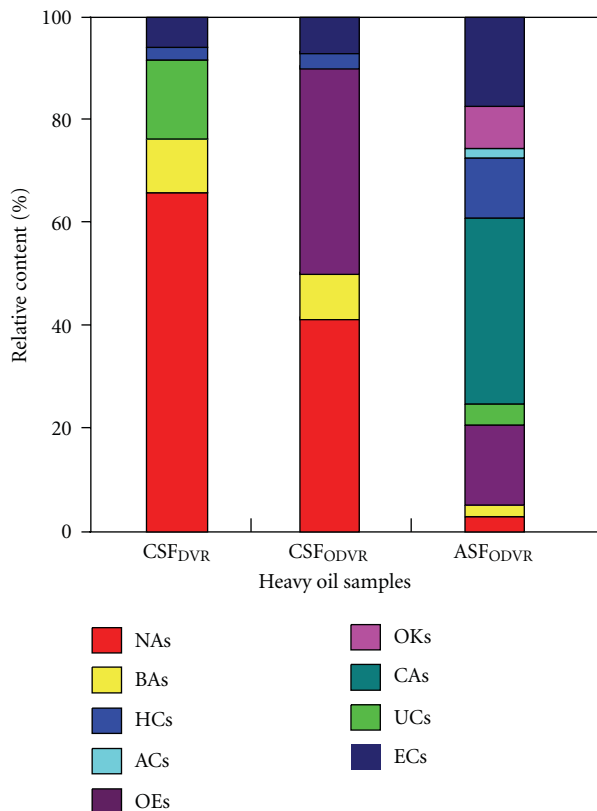


FIGURE 5: Distributions of group components in solution of CSF_{DVR}, CSF_{ODVR} and ASF_{ODVR}.

oxidized into ACs. Thirdly, deep oxidation or elimination proved that HCs and UCs have been converted into CAs or OEs. Fourthly, esterification of CAs and HCs causes the yield of OEs. Finally, the reaction between UCs and HCs is Michael addition reaction.

4. Conclusions

Most of OMs in DVR was depolymerized and converted into high-polarity OOCs successfully, which are soluble species in cyclohexane or acetone through PCO, and their relative contents reach above 92%. Even NAs can be also oxidized to form HCs in PCO, and their contents decrease from 65.67% to 44.55%.

Main products of OOCs, including CAs, OEs, HCs, and OKs, are all essential industry materials. As for oxalates, it can be used as the intermediate to make chemical cold-light illuminator. So PCO depolymerization of DVR is an effective way, not only to analyze the structure of DVR but also to realize the effective conversion or application of DVR.

The color of system and the viscosity of DVR were reduced gradually with the generating of hydroxyl radicals in the photo-catalytic oxidation reaction. The change of DVR color, viscosity, and polarity is favorable to solve environmental protection question, which is caused by heavy oil in the course of transportation, reserving, and utilizing.

The synergistic effect of TiO₂ and H₂O₂ is the most effective to the reaction.

Acknowledgment

This work was supported by the Special Fund for Major State Basic Research Project (Project no. 2004CB217601), National Natural Science Foundation of China (Project no. 50974121), and the Program of the Universities in Jiangsu Province for Development of High-Tech Industries (Project no. JHB05-33).

References

- [1] D. G. Lee and N. A. Noureldin, "Effect of water on the low-temperature oxidation of heavy oil," *Energy & Fuels*, vol. 3, no. 6, pp. 713–715, 1989.
- [2] M. Xiang-Hai, X. Chun-Ming, L. Li, and G. Jin-Sen, "Studies on the kinetics of heavy oil catalytic pyrolysis," *Industrial and Engineering Chemistry Research*, vol. 42, no. 24, pp. 6012–6019, 2003.
- [3] S. R. Stoyanov, S. Gusarov, S. M. Kuznicki, and A. Kovalenko, "Theoretical modeling of zeolite nanoparticle surface acidity for heavy oil upgrading," *Journal of Physical Chemistry C*, vol. 112, no. 17, pp. 6794–6810, 2008.
- [4] A. Ambalae, N. Mahinpey, and N. Freitag, "Thermogravimetric studies on pyrolysis and combustion behavior of a heavy oil and its asphaltenes," *Energy and Fuels*, vol. 20, no. 2, pp. 560–565, 2006.
- [5] E. Fumoto, A. Matsumura, S. Sato, and T. Takanohashi, "Recovery of lighter fuels by cracking heavy oil with zirconia-alumina-iron oxide catalysts in a steam atmosphere," *Energy and Fuels*, vol. 23, no. 3, pp. 1338–1341, 2009.
- [6] Y. Q. Wang, L. X. Zhou, Z. M. Zong et al., "Synergistic catalytic hydrogenation of catalysts co-operation on the draft from supercritical fluid extraction of Dagang vacuum residue," *Applied Chemical Industry*, vol. 35, no. 11, pp. 887–892, 2006.
- [7] A. Fujishima and K. Honda, "Electrochemical photolysis of water at a semiconductor electrode," *Nature*, vol. 238, no. 5358, pp. 37–38, 1972.
- [8] N. C. Han, S. H. Cho, Y. J. Park, W. L. Dai, and W. Y. Lee, "Sol-gel-immobilized Tris(2,2-bipyridyl)ruthenium(II) electrogenerated chemiluminescence sensor for high-performance liquid chromatography," *Analytica Chimica Acta*, vol. 541, no. 1–2, pp. 47–56, 2005.
- [9] M. R. Hoffmann, S. T. Martin, W. Choi, and D. W. Bahnemann, "Environmental applications of semiconductor photocatalysis," *Chemical Reviews*, vol. 95, no. 1, pp. 69–96, 1995.
- [10] O. Legrini, E. Oliveros, and A. M. Braun, "Photochemical processes for water treatment," *Chemical Reviews*, vol. 93, no. 2, pp. 671–698, 1993.
- [11] Y. Inel and I. A. Balcioglu, "Photocatalytic degradation of organic contaminated in semiconductor suspensions with added H₂O₂," *Journal of Environmental Science and Health, Part A*, vol. 31, no. 1, pp. 123–128, 1996.
- [12] R. Asahi, T. Morikawa, T. Ohwaki, K. Aoki, and Y. Taga, "Visible-light photocatalysis in nitrogen-doped titanium oxides," *Science*, vol. 293, no. 5528, pp. 269–271, 2001.
- [13] G. Li Puma and P. L. Yue, "A novel fountain photocatalytic reactor: model development and experimental validation,"

- Chemical Engineering Science*, vol. 56, no. 8, pp. 2733–2744, 2001.
- [14] W. Cui, L. Feng, C. Xu, S. Lü, and F. Qiu, “Hydrogen production by photocatalytic decomposition of methanol gas on Pt/TiO₂ nano-film,” *Catalysis Communications*, vol. 5, no. 9, pp. 533–536, 2004.
- [15] M. Zäch, C. Hägglund, D. Chakarov, and B. Kasemo, “Nanoscience and nanotechnology for advanced energy systems,” *Current Opinion in Solid State and Materials Science*, vol. 10, no. 3–4, pp. 132–143, 2006.
- [16] K. Hashimoto, T. Kawai, and T. Sakata, “Photocatalytic reactions of hydrocarbons and fossil fuels with water. Hydrogen production and oxidation,” *Journal of Physical Chemistry*, vol. 88, no. 18, pp. 4083–4088, 1984.
- [17] R. Dlugi and H. Gusten, “The catalytic and photocatalytic activity of coal fly ashes,” *Atmospheric Environment*, vol. 17, no. 9, pp. 1765–1771, 1983.
- [18] R. F. Lee, “Photo-oxidation and photo-toxicity of crude and refined oils,” *Spill Science and Technology Bulletin*, vol. 8, no. 2, pp. 157–162, 2003.
- [19] J. G. Fang and G. H. Xu, “Research progress in the synthesis of oxalate,” *Chemical Propell & Poly Mater*, vol. 2, no. 2, pp. 18–21, 2004.
- [20] M. M. Rauhut, L. G. Bollyky, and B. G. Roberts, “Chemiluminescence from reactions of electrto-negatively substituted aryl oxalates with hydrogen peroxide and fluorescent compounds,” *Journal of the American Chemical Society*, vol. 89, no. 25, pp. 6515–6522, 1967.
- [21] D. M. Fenton and P. J. Steinwand, “Preparation of oxalates,” 1967, US P 3393136.
- [22] D. M. Fenton and P. J. Steinwand, “Noble metal catalysis IV preparation of dialkyl oxalates by oxidative carbonylation,” *Journal of Organic Chemistry*, vol. 39, no. 5, pp. 701–703, 1974.
- [23] H. S. Xie, Y. R. Zhu, A. M. Li, and L. Lu, “Application of TiO₂ powder in treating wastewater from paper-making factory,” *Photographic Science and Photochemistry*, vol. 24, no. 4, pp. 312–317, 2006.
- [24] S. W. Bi, B. Wang, and Y. Z. Gao, “Mechanistic study on reaction of [Cp*Rh(CO)₂Me]BF₄ with NBD,” *Chinese Journal of Inorganic Chemistry*, vol. 22, no. 1, pp. 13–20, 2006.

Research Article

Photocatalytic Activity of Nanosized Cadmium Sulfides Synthesized by Complex Compound Thermolysis

Yingchun Yu, Youxian Ding, Shengli Zuo, and Jianjun Liu

Faculty of Sciences, Beijing University of Chemical Technology, Beijing 100029, China

Correspondence should be addressed to Jianjun Liu, jjliu717@yahoo.com.cn

Received 15 June 2010; Accepted 15 August 2010

Academic Editor: Mohamed Sabry Abdel-Mottaleb

Copyright © 2011 Yingchun Yu et al. This is an open access article distributed under the Creative Commons Attribution License, which permits unrestricted use, distribution, and reproduction in any medium, provided the original work is properly cited.

The nanosized cadmium sulfides (CdSs) containing different phase structures were synthesized via the complex compound thermolysis method using different molar ratio of thiourea to acetate cadmium (S/Cd) and characterized by XRD, TEM, UV-Vis, and IR spectra. The results of photocatalytic degradation of rhodamine B (RB) show that the activity order of CdS concerning the phase compositions is of cubic > hexagonal > cubic + hexagonal, where the CdS with the cubic phase has the best photocatalytic degradation activity of RB due to its larger abilities of adsorption and absorbance and smaller particle size of about 10~13 nm.

1. Introduction

Nanomaterials are assemblies with particles or crystal size between 1 nm and 100 nm, which include different types of nanoparticles, nanowires, nanotubes, and nanofilms and other nanobulk materials. Nanomaterials possess many unique physical and chemical properties different from their bulk counterparts due to the obvious quantum size effect and small size effect [1, 2]. Photocatalysis is one of the key technologies to solve both energy and environmental problems using solar energy, in which an efficient photocatalyst is necessary. Although remarkable progress has been made in recent years for photocatalysts working under ultraviolet light, there are limitations for the photocatalysts to be applied under visible light. The problem could be resolved by using visible light-induced photocatalysts with proper band gap energy, such as CdS, WO₃, or Fe₂O₃. Although CdS is a good candidate for photocatalytic water reduction and pollutant oxidation, it has the fatal photocorrosion problem due to the oxidation of itself by the photogenerated hole [3]. Usually, CdSs are of cubic phase and hexagonal phase and the cubic phase can transform into hexagonal one when heated to certain temperatures [4]. At present, there are many studies on the synthesis of hexagonal CdS. Lin et al. [5] and Bao et al. [6] found that the hexagonal

CdS nanoparticles synthesized via solvothermal method have much better photocatalytic activity for degradation of methylene blue and better hydrogen production activity for water photolysis, using thiourea and cadmium acetate as raw materials. Jing and Guo [7] reported a CdS catalyst system with a high hydrogen production activity for water photolysis using cadmium acetate as cadmium source and H₂S as sulfur source. The CdS synthesized under solvothermal or heating conditions is usually of stable hexagonal phase, but there are a few reports on the synthesis of metastable cubic CdS. Many factors can influence the photocatalytic activity of CdS, such as phase composition, crystallite size, morphology, specific surface area, and energy gap. For example, Degussa P25 (made in Germany), a type of commercial nanosized titania which possesses a high photocatalytic activity, exists in polymorphs composed of about 80% anatase and 20% rutile [8]. Therefore, it is very important to study how to get the CdS photocatalysts with different phase compositions and their photocatalytic activities by controlling reaction conditions.

In this study, the CdS nanocrystals with different phase compositions were synthesized via thermal decomposition of thiourea-cadmium complexes using cadmium acetate and thiourea as raw materials. The photocatalytic activities of the synthesized CdS nanocrystals for the degradation of Rhodamine B under visible light were also studied.

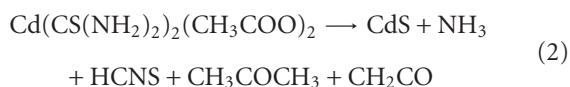
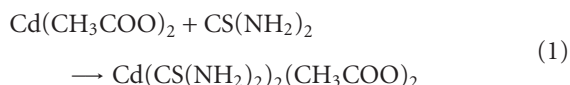
TABLE 1: Synthesis conditions, phase composition, and crystalline size of CdS photocatalysts.

Sample no.	$c(\text{CS}(\text{NH}_2)_2)/(\text{mol} \cdot \text{l}^{-1})$	$c(\text{Cd}^{2+})/(\text{mol} \cdot \text{l}^{-1})$	$n(\text{S})/n(\text{Cd})$	Phase composition	Grain size/nm
A	0.07	0.14	0.5	CdS(cubic) + CdO	10
B	0.14	0.14	1	Cubic	13
C	0.21	0.14	1.5	Cubic + hexagonal	17
D	0.28	0.14	2	Hexagonal	26
E	0.42	0.14	3	Hexagonal	26

*The grain size of CdS can be calculated by using the crystal plane of cubic (111) and hexagonal (002), respectively.

2. Experimental

2.1. Synthesis of CdS. All chemicals were of analytical grade and used without further purification. The preparation conditions and analysis results of CdS samples synthesized using different S/Cd ratios are listed in Table 1. The synthesis procedure of nanosized CdS was as follows: (a) to prepare a series of aqueous solutions including $\text{CS}(\text{NH}_2)_2$ and $\text{Cd}(\text{CH}_3\text{COO})_2$ according to their concentration listed in Table 1; (b) 50 mL $\text{CS}(\text{NH}_2)_2$ solution was dropped into 50 mL $\text{Cd}(\text{CH}_3\text{COO})_2$ solution to form transparent solution under stirring for 30 min and then heated at 100°C for 10 h so as to get a yellow single resource complex precursor of $\text{Cd}(\text{CS}(\text{NH}_2)_2)_2(\text{CH}_3\text{COO})_2$ (1) which will turn to CdS after calcination at 300°C for 0.5 h. All other products were gaseous (2). Thus there are no any other byproducts in the thermolysis process. The final products were washed twice by ethanol and deionized water followed by drying at 100°C for 10 h. The synthesized CdS samples are used after grinding to powder,



2.2. Characterization of Photocatalysts. The powder X-ray diffraction (XRD) patterns were recorded on a Rigaku D/MAX-2500 diffractometer with $\text{Cu K}\alpha$ ($\lambda = 1.5406 \text{ \AA}$) radiation. The transmission electron microscope (TEM) images were taken on a Hitachi800 electron microscope. The UV-vis diffuse reflectance spectra were measured on a Shimadzu UV-2550 spectrometer. The FT-IR spectra of the samples dispersed in KBr pellets were obtained within the $4000\text{--}400 \text{ cm}^{-1}$ wavenumbers on a Nicolet 370MCT spectrometer.

2.3. Photocatalytic Testing. A 500-W Xe lamp was used as the light source and the visible wavelength was controlled through a 420-nm cut filter (LF420, China), which was hanged in a dark box and kept at about 15 cm above the liquid level. Aqueous suspensions of Rhodamine B (RB) dye (100 mL, with an initial concentration of $1.5 \times 10^{-4} \text{ M}$) and photocatalyst powder (100 mg) were placed in a 250 mL beaker. Prior to irradiation, the suspensions were magnetically stirred for 10 min under dark condition to

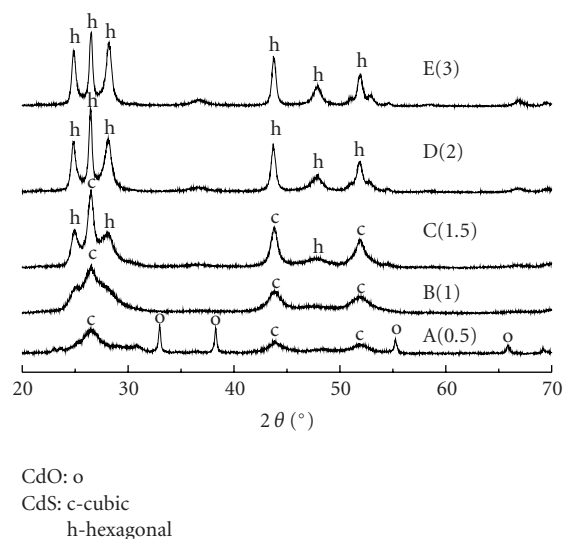


FIGURE 1: XRD patterns of CdS samples synthesized by different $n(\text{S})/n(\text{Cd})$ ratios of A: 0.5, B: 1, C: 1.5, D: 2, and E: 3.

establish an adsorption/desorption equilibrium between dye and photocatalyst surface. Under stirring, aliquots of a small amount of suspension (about 4 mL) were taken out every 10 minutes under irradiation conditions, then centrifuged and analyzed using a SP-2000UV spectrophotometer (made in China).

3. Results and Discussion

3.1. XRD Characterization. XRD patterns of the CdS products are depicted in Figure 1. All the diffraction peaks of the nanocrystals are well indexed either as cubic CdS (JCPDF # 65-2887) or as hexagonal CdS (JCPDF # 77-2306) which have been marked by the symbol "c" or "h." When increasing thiourea/Cd molar ratio from 0.5 to 1, 1.5, 2, and then to 3, a mixture of cubic CdS and CdO (Figure 1A), a cubic CdS (Figure 1B), a mixture of cubic and hexagonal CdS (Figure 1C), and hexagonal CdS (Figures 1D and 1E) were obtained, respectively.

The crystal phase of synthesized CdS changes regularly, from cubic phase \rightarrow mixed phase \rightarrow hexagonal phase. With the thiourea/Cd molar ratio of 0.5, the excess cadmium acetate decomposes into CdO under heating condition. During the process of reaction, the cadmium acetate and thiourea molecules form a single source precursor of

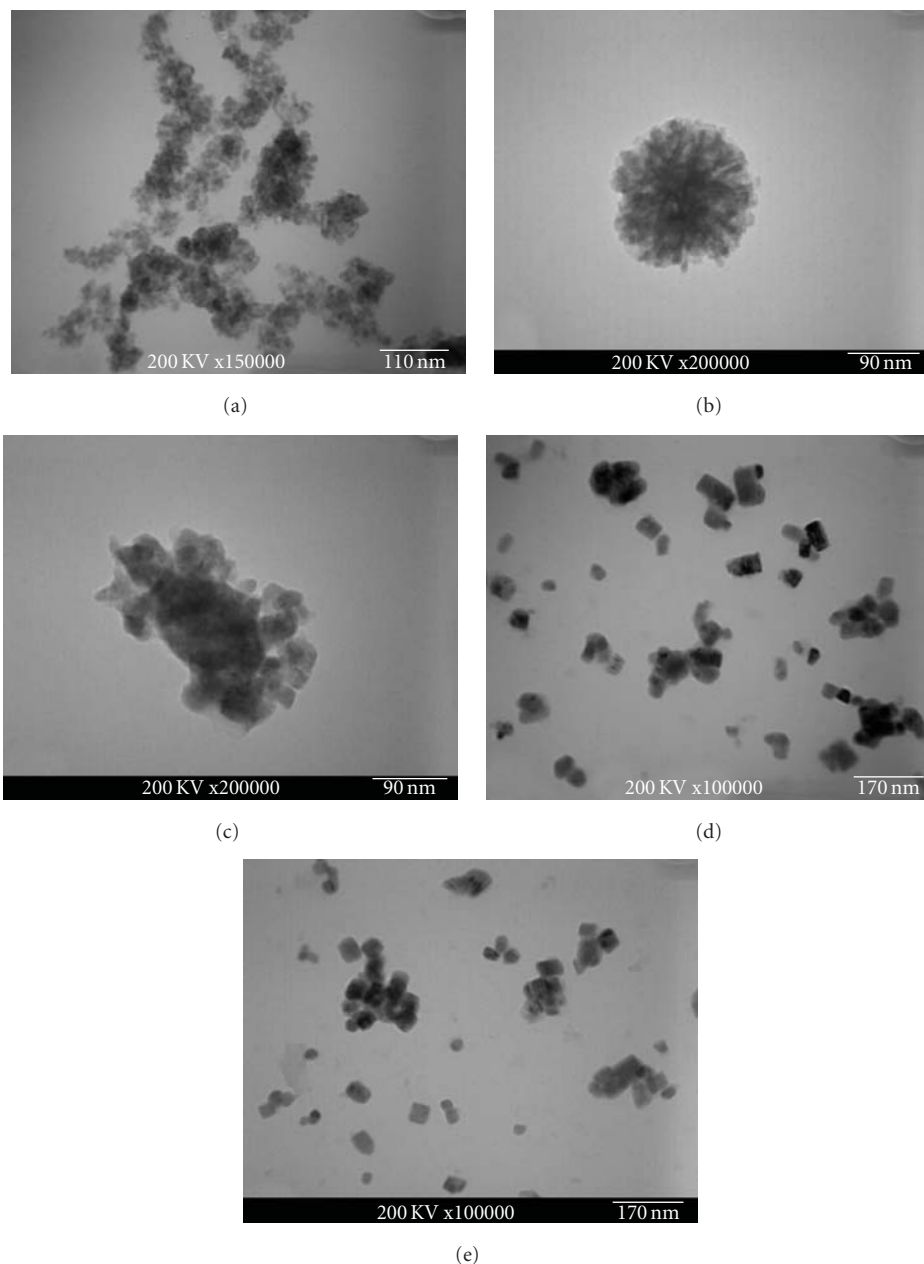


FIGURE 2: TEM images of CdS samples synthesized by different $n(S)/n(Cd)$ ratios of A: 0.5, B: 1, C: 1.5, D: 2, and E: 3.

Cd-thiourea complex $Cd(SC(NH_2)_2)_2(CH_3COO)_2$, in which the Cd ion coordinates with four S atoms to form tetrahedral CdS_4 block. In the cubic zinc blende structure, the pairs of interpenetrating tetrahedra are in the staggered conformation, while in the hexagonal wurtzite structure, these tetrahedra are in the eclipsed conformation. In the present study, for the Cd-thiourea- CH_3COO —complex with a low thiourea/Cd ratio, the symmetry of the ligands is low, and there are steric hindrances to the formation of the $S_3Cd-SCd_3$ group in the eclipsed conformation [9]. Thus, the lower symmetry of the first coordination sphere of Cd in a thiourea complex leads to a lower symmetry of the cubic CdS structure. In contrast, there are no such hindrances for the

Cd-thiourea- CH_3COO —complex with a large thiourea/Cd ratio, and CdS crystallizes in the hexagonal wurtzite structure [10], which is thermodynamically more stable.

With increased S/Cd molar ratio, the grain size of CdS increases from 10 nm of the cubic phase (Figure 1A), to 26 nm of the hexagonal phase (Figure 1E), as shown in Table 1, that indicates that the change of grain size is an important factor affecting the phase transition of CdS [11] except for the symmetry change abovementioned.

3.2. TEM Characterization. The TEM images of CdS samples synthesized with different S/Cd ratios were shown in Figure 2. It is shown that the particles of sample A consisting

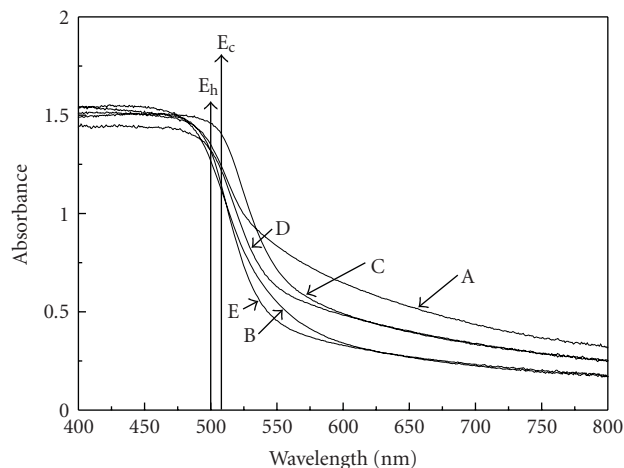


FIGURE 3: UV-vis spectra of CdS samples synthesized by different $n(S)/n(Cd)$ ratios of A: 0.5, B: 1, C: 1.5, D: 2, and E: 3.

of CdO and cubic CdS are about 10 nm exhibiting chain-like aggregates. The morphology of sample B seems as flocculent flower with diameter of about 100 nm which is consisting of much smaller particles and fiber aggregates. In the center of sample C, a number of particles with the diameter of 10 to 20 nm are separated out corresponding to the mixed phases of cubic and hexagonal CdS, as shown in Figure 1C. With increased S/Cd molar ratio, the morphology of the samples becomes more perfect and homogeneous crystal of cubic CdS with diameter of about 20~30 nm that is a good agreement in the calculation results (Table 1), as shown in Figures 2(d) and 2(e). It is worth mentioning that the morphologies of CdS change subtly with a gradual increase of S/Cd ratio, suggesting that the S/Cd ratio plays a key role in the formation of diverse CdS nanostructures.

3.3. UV-Vis Characterization. All CdS samples synthesized with different S/Cd ratios show strong light absorption at the wavelength of less than 550 nm, and the consequent weak absorption even extends to 800 nm, as shown in Figure 3 which indicates that the CdS samples have broad light absorption in the whole visible region. The absorbance has the order of: $A > (C, D) > (B, E)$, in which samples A and C are the mixed phase of cubic CdS and CdO, or of cubic and hexagonal CdS, respectively, while sample B is the pure cubic CdS, and samples D and E are pure hexagonal CdS. It is well known that the intrinsic energy gap of pure cubic or hexagonal CdS is $E_{cubic} = 2.41$ eV or $E_{hexagonal} = 2.47$ eV [12], corresponding to the cutoff absorption wavelength of E_c ($\lambda = 515$ nm) or E_h ($\lambda = 502$ nm), respectively, as shown by the vertical lines in Figure 3. Thus all CdS samples synthesized with different S/Cd ratios undergo a redshift compared to the intrinsic adsorption of cubic or hexagonal CdS.

3.4. IR Characterization. The absorption bands of 3300–3400 cm^{-1} and 1607–1645 cm^{-1} are assigned to the N–H stretching and $-NH_2$ bending vibrations of thiourea molecule [13], respectively, whose intensities gradually

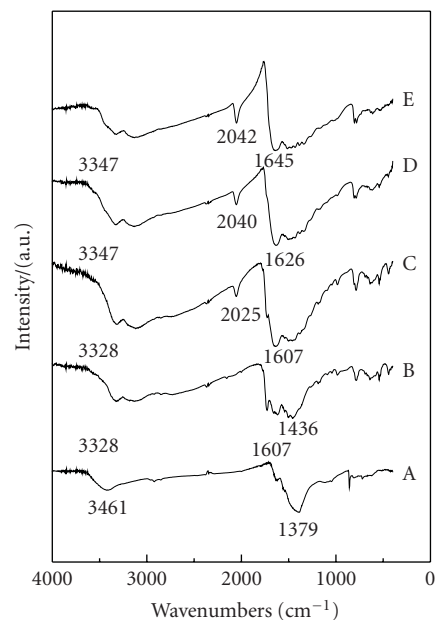


FIGURE 4: IR spectra of CdS samples synthesized by different $n(S)/n(Cd)$ ratios of A: 0.5, B: 1, C: 1.5, D: 2, and E: 3.

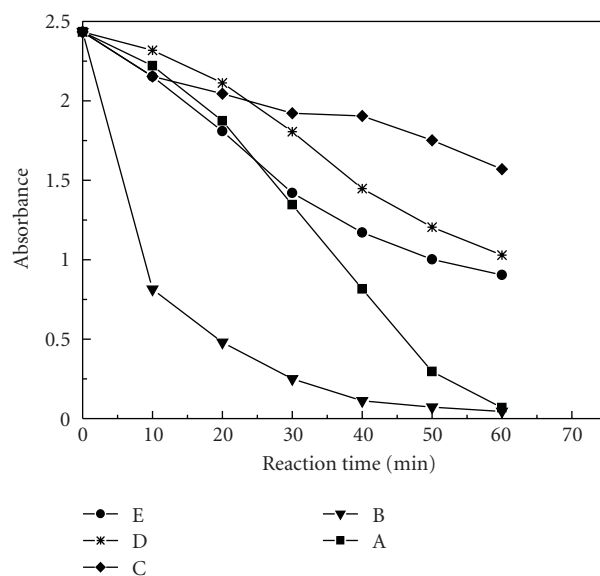


FIGURE 5: Photocatalytic degradation curves of RB using CdS samples synthesized by different $n(S)/n(Cd)$ ratios of A: 0.5, B: 1, C: 1.5, D: 2, and E: 3.

increase with increasing S/Cd ratios, as shown in Figure 4. Similarly, the absorption bands of 2040 cm^{-1} also gradually increase in samples of C, D, and E, which is attributed to the infrared vibration of $-C\equiv N$ bond of thiocyanate (HCNS, $H-S-C\equiv N$) produced in reaction (2). However, the characteristic diffraction peaks of thiocyanate or its derivatives do not appear in Figure 1, which indicates that the real content of decomposed products in the CdS sample is very low (<1%). In contrast to the above situation, the IR absorption peaks near 2040 cm^{-1} of thiocyanate do not

appear in the samples of A(0.5) and B(1.0), indicating that there is no excess thiourea to be decomposed into thiocyanate.

3.5. Photocatalytic Activities. The curves of photocatalytic degradation of RB using different CdS samples are shown in Figure 5. With the residual absorbance of RB after 60 min as evaluation index, the degradation activity is in the order of $B \approx A > E > D > C$. Sample B has relatively rapid degradation within the first 10 min, which can be attributed to its strong adsorption of RB due to the flocculent particle morphology with larger surface area, as shown in Figure 2(b). Furthermore, sample A has the strongest absorption in visible region and the smallest grain size (10 nm), so it has a higher photocatalytic activity. While $n(S)/n(Cd) > 1$, the catalytic activities of samples E, D, and C are lower than that of A and B. It is known from Figure 4 that the excess thiocyanate remains on the surface of samples E, D, and C, in which the S^{2-} ions can act as a photoinduced hole sacrificial reagent and compete with the oxidation of RB dye, resulting in the decrease of the photocatalytic activity [14]. On the other hand, the order of phase composition effect on the catalytic activity is cubic > hexagonal > mixed. As shown in Figure 2, the hexagonal CdS samples of D and E are in good crystallinity and homogeneous particle dispersion. However, the mixed phase CdS of C is an aggregate containing many defects between the two-phase interface, accounting for the lower photocatalytic activity.

4. Conclusions

The cubic CdS, hexagonal CdS, and their mixed phase were synthesized under the conditions of thiourea/Cd (S/Cd) molar ratios (0.5~3) of ≤ 1 , ≥ 2 , and 1.0~1.5, respectively. The grain size of CdS increases with the increased S/Cd ratio. The photocatalytic activity is in order of cubic > hexagonal > mixed phase, in which the cubic phase CdS has the best photocatalytic activity for RB degradation due to its strong adsorption, intense absorbance in visible region, and the smaller grain size.

Acknowledgments

This work was financially supported by the Chinese National TCM Project in the 11th Five-Year Period through the Grant 2007BAK26B08. The authors acknowledge the Chinese People's Security University for its full cooperation.

References

- [1] W. Kelsall, I. W. Hamley, and M. Geoghegan, *Nanoscale Science and Technology*, John Wiley & Sons, New York, NY, USA, 2005.
- [2] C. P. Poole and F. J. Owens, *Introduction to Nanotechnology*, John Wiley & Sons, New York, NY, USA, 2003.
- [3] D. Meissner, R. Memming, and B. Kastening, "Photoelectrochemistry of cadmium sulfide. 1. reanalysis of photocorrosion and flat-band potential," *Journal of Physical Chemistry*, vol. 92, no. 12, pp. 3476–3483, 1988.
- [4] N. Sahu, M. K. Arora, S. N. Upadhyay, and A. S. K. Sinha, "Phase transformation and activity of cadmium sulfide photocatalysts for hydrogen production from water: role of adsorbed ammonia on cadmium sulfate precursor," *Industrial and Engineering Chemistry Research*, vol. 37, no. 12, pp. 4682–4688, 1998.
- [5] G. Lin, J. Zheng, and R. Xu, "Template-free synthesis of uniform CdS hollow nanospheres and their photocatalytic activities," *Journal of Physical Chemistry C*, vol. 112, no. 19, pp. 7363–7370, 2008.
- [6] N. Bao, L. Shen, T. Takata et al., "Facile Cd—thiourea complex thermolysis synthesis of phase-controlled CdS nanocrystals for photocatalytic hydrogen production under visible light," *Journal of Physical Chemistry C*, vol. 111, no. 47, pp. 17527–17534, 2007.
- [7] D. Jing and L. Guo, "A novel method for the preparation of a highly stable and active CdS photocatalyst with a special surface nanostructure," *Journal of Physical Chemistry B*, vol. 110, no. 23, pp. 11139–11145, 2006.
- [8] J. Liu, W. Qin, S. Zuo, Y. Yu, and Z. Hao, "Solvothermal-induced phase transition and visible photocatalytic activity of nitrogen-doped titania," *Journal of Hazardous Materials*, vol. 163, no. 1, pp. 273–278, 2009.
- [9] A. V. Naumov, V. N. Semenov, and E. G. Goncharov, "Properties of CdS films prepared from thiourea complexes of cadmium salts," *Inorganic Materials*, vol. 37, no. 6, pp. 539–543, 2001.
- [10] V. Swayambunathan, D. Hayes, K. H. Schmidt, Y. X. Liao, and D. Meisel, "Thiol surface complexation on growing CdS clusters," *Journal of the American Chemical Society*, vol. 112, no. 10, pp. 3831–3837, 1990.
- [11] N. Herron, Y. Wang, and H. Eckert, "Synthesis and characterization of surface-capped, size-quantized CdS clusters. Chemical control of cluster size," *Journal of the American Chemical Society*, vol. 112, no. 4, pp. 1322–1326, 1990.
- [12] D. J. Kim, Y.-M. Yu, J. W. Lee, and Y. D. Choi, "Investigation of energy band gap and optical properties of cubic CdS epilayers," *Applied Surface Science*, vol. 254, no. 22, pp. 7522–7526, 2008.
- [13] G. W. C. Kaye and T. H. Laby, *Tables of Physical and Chemical Constants*, Longman Press, London, UK, 16th edition, 1995.
- [14] I. Tsuji, H. Kato, and A. Kudo, "Photocatalytic hydrogen evolution on ZnS-CuInS₂-AgInS₂ solid solution photocatalysts with wide visible light absorption bands," *Chemistry of Materials*, vol. 18, no. 7, pp. 1969–1975, 2006.

Research Article

Structure and Physical Properties of Polymer Composite Films Doped with Fullerene Nanoparticles

R. M. Ahmed¹ and S. M. El-Bashir^{2,3}

¹Department of Physics, Faculty of Science, Zagazig University, Zagazig 44519, Egypt

²Department of Physics and Astronomy, Science College, King Saud University Riyadh 11451, Saudi Arabia

³Department of Physics, Faculty of Science, Banha University, Egypt

Correspondence should be addressed to R. M. Ahmed, rania8_7@hotmail.com

Received 3 July 2010; Accepted 30 September 2010

Academic Editor: Mohamed Sabry Abdel-Mottaleb

Copyright © 2011 R. M. Ahmed and S. M. El-Bashir. This is an open access article distributed under the Creative Commons Attribution License, which permits unrestricted use, distribution, and reproduction in any medium, provided the original work is properly cited.

Fullerene C₆₀ has stimulated intense interest for scientific, industrial, and medical community because of its unique structure and properties. In the present study we prepared fullerene-doped nanocomposite films based on PMMA, PVAc, and PMMA/PVAc blend. Observations made by transmission electron microscope (TEM) showed the uniform dispersion of C₆₀ nanoparticles in the polymer matrices. Also, X-ray diffraction measurements indicated that C₆₀ has a tendency to form crystallites in the polymer matrices. In addition, the concentration effect of fullerene C₆₀ was investigated using optical absorption and photoluminescence spectroscopy. The spectroscopic properties of such films recommended their application in photonics and solar energy conversion.

1. Introduction

Recently, polymers are finding an important place in different research laboratories for the study of their various properties [1]. Many polymers have been proved suitable matrices in the development of composite structures due to their ease production and processing, good adhesion with reinforcing elements, resistance to corrosive environment, light weight, and in some cases ductile mechanical performance [2]. Fullerenes have been widely studied due to their unique structural, electronic and spectroscopic properties, which may be exploited for their diverse applications in chemistry, biology, and nanoscience [3].

Lately interest of researchers engaged in different fields of knowledge is seen to be focused on determination of the action of nanomaterial addition, such as fullerenes and nanotubes, on properties of polymers and their compositions. Incorporation of fullerene and nanotubes into chemical composition of polymers gives one more opportunities for their study and application as composite materials, films, and fibers serving different purposes [4].

Also, the research of polymer material has been directed to blend or copolymer of different polymers to obtain

new products having some of the desired properties of each component [5]. PMMA (polymethylmethacrylate) and its derivatives are known for their medical applications, particularly for hard tissue repair and regeneration. PMMA and (polyvinyl acetate) PVAc form an important and unique pair of polymers although they are chemically different [6].

The aim of the present work concerns on studying the change in the optical absorption, the optical parameters and photoluminescence spectra for the samples of fullerene polymer composites which are recorded at room temperature. In addition, X-ray diffraction (XRD) and transmission electron microscope (TEM) are used to characterize the fullerene/Polymer nanocomposites.

2. Materials and Methods

2.1. Materials. Both PMMA (poly methyl methacrylate) and PVAc (poly vinyl acetate) used in this study were obtained from Sigma-Aldrich (Germany) and were reported to have molecular weights of 996,000 and 167,000 g·mol⁻¹, respectively. Moreover, Buckminster fullerene powder C₆₀, has purity of 97% and Mr = 720.66 and was obtained from Fluka (USA). In addition, chloroform has purity of 99.8%

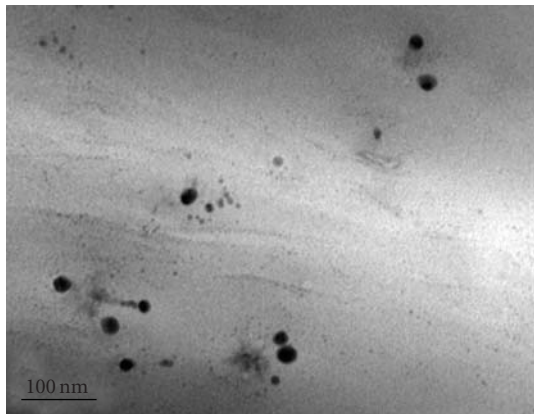


FIGURE 1: The TEM photograph of fullerene C_{60} doped in (50/50 PMMA/PVAc) blend.

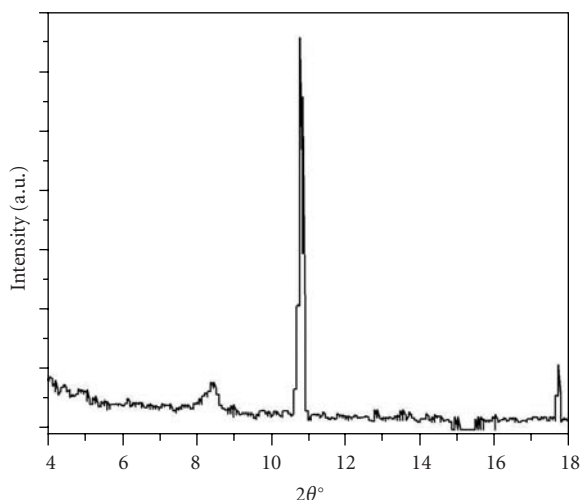


FIGURE 2: X-ray diffraction patterns of (50/50 PMMA/PVAc) blend doped with 1×10^{-4} of fullerene C_{60} .

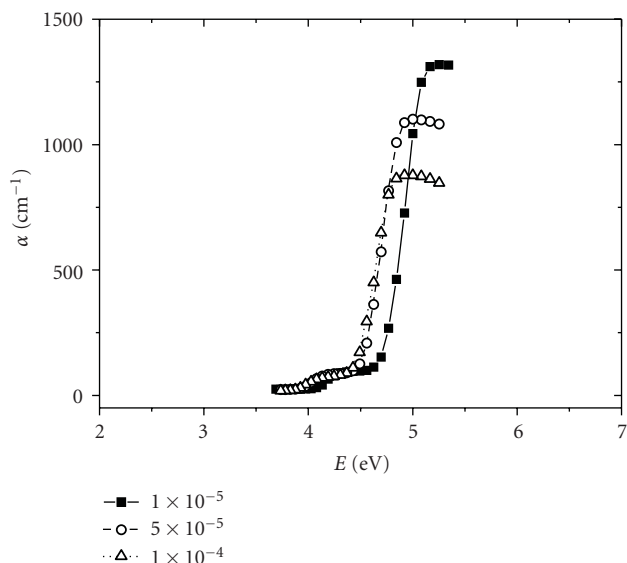


FIGURE 3: Absorption coefficient as a function of photon energy for different concentration of fullerene doped PMMA.

(HPLC) was used as a common solvent for PVAc, PMMA, and C_{60} .

2.2. Preparation of the Samples. Composite films (thickness $60 \pm 10 \mu\text{m}$) of PMMA, PVAc and a blend of (PMMA/PVAc 50/50) doped with C_{60} were prepared by using solution-cast technique. PMMA, PVAc, and C_{60} were dissolved separately in chloroform and stirred for 48 h at 40°C . After that, C_{60} was mixed with homopolymers and also in their blend with different concentrations and subsequently cast onto glass dishes and then left to be dry. After drying, the films were removed and heated at 100°C to evaporate the confined solvent molecules. The concentrations of C_{60} in the two homopolymers and their blend are 1×10^{-5} , 5×10^{-5} and 1×10^{-4} mol. %.

2.3. Film Characterization. TEM was performed by Transmission Electron Microscope, JEOL JEM-1400, Japan. X-ray diffraction patterns were recorded by using a Philip XRD-500 X-ray diffraction analyzer with nickel-filtered Cu-K α radiation at 30 kV and 20 mA.

2.4. Spectroscopic Properties. The absorption spectra were recorded using a UV-VIS spectrophotometer (UNICAM, Helios Co., Germany) in a range of wavelength from 190 to 900 nm. Spectrofluorimeter (Shimadzu RF-5301, PC, Japan) has been used for recording the photoluminescence spectra of C_{60} doped in PMMA, PVAc, and a blend of them. The samples were measured at room temperature and at an excitation wavelength of 400 nm.

3. Results and Discussion

3.1. Characterization of the Samples. Figure 1 presents the TEM photograph of fullerene C_{60} molecules dispersed in (50/50 PMMA/PVAc) blend, it is clear that C_{60} nanocrystals have a spherical shape. Figure 2 shows the XRD pattern for fullerene nanocrystals, sharp peaks are clearly noticed characterizing fullerene C_{60} at $2\theta \sim 10.8^\circ$ and also at $\sim 17.7^\circ$ in agreement with the literature [7, 8]. XRD results show that C_{60} embedded in the polymer blend are very prone to coalesce into crystallites [7].

3.2. Fundamental Absorption Edge. The variation of the optical bulk absorption coefficient, α , with wavelength is a unique parameter of the medium, it provides the most valuable optical information available for material identification. The absorption coefficient (α) at angular frequency (ω) of radiation was calculated using [9]

$$\alpha(\nu) = \frac{[2.303P]}{d}, \quad (1)$$

where P is the absorbance and d is the film thickness. The fundamental absorption edge is one of the most important features of the absorption spectrum of crystalline and amorphous materials. The increased absorption near the edge is due to the generation of neutral excitations

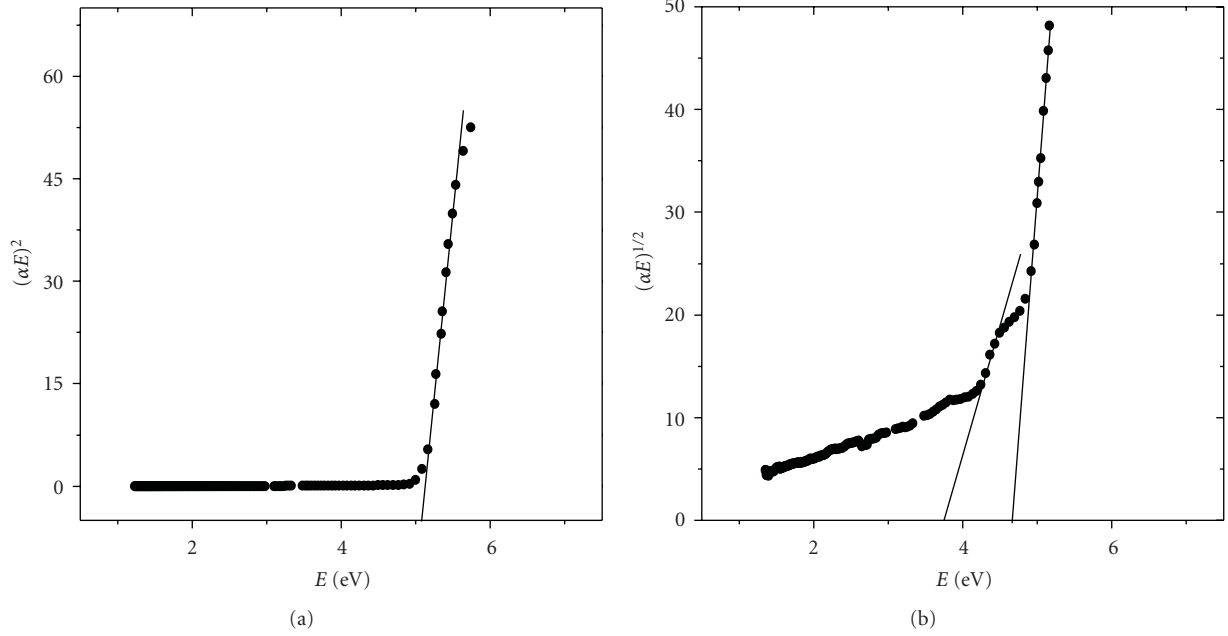


FIGURE 4: Dependence of $(\alpha h\nu)^2$ and $(\alpha h\nu)^{1/2}$ on photon energy ($E = h\nu$) for a concentration of fullerene 1×10^{-5} doped in (50/50 PMMA/PVAc) blend.

and/or the transition of electrons from the valence band to the conduction band [10, 11]. Plotting the absorption coefficient against photon energy for different concentration of fullerene doped the polymer illustrates that the absorption coefficient exhibits a steep rise near the absorption edge and also a straight line relationship is observed in the high α -region as seen in Figure 3. It is clear that the value of the absorption edge decreases with increasing the fullerene concentration doped in the polymer. The intercept of extrapolation to zero absorption with photon energy axis is taken as the value of absorption edge [12].

3.3. Optical Band Gaps. The fundamental absorption is related to band-to-band transitions, and is subject to certain selection rules [13]. The usual method to determine the energy of the band gap is to plot a graph between $(\alpha h\nu)^{1/n}$ and $h\nu$ looking for the value of n (depends on the nature of transition) that gives the best linear fit of a given data set [14]. The allowed direct and indirect transitions are given by the values of n as $1/2$ and 2 , respectively:

$$\alpha h\nu = A(h\nu - E_{gd})^{1/2},$$

$$\alpha h\nu = B \left[\frac{(h\nu - E_{gi} + E_p)^2}{\exp(E_p/kT) - 1} + \frac{(h\nu - E_{gi} - E_p)^2}{1 - \exp(-E_p/kT)} \right], \quad (2)$$

where A and B are constants, E_{gd} and E_{gi} are the direct and indirect energy gaps respectively and E_p is the phonon energy [13]. All the samples of different concentrations of fullerene polymer composites have the same behavior in their direct and allowed transitions. According to (2), there will be a single straight line for direct transitions and two linear

portions for indirect transitions. It could be observed that from Figure 4(a) plotting $(\alpha h\nu)^2$ against $h\nu$ brought in to view a linear behavior that can be considered as an evidence of the direct transition and the optical gap, E_{gd} , can be estimated from the intercept on the energy axis of the linear fit of the large energy data of the plot [15].

On the other hand, Figure 4(b) shows that plotting $(\alpha h\nu)^{1/2}$ against $h\nu$ for indirect transition may be resolved into two distinct straight-line portions. The straight line obtained at lower photon energies, corresponding to phonon-absorption process, cuts the energy axis at $E_{gi} - E_p$. The other line represents the dependence in the high energy range corresponding to a phonon-emission process and cuts the energy axis at $E_{gi} + E_p$. From the energy intercept of the two straight line portions, the values of E_{gi} and E_p could be estimated [14].

The values of E_{gd} , E_{gi} , and E_p are listed in Table 1 which illustrate that the values of E_{gd} and E_{gi} decrease with increasing the concentration of fullerene doped in the polymer sample.

In the mean time, the absorption tails in amorphous and semi crystalline materials could be interpreted in terms of the Dow-Redfield effect [16] taking the form of Urbach rule [17] as follows:

$$\alpha(h\nu) = \alpha_o \exp\left(\frac{h\nu}{E_e}\right), \quad (3)$$

where α_o is a constant and E_e is the width of the tail of the localized states in the band gap. The values of E_e which are listed in Table 1 can be calculated as the reciprocal gradient of the linear portion of plotting $\ln(\alpha)$ against $h\nu$. In addition, Table 1 illustrates that with increasing the concentration of the doped fullerene, the values of E_e increased. It is noted that

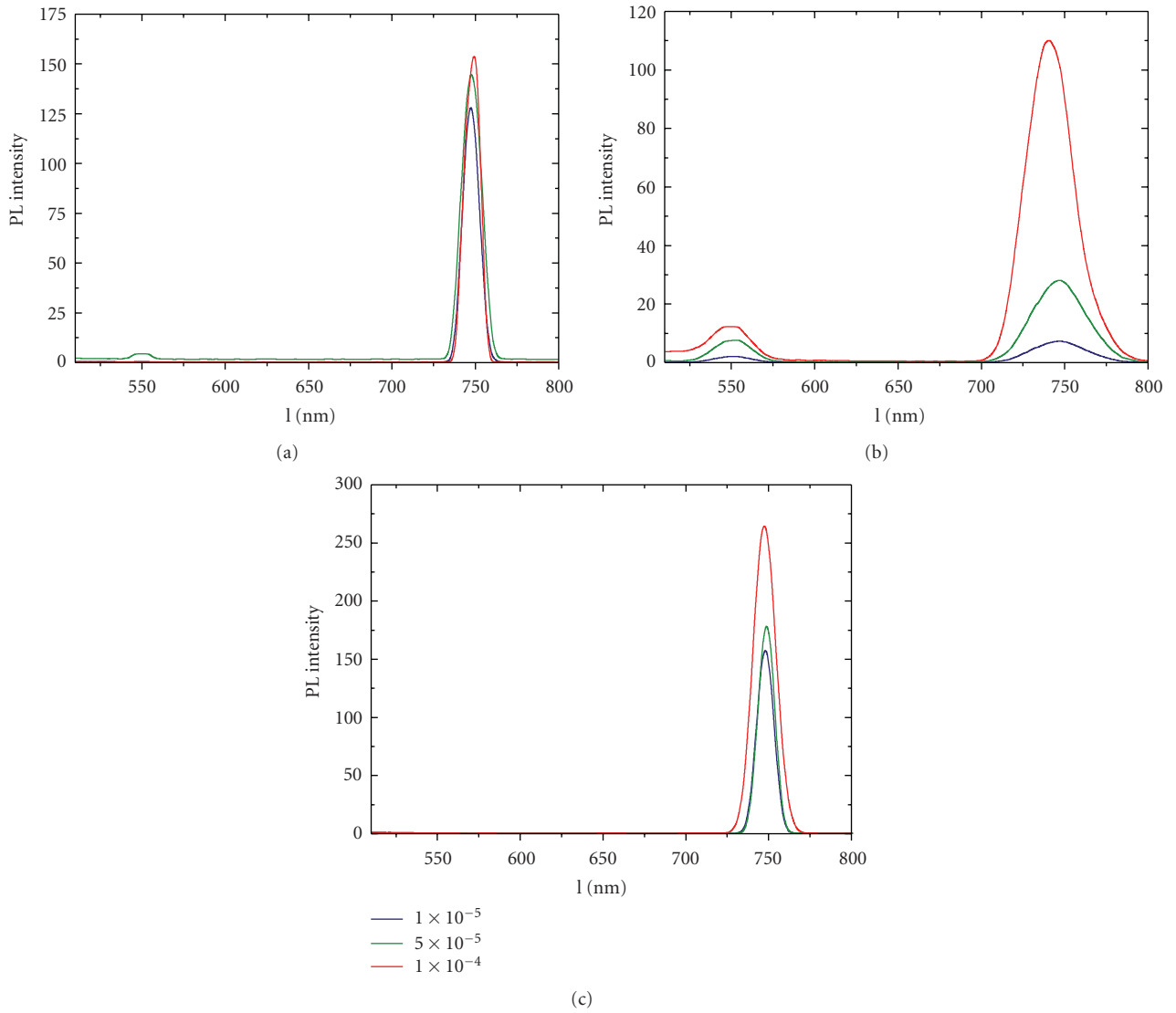


FIGURE 5: Photoluminescence spectra of different concentrations of fullerene doped (a) PMMA, (b) PVAc, and (c) (PMMA/PVAc 50/50) blend excited at 400 nm at the room temperature.

TABLE 1: The values of band tails, optical energy gaps, phonon energy, and the phonon equivalent temperature (given by $T_p = E_p/k_B$, where k_B is Boltzmann's constant, at the room temperature [14]) for different fullerene polymer composites.

Sample	Concentration (mol. %)	E_{gd} (eV)	E_{gi} (eV)	E_p (eV)	T_p (K)	E_u (eV)
C_{60} /PMMA	1×10^{-5}	4.80	4.00	0.32	3687	0.18
	5×10^{-5}	4.55	3.95	0.31	3572	0.19
	1×10^{-4}	4.49	3.84	0.29	3342	0.20
C_{60} /PMMA/PVAc50/50	1×10^{-5}	5.07	4.20	0.46	4724	0.23
	5×10^{-5}	4.85	3.17	0.38	4379	0.25
	1×10^{-4}	4.79	2.90	0.34	3918	0.25
C_{60} /PVAc	1×10^{-5}	5.31	3.62	0.45	5185	0.27
	5×10^{-5}	5.26	3.28	0.45	5185	0.28
	1×10^{-4}	5.21	2.94	0.45	5185	0.29

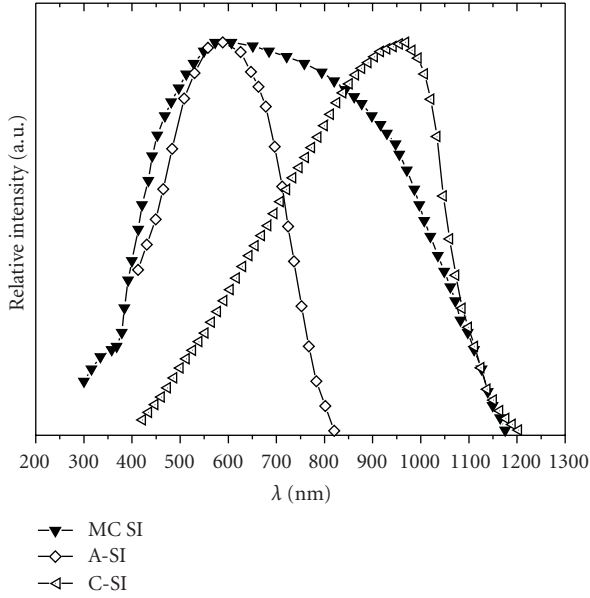


FIGURE 6: The sensitivity of different types of silicon solar cells.

the dependence of E_g on the sample preparation does not match with E_e values because the sample having a narrower band gap expected to have a wider band tail. The change in E_e is probably affected by potential fluctuations associated with the polymer structure but not the change in E_g , because the initial and final states are practically have the same potential [18].

3.4. Photoluminescence Spectroscopy of Doped Composites. The photoluminescence (PL) spectra of different concentrations of fullerene doped in PMMA, PVAc, and their blend, at room temperature, is shown in Figure 5. The full symmetry of C_{60} molecules is that of the icosahedra point group I_h , and the highest occupied molecular orbital (HOMO) and the lowest unoccupied molecular orbital (LUMO), of C_{60} molecules are fivefold-degenerate h_u , and threefold-degenerate t_{1u} orbital, respectively. Consequently, the optical transitions between the h_u -derived valence band and the t_{1u} -derived conduction band are parity forbidden. However, these transitions can be rendered by either solid state effects or interactions between C_{60} and surrounding solvent molecules. Thus the PL spectrum for C_{60} /PMMA films [19] and also that of the others can be interpreted as a result of radiative transitions between the h_u -derived valence band and the t_{1u} -derived conduction band. In addition, it is observed that the photoluminescence intensity of the all samples is improved by increasing the concentration of the fullerene doped in the polymer.

Moreover, Figure 5 illustrates that the PL peak intensity for each concentration of C_{60} doped in (PMMA/PVAc 50/50) blend is greater than the corresponding concentration doped in PMMA and also PVAc composites. Consequently, it could be deduced that (PMMA/PVAc 50/50) blend has modified the optical properties of its homopolymers in agreement with the literature [20]. Also, it is illustrated that there is a

region of PL band centered at 745 ± 5 nm for all the samples. This high luminescence peak of C_{60} always lies below the transition forbidden HOMO-LUMO gap which depends upon the excitation energy [21]. In addition, a band centered at 550 nm, is observed for fullerene/PVAc composites, which is interpreted as a result of relaxed forbidden transitions of excited carriers between HOMO and LUMO of C_{60} [19]. The symmetry of C_{60} is lowered greatly which induces the relaxation of selection rules and a peak of PL [22].

Furthermore, the fluorescence quantum yield has been calculated relative to Rhodamine B as a reference ($\phi_f = 31\%$ in water) from [23]

$$\Phi_s = \Phi_r \left(\frac{D_s}{D_r} \right) \left(\frac{n_s}{n_r} \right)^2 \left(\frac{1 - 10^{-OD_r}}{1 - 10^{-OD_s}} \right), \quad (4)$$

where D_s and D_r are the integrated area under the corrected fluorescence spectra for the sample and reference, n_s and n_r are the refractive indices of the sample and reference, respectively. The calculated values for ϕ_{ref} from the lowest to the highest concentration of fullerene are (8, 10, and 13%) for fullerene/PMMA composites, (0.8, 2 and 5%) for fullerene/PVAc composites and (15, 19, and 23%) for fullerene doped in (PMMA/PVAc 50/50) blend. It is clear that the fluorescence quantum yield values strongly depend on the concentration of fullerene doped in the polymer.

Besides this, it is important that the spectral region of the samples luminescence fits the spectral region of sensitivity of the photovoltaic cells. The sensitivity of photovoltaic cell must be adjusted to match the spectral emission of the sample. The spectral sensitivity of silicon is influenced by its production method [24]. Figure 6 shows the spectral sensitivity of some types of silicon solar cells and their range of sensitivity as multicrystalline (MC-SI) from 375 to 1100 nm, amorphous (A-SI) from 410 to 775 nm and crystalline (C-SI) from 500 to 1125 nm. The maximum PL for all the samples as indicated before could be detected by one of these silicon cells.

4. Conclusions

Different concentrations of fullerene C_{60} doped in PVAc, PMMA, and their blend were prepared by solvent casting method. TEM and XRD measurements illustrated that the fullerene doped in the polymer is crystallite. In addition, the phonon energy and the direct and indirect energy gap were calculated for the samples which were decreasing by increasing the concentration of fullerene. On the other hand, the values of the band tail width were inversely proportional to the fullerene concentration as the sample having a narrower band gap expected to have a wider band tail. Moreover, the photoluminescence spectra were detected for the samples which clarified its improvement by increasing the concentration of the fullerene-doped in the polymer as well as the fluorescence quantum yield. Also, PMMA/PVAc blend has modified the optical properties of its homopolymers which is suggested to be a good host matrix for the solar concentrators. Besides, the measured spectral sensitivity of silicon solar cells illustrated the applicability fullerene doped

polymers coatings as luminescent downshifters, to overcome their poor performance at short wavelengths [25].

Acknowledgments

The authors are grateful the Woman Student Medical Studies and Science Section Research Center of Deanship of Academic Research in King Saud University for Supporting this work.

References

- [1] A. Tanwar, K. K. Gupta, P. J. Singh, and Y. K. Vijay, "Dielectric parameters and a.c. conductivity of pure and doped poly (methyl methacrylate) films at microwave frequencies," *Bulletin of Materials Science*, vol. 29, no. 4, pp. 397–401, 2006.
- [2] A. Patsidis and G. C. Psarras, "Dielectric behaviour and functionality of polymer matrix—ceramic BaTiO₃ composites," *Express Polymer Letters*, vol. 2, no. 10, pp. 718–726, 2008.
- [3] H. W. Kroto, J. R. Heath, S. C. O'Brien, R. F. Curl, and R. E. Smalley, "C₆₀: buckminsterfullerene," *Nature*, vol. 318, no. 6042, pp. 162–163, 1985.
- [4] K. B. Zhogova, I. A. Davydov, V. T. Punin, B. B. Troitskii, and G. A. Domvachiev, "Investigation of fullerene C₆₀ effect on properties of polymethylmethacrylate exposed to ionizing radiation," *European Polymer Journal*, vol. 41, no. 6, pp. 1260–1264, 2005.
- [5] K. El-Salmawi, M. M. Abu Zeid, A. M. El-Naggar, and M. Mamdouh, "Structure-property behavior of gamma-irradiated poly(styrene) and poly(methyl methacrylate) miscible blends," *Journal of Applied Polymer Science*, vol. 72, no. 4, pp. 509–520, 1999.
- [6] H. M. Zidan, A. Tawansi, and M. Abu-Elnader, "Miscibility, optical and dielectric properties of UV-irradiated poly(vinylacetate)/poly(methylmethacrylate) blends," *Physica B*, vol. 339, no. 2-3, pp. 78–86, 2003.
- [7] G. Ma, W. Cheng, G. Chen, and N. Ming, "Orientation and photoluminescence of C₆₀ crystallites in C₆₀-polymethyl methacrylate films," *Thin Solid Films*, vol. 375, no. 1-2, pp. 292–295, 2000.
- [8] W. C. Oh, A. R. Jung, and W. B. Ko, "Preparation of fullerene/TiO₂ composite and its photocatalytic effect," *Journal of Industrial and Engineering Chemistry*, vol. 13, no. 7, pp. 1208–1214, 2007.
- [9] S. K. J. Al-Ani, Y. Al-Ramadin, M. S. Ahmad et al., "Optical properties of polymethylmethacrylate polymer dispersed liquid crystals," *Polymer Testing*, vol. 18, no. 8, pp. 611–619, 1999.
- [10] A. Miller, *Handbook of Optics*, vol. 1, chapter 9, McGraw-Hill, New York, NY, USA, 1994.
- [11] F. H. Abd El-Kader, W. H. Osman, H. S. Ragab, A. M. Shehah, M. S. Rizk, and M. A. F. Basha, "Electrical and optical properties of polyvinyl alcohol thin films doped with metal salts," *Journal of Polymer Materials*, vol. 21, no. 1, pp. 49–60, 2004.
- [12] F. H. Abd-El Kader, G. Said, G. Attia, and A. M. Abo-El Fadl, "Study of structural and optical properties of ethylene vinyl acetate copolymer films irradiated with γ -Rays," *Search Results Egyptian Journal of Physics*, vol. 37, no. 2, pp. 111–126, 2006.
- [13] J. I. Pankove, *Optical Processes in Semiconductors*, Prentice Hall, Upper Saddle River, NJ, USA, 1972.
- [14] M. A. Gaffar, A. Abu El-Fadl, and S. Bin Anooz, "Electron irradiation-induced effects on optical spectra of (NH₄)₂ZnCl₄: X Sr²⁺ single crystals," *Crystal Research and Technology*, vol. 38, no. 1, pp. 83–93, 2003.
- [15] E. Márquez, T. Wagner, J. M. González-Leal et al., "Controlling the optical constants of thermally-evaporated Ge₁₀Sb₃₀S₆₀ chalcogenide glass films by photodoping with silver," *Journal of Non-Crystalline Solids*, vol. 274, no. 1, pp. 62–68, 2000.
- [16] J. D. Dow and D. Redfield, "Electroabsorption in semiconductors: the excitonic absorption edge," *Physical Review B*, vol. 1, no. 8, pp. 3358–3371, 1970.
- [17] F. Urbach, "The long-wavelength edge of photographic sensitivity and of the electronic Absorption of Solids," *Physical Review*, vol. 92, no. 5, p. 1324, 1953.
- [18] S. M. El-Bashir, *Preparation and characterization of fluorescent solar concentrators*, M.S. thesis, Zagazig University, Benha, Egypt, 2001.
- [19] G. Ma, Y. Yang, and G. Chen, "Anomalous photoluminescence from C₆₀/polymethyl methacrylate films," *Materials Letters*, vol. 34, no. 3–6, pp. 377–382, 1998.
- [20] R. M. Ahmed, "Optical study on poly(methyl methacrylate)/poly(vinyl acetate) blends," *International Journal of Photoenergy*, vol. 2009, Article ID 150389, 7 pages, 2009.
- [21] L. Zhu, Y. Li, J. Wang, and J. Shen, "Structural and optical characteristics of fullerenes incorporated inside porous silica aerogel," *Chemical Physics Letters*, vol. 239, no. 4–6, pp. 393–398, 1995.
- [22] Y. Zhao, Y. Fang, and Y. Jiang, "Fluorescence study of fullerene in organic solvents at room temperature," *Spectrochimica Acta—Part A*, vol. 64, no. 3, pp. 564–567, 2006.
- [23] J. N. Demas and G. A. Crosby, "The measurement of photoluminescence quantum yields. A review," *The Journal of Physical Chemistry*, vol. 75, no. 8, pp. 991–1024, 1971.
- [24] N. Neuroth and R. Haspel, "Glasses for luminescent solar concentrators," *Solar Energy Materials*, vol. 16, no. 1–3, pp. 235–242, 1987.
- [25] E. Klampaftis, D. Ross, K. R. McIntosh, and B. S. Richards, "Enhancing the performance of solar cells via luminescent down-shifting of the incident spectrum: a review," *Solar Energy Materials and Solar Cells*, vol. 93, no. 8, pp. 1182–1194, 2009.

Research Article

Structure-Dependent 4-Tert-Butyl Pyridine-Induced Band Bending at TiO₂ Surfaces

Mats Göthelid,¹ Shun Yu,¹ Sareh Ahmadi,¹ Chenghua Sun,^{1,2} and Marcelo Zuleta³

¹Materialfysik, ICT, KTH, Electrum 229, 16440 Stockholm, Sweden

²The University of Queensland, ARC Centre of Excellence for Functional Nanomaterials and Centre for Computational Molecular Science, Australia Institute for Bioengineering and Nanotechnology, The University of Queensland, Qld 4072, Australia

³Physical & Analytical Chemistry Department, Uppsala University, Lägerhyddsvägen 1, 752 37 Uppsala, Sweden

Correspondence should be addressed to Mats Göthelid, gothelid@kth.se

Received 31 May 2010; Accepted 17 August 2010

Academic Editor: J. Anthony Byrne

Copyright © 2011 Mats Göthelid et al. This is an open access article distributed under the Creative Commons Attribution License, which permits unrestricted use, distribution, and reproduction in any medium, provided the original work is properly cited.

The role of 4-tert butyl pyridine (4TBP) adsorption on TiO₂ surface band bending has been studied using photoelectron spectroscopy. Surface oxygen vacancies pin the Fermi level near the conduction band edge on rutile (110). 4TBP preferentially adsorbs in those vacancies and shift the Fermi level to lower binding energy in the band gap. This is done by transferring vacancy excess charge into the empty π^* orbital in the pyridine ring. The anatase (100) surface contains much less oxygen vacancies although the surface is much rougher than the rutile (110). 4TBP adsorption does not have any significant effect on the surface band bending. Thus the positive role associated with 4TBP addition to solar cell electrolytes is suggested to protection against adsorption of other electrolyte components such as Li and I.

1. Introduction

Dye sensitized solar cells (DSSCs) are very complex with a working electrode made of a TiO₂ nanostructured network decorated by light harvesting dye molecules contacted to a counter electrode through an electrolyte [1]. It was discovered many years ago that addition of 4-terbutyl pyridine (4TBP) to an (I₃⁻/I⁻) electrolyte increases the fill factor and the open circuit voltage (V_{oc}) from 0.38 to 0.72 V, while the short circuit current is not influenced [2]. Several explanations have been put forward, including 4TBP-induced band bending towards lower binding energies [3], reduction of the amount of adsorbed protons, Li⁺ and/or other cations present in the electrolyte [4, 5], decreasing the electron recombination from TiO₂ to tri-iodide in the electrolyte by blocking the tri-iodide from reaching the surface [5] or removing adsorbed iodine [6].

Surface or interface defects are known to alter the electrical properties of semiconductor contacts [7] and this is the case also for DSSC's. Oxygen vacancies are commonly observed on oxides and they play a significant role on the surface properties [8, 9]. Naturally the density and character

of those defects determine the Fermi level position at the interface. The removal of oxygen from TiO₂(110) leave charged vacancies with Ti³⁺ ions. This process generates surface states located within the band gap, ~1 eV below the Fermi level, that controls the Fermi level position [8, 10, 11]. Measurements on nanocrystalline TiO₂ indicated that 4TBP reduces the density of defects and the charge carrier recombination [12], through bonding to specific sites. Whether 4TBP prefers to adsorb at those "specific sites" or not, and whether this is the essential reason for the band shift have not been clarified. This is not an easy task since solar cells contain nanocrystalline TiO₂ which has the potential to hold a multitude of various structures and defects; thereby it is very difficult, not to say impossible, to make a unique identification of the essential contribution of each and every one of those defects to the observed shift. Although single crystal substrates are far from realistic in a solar cell they allow for preparation of surfaces with reasonably well controlled amounts and types of defects. In a recent paper we showed that 4TBP prefers to bind directly to oxygen vacancies on rutile TiO₂(110) giving a 0.2 eV upward shift of the band edges through a combination of photoelectron

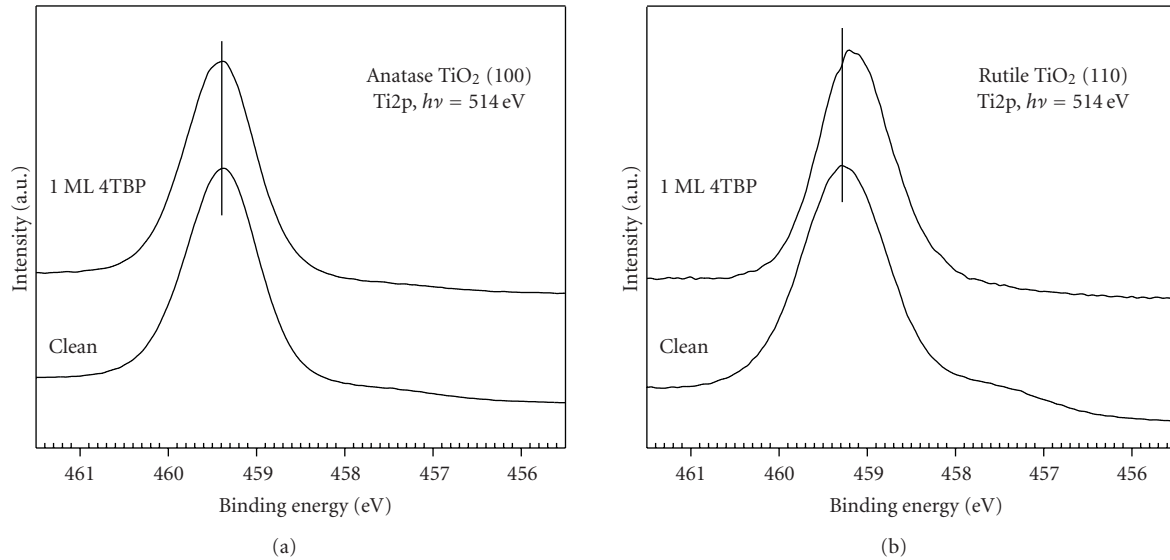


FIGURE 1: Ti2p spectra from clean and 4TP-covered TiO₂(100) and TiO₂(110) surfaces. The photon energy was 514 eV.

spectroscopy (PES) and density functional theory (DFT) [13]. In this paper, we extend this study to compare with anatase TiO₂(100). Contrary to the rutile surface we do not observe oxygen vacancies and the band edges do not shift upon 4TBP adsorption. Based on the present result one can suggest that the major role of 4TBP in DSSC electrolyte is to protect the surface from adsorption of ionic components in the electrolyte. However, more work is needed to clarify this in detail since nanostructured TiO₂ contains many crystal planes and adsorption sites.

2. Experimental Methods

Experiments were done at beamline I511-1, MAX-lab, Lund, Sweden. This is an undulator-based beamline giving horizontally polarized light between 100 and 1200 eV selected by a modified Zeiss SX-700 monochromator. Photoelectron spectra were recorded using a Scienta R4000 spectrometer which is rotatable around the axis of the photon beam in the analysis chamber. The preparation chamber holds a sputter gun, sample annealing, and low energy electron diffraction (LEED) optics. The base pressure was lower than 1×10^{-10} mbar. A load lock chamber is connected to the preparation chamber for fast sample entry and molecule deposition.

The rutile TiO₂(110) crystal was aligned to within 0.2° from the (110) plane and purchased from Surface Preparation Laboratory, the Netherlands. Thermal treatment above 1000 K for two hours in UHV generates bulk oxygen vacancies, changing the sample color from transparent to blue and increasing the conductivity. Before each deposition, the surface was cleaned by several rounds of Ar⁺ sputtering followed by annealing in UHV, which gave a sharp (1×1) LEED pattern. The anatase sample was $10 \times 3 \times 1$ mm³ aligned to $\approx 0.1^\circ$ from the (100) plane purchased from Surface Preparation Laboratory. The sample was cleaned by

repeated cycles of Ar⁺-sputtering and annealing at 550°C, until a sharp LEED pattern was obtained. The sputtering was conducted varying the sputter energy from low energy (50–400 eV) to higher energy up to 1000 eV. The argon pressure, P_{Ar^+} , was $2.0 \cdot 10^{-7}$ mbar. The annealing was performed during 45 min.

4TBP (Sigma-Aldrich, 99% purity) was dosed, after a few pumping cycles, at room temperature through a precision leak valve on the load lock. The base pressure in the load lock was 6×10^{-10} mbar. During deposition the substrate was held at room temperature. Formation of the saturated single monolayer is reached when spectra do change, neither from molecule nor from substrate after further exposure. Photoelectron spectra of core level and valence band were collected after each deposition. To avoid beam damage to the organic layers, the sample was moved ($0.1 \mu\text{m}/\text{min}$) during X-ray exposure. The energy scale was calibrated to the Fermi level, recorded from a tantalum foil in electrical contact with the sample.

3. Results and Discussion

A set of Ti2p_{3/2} spectra is plotted in Figure 1, the left hand side from anatase TiO₂(100) and the right hand side from rutile TiO₂(110). The lower spectra are from the clean substrate and spectra above after deposition of one 4TBP monolayer (ML). On the clean anatase surface the bulk peak lies at 459.4 eV, while on the rutile surface it is at 459.3 eV. In the spectrum from the rutile surface there is an additional weak hump around 457.5 eV due to Ti³⁺, either at the surface or in the bulk. The surface related Ti³⁺ ions are located in the oxygen vacancies, generated from removal of bridging oxygen. This peak is hardly visible on anatase, suggesting a much lower density of oxygen vacancies. On a well-prepared rutile (110) surface the density of oxygen vacancies is around 8% [14]. Adsorption of one ML of 4TBP on anatase (100)

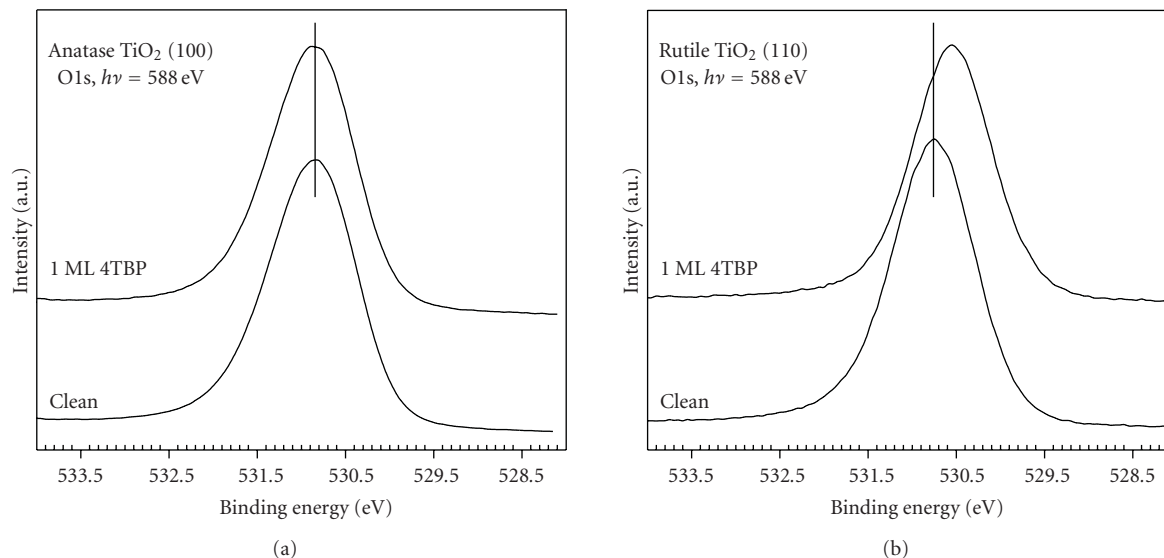


FIGURE 2: O1s spectra from clean and 4TBP covered $\text{TiO}_2(100)$ and $\text{TiO}_2(110)$ surfaces. The photon energy was 588 eV.

does not induce any shape changes of the spectral line; moreover the binding energy is unaffected and no new shifted peaks appear. On the contrary on rutile (110) the Ti^{3+} related component is strongly reduced, which even happens at low coverage [13]. This result clearly indicates that the O-vacancy is a preferred bond site for 4TBP. In addition, the main Ti^{4+} peak shifts 0.2 eV to lower binding energy. Such shifts indicate adsorption-induced band bending, in line with previous work [3–6].

Figure 2 shows O1s spectra from the same surfaces and preparations as in Figure 1. Spectra from the pristine surfaces, bottom spectra, contain only one component at 530.85 eV. Upon adsorption of 1 ML of 4TBP the line shapes are essentially unaffected. The binding energy on anatase does not change while O1s from rutile shifts to lower binding energy by 0.25 eV. This result agrees with Ti2p, and 4TBP induces surface band bending on rutile but not on anatase. It was previously observed that O1s shifts back to lower binding energy after healing the oxygen vacancies with oxygen [11]. Our observation of a shift to lower binding energy and the removal of Ti^{3+} from Ti2p spectra support that finding and suggest that 4TBP reduces the surface charge on rutile TiO_2 .

C1s spectra from three different coverages are shown in Figure 3; 0.02 ML, 0.2 ML, and 1 ML from both substrates. The coverage was determined from setting the intensity at saturation to 1 ML. Other spectra were normalized to this intensity. There may be errors related to this treatment, in particular for the lowest coverage, but the exact coverage is not of central importance here. The spectra from the lowest coverage are broader than that at monolayer coverage, but no shifted components are resolved. What is clear though is a shift to higher binding energy with increasing coverage. The monolayer binding energies are 286.2 eV on anatase and 285.9 eV on rutile, while the 0.2 ML binding energies are 285.6 eV on anatase and 285.3 eV on rutile and finally at the lowest coverage the binding energies are 285.3 eV on anatase and 285.05 on rutile. Thus there is a general trend

that binding energies are lower on rutile than on anatase by 0.3 eV. Therefore, it can be concluded that the coverage-dependent shifts to higher binding energy are same for the two surfaces.

It is known from previous studies that 4TBP adsorbs in an upright geometry with nitrogen coordinating to incompletely coordinated titanium; as suggested from Raman spectroscopy, IR spectroscopy and XPS on nanocrystalline anatase [6] and density functional theory for 4TBP on $\text{TiO}_2(110)$ [15]. Furthermore, our previous DFT optimizations showed that 4TBP prefers standing up both on fivefold coordinated Ti (Ti^{5f}) and oxygen vacancies, even if other geometries are set as the starting geometry [13]. The bonding has two main contributions; a σ -type Ti-N contribution and a $\text{Ti}3d-\pi^*$ contribution.

The band bending to lower binding energy implies a charge transfer from the oxygen vacancies into the 4TBP empty π^* orbitals on the carbon ring. Such charge transfer ceases when the vacancies are filled, which is seen in the saturation of the Ti2p and O1s core level shifts, that is, the band bending, while the C1s core level continues to shift with the adsorption of 4TBP. Using the core level binding energy as a simple measure of the local electron density, it is found that higher surface density of 4TBP reduces the average charge on the molecules. This is not surprising and can be understood as due to dipole repulsion, which is distance dependent and charge dependent. The dipole repulsion thus redistributes the charge within the molecular layer and reducing the charge on each molecule allowing a higher density. Our observation thus implies that the σ -type Ti-N bond dominates the $\text{Ti}3d-\pi^*$ bond in determining the bond site and bond strength.

The coverage-dependent shift is similar on anatase despite the lack of band bending and oxygen vacancies. This would suggest that the molecule-molecule repulsion is similar within the 4TBP layer. It also indicates that the molecular dipoles are comparable and that the average

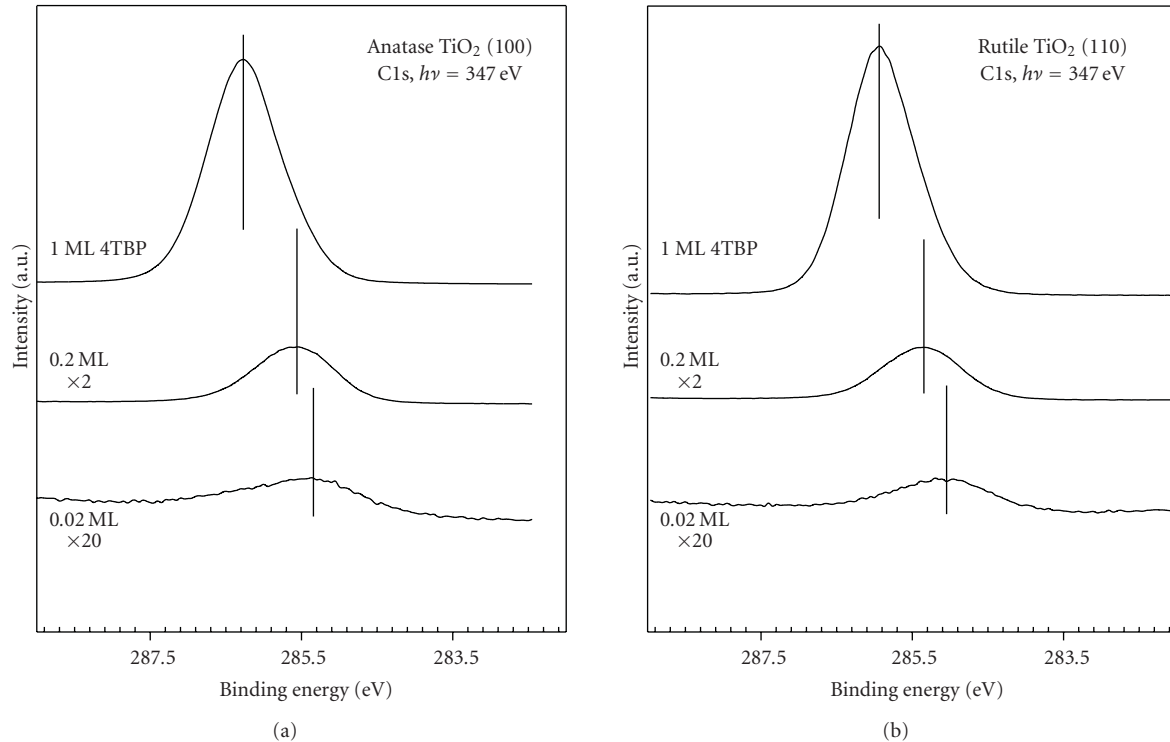


FIGURE 3: C1s spectra from 4TBP at different coverages. Incident photon energy 347 eV.

charge transferred is similar. On the other hand, there is a difference in binding energy, 0.3 eV higher on anatase than on rutile. This could indicate a larger charge transfer on rutile than on anatase, presumably due to the oxygen vacancies. However, the binding energy of a core level is a complex function of charge density, initial state effects, and flexibility in the system upon ionization, final state effects. The screening of the ionic molecule will be influenced by the substrate, to the distance and availability and mobility of electrons. On a semiconductor it will also be influenced by the Fermi level position and surface band bending. Taking the core level to valence band edge as a measure of the core level binding energy we can conclude that the C1s binding energy on rutile shifts more than that on anatase, thus supporting a larger charge transfer due to the oxygen vacancies. It is also clear that there is a coverage-dependent variation in the charge density on the carbon ring and thus charge transfer does happen on anatase, just not large enough to induce band bending as observed on rutile.

Spectra from the top of the valence band (VB) from clean and 4TBP covered surfaces are shown in Figure 4. This region includes the valence band edge and the vacancy-induced state in the band gap. Note that the intensity scales are the same in spectra from the same surface but different in spectra from the two surfaces. This is to enhance line profile. The gap state is located at approximately 0.9 eV below Fermi level on rutile and is attributed to nonbonding Ti3d electrons at oxygen vacancies. Other origins have been discussed, but the oxygen vacancy is by far the largest contributor on TiO₂(110) [9, 16, 17].

Adsorption of 1 ML 4TBP on rutile shifts of the whole VB towards the vacuum level by ~ 0.2 eV, as seen at the band edge just above 3.1 eV binding energy. The edge is not sharp and the exact binding energy position is not easily extracted, especially after adsorption. Instead we use the shift of a stronger peak in the valence band (not shown). Adsorption of 4TBP also reduces the surface state intensity. This reduction is much stronger than the intensity reduction of the rest of the valence band (not shown). However, the gap state is not completely removed and the remains may be assigned to other kinds of defects such as subsurface vacancies and interstitials that are not within reach for the 4TBP [17].

On anatase the intensity of the state is lower than on rutile and it does not change upon 4TBP adsorption, see Figure 4(a). This suggests that oxygen vacancies are not present on this surface, or that if they are they do not play a significant role in the adsorption process. The small intensity thus stems from subsurface vacancies, interstitials, or impurities. The anatase sample was cut from a natural crystal and may contain small amounts of impurities. The band edge at 3.25 eV stays firm, in agreement with the absence of core level shifts in Ti2p and O1s. The peak at 1 eV also retains its binding energy. One striking observation is the Fermi edge, the surface is metallic. This is not visible; the intensity scale is adapted for the whole valence band spectrum. However, when scaled differently it is obvious. A possible reason for this metallicity is subsurface impurities, which varies between samples from different sources and preparation methods.

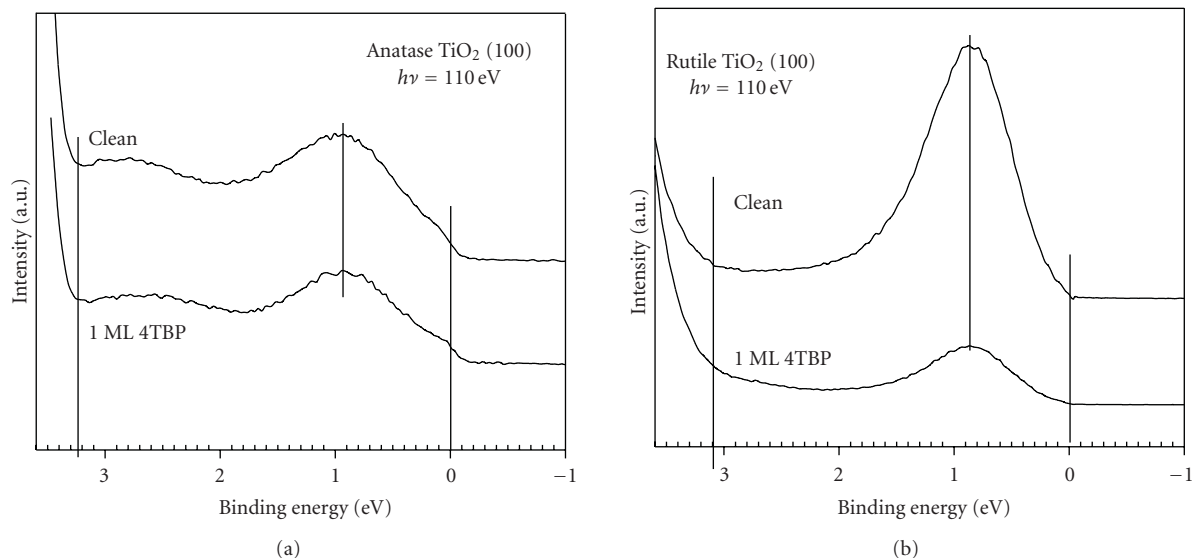


FIGURE 4: Spectra from the top of the valence band and the Fermi level region from 4TBP/TiO₂ interfaces compared with that of clean samples.

4. Summary and Conclusions

The appearance of oxygen vacancies on rutile TiO₂(110) plays a key role in determining the Fermi level position. The removal of oxygen leaves a charged vacancy with two unpaired electrons in the 3d orbitals [18, 19]. 4TBP adsorbs preferentially in those vacancies and moves the surplus charge from the surface into the π^* orbitals on the 4TBP carbon ring. Removal of the additional surface electrons shifts the Fermi level 0.2 eV towards lower binding energy. Following adsorption on five coordinated surface Ti, does not further change the band bending, but the dipole repulsion between 4TBP redistributes the charge within the molecular layer. This is seen through a coverage-dependent C1s core level shift.

Our results point to a low density of oxygen vacancies on anatase TiO₂(100); the Ti³⁺ state in the Ti2p core level and the state in the band gap are much smaller than on rutile, and they do not change upon 4TBP adsorption. Furthermore, the Fermi level position with respect to the band edges is insensitive to 4TBP adsorption. The coverage dependent molecular dipole repulsion is observed also on this surface. From the above discussion the increased output voltage from cells with 4TBP added to the electrolyte [2] cannot be explained by a surface band bending due to oxygen vacancies in the case of anatase. Its positive role as additive in DSSC is suggested to protect the surface from adsorption of ionic components on the electrolyte. However, the solar cell material, nanostructured TiO₂, is not made from (100) oriented crystallites and our results do not necessarily represent a realistic situation. More work, both experimental and theoretical, is indeed needed before a final conclusion can be made.

Acknowledgments

The authors acknowledge Dr. Tomas Edvinsson, Dr. Gerrit Boschloo, Dr. Shanghua Li, and Dr. Jian Qin for helpful discussions. Great thanks go to the kind staff at Max-lab. The Swedish Energy Agency (STEM), the Swedish Research Council (VR), the Göran Gustafsson, Carl Trygger Foundations, and Queensland government are kindly acknowledged for financial support.

References

- [1] B. O'Regan and M. Grätzel, "A low-cost, high-efficiency solar cell based on dye-sensitized colloidal TiO₂ films," *Nature*, vol. 353, no. 6346, pp. 737–740, 1991.
- [2] M. K. Nazeeruddin, A. Kay, I. Rodicio et al., "Conversion of light to electricity by cis-X2bis(2,2'-bipyridyl-4,4'-dicarboxylate)ruthenium(II) charge-transfer sensitizers (X = Cl⁻, Br⁻, I⁻, CN⁻, and SCN⁻) on nanocrystalline TiO₂ electrodes," *Journal of the American Chemical Society*, vol. 115, no. 14, pp. 6382–6390, 1993.
- [3] G. Schlichthörl, S. Y. Huang, J. Sprague, and A. J. Frank, "Band edge movement and recombination kinetics in dye-sensitized nanocrystalline TiO₂ solar cells: a study by intensity modulated photovoltage spectroscopy," *Journal of Physical Chemistry B*, vol. 101, no. 41, pp. 8141–8155, 1997.
- [4] S. Nakade, T. Kanzaki, W. Kubo, T. Kitamura, Y. Wada, and S. Yanagida, "Role of electrolytes on charge recombination in dye-sensitized TiO₂ solar cell (1): the case of solar cells using the I⁻/I₃⁻ redox couple," *Journal of Physical Chemistry B*, vol. 109, no. 8, pp. 3480–3487, 2005.
- [5] G. Boschloo, L. Häggman, and A. Hagfeldt, "Quantification of the effect of 4-tert-butylpyridine addition to I⁻/I₃⁻ redox electrolytes in dye-sensitized nanostructured TiO₂ solar cells," *Journal of Physical Chemistry B*, vol. 110, no. 26, pp. 13144–13150, 2006.

- [6] C. Shi, S. Dai, K. Wang, X. Pan, F. Kong, and L. Hu, "The adsorption of 4-tert-butylpyridine on the nanocrystalline TiO₂ and Raman spectra of dye-sensitized solar cells in situ," *Vibrational Spectroscopy*, vol. 39, no. 1, pp. 99–105, 2005.
- [7] W. Mönch, *Semiconductor Surface and Interfaces*, Springer, Berlin, Germany.
- [8] A. L. Linsebigler, G. Lu, and J. T. Yates Jr., "Photocatalysis on TiO₂ surfaces: principles, mechanisms, and selected results," *Chemical Reviews*, vol. 95, no. 3, pp. 735–758, 1995.
- [9] U. Diebold, "The surface science of titanium dioxide," *Surface Science Reports*, vol. 48, no. 5–8, pp. 53–229, 2003.
- [10] E. L. D. Hebenstreit, W. Hebenstreit, H. Geisler et al., "Sulfur on TiO₂(110) studied with resonant photoemission," *Physical Review B*, vol. 64, no. 11, Article ID 115418, pp. 1–11, 2001.
- [11] K. E. Smith, J. L. MacKay, and V. E. Henrich, "Interaction of SO₂ with nearly perfect and defect TiO₂(110) surfaces," *Physical Review B*, vol. 35, no. 11, pp. 5822–5829, 1987.
- [12] M. Dürr, A. Yasuda, and G. Nelles, "On the origin of increased open circuit voltage of dye-sensitized solar cells using 4-ferf-butyl pyridine as additive to the electrolyte," *Applied Physics Letters*, vol. 89, no. 6, Article ID 061110, 2006.
- [13] S. Yu, S. Ahmadi, P. Palmgren, F. Hennies, M. Zuleta, and M. Göthelid, "4-tert-butyl pyridine bond site and band bending on TiO₂(110)," *Journal of Physical Chemistry C*, vol. 114, pp. 2315–2320, 2009.
- [14] P. Palmgren, B. R. Priya, N. P. P. Niraj, and M. Göthelid, "Bonding of metal-free phthalocyanine to TiO₂(110) single crystal," *Solar Energy Materials and Solar Cells*, vol. 90, no. 20, pp. 3602–3613, 2006.
- [15] B.-T. Xiong, B.-X. Zhou, Z.-Y. Zhu et al., "Adsorption of 4-tert-butylpyridine on TiO₂ surface in dye-sensitized solar cells," *Chinese Journal of Chemistry*, vol. 26, no. 1, pp. 70–76, 2008.
- [16] C. M. Yim, C. L. Pang, and G. Thornton, "Oxygen vacancy origin of the surface band-gap state of TiO₂(110)," *Physical Review Letters*, vol. 104, no. 3, Article ID 036806, 2010.
- [17] S. Wendt, P. T. Sprunger, E. Lira et al., "The role of interstitial sites in the Ti3d defect state in the band gap of titania," *Science*, vol. 320, no. 5884, pp. 1755–1759, 2008.
- [18] T. Bredow and G. Pacchioni, "Electronic structure of an isolated oxygen vacancy at the TiO₂(1 1 0) surface," *Chemical Physics Letters*, vol. 355, no. 5-6, pp. 417–423, 2002.
- [19] B. J. Morgan and G. W. Watson, "A DFT + *U* description of oxygen vacancies at the TiO₂ rutile (1 1 0) surface," *Surface Science*, vol. 601, no. 21, pp. 5034–5041, 2007.

Research Article

Nanocomposite Hole-Extraction Layers for Organic Solar Cells

Jiao Li,^{1,2} Juncheng Liu,¹ Congjie Gao,² and Guohua Chen²

¹ School of Materials Science and Engineering, Shandong University of Technology, Zibo 255049, China

² College of Chemistry and Chemical Engineering, Ocean University of China, Qingdao 266003, China

Correspondence should be addressed to Juncheng Liu, jchliu01@163.com

Received 15 August 2010; Accepted 9 November 2010

Academic Editor: Mohamed Sabry Abdel-Mottaleb

Copyright © 2011 Jiao Li et al. This is an open access article distributed under the Creative Commons Attribution License, which permits unrestricted use, distribution, and reproduction in any medium, provided the original work is properly cited.

The influence of nanocomposite hole-extraction layers on the performance of organic photovoltaic (OPV) cells based on blends of poly(3-hexylthiophene) (P₃HT) and [6,6]-phenyl-C-61-butyric acid methyl ester (PCBM) has been investigated. The hole-extraction layers consist of poly(3,4-ethylene dioxythiophene) polystyrene sulfonic acid (PEDOT:PSS) doped with different concentrations of multiwall carbon nanotubes (MWCNTs). Compared with a pristine device (i.e., without MWCNTs), the MWCNTs-doped OPV cells shows an improved short-circuit current density, fill factor, and power conversion efficiency from 8.82 to 9.03 mA/cm², 0.43 to 0.474, and 2.12% to 2.39% (i.e., by about 13%), respectively. Reasons for the improved performance of the devices are discussed. It shows that the reduction of series resistance of the devices might be correlated with the improvement of the OPV cells, performance achieved through the incorporation of MWCNTs into the hole-extraction layer of PEDOT:PSS.

1. Introduction

Organic photovoltaic (OPV) cells have attracted much attention in recent years due to their advantages of low-cost manufacturing, light weight, and good flexibility [1–4]. OPV cells are thin film structures, in which organic photoactive materials are sandwiched between two electrodes. The ITO glass is generally employed as the anode in OPV cells because of its good electrical conductivity, high transparency over the visible region, and ease of patterning. However, the work function of ITO is quite low (~ 4.6 eV) [5]. As a result, great efforts have been made to modify the ITO anode, such as various treatments of the ITO surface [6, 7] and the deposition of very thin buffer layers between the ITO and the photoactive layer [8–10] in order to enhance OPV cells, performance. Thin films of PEDOT:PSS are well known as efficient hole-extracting layers in OPV cells, combining a high work function [11], good optical transparency, and ease of processing from solution [12, 13]. But, it was observed that applying this extra PEDOT:PSS layer results in a decrease of the short-circuit current (I_{sc}) and fill factor (FF) owing to the bulk resistance of PEDOT:PSS [14]. In addition, it has also been suggested that the increase of series resistance will reduce the effective internal electric field

in the active layer, which is essential for efficient charge collection to the electrodes from an organic photovoltaic model [15]. Therefore, the conductivity of PEDOT:PSS plays an important role in the polymer solar cells.

Devices with a better performance were achieved by inclusion of some good conductivity filler in the hole extraction layer. It has been reported that adding polyalcohols to PEDOT:PSS increases the conductivity and improves the efficiency of polymer PVs [16, 17]. Ko et al. [18] reported that improved power conversion efficiency has been observed by reducing the resistance of PEDOT:PSS after doping mannitol into the PEDOT:PSS.

Carbon nanotubes (CNTs) can also serve as a good filler for conducting polymer. It has been reported that incorporating CNTs into conventional conducting polymers improves the conductivity of CNTs/polymer composites by many orders of magnitude [19–23], which could be attributed to CNTs' large contact area, high dimensional aspect ratio, and exceptional electrical conductivity [24]. Our previous studies found that the conductivity of the PEDOT:PSS films increased drastically after inclusion of MWCNTs fillings [25].

In this article, the PEDOT:PSS doped with multi-walled carbon nanotubes (MWCNTs) film was fabricated and used

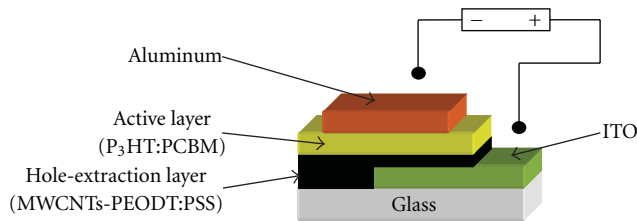


FIGURE 1: Schematic device structure for organic solar cells doped with MWCNTs.

as hole-extraction layer for OPV cells. The effect of MWCNTs concentration on the photovoltaic performance of the device based on P₃HT:PCBM blend was investigated. Reasons for the improved performance of the devices were also discussed.

2. Experimental

Multi-walled carbon nanotubes (MWCNTs) (diameter: 10~30 nm, length: 5~15 μm , purity: >95%) were purchased from Beijing Nachen Nanotech Co. Ltd., and the MWCNTs were further purified with strong acid. In a typical procedure, 30 mg of MWCNTs was added into an acid solution of concentrated sulphuric acid (15 mL) and concentrated nitric acid (5 mL). The mixture was ultrasonicated for 20 minutes, stirred for 1 hour in reflux at 130°C, vacuum filtered through a 0.2 μm milli-pore polycarbonate membrane, washed with excess-distilled water until the pH 7.0, and filtrated then dried under vacuum for 12 h at 60°C.

PEDOT:PSS aqueous solution (1.3 wt% dispersed in H₂O) from Aldrich (as supplied) was filtered with a 0.45 μm polyvinyl difluoride (PVDF) syringe filter. Some amount of acid-treated MWCNTs were added into the PEDOT:PSS solution to form the nanocomposites. The composites were treated in ultrasonic bath for about 12 hours before using for spin coating.

All the devices in this work were fabricated using indium-tin-oxide- (ITO-) coated glass substrates (<10 Ω/\square). The ITO substrates were ultrasonically cleaned with a series of organic solvents (ethanol, methanol, and acetone), then rinsed in ultrasonic bath with deionized water and dried in a vacuum oven. Residual organic contaminations were subsequently removed by exposing to a UV-ozone lamp for 30 min. Nanocomposites of MWCNTs and PEDOT:PSS were spin coated on top of the ITO surface to form an (90–100 nm) layer before drying the substrates at 120°C in an oven for more than 30 min. The P₃HT:PCBM was dissolved in dichlorobenzene at a weight ratio of 1 : 0.8 and stirred for more than 72 h in the glovebox before spin casting to form the blend layer. Finally an Al electrode of about 100 nm in thickness was deposited by thermal evaporation at a pressure of 2.4×10^{-4} Pa through a shadow mask. No buffer layer between the organic layer and cathode is used. The basic structure of the OPV devices is shown in Figure 1.

The surface morphology of MWCNTs was carried out by field emission scanning electron microscopy (FESEM, JEOL,

JSM-6335 F). The optical property of the composite films was characterized with a TU-1901 Dual-beam UV-Visible spectrophotometer. Current density-voltage (I-V) characteristics of the PV cells were measured using a computer-controlled Keithley 2400 Source Meter in the dark and under a simulated light intensity of 100 mW/cm² (AM 1.5 G) calibrated by an optical power meter from a halogen lamp. The power conversion efficiency (PCE) was calculated from the I-V characteristics. The devices were tested in air without encapsulation.

3. Results and Discussion

Figure 2. compares the surface morphology of the MWCNTs before acid treatment (Figure 2(a)) and after acid treatment (Figure 2(b)). It can be see that particle-like impurity of MWCNTs is removed and the morphology, as in terms of the surface smoothness, is improved after the acid treatment. Moreover, the MWCNTs after acid treatment can be dispersed into aqueous PEDOT:PSS solution and no precipitation is observed in the solution after several weeks.

The transmittance of the nanocomposites is shown in Figure 3. The pristine PEDOT:PSS film gives a good optical transmittance (93.2% average) on the wavelength range from 550 nm to 950 nm, which corresponds to the power density of ambient sunlight on the Earth's surface [26]. However, the transmittance of PEDOT : PSS film decreases with increasing amount of MWCNTs. With the MWCNTs concentration increasing to 0.20 wt%, the transmittance of composite film dropped by 7.5% (86.2% average). This may result from the formation of the conductive network of MWCNTs and some absorptions of MWCNTs in the above wavelength range [27, 28].

Solar cells generally have a series resistance and shunt resistance associated with them. In practice, a high shunt resistance and a low series resistance are required simultaneously for an ideal photovoltaic device [29]. The shunt resistance usually reflects the degree of leakage current through the device, which relates to the overall quality of the films. Meanwhile, the series resistance is attributed to the ohmic loss in the whole device, which includes the resistance of the active layer, metal-organic contacts, the electrodes, and the conductivity of the hole-extraction layer [30].

The influence of the doping on the shunt resistance of the device can be observed in the I-V curves under lower bias in the dark. As appeared in Figure 4, at reverse negative bias and at the linear regime of forward bias, where the current is limited by shunt resistance due to the leakage current, the current gradually increases with the dopant concentration. The increasing current with doping concentration may be induced by random leakage current in higher conductivity M-PEDOT:PSS layer. Some phase separation and more defects caused by MWCNTs-doping in the PEDOT:PSS may have induced some leakage current through the device.

Figure 5 shows the current density-voltage curves of photovoltaic cells with different doping concentrations of MWCNTs in the PEDOT:PSS. The detailed parameters of devices are summarized in Table 1.

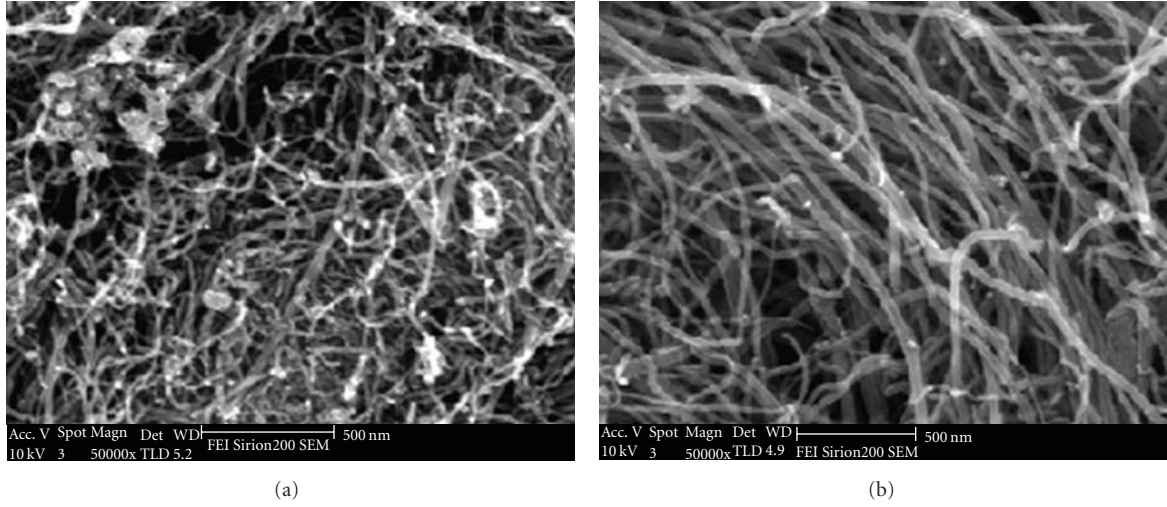
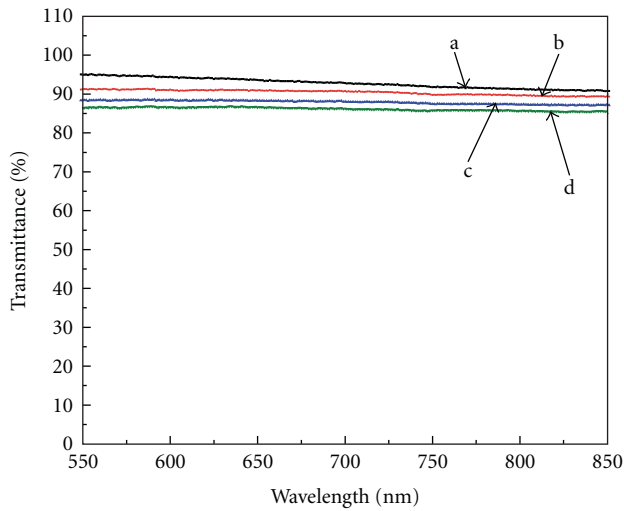


FIGURE 2: SEM of untreated and treated MWCNTs- (a) untreated MWCNTs; (b) treated MWCNTs

TABLE 1: PV parameters of OPVs for MWCNTs doping.

Style	Structure	V_{oc} (V)	I_{sc} (mA/cm ²)	FF (%)	η (%)
A	ITO/PEDOT:PSS/P ₃ HT:PCBM/Al	0.56	8.82	43.0	2.12%
B	ITO/M (0.04 wt%)-PEDOT:PSS/P ₃ HT:PCBM/Al	0.56	9.03	47.4	2.39%
C	ITO/M (0.10 wt%)-PEDOT:PSS/P ₃ HT:PCBM/Al	0.55	9.52	44.8	2.35%
D	ITO/M (0.20 wt%)-PEDOT:PSS/P ₃ HT:PCBM/Al	0.55	9.34	43.4	2.22%



a: PEDOT:PSS c: M (0.1 wt%)-PEDOT:PSS
 b: M (0.04 wt%)-PEDOT:PSS d: M (0.2 wt%)-PEDOT:PSS

FIGURE 3: The optical transmittance of films as a function of weight fraction of MWCNTs.

A small change in V_{oc} with increase in MWCNTs amount was observed as shown in Table 1, where the values slightly vary around 0.56 V. It was found that the open circuit voltage of the solar cell correlates directly with the work function of the electrodes or the buffer layers, that is, it is determined by the work function of PEDOT:PSS film [14, 17]. So the

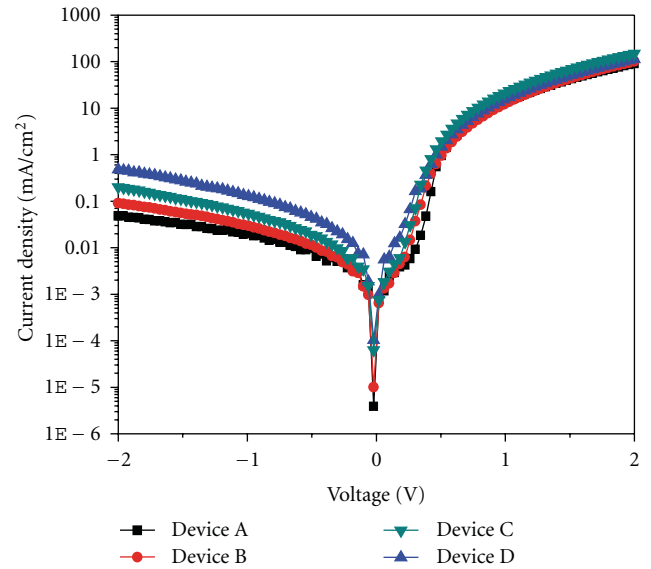


FIGURE 4: The dark I-V characteristics of devices with different concentrations of MWCNTs. Device A: pristine PEDOT:PSS film; Device B: M (0.04 wt%)-PEDOT:PSS film; Device C: M (0.10 wt%)-PEDOT:PSS film; Device D: M (0.20 wt%)-PEDOT:PSS film.

addition of MWCNTs into PEDOT:PSS may not affect the work functions of PEDOT:PSS films in the solar cell.

Table 1 also shows the increase in I_{sc} from about 8.82 mA/cm² of the reference device A (0 wt% doping) to

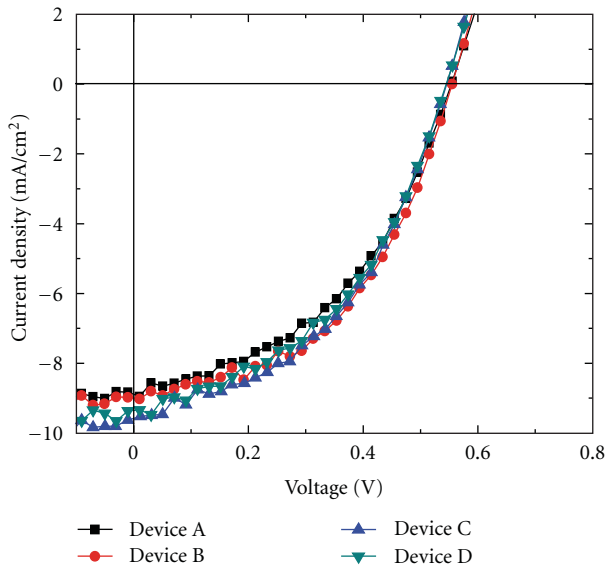


FIGURE 5: The I-V characteristics of devices with different concentrations of MWCNTs. Device A: pristine PEDOT:PSS film; Device B: M (0.04 wt%)-PEDOT:PSS film; Device C: M (0.10 wt%)-PEDOT:PSS film; Device D: M(0.20 wt%)-PEDOT:PSS film.

9.52 mA/cm² of the device C (0.10 wt% doping), and after that the I_{sc} decreases to become 9.34 mA/cm² of the device D (0.20 wt% doping). Since these devices are fabricated with the same materials and the same procedure, and the only difference is the hole-extraction layer, the increased current is unlikely on account of other reasons, but due to the high conductivity of the composite hole-extraction layers, leading to a lower series resistance of the device. The generated hole carriers in the P₃HT:PCBM active layer easily move into the anode through the MWCNTs-doped PEDOT:PSS layer. While the decrease in I_{sc} after adding more amount of MWCNTs may be due to the decrease of the transmittance of composite films in the wavelength around of 700 nm (as shown in Figure 3), which has effects on the photon absorption yield and the charge-carrier-transport yield of the PV cells [26]. The lowering of serial resistivity in hole-extraction layers with increased MWCNT concentration is also responsible for increase in the fill factor from 0.43 to 0.474. But as shown in Figure 4, extra amounts of the MWCNTs tend to decrease the OPV cells, shunt resistance, which can affect fill factor of OPV cells [29, 31]. Then lower fill factor is obtained in device C and device D.

The enhancement in both I_{sc} and FF by introducing MWCNTs into solar cell structure tends to cause improvement in the power conversion efficiency from 2.12% to 2.39%, that is, by about 13%.

4. Conclusion

In summary, We developed efficient OPV cells based on P₃HT:PCBM blend by incorporating MWCNTs into hole-extraction layer of PEDOT:PSS. Compared with the pristine OPV device without adding MWCNTs to the hole-extraction

layer, the MWCNTs-doped OPV cells show an improved short-circuit current density, fill factor, and power conversion efficiency from 8.82 to 9.03 mA/cm², 0.43 to 0.474, and 2.12% to 2.39% (i.e., by about 13%), respectively. The high electrical conductivity properties of the composite films might contribute to facility the hole-extraction and hole-transport ability of PEDOT:PSS, which leads to the reduction of series resistance of the devices.

Acknowledgment

Financial support from the program for New Century Excellent Talents in University (NCET, Grant no. NCET-04-0648) is gratefully acknowledged.

References

- [1] T. D. Nielsen, C. Cruickshank, S. Foged, J. Thorsen, and F. C. Krebs, "Business, market and intellectual property analysis of polymer solar cells," *Solar Energy Materials and Solar Cells*, vol. 94, no. 10, pp. 1553–1571, 2010.
- [2] B. Kippelen and J. L. Brédas, "Organic photovoltaics," *Energy and Environmental Science*, vol. 2, no. 3, pp. 251–261, 2009.
- [3] M. Helgesen, R. Søndergaard, and F. C. Krebs, "Advanced materials and processes for polymer solar cell devices," *Journal of Materials Chemistry*, vol. 20, no. 1, pp. 36–60, 2010.
- [4] F. C. Krebs, "Fabrication and processing of polymer solar cells: a review of printing and coating techniques," *Solar Energy Materials and Solar Cells*, vol. 93, no. 4, pp. 394–412, 2009.
- [5] D. Y. Kim, F. So, and Y. Gao, "Aluminum phthalocyanine chloride/C organic photovoltaic cells with high open-circuit voltages," *Solar Energy Materials and Solar Cells*, vol. 93, no. 9, pp. 1688–1691, 2009.
- [6] J. S. Kim, J. H. Park, J. H. Lee, J. Jo, D. Y. Kim, and K. Cho, "Control of the electrode work function and active layer morphology via surface modification of indium tin oxide for high efficiency organic photovoltaics," *Applied Physics Letters*, vol. 91, no. 11, pp. 2111–2113, 2007.
- [7] C. C. Wu, C. I. Wu, J. C. Sturm, and A. Kahn, "Surface modification of indium tin oxide by plasma treatment: an effective method to improve the efficiency, brightness, and reliability of organic light emitting devices," *Applied Physics Letters*, vol. 70, no. 11, pp. 1348–1350, 1997.
- [8] F. Liu, S. Shao, X. Guo, Y. Zhao, and Z. Xie, "Efficient polymer photovoltaic cells using solution-processed MoO₃ as anode buffer layer," *Solar Energy Materials and Solar Cells*, vol. 94, no. 5, pp. 842–845, 2010.
- [9] S. W. Tong, C. F. Zhang, C. Y. Jiang et al., "Improvement in the hole collection of polymer solar cells by utilizing gold nanoparticle buffer layer," *Chemical Physics Letters*, vol. 453, no. 1–3, pp. 73–76, 2008.
- [10] R. A. Hatton, N. P. Blanchard, L. W. Tan, G. Latini, F. Cacialli, and S. R. P. Silva, "Oxidised carbon nanotubes as solution processable, high work function hole-extraction layers for organic solar cells," *Organic Electronics*, vol. 10, no. 3, pp. 388–395, 2009.
- [11] T. M. Brown, J. S. Kim, R. H. Friend, F. Cacialli, R. Daik, and W. J. Feast, "Built-in field electroabsorption spectroscopy of polymer light-emitting diodes incorporating a doped poly(3,4-ethylene dioxythiophene) hole injection layer," *Applied Physics Letters*, vol. 75, no. 12, pp. 1679–1681, 1999.

- [12] G. Heywang and F. Jonas, "Poly(alkylenedioxythiophene)s—new, very stable conducting polymers," *Advanced Materials*, vol. 4, no. 2, pp. 116–118, 1992.
- [13] L. Groenendaal, F. Jonas, D. Freitag, H. Pielartzik, and J. R. Reynolds, "Poly(3,4-ethylenedioxythiophene) and its derivatives: past, present, and future," *Advanced Materials*, vol. 12, no. 7, pp. 481–494, 2000.
- [14] T. Aernouts, W. Geens, J. Poortmans, P. Heremans, S. Borghs, and R. Mertens, "Extraction of bulk and contact components of the series resistance in organic bulk donor-acceptor-heterojunctions," *Thin Solid Films*, vol. 403–404, pp. 297–301, 2002.
- [15] B. Mazhari, "An improved solar cell circuit model for organic solar cells," *Solar Energy Materials and Solar Cells*, vol. 90, no. 7–8, pp. 1021–1033, 2006.
- [16] F. Zhang, M. Johansson, M. R. Andersson, J. C. Hummelen, and O. Inganäs, "Polymer photovoltaic cells with conducting polymer anodes," *Advanced Materials*, vol. 14, no. 9, pp. 662–665, 2002.
- [17] F. L. Zhang, A. Gadisa, O. Inganäs, M. Svensson, and M. R. Andersson, "Influence of buffer layers on the performance of polymer solar cells," *Applied Physics Letters*, vol. 84, no. 19, pp. 3906–3908, 2004.
- [18] C. J. Ko, Y. K. Lin, F. C. Chen, and C. W. Chu, "Modified buffer layers for polymer photovoltaic devices," *Applied Physics Letters*, vol. 90, no. 6, Article ID 063509, 2007.
- [19] H. Peng and X. Sun, "Highly aligned carbon nanotube/polymer composites with much improved electrical conductivities," *Chemical Physics Letters*, vol. 471, no. 1–3, pp. 103–105, 2009.
- [20] Z. Yang, H. Pu, J. Yuan, D. Wan, and Y. Liu, "Phthalocyanines-MWCNT hybrid materials: fabrication, aggregation and photoconductivity properties improvement," *Chemical Physics Letters*, vol. 465, no. 1–3, pp. 73–77, 2008.
- [21] M. C. Wu, Y. Y. Lin, S. Chen et al., "Enhancing light absorption and carrier transport of P3HT by doping multi-wall carbon nanotubes," *Chemical Physics Letters*, vol. 468, no. 1–3, pp. 64–68, 2009.
- [22] K. R. Reddy, B. C. Sin, K. S. Ryu, J. C. Kim, H. Chung, and Y. Lee, "Conducting polymer functionalized multi-walled carbon nanotubes with noble metal nanoparticles: synthesis, morphological characteristics and electrical properties," *Synthetic Metals*, vol. 159, no. 7–8, pp. 595–603, 2009.
- [23] T. M. Wu, H. L. Chang, and Y. W. Lin, "Synthesis and characterization of conductive polypyrrole/multi-walled carbon nanotubes composites with improved solubility and conductivity," *Composites Science and Technology*, vol. 69, no. 5, pp. 639–644, 2009.
- [24] R. H. Baughman, A. A. Zakhidov, and W. A. De Heer, "Carbon nanotubes—the route toward applications," *Science*, vol. 297, no. 5582, pp. 787–792, 2002.
- [25] C. Gao, J. Li, J. Liu, J. Zhang, and H. Sun, "Influence of MWCNTs doping on the structure and properties of PEDOT:PSS films," *International Journal of Photoenergy*, vol. 2009, Article ID 650509, 5 pages, 2009.
- [26] B. R. Saunders and M. L. Turner, "Nanoparticle-polymer photovoltaic cells," *Advances in Colloid and Interface Science*, vol. 138, no. 1, pp. 1–23, 2008.
- [27] S. Ghosh and O. Inganäs, "Self-assembly of a conducting polymer nanostructure by physical crosslinking: applications to conducting blends and modified electrodes," *Synthetic Metals*, vol. 101, no. 1–3, pp. 413–416, 1999.
- [28] J. K. W. Sandler, J. E. Kirk, I. A. Kinloch, M. S. P. Shaffer, and A. H. Windle, "Ultra-low electrical percolation threshold in carbon-nanotube-epoxy composites," *Polymer*, vol. 44, no. 19, pp. 5893–5899, 2003.
- [29] H. Z. Yu and J. B. Peng, "Influence of the solvent and device structure on the performance of the MEH-PPV:PCBM solar cell," *Acta Physico-Chimica Sinica*, vol. 23, no. 10, pp. 1637–1641, 2007 (Chinese).
- [30] J. Xue, S. Uchida, B. P. Rand, and S. R. Forrest, "4.2% efficient organic photovoltaic cells with low series resistances," *Applied Physics Letters*, vol. 84, no. 16, pp. 3013–3015, 2004.
- [31] D. Gupta, S. Mukhopadhyay, and K. S. Narayan, "Fill factor in organic solar cells," *Solar Energy Materials and Solar Cells*, vol. 94, no. 8, pp. 1309–1313, 2010.

Research Article

Nanostructural Materials for Energy Storage Systems

Bronislaw Buczek

Faculty of Energy and Fuels, AGH University of Science and Technology, 30 Mickiewicza Avenue, 30-059 Cracow, Poland

Correspondence should be addressed to Bronislaw Buczek, bbuczek@agh.edu.pl

Received 31 August 2010; Revised 9 November 2010; Accepted 24 December 2010

Academic Editor: Mohamed Sabry Abdel-Mottaleb

Copyright © 2011 Bronislaw Buczek. This is an open access article distributed under the Creative Commons Attribution License, which permits unrestricted use, distribution, and reproduction in any medium, provided the original work is properly cited.

The aim of this study was to assess of carbonaceous monoliths used for adsorption cooling systems. The carbonaceous monoliths prepared from coal precursors are obtained. The porous structure of monoliths was evaluated on the basis of nitrogen adsorption-desorption data. The investigated monoliths have significantly developed microporous structure. The large specific area of carbonaceous monoliths (about 2000 m²/g) and volume of micropores are observed. Methanol adsorption isotherms and heat of wetting using methanol was determined. Results show that monoliths materials are high adsorption capacity of methanol and heat of wetting, which can improve of heat exchange and efficiency in processes of refrigeration and air conditioning.

1. Introduction

Processes of mass and energy storage with application of microporous adsorbent can be included into prospective directions of the adsorption technology development. The application of carbonaceous adsorbents for heat storage can be used in adsorptive refrigerators utilizing closed thermodynamic cycles [1]. The most interesting system is methyl alcohol and microporous carbon material pair [2]. Because of its ability to selectively adsorb vapours and gases, extended internal porosity, and large specific surface area, active carbon is a good adsorbent for storage of mass and energy [3]. Methanol is more easily desorbed, and its working pressure is always lower than atmospheric pressure, which allows for a rapid identification of any faults in a cooling system. The temperature of desorption of methanol from an adsorbent is considerably lower than for water vapour systems. For all these reasons the methanol-active carbon pair can be used for mass and energy storage.

The wide developing techniques of solar heating with use of different types of solar collectors found the use also in adsorption cooling system. The adsorption cooling system with solar collector was presented in Figure 1.

The performance of an adsorbent in a thermodynamic system depends upon properties such as specific area, type and number of pores, adsorbent form, and adsorption

enthalpy of the adsorbate and its thermal conductivity. Therefore, any method of modification of active carbon has to improve carbon structural features and to increase the heat and mass transfer [4].

The good adsorbent should have not only developed microporous structure but also large bulk density, which improve packing and heat conductivity on adsorbent bed [5]. It depends on shape of adsorbent: powder, granular, or disk monolith [6, 7]. We can increase the packing up of the particles in order to prepare microporous monoliths and simultaneously to increase heat conductivity of its bed.

Active carbon-methanol pair appears to be suitable for different adsorptive cooling systems. This pair can be successfully used as fridge for storage of food and medicines and ice manufacture, in air conditioning devices and heat pumps [8].

2. Experimental and Results

Investigations were carried on four carbonaceous monoliths. The aim of this study was to assess the monoliths used for adsorption cooling systems. The carbonaceous monoliths prepared from hard coal precursors are obtained from Faculty of Chemistry, Wroclaw University of Technology [9]. Preparations of carbon monoliths are presented in Figure 2.

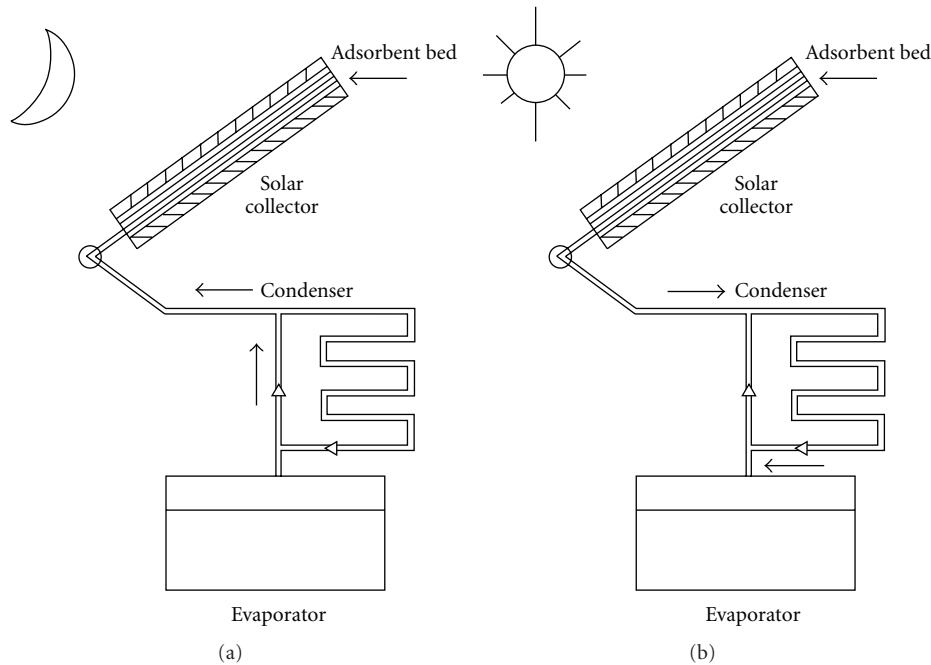


FIGURE 1: Scheme of adsorption solar refrigerator [8].

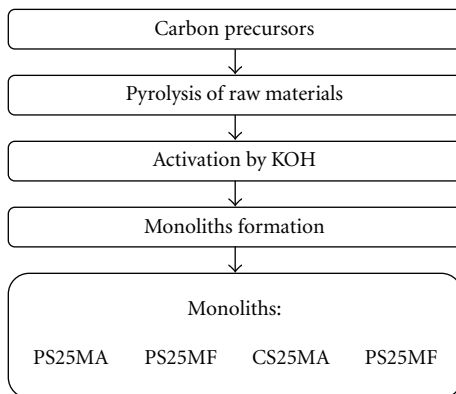


FIGURE 2: Preparation of carbon monoliths.

TABLE 1: Raw material characteristic of monoliths.

Monoliths	Carbon precursors	Binder
PS25MA	Semicoke from coal pitch from coking plant	10% polyvinyl alcohol (PVA)
PS25MF	Makoszowy	10% polyvinylidene fluoride (PVDF)
CS25MA	Semicoke from coal from coking plant	7,5% PVA
CS25MF	Szczygłowiec	8,5% PVDF

Powder product of activation by KOH was mixed with polymer binder, and then tablet was formed by 18mm diameter and 7–10 mm height. The technological characteristic and designation monoliths are presented in Table 1.

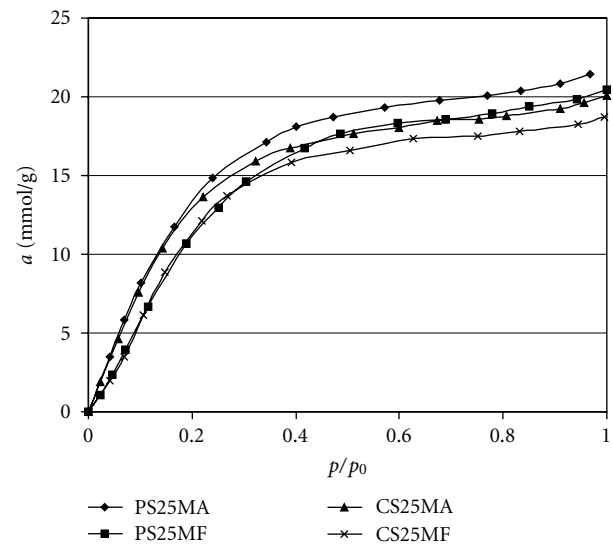


FIGURE 3: Methanol adsorption isotherms of monoliths.

2.1. Analysis of Porous Structure. The porous structure of monoliths were evaluated on the basis of nitrogen adsorption-desorption data. Isotherms were determined by a volumetric method using the Sorptomatic 1900 apparatus. Measurements were taken at a temperature of 77.5 K, and range of pressure was $p/p_0 = 0.00001 - 0.999$. The volumes of micropores (W_0) and characteristic energy of adsorption (E_0) have been determined according to Dubinin-Radushkevich equation [10], and specific surface area was obtained using the BET equation [11]. Total volume of micropores (V_p) has been read for nitrogen adsorption

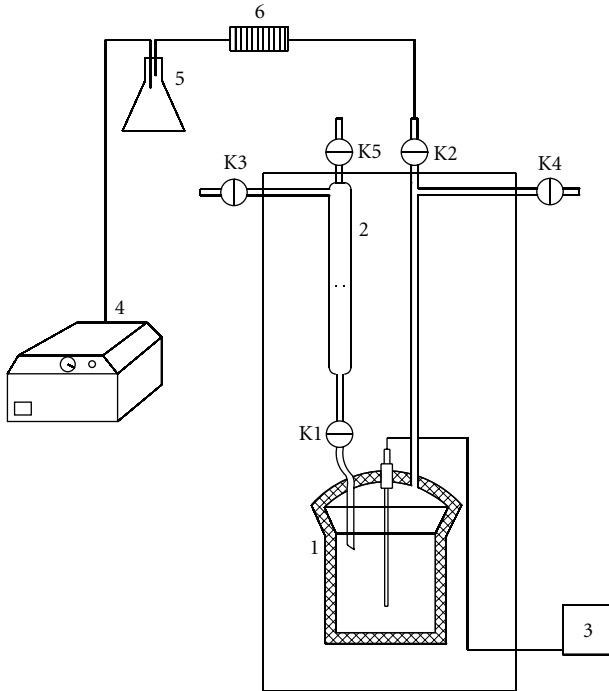


FIGURE 4: Scheme of equipment for measuring the heat of wetting: 1-calorimetric cell, 2-container of methanol, 3-electronic system to temperature measurement, 4-vacuum pump, 5-control vessel, 6-filter.

TABLE 2: Structural properties of monoliths.

Monolith	W_0 cm ³ /g	E_0 kJ/mol	S_{BET} m ² /g	V_p cm ³ /g
PS25MA	0.714	18.3	1910	0.925
PS25MF	0.672	18.1	1830	0.887
CS25MA	0.709	18.4	1880	0.876
CS25MF	0.689	18.4	1805	0.854

isotherms of value $p/p_0 = 0.99$. The results of calculations are shown in Table 2.

The carbonaceous monoliths are characterized by significantly developed microporous structure. They achieved a large volume of micropores (0.672–0.714 cm³/g) and very impressive specific surface area (1805–1910 m²/g). The biggest microporous structure for monoliths formed with polyvinyl alcohol (PVA) is observed.

2.2. Methanol Adsorption. Methanol adsorption isotherms of monoliths were measured volumetrically. The measurements were carried out in the temperature 298 K.

The adsorption isotherms of methanol vapours for monoliths are presented in Figure 3.

All of the samples readily adsorb methanol giving reversible isotherms of type I. Adsorption capacity decreases simultaneously when the temperature rises. It is characteristic for highly microporous adsorbent. The investigated monoliths have related structural properties, and the course of isotherms is very similar in whole range of pressures. The monolith PS25MA characterizes insensibly larger adsorptive

TABLE 3: Heat effect and heat of wetting of monoliths.

Monoliths	ΔT	Q , J/g	dT/dt
PS25MA	7.6	159.83	177.0
PS25MF	5.3	111.03	331.2
CS25MA	7.9	165.14	35.9
CS25MF	7.6	160.43	119.8

capacity. It can be noticed also that larger methanol adsorptive capacity for monoliths with PVA as binder is observed.

2.3. Heat Effects. The important factor of designing systems of adsorptive refrigerating, decisive for their performance, is the thermal effects of the process. Energetic effects of adsorption can be directly determined by calorimetric measurements. They can also be estimated by computing methods from the adsorption isotherms measured at various temperatures (the isosteric heat of adsorption).

For the estimation of the energetic effects characterizing the investigated monoliths, the heat of their wetting by methanol has been determined. The heat of wetting, evolved as a result of the mutual interaction of the molecules of the wetting liquid and the adsorbent surface, is a valuable source of information. The measurements of the heat of wetting were carried out in the original apparatus, which is presented in Figure 4 [12].

For the estimation of the energetic effects characterizing the investigated monoliths, the heat of their wetting by methanol has been determined. The values of the heat of wetting Q , the values of the temperature increase ΔT , dT/dt are collected in Table 3.

Monoliths were characterized by significantly great energetic effects related to the heat of wetting with methanol. Heat effects and determined heat of wetting for monoliths are very high. The largest thermal effect (165,14 J/g) as well as the quickest increase of temperature ($dT/dt = 35,9$) was noted down for monolith CS25MA. For monoliths what use polyvinyl alcohol as binder (PS25MA, CS25MA) the larger heat of wetting than monoliths with polyvinylidene fluoride (PS25MF, CS25MF) is observed.

3. Conclusion

In this study, the porous structure of monoliths was analysed, and adsorption equilibrium and heat effects of wetting by methanol have been determined. We could evaluate of carbon monoliths used for adsorption cooling system.

Pyrolysis of raw materials (carbon precursors), activation by KOH, and monoliths formation give us very attractive materials as an adsorbent for energy storage systems. The investigated monoliths have significantly developed microporous structure. The large specific area of carbonaceous monoliths (about 2000 m²/g) and volume of micropores are observed. The methanol adsorptive capacity of all monoliths is also impressive.

Experimental results show that carbon monoliths materials have very high adsorption capacity of methanol and heat

of wetting, which can improve heat exchange and efficiency in processes of cooling and air conditioning.

The carbonaceous monoliths are also characterized by large energetic effects related to the heat of wetting with methanol. All these advantages improve the performance and efficiency of the system in adsorptive refrigeration.

Acknowledgment

The authors are grateful to AGH (Project no. 11.11.210.125) for its financial support of this work.

References

- [1] F. Meunier, "Adsorptive cooling: a clean technology," *Clean Products and Processes*, vol. 3, no. 1, pp. 8–20, 2001.
- [2] A. P. F. Leite, M. B. Grilo, R. R. D. Andrade, F. A. Belo, and F. Meunier, "Experimental evaluation of a multi-tubular adsorber operating with activated carbon-methanol," *Adsorption*, vol. 11, no. 1, pp. 543–548, 2005.
- [3] H. Marsh and F. Rodriguez-Reinoso, *Activated Carbon*, Elsevier, 2006.
- [4] B. Buczek and E. Wolak, "Nanostructural active carbons from vegetable precursors for heat storage system," *Chemical and Process Engineering*, vol. 30, no. 1, pp. 173–180, 2009.
- [5] G. Cacciola, G. Restuccia, and L. Mercadante, "Composites of activated carbon for refrigeration adsorption machines," *Carbon*, vol. 33, no. 9, pp. 1205–1210, 1995.
- [6] B. S. Akkimaradi, M. Prasad, P. Dutta, and K. Srinivasan, "Effect of packing density and adsorption parameters on the throughput of a thermal compressor," *Carbon*, vol. 40, no. 15, pp. 2855–2859, 2002.
- [7] J. Walendziejewski and J. Trawczyński, "Wpływ kształtu ziarna katalizatora HDS na jego właściwości fizykochemiczne i aktywność hydroodsiarczająca," *Przem Chem*, vol. 74, p. 138, 1993.
- [8] E. Wolak and B. Buczek, "Kierunki badań i praktycznych zastosowań układu węgla aktywno-metanol," *Inżynieria i Aparatura Chemiczna*, vol. 6, pp. 11–16, 2005 (Polish).
- [9] K. Kierzek, H. Machnikowska, G. Gryglewicz, and J. Machnikowski, "Methane storage capacity of monoliths made of activated carbons of different porosity development," in *Proceedings of the International Conference on Coal Science and Technology (ICCS&T'07)*, Nottingham, UK, August 2007, (CD-ROM).
- [10] M. M. Dubinin, "Adsorption properties and microporous structures of carbonaceous adsorbents," *Carbon*, vol. 25, no. 5, pp. 593–598, 1987.
- [11] R. M. A. Roque-Malherbe, *Adsorption and Diffusion in Nanoporous Materials*, CRC Press, Taylor & Francis, Boca Raton, Fla, USA, 2007.
- [12] B. Buczek and E. Wolak, "Potassium hydroxide modified active carbon for adsorptive refrigerators," *Adsorption*, vol. 14, no. 2–3, pp. 283–287, 2008.